Oceanologia

Official Journal of the Polish Academy of Sciences: Institute of Oceanology and Committee on Maritime Research

This journal is supported by the Ministry of Science and Higher Education, Warsaw, Poland

Indexed in: ISI Journal Master List, Science Citation Index Expanded, Scopus, Current Contents, Zoological Record, Thomson Scientific SSCI, Aquatic Sciences and Fisheries Abstracts, DOAJ

IMPACT FACTOR ANNOUNCED FOR 2018 IN THE 'JOURNAL CITATION REPORTS' IS 1.988; 5-year IF is 2.112. CITESCORE ANNOUNCED FOR 2018 IS 2.16

Publisher
Elsevier B.V.
Radarweg 29
1043 NX Amsterdam
The Netherlands

Associate Publisher
Chen Lin
c.lin@elsevier.com
+86-10-8520 8768

ISSN 0078-3234

Oceanologia (2020) 62, 117—125

Available online at www.sciencedirect.com

ScienceDirect

journal homepage: www.journals.elsevier.com/oceanologia

ORIGINAL RESEARCH ARTICLE

Significance of nutrient fluxes via submarine groundwater discharge in the Bay of Puck, southern Baltic Sea

Beata Szymczycha*, Żaneta Kłostowska, Monika Lengier, Lidia Dzierzbicka-Głowacka

Institute of Oceanology, Polish Academy of Sciences, Sopot, Poland

Received 29 August 2019; accepted 30 December 2019
Available online 10 January 2020

KEYWORDS
Biogeochemistry;
SGD;
Coastal zones;
Return flux;
Nitrogen;
Phosphorous;
Bay of Puck (Baltic Sea)

Summary In this study, we collected submarine groundwater discharge (SGD) and seawater samples at six sites in the Bay of Puck, in the southern Baltic Sea, in order to estimate the nutrient distribution in groundwater affected areas. In addition, we estimated nutrient fluxes via SGD, including both fresh SGD (FSGD) and recirculated seawater SGD (RSGD), to the entire Bay of Puck. Phosphate (PO_4^{3-}) concentrations varied significantly among study sites and seasons, while both ammonium (NH_4^+) and nitrates (NO_3^-) concentrations varied only seasonally. The N:P ratio indicated P limitation in most of the samples. The estimated seasonal and annual loads, via SGD, of both dissolved inorganic nitrogen (DIN; 9303 t yr^{-1}) and PO_4^{3-} (950 t yr^{-1}), were the most significant source of nutrients to the Bay of Puck, and notably higher than quantified before (FSGD nutrient loads of 50 t yr^{-1} and 56 t yr^{-1} for DIN and PO_4^{3-}, respectively). The SGD fluxes reported here indicate some of the highest rates of sediment-water fluxes reported in the Baltic Sea. These results suggest that SGD (both FSGD and RSGD) should be considered as source of chemical substances to the marine environment.

* Corresponding author at: Department of Marine Chemistry and Biochemistry, Institute of Oceanology, Polish Academy of Sciences, Powstańców Warszawy 55, 81—712 Sopot, Poland. Tel.:+48587311834.
E-mail address: beat.sz@iopan.gda.pl (B. Szymczycha).
Peer review under the responsibility of the Institute of Oceanology of the Polish Academy of Sciences.

Production and hosting by Elsevier

https://doi.org/10.1016/j.oceano.2019.12.004

1. Introduction

The Baltic Sea is one of the largest, semi-enclosed, brackish seas in the world. It is nearly entirely land-locked and has little water exchangege with the North Sea. The special geographical and oceanographic features of the Baltic Sea make it highly vulnerable to the environmental effects of human activity, not only in its open waters but also in its catchment area, where more than 85 million people live. This high population, together with the area's agricultural and other human activities, such as fossil fuel combustion for energy production and transport, cause large inputs of nutrients, mostly compounds of nitrogen and phosphorus, to enter the Baltic Sea. Due to this excess of nutrients and the accompanying eutrophication, none of the sea's basins currently has a satisfactory environmental status (BACC II, 2015). Several recommendations to reduce nutrient loading into the Baltic Sea have been implemented in the region since the 1970s. However, with further economic development in some countries and an increase in animal protein consumption by humans, the nutrient loads entering the Baltic Sea are likely to increase, which will result in further eutrophication and oxygen depletion (hypoxia).

Although eutrophication in the Baltic Sea was recognized decades ago, some aspects of the process require more consideration and examination (Savchuk, 2018). It has been demonstrated that, depending on the effectiveness of the biogeochemical processes occurring within the coastal zone, the nutrient loads from the land are filtered and do not all enter the open Baltic Sea. Asmala et al. (2017) estimated that the coastal filter of the entire Baltic Sea removes 16% of nitrogen inputs and 53% of phosphorus inputs from adjacent land. Edman et al. (2018) suggested that the average nutrient filter efficiency of the entire Swedish coastline is about 54% and 70% for nitrogen and phosphorus, respectively. However, none of these studies included nutrient loads coming from submarine groundwater discharge (SGD). This is chiefly because the main sources of nutrients in the Baltic Sea region are identified as rivers, point sources, and airborne deposition. However, globally, more and more studies have demonstrated that SGD is a significant source of nutrients entering coastal areas (Valiela et al., 2002; Wang et al., 2015; Zhang et al., 2017). The high concentration of nutrients in SGD is generally caused by nitrogen and phosphorus leakage to an aquifer from agriculture and sewage plants (Bishop et al., 2017).

Several studies have been dedicated to the study of SGD in the Baltic Sea region, with a focus on identifying SGD or groundwater discharge flux (e.g. Lidzbarski, 2011; Peltonen, 2002; Piekarek-Jankowska, 1994; Virtasalo et al., 2019). In the Gulf of Finland, the total amount of fresh SGD (FSGD) was calculated to be 0.6 $km^3\ yr^{-1}$ (Viventsowa and Voronow, 2003). Lidzbarski (2011) estimated the approximate amount of FSGD entering the Gulf of Gdańsk to reach 0.07 $km^3\ yr^{-1}$. Peltonen (2002) estimated the amount of groundwater discharge entering the entire Baltic Sea using a combination of hydrological and hydrogeological methods. The amount of groundwater discharge in the Baltic Sea was small compared with total runoff — around 1% or even less (around 4.4 $km^3\ yr^{-1}$). The above-mentioned calculations relate to FSGD and do not include a recirculated seawater component (RSGD). The perceived low importance of SGD as a source of fresh water has been, most likely, why scientific communities have treated SGD as an insignificant factor influencing the ecosystem of the Baltic Sea. Recently, Krall et al. (2017) indicated, on the basis of a ^{224}Ra mass balance model, that the SGD flow rate ranges from $(5.5 \pm 3.0) \cdot 10^3$ $m^3\ d^{-1}$ to $(950 \pm 520) \cdot 10^3\ m^3\ d^{-1}$. These rates are up to two orders of magnitude higher than those determined from local hydrological models, which consider only the fresh component of SGD.

The Bay of Puck, in the southern Baltic Sea, is an example of the area where SGD has been intensively studied. Piekarek-Jankowska (1994) calculated that the groundwater discharge coming from Quaternary, Neogene, Paleogene, and Upper Cretaceous aquifers into the Bay of Puck equals 0.03 $km^3\ yr^{-1}$. Matciak et al. (2015) observed salinity anomalies in the bottom-water of the Bay of Puck and suggested that the less saline water appeared and changed the seawater salinity. The volume of freshwater must have been significant to reduce the bottom-water salinity. Bublijewska et al. (2017) also investigated outflows of fresh groundwater through a thermal imaging, filtrometer and gradientmeter of the Bay of Puck. In addition, SGD has been recognized as an important source of chemical substances, such as methane, nutrients (mainly ammonium, phosphate, and silicate) and dissolved organic carbon, to the coastal area off town Hel (Donis et al., 2017; Szymczycha et al., 2012, 2014, 2016) and, as such, is a factor affecting the local meiofaunal community (Kotwicki et al., 2014). Given the absence of previous estimates of SGD nutrients, Szymczycha et al. (2012) projected inputs from one study area, located off town Hel, to the entire Bay of Puck, using the FSGD flux rates from Piekarek-Jankowska (1994). The preliminary extrapolations indicated that SGD contributes a significant proportion of the phosphate load but only an insignificant proportion of the dissolved inorganic nitrogen (DIN) load. The estimation was based on the nutrient concentrations in SGD samples characteristic only of FSGD, collected from one study site only. In addition, only the fresh component of SGD was included in the calculations (Szymczycha et al., 2012). There is high uncertainty in the nutrient fluxes obtained by Szymczycha et al. (2012), which could result in an incorrect understanding not only of biogeochemical recycling processes but also of eco-environmental processes in the Bay of Puck.

This study is the second part of the study in this journal on SGD in the Bay of Puck. The first paper addressed hydrochemistry and SGD flux rates into the Bay of Puck, including both FSGD and RSGD (Kłostowska et al., 2019). The calculation was based on a one-dimensional, advection-diffusion model. The SGD rate to the entire Bay of Puck ranged from 9.2 $m^3\ s^{-1}$ to 127.7 $m^3\ s^{-1}$, depending on the discharge area used for extrapolation. These results were up to 130 times higher than the results obtained by Piekarek-Jankowska (1994). The main aim of this study was to quantify the SGD nutrient fluxes including the flux rates obtained by Kłostowska et al. (2019). SGD and seawater samples were collected from 6 sites that significantly differed in terms of land use and hydrogeology, in order to assign represen-

tative nutrient concentrations and include spatial and seasonal variability.

2. Material and Methods

2.1. Description of the study area

The Bay of Puck is located at the western part of the Gulf of Gdańsk and is separated from the open Baltic Sea waters by the Hel Peninsula. The Bay of Puck is divided into inner and outer parts. The bay has a surface area of 362 km^2. It is 2 m deep at the shallowest point – at the most western end – and around 40–50 m deep in the centre of the entrance to the Gulf of Gdańsk. The sediments in the Bay of Puck are highly diverse: medium- and coarse-grain sand appears in the western part and along the Hel Peninsula, while in the outer part of the bay the proportions of mud and clay are high. The Bay of Puck has complex, hydrological (hydrogeological) systems consisting of Cretaceous, Tertiary, and Quaternary aquifers (Kozerski, 2007; Kryza and Kryza, 2006; Piekarek-Jankowska and Łęczyński, 1993). The detailed hydrogeological characteristics and drainage zones of the fresh groundwater in the Bay of Puck were presented by Piekarek-Jankowska (1996). The bay receives fresh water from numerous watercourses such as rivers and springs, including the Płutnica, Reda and Gizdepka Rivers, and the Błądzikowski Stream. Of these, the Reda River has the largest runoff (equalling 5 $m^3\ s^{-1}$). The bay is mainly an agricultural area; however, growing tourism (chiefly due to water sports and beaches), specifically agrotourism, has started to play an important role in the area (Dzierzbicka-Głowacka et al., 2019a). The average monthly precipitation measured in the Hel station from August 2017 to August 2018 ranged from 0.78 mm in May to 6.56 mm in July 2018. Similar variability in average precipitation was observed in Gdynia station (data available from the Institute of Meteorology and Water Management (IMGW) database). The total average precipitation measured in that period was 46.3 mm and 47.3 mm in Hel and Gdynia, respectively.

2.2. Sampling and laboratory analyses

Samples were collected seasonally from autumn 2017 to summer 2018 along the shoreline of the Bay of Puck (Fig. 1). The SGD samples were collected from coastal areas of both the Hel Peninsula (including Hel, Jurata, and Chałupy), and the mainland (including Swarzewo, Puck, and Osłonino) (Fig. 1). Coastal sampling was designed to generate snapshots of the biogeochemical conditions across the freshwater, brackish, and saline zones within the region of groundwater discharge. Coastal samples (SGD, n=86) were collected, at points perpendicular to the shore, at 5-m transects and at a depth of 5 cm. Pore water depth profiles of up to 40 cm were also collected at the most active groundwater discharge sites – in Chałupy and Swarzewo. Seawater samples (n=6) were also collected at each coastal site.

The SGD samples were collected via stainless-steel lances and were brought to the surface by acid-washed Teflon tubing connected to nylon tubing by a peristaltic pump. We used a multimeter (Hach-Lange) to record stabilized values for salinity, dissolved oxygen concentration (DO), oxidation reduction potential (ORP), pH, and temperature. ORP readings were converted to Eh (mV) units by adding 200 to the values (Kroeger et al., 2007). Samples for determination of nutrient concentrations were passed through syringes with polyethersulfone filters (0.45 mm pore size) into acid-washed polyethylene sample bottles. The samples were then stored on ice until they were returned to the laboratory, at which point they were frozen until analyzed.

The nutrients were analyzed using colorimetric methods described by Strickland and Parsons (1967) and Salley et al. (1986). Repeated measurements of the certified reference material (RM-BU; National Metrology Institute of Japan) were performed to assess the accuracy and precision of the nutrient analyses. Nitrate and nitrite were not quantified separately, and in this paper, their sum is referred to as ''nitrate''. DIN is the sum of nitrite, nitrate and ammonium. The average relative standard deviations were 0.4% for $NO_3^- + NO_2^-$, 0.3% for NH_4^+, and 1.4% for PO_4^{3-}. The analyses indicated recoveries of 96.2% for $NO_3^- + NO_2^-$, 98.3% for NH_4^+, and 99.1% for PO_4^{3-}.

2.3. Quantification of the nutrient fluxes via submarine groundwater discharge

In order to estimate the nitrate, ammonium, and phosphate fluxes via SGD we used nutrient concentrations, measured within the salinity gradients and depth profiles, while the SGD was adopted from the previous study by Kłostowska et al. (2019). In short, a vertical, one-dimensional, advection-diffusion model was used to estimate SGD which is based on pore water profiles of chloride (Cl^-) (Schlüter et al., 2004). The identified nutrient concentrations in SGD samples did not have a normal distribution, and therefore we calculated nutrient loads using median concentrations. The seasonal fluxes of nutrients via SGD were calculated by multiplying median concentrations, minimum, and maximum rates (Kłostowska et al., 2019). Finally, the obtained nutrient loads corresponded to the minimum, average and maximum values.

2.4. Statistical analyses

All data were tested for their distribution. We used the Kruskal-Wallis test in order to check the significant differences between the selected groups. The statistical significance of the data sets was determined at $p<0.05$. The analyses were conducted using STATISTICA software. The salinity data did not have a normal distribution, and therefore we used a nonparametric test (Kruskal–Wallis test) based on median values. We divided all data according to their salinity distribution, by study area and season, and we tested whether the median values showed significant differences.

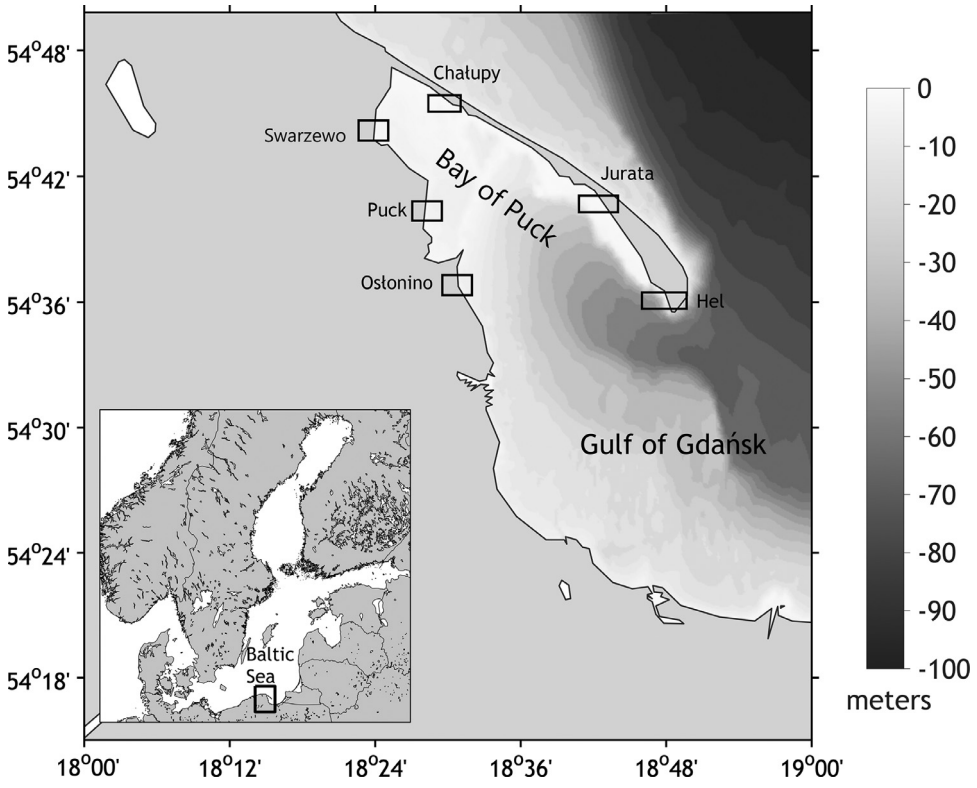

Figure 1 Map showing the Bay of Puck and study sites located on the Hel Peninsula: Hel, Jurata, and Chałupy; and on the mainland: Swarzewo, Puck, and Osłonino.

3. Results

The salinity distribution at the study sites has been characterized in detail by Kłostowska et al. (2019). In summary, the salinity surveys at all sites designated a high spatial variability of salinity, indicating that, in each case and at the time of sampling, a certain portion of the sediments was influenced by SGD. The variability of SGD can be partially attributed to the movement of the interfaces between the fresh and saline water masses caused by short-term scale factors (wind direction and monthly precipitation) and long-term scale factors (large-scale sea level variations) (Kłostowska et al., 2019; Szymczycha et al., 2012).

Within all the collected samples, the oxidation-reduction potential (Eh) ranged from -11.6 to 36 mV, the DO concentrations ranged from 0.7 to 9.8 mg L^{-1}, and the pH levels ranged from 4.9 to 8.3. The nutrient concentrations ranged from 0.2 to 45.1 μmol L^{-1} for PO_4^3, from 3.1 to 488.9 μmol L^{-1} for NH_4^+, and from 0.0 to 506.6 μmol L^{-1} for NO_3^- in all collected samples (Table 1). Szymczycha et al. (2012) obtained similar results for PO_4^{3-} and NH_4^+, though the nitrate concentrations observed in autumn were significantly higher in this study.

Within the minimum and maximum concentrations of NO_3^-, NH_4^+, and PO_4^{3-} in the SGD samples, there were a few outliers and extreme values observed. However, in general, higher concentrations of DIN and PO_4^{3-} occurred in FSGD, and the lowest levels were observed in higher salinity SGD, where there was mixing with recirculated seawater. Usually, in groundwater discharge areas several distinct zones can be distinguished in terms of both (i) water and nutrient sources and (ii) biogeochemical setting and nutrients chemistry (Kroeger and Charette, 2008). Interestingly, in this study, no significant spatial variability of ammonium and nitrates was observed, yet phosphate concentrations differed significantly among the study sites (Fig. 2a). The most significant changes in concentrations were observed seasonally (Fig. 2b). The minimum, maximum, median, and average values of nutrient concentrations are provided in the supplementary material (supplementary material Table 1S). The highest nitrate concentrations were observed in autumn 2017, when the median and average concentrations were 5.6 μmol L^{-1} and 93.8 μmol L^{-1}, respectively. In other seasons, the median and average nitrate concentrations were not higher than 8.0 μmol L^{-1}. In contrast to nitrates, the highest median and average concentrations of ammonium were observed in spring and summer 2018, while the lowest median and average concentrations were observed in autumn 2017, and were 47.5 μmol L^{-1} and 92.3 μmol L^{-1}, respectively. The highest median and average PO_4^{3-} concentrations were observed in spring 2018.

4. Discussion

4.1. Seasonal distribution of nutrients

The seasonal variability of nutrients can be partly explained by the seasonal discharge of nutrients from anthropogenic

Table 1 Summarized statistics for the biogeochemical conditions and nutrient concentrations in the collected SGD and seawater samples. The oxidation-reduction potential (Eh) is given in units of mV, dissolved oxygen (DO) is given in units of mg L^{-1} and nitrate (NO_3^-,), ammonium (NH_4^+), and phosphate (PO_4^{3-}) concentrations are given in units of μmol L^{-1}.

All samples	Salinity	Eh	DO	pH	NO_3^-	NH_4^+	PO_4^{3-}
min-max	0.1–7.2	−11.6–36.0	0.7–9.8	4.9–8.3	0.0–506.6	3.1–488.8	0.2–45.1
median	1.0	9.0	2.9	6.9	5.6	47.5	7.6
average	2.1	8.3	2.5	6.9	93.8	92.3	9.1

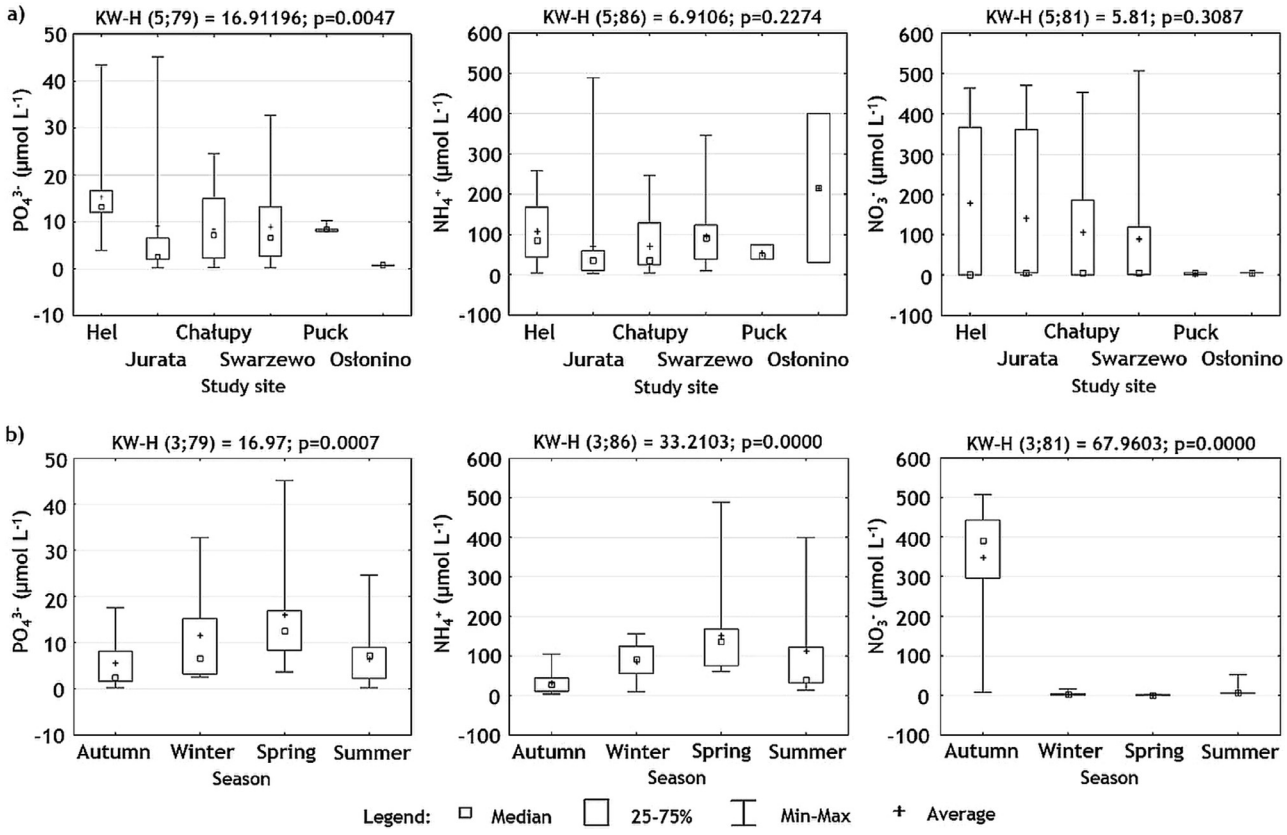

Figure 2 Nitrate (NO_3^-), ammonium (NH_4^+), and phosphate (PO_4^{3-}) concentrations in the collected SGD samples, in units of μmol L^{-1}, divided into a) study sites (Hel, Jurata, Chałupy, Swarzewo, Puck, and Osłonino) and b) seasons. The symbol KW-H indicates the Kruskal–Wallis test.

sources (Bishop et al., 2017; Knee and Paytan, 2011). In comparison to pristine settings, coastal areas affected by human activities frequently have much higher nitrate concentrations (Knee and Paytan, 2011). These concentrations can originate from point sources, such as sewage leaks, chemical facilities, or animal feedlot, and nonpoint sources and local and regional land users (Knee and Paytan, 2011). Several studies have correlated urban development and high population densities to enriched groundwater NO_3^- concentrations (Choi et al., 2007). However, in some suboxic or anaerobic aquifers, ammonium can be the dominant form of DIN (Slomp and Van Cappellen, 2004). It is especially true if ammonium-rich wastewater can intrude to aquifers or if the mineralization and decomposition of nitrogen-containing organic matter occurs under anaerobic conditions (Slomp and Van Cappellen, 2004). Dissolved inorganic phosphorus, typically in the form of phosphate (PO_4^{3-}), can enter groundwater from dissolution of the minerals which make up the aquifer substrate, decomposition of organic matter in soils, or anthropogenic activity (Knee and Paytan, 2011). In the Puck district, the use of nitrogen fertilizers was higher than the average consumption across Poland and in the Pomeranian Voivodeship (Province), while the use of phosphorus fertilizers was higher than in the Pomeranian Voivodeship, but lower when compared to the country as a whole (Dzierzbicka-Głowacka et al., 2019b). The high nitrate concentration in autumn might suggest leakage from agriculture areas on the mainland, while increased ammonium and phosphate concentrations might suggest the presence of a wastewater plume. The increased wastewater plume in spring and summer could be related to population growth as a result of tourism during late spring, summer, and early autumn. Similar to this study, Szymczycha et al. (2012) observed variations in

nutrient concentrations over the year, indicating pronounced seasonal changes in the groundwater nutrient content. Ammonium reached its highest average value in FSGD samples collected during the summer months (239 μmol L^{-1}) and its lowest value (55 μmol L^{-1}) in FSGD samples collected during the spring. The highest average phosphate concentration was observed in FSGD samples collected during the autumn (76.6 μmol L^{-1}), while the lowest was in FSGD samples collected during the spring (49 μmol L^{-1}). The concentrations of NO_3^- and NO_2^- were less temporally variable. Wojciechowska et al. (2018) measured the concentrations of nitrogen and phosphorus compounds during a one-year research period (July 2017–June 2018) at three watercourses – Płutnica River, Reda River, and Błądzikowski Stream – flowing into the Bay of Puck. The concentrations ranged from 5.4 to 44.0 μmol L^{-1} for PO_4^{3-}, from 123.4 to 2388.3 μmol L^{-1} for NO_3^-, and from 2.7 to 53.3 μmol L^{-1} for NH_4^+ (Wojciechowska et al., 2018). Seasonal changes in nutrient concentrations were observed, with maximum concentrations of nitrates in August and September, after the application of fertilizers to land. With regard to SGD the three watercourses displayed similar seasonal trends in changes in nutrient concentrations, however, significantly higher concentrations were observed for nitrates. Leakage of nitrates from fields to surface water and groundwater may occur, but due to geochemical processes taking place in aquifers prior to discharge, the nitrate concentration may actually diminish in groundwater. Phosphates were higher in SGD than in the watercourses. However, similar to the watercourses, the N:P ratio in SGD showed mostly P-limitation (supplementary material Tab. 1S). Liu et al. (2016) also observed higher N:P proportions (175:1) than the Redfield ratio in SGD in the Southern Yellow Sea. It was proposed therein that this non-Redfield input of nutrients may change the nutrient concentrations in coastal waters, destroy the original nutrient structure, and increase the probability of the occurrence of green tides, eutrophication and other ecological problems.

4.2. SGD-derived nutrient fluxes

The chemical loads carried by SGD are typically calculated as the product of the groundwater discharge rate and the average concentration of the element or compound of interest in coastal groundwater. Inherent in those calculations is the assumption that chemical transport through the coastal aquifer and sediments is conservative (Kroeger and Charette 2008). In aquifers, or as the groundwater is moved seaward, processes for removal of several nutrients can occur. Nitrates can be removed via denitrification (Szymczycha et al., 2017), ammonium can be removed via anammox (Wang et al., 2017), and phosphates can be reduced by biological uptake, sorption, and precipitation (Corbett et al., 2002; Szymczycha et al., 2012). As mentioned above, nutrient concentrations in SGD samples did not have a normal distribution and contained few outliers. This is most probably due to different sources of nutrients, and the variable influence of N and P removal or addition processes. Therefore, to estimate nutrient fluxes via SGD, we used the seasonal median nutrient concentration of each compound and the seasonal flow rate obtained from a one-dimensional, advection-diffusion model (Kłostowska et al., 2019). Fig. 3 presents the average nutrient load for each season based on the minimum and maximum SGD rate for each season (Kłostowska et al., 2019). In general, the nutrient loads showed significant seasonal variability. The highest nitrate loads were observed in autumn and spring, and were 10.2 × 10^6 mol yr^{-1} and 10.3 × 10^6 mol yr^{-1}, respectively. The highest ammonium and phosphate loads were observed in spring, and were 249.2 × 10^6 mol yr^{-1} and 22.3 × 10^6 mol yr^{-1}, respectively . The obtained results may indicate the response of SGD-derived nutrients levels to both agriculture activities (Dzierzbicka-Głowacka et al., 2019b; Wojciechowska et al., 2018) and waste water leakage (Dzierzbicka-Głowacka et al., 2019a). In addition, the obtained nutrient fluxes were significantly higher than those obtained by Szymczycha et al. (2012) (Table 2). In our previous study, the concentrations used to calculate fluxes were characteristic only of the small areas of the Bay of Puck and were based on the FSGD rate. It is most probable that this approach led to the underestimated results. In Table 2 the SGD nutrient fluxes are compared to other sources, and SGD turned out to be the most important source of nutrients. Nutrient input to the Bay of Puck via SGD is a potentially important source and must be considered when assessing the nutrient budgets. Liu et al. (2016) also observed increased nutrient fluxes via SGD (both FSGD and RSGD) on the background of other sources, in the Southern Yellow Sea, however, in comparison to this study they were approximately 600 times higher for DIN and 80 times lower for PO_4^{3-}. The Southern Yellow Sea, though, has a surface area of 30.9 × 10^4 km^2, which is approximately 90 times bigger than the Bay of Puck. Wang et al. (2017) suggested that nutrients carried by SGD account for 95–97% of the oxidized inorganic nitrogen, 79–87% of the phosphate, and 97–98% of the silicate in the nutrient source in Sanya Bay. SGD may compensate for at least 90% of the oxidized inorganic nitrogen, 15% of the phosphate, and 60% of the silicate in the nutrient sink in that bay and satisfy all nitrogen and silicate requirements for phytoplankton growth in the bay in the dry season.

Table 2 Sources of dissolved inorganic nitrogen (DIN) and phosphates (PO_4^{3-}) in the Bay of Puck, in units of t yr^{-1}.

Source	DIN	PO_4^{3-}
Atmosphere*	485	18
Rivers and point sources*	220	70
Resuspension*	825	97
F SGD**	50	56
SGD (F+S)***	9303	950

* Korzeniewski, 2003
** Szymczycha et al., 2012
*** this study

The impact of SGD on the Baltic Sea ecosystem is still not well understood. Accurate determination of SGD-driven nutrient loads to the Baltic Sea should represent an important area of future research, especially with regard to predicting the future ecosystem status of the Baltic Sea. Nutrient mass balance models or budgets still indicate sediments as the major Baltic Sea sink. In Table 3 the nutrient

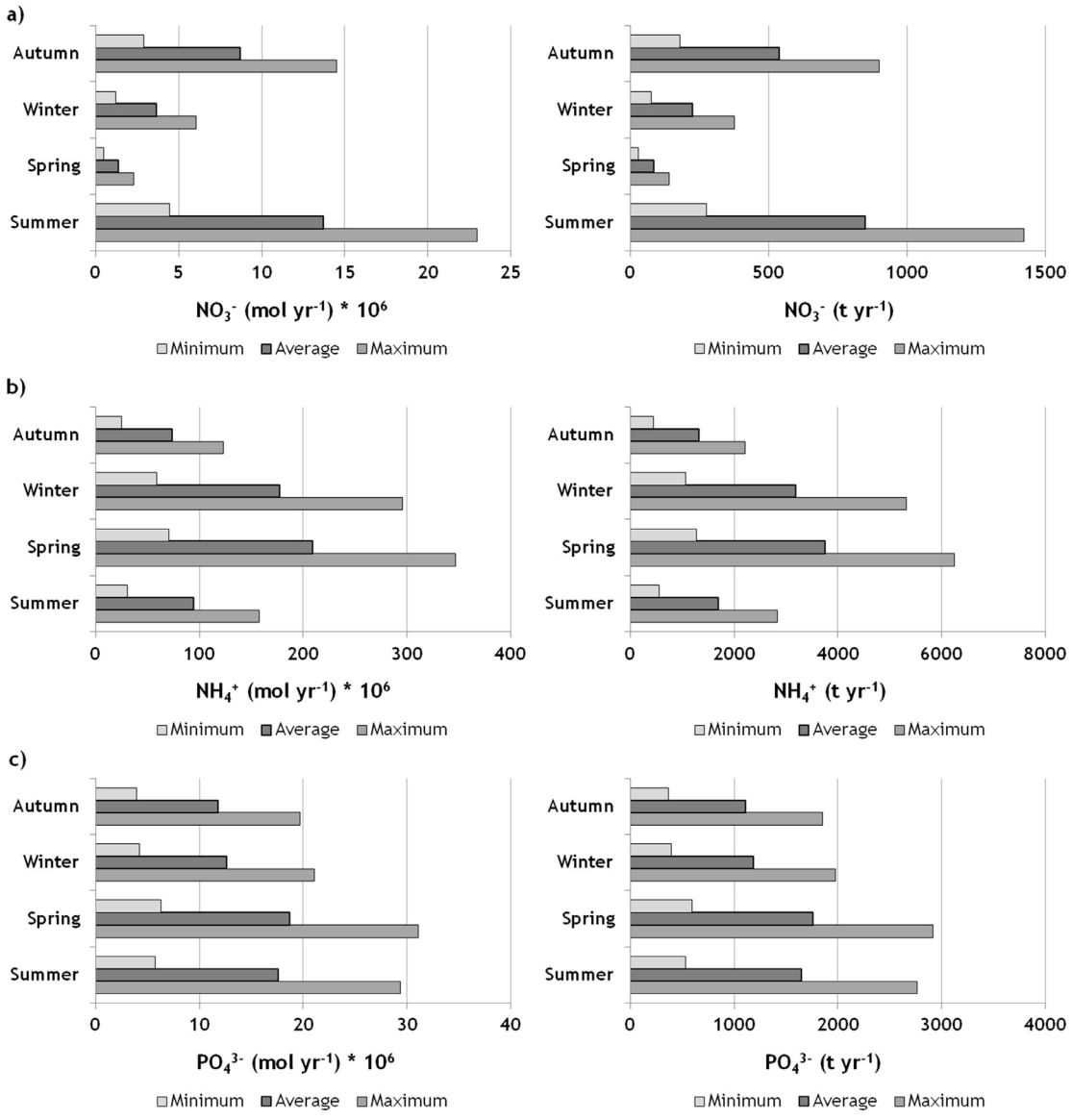

Figure 3 Seasonal fluxes of nutrients to the Bay of Puck a) nitrate (NO_3^-), b) ammonium (NH_4^+), c) phosphate (PO_4^{3-}).

Table 3 The sediment return fluxes in different Baltic Sea regions, in units of μmol m^{-2} d^{-1}.

Area	NO_3^-	NH_4^+	PO_4^{3-}	Reference
Bay of Puck	4.4–1378.0	213.2–21368.5	15.2–1912.9	This study
mix-max	637.0	11746.6	1366.0	
average				
Gulf of Gdańsk	nd**	nd	2.12–37.1	Łukawska-Matuszewska and
min-max				Burska, 2011
Gdańsk Deep	nd	1003.2±283.2	100.8±38.4	Graca et al., 2006
average±SD*				
Gulf of Finland	−360–480	0–1250	nd	Conley et al., 1997
min-max				

* standard deviation
** no data

return fluxes in different Baltic Sea regions are listed. SGD is presented also as the sediment-water flux and, interestingly, contributes significantly to DIN on the top of other studies. This study shows that in groundwater-impacted areas sediments are a significant source of nutrients. At present, little is known regarding SGD in different Baltic Sea coastal areas, and even less in terms of the accompanying fluxes of nutrients. However, it has to be acknowledged that in coastal areas, where variations in bottom water oxygen concentrations occur, SGD can be an additional driver of phosphate release. Given the large quantities of inorganic phosphorus compounds stored in Baltic Sea sediments, reduced oxygen conditions together with SGD would greatly increase sediment water phosphorus fluxes. In this study, high phosphate fluxes occurred in spring and summer, and might exacerbate both spring and summer algal blooms.

5. Conclusions

Phosphate (PO_4^{3-}) concentrations significantly varied among study sites and seasons while both ammonium (NH_4^+) and nitrate (NO_3^-) concentrations varied only seasonally. The N:P ratio indicated P limitation in most of the samples. The obtained nutrient fluxes via SGD are higher than in our previous study including only a FSGD component. In addition, the obtained results indicate that SGD is an important driver of nutrient release from sediments, in comparison to sediment return fluxes reported in other Baltic Sea areas. Eutrophication areas are primarily located near the coast (e.g. Diaz and Rosenberg, 2008) due to land-based inputs. SGD can significantly contribute to Baltic Sea nutrient concentrations, thus increasing spring and summer algal blooms.

Acknowledgments

The reported results were obtained within the framework of the statutory activities of the Institute of Oceanology of the Polish Academy of Sciences and the following research projects: WaterPUCK BIOSTRATEG3/343927/3/NCBR/2017 financed by the National Centre for Research and Development (NCBiR) within the BIOSTRATEG III program; PharmSeepage 2016/21/B/ST10/01213 and SALSA 2015/19/B/ST10/02120 funded by the Polish National Science Centre. In addition, we thank Maciek Janecki for technical support.

Supplementary materials

Supplementary material associated with this article can be found, in the online version, at doi:10.1016/j.oceano.2019.12.004.

References

Asmala, E., Carstensen, J., Conley, D.J., Slomp, C.P., Stadmark, J., Voss, M., 2017. Efficiency of the coastal filter: Nitrogen and phosphorus removal in the Baltic Sea. Limnol. Oceanogr. 62 (S1), S222—S238, https://doi.org/10.1002/lno.10644.

BACC II Author Team, 2015. Second Assessment of Climate Change for the Baltic Sea Basin. Springer, Chem 501 pp., https://doi.org/10.1007/978-3-319-16006-1.

Bishop, J.M., Glenn, C.R., Amato, D.W., Dulai, H., 2017. Effect of land use and groundwater flow path on submarine groundwater discharge nutrient flux. J. Hydrol.: Reg. Stud. 11, 194—218, https://doi.org/10.1016/j.ejrh.2015.10.008.

Bublijewska, E., Łęczyński, L., Marciniak, M., Chudziak, Ł., Kłostowska, Ż., Zarzeczańska, D., 2017. In situ measurements of submarine groundwater supply from the Puck Lagoon. Prz. Geol. 65 (11/2), 1173—1178.

Choi, W.-J., Han, G.-H., Lee, S.-M., Lee, G.-T., Yoon, K.-S., Choi, S.-M., Ro, H.-M., 2007. Impact of land-use types on nitrate concentration and δ 15N in unconfined groundwater in rural areas of Korea. Agr. Ecosyst. Environ. 120, 259—268, https://doi.org/10.1016/j.agee.2006.10.002.

Conley, D.J., Stockenberg, R., Carman, R.W., Johnstone, R.W., Rahm, L., Wulff, F., 1997. Sediment-water Nutrient Fluxes in the Gulf of Finland, Baltic Sea. Estuar. Coast. Shelf S. 45 (5), 591—598, https://doi.org/10.1006/ecss.1997.0246.

Corbett, D.R., Dillon, K., Burnett, W., Schaefer, G., 2002. The spatial variability of nitrogen and phosphorus concentration in a sand aquifer influenced by onsite sewage treatment and disposal systems: a case study on St. George Island, Florida. Environ. Pollut. 117 (2), 337—345, https://doi.org/10.1016/S0269-7491(01)00168-3.

Diaz, R., Rosenberg, R., 2008. Spreading Dead Zones and Consequences for Marine Ecosystems. Science 321 (5891), 926—929, https://doi.org/10.1126/science.1156401.

Donis, D., Janssen, F., Liu, B., Wenzhöfer, F., Dellwig, O., Escher, P., Spitzy, A., Böttcher, M.E., 2017. Biogeochemical impact of submarine groundwater discharge on coastal surface sands of the southern Baltic Sea. Estuar. Coast. Shelf S. 189, 131—142, https://doi.org/10.1016/j.ecss.2017.03.003.

Dzierzbicka-Głowacka, L., Janecki, M., Dybowski, D., Szymczycha, B., Obarska-Pempkowiak, H., Wojciechowska, E., Zima, P., Pietrzak, S., Pazikowska-Sapota, G., Jaworska-Szulc, B., Nowicki, A., Kłostowska, Ż., Szymkiewicz, A., Galer-Tatarowicz, K., Wichorowski, M., Białoskórski, M., Puszkarczuk, T., 2019a. A New Approach for Investigating the Impact of Pesticides and Nutrient Flux from Agricultural Holdings and Land-Use Structures on Baltic Sea Coastal Waters. Pol. J. Environ. Stud. 28 (4), 2531—2539, https://doi.org/10.15244/pjoes/92524.

Dzierzbicka-Głowacka, L., Pietrzak, S., Dybowski, D., Białoskórski, M., Marcinkowski, T., Rossa, L., Urbaniak, M., Majewska, Z., Juszkowska, D., Nawalany, P., Pazikowska-Sapota, G., Kamińska, B., Selke, B., Korthals, P., Puszkarczuk, T., 2019b. Impact of agricultural farms on the environment of the Puck Commune: Integrated agriculture calculator — CalcGosPuck. PeerJ 7, e6478, https://doi.org/10.7717/peerj.6478.

Edman, M, Eilola, K, Almroth-Rosell, E, Meier, H.E.M., Wåhlström, I., Arneborg, L., 2018. Nutrient Retention in the Swedish Coastal Zone. Front. Mar. Sci. 5, 415, https://doi.org/10.3389/fmars.2018.00415.

Graca, B., Witek, Z., Burska, D., Białkowska, I., Łukawska-Matuszewska, K., Bolałek, J., 2006. Pore water phosphate and ammonia below the permanent halocline in the south-eastern Baltic Sea and their benthic fluxes under anoxic conditions. J. Marine Syst. 63, 141—154, https://doi.org/10.1016/j.jmarsys.2006.06.003.

Institute of Meteorology and Water Management (IMGW) database (https://dane.imgw.pl/data; accessed on 21.08.2019).

Kłostowska, Ż., Szymczycha, B., Lengier, M., Zarzeczańska, D., Dzierzbicka-Głowacka, L., 2019. Hydrogeochemistry and magnitude of SGD in the Bay of Puck, southern Baltic Sea. Oceanologia 62 (1), 1—11, https://doi.org/10.1016/j.oceano.2019.09.001.

Knee, K.L., Paytan, A., 2011. 4.08 — Submarine Groundwater Discharge: A Source of Nutrients, Metals, and Pollutants to the Coastal Ocean, Reference Module in Earth Systems and

Environmental Sciences. Treatise on Estuarine and Coastal Science 4, 205—233, https://doi.org/10.1016/B978-0-12-374711-2.00410-1.

Korzeniewski, K. (Ed.), 2003. Zatoka Pucka. Instytut Oceanografii Uniwersytetu Gdańskiego, Gdynia.

Kotwicki, L., Grzelak, K., Czub, M., Dellwig, O., Gentz, T., Szymczycha, B., Böttcher, M.E., 2014. Submarine groundwater discharge to the Baltic coastal zone: Impacts on the meiofaunal community. J. Marine Syst. 129, 118—126, https://doi.org/10.1016/j.jmarsys.2013.06.009.

Kozerski, B., 2007, Gdański System Wodonośny, 1st edn. In: Jaworska-Szulc, B., Piekarek-Jankowska, H., Pruszkowska, M., Przewłócka, M. (Eds.). Wyd. PG, Gdańsk, 113 pp.

Krall, L., Trezzi, G., Garcia-Orellana, J., Rodellas, V., Mörth, C.-M., Andersson, P., 2017. Submarine groundwater discharge at Forsmark, Gulf of Bothnia, provided by Ra isotopes. Mar. Chem. 196, 162—172, https://doi.org/10.1016/j.marchem.2017.09.003.

Kroeger, K.D., Charette, M.A., 2008. Nitrogen biogeochemistry of submarine groundwater discharge. Limnol. Oceanogr. 53 (3), 1025—1039, https://doi.org/10.4319/lo.2008.53.3.1025.

Kroeger, K.D., Swarzenski, P.W., Greenwood, Wm.J., Reich, C., 2007. Submarine groundwater discharge to Tampa Bay: Nutrient fluxes and biogeochemistry of the coastal aquifer. Mar. Chem. 104 (1—2), 85—97, https://doi.org/10.1016/j.marchem.2006.10.012.

Kryza, J, Kryza, H, 2006. The analytic and model estimation of the direct groundwater flow to Baltic Sea on the territory of Poland. Geologos 10, 153—166.

Lidzbarski, M., 2011. Groundwater Discharge in the Baltic Sea Basin. In: Uścinowicz, Sz. (Ed.), Geochemistry of Baltic Sea Surface and Sediments. Polish Geological Institute-National Research Insitute, Warsaw, Poland, 138—145.

Liu, J., Su, N., Wang, X., Du, J., 2016. Submarine groundwater discharge and associated nutrient fluxes into the Southern Yellow Sea: A case study for semi-enclosed and oligotrophic seas — implication for green tide bloom. J. Geophys. Res. Oceans 122, 139—152, https://doi.org/10.1002/2016JC012282.

Łukawska-Matuszewska, K., Burska, D., 2011. Phosphate exchange across the sediment-water interface under oxic and hypoxic/anoxic conditions in the southern Baltic Sea. Oceanol. Hydrobiol. St. 40 (2), 57—71, https://doi.org/10.2478/s13545-011-0017-4.

Matciak, M., Bieleninik, S., Botur, A., Podgórski, M., Trzcińska, K., Dragańska, K., Jaśniewicz, D., Kurszewska, A., Wenta, M., 2015. Observations of presumable groundwater seepage occurrence in Puck Bay (the Baltic Sea). Oceanol. Hydrobiol. St. 44 (2), 267—272, https://doi.org/10.1515/ohs-2015-0025.

Peltonen, K., 2002. Direct Groundwater Inflow to the Baltic Sea. TemaNord, Nordic Councils of Ministers, Copenhagen, Netherlands, 79 pp.

Piekarek-Jankowska, H., Łęczyński, L., 1993. Morfologia dna. In: Korzeniewski, K. (Ed.), Zatoka Pucka. Fundacja Rozwoju UG, Gdańsk, 222—281.

Piekarek-Jankowska, H., 1994. Zatoka Pucka jako Obszar Drenażu Wód Podziemnych. Wyd. UG, Gdańsk, 31—32 Rozp. Monogr. 204 pp.

Piekarek—Jankowska, H., 1996. Hydrochemical effects of submarine groundwater discharge to the Puck Bay (southern Baltic Sea, Poland). Geographica Polonica 67, 103—119.

Salley, B.A., Bradshaw, J.B., Neillo, B.J., 1986. Results of Comparative Studies of Preservation Techniques for Nutrient Analysis on Water Samples. Virginia Institute of Marine Science, Gloucester Point, The United States, 89 pp.

Savchuk, O.P., 2018. Large-Scale Nutrient Dynamics in the Baltic Sea, 1970—2016. Front. Mar. Sci. 5, 95, https://doi.org/10.3389/fmars.2018.00095.

Schlüter, M., Sauter, E.J., Andersen, C.E., Dahlgaard, H., Dando, P.R., 2004. Spatial distribution and budget for submarine 749 groundwater discharge in Eckernförde Bay (Western Baltic Sea). Limnol. Oceanogr. 49 (1), 157—167, https://doi.org/10.4319/lo.2004.49.1.0157.

Slomp, C.P., Van Cappellen, P., 2004. Nutrient inputs to the coastal ocean through submarine groundwater discharge: controls and potential impact. J. Hydro. 295, 64—86, https://doi.org/10.1016/j.jhydrol.2004.02.018.

Strickland, J.D.H., Parsons, T.R., 1967. A Practical Handbook of Seawater analysis. Fisheries Research Board of Canada Bulletin, Ottawa, 328 pp.

Szymczycha, B., Vogler, S., Pempkowiak, J., 2012. Nutrient fluxes via submarine groundwater discharge to the Bay of Puck, southern Baltic Sea. Sci. Total Environ. 438, 86—93, https://doi.org/10.1016/j.scitotenv.2012.08.058.

Szymczycha, B., Maciejewska, A., Winogradow, A., Pempkowiak, J., 2014. Could submarine groundwater discharge be a significant carbon source to the southern Baltic Sea? Oceanologia 56 (2), 327—347, https://doi.org/10.5697/oc.56-2.327.

Szymczycha, B., Kroeger, K.D., Pempkowiak, J., 2016. Significance of groundwater discharge along the coast of Poland as a source of dissolved metals to the southern Baltic Sea. Mar. Pollut. Bull. 109 (1), 151—162, https://doi.org/10.1016/j.marpolbul.2016.06.008.

Szymczycha, B., Kroeger, K.D., Crusius, J., Bratton, J.F., 2017. Depth of the vadose zone controls aquifer biogeochemical conditions and extent of anthropogenic nitrogen removal. Water Res. 123, 794—801, https://doi.org/10.1016/j.watres.2017.06.048.

Valiela, I., Bowen, J.L., Kroeger, K.D., 2002. Assessment of models for estimation of land-derived nitrogen loads to shallow estuaries. Appl. Geochem. 17, 935—953, https://doi.org/10.1016/S0883-2927(02)00073-2.

Virtasalo, J.J., Schröder, J.F., Luoma, S., Majaniemi, J., Mursu, J., Scholten, J.C., 2019. Hydrographic data, surface seawater radon-222 concentration, and loss on ignition and caesium-137 values of sediment samples from the Hanko submarine groundwater discharge site, northern Baltic Sea. PANGAEA, Finland https://doi.org/10.1594/PANGAEA.898674.

Viventsowa, E.A., Voronow, A.N., 2003. Groundwater discharge to the Gulf of Finland (Baltic Sea): ecological aspects. Environ. Ecol. 45, 221—225.

Wang, X., Li, H., Jiao, J.J., Barry, D.A., Li, L., Luo, X., Wang, C., Wan, L., Wang, X., Jiang, X., Ma, Q., Qu, W., 2015. Submarine fresh groundwater discharge into Laizhou Bay comparable to the Yellow River flux. Sci. Rep. 5, https://doi.org/10.1038/srep08814.

Wang, S., Radny, D., Huang, S., Zhuang, L., Zhao, S., Berg, M., Jetten, M.S.M., Zhu, G., 2017. Nitrogen loss by anaerobic ammonium oxidation in unconfined aquifers soils. Sci. Rep. 7, 40173, https://doi.org/10.1038/srep40173.

Wojciechowska, E., Nawrot, N., Matej-Łukowicz, K., Gajewska, M., Obarska-Pempkowiak, H., 2018. Seasonal changes of the concentrations of mineral forms of nitrogen and phosphorus in watercourses in the agricultural catchment area (Bay of Puck, Baltic Sea, Poland). Water Supply 19 (3), 986—994, https://doi.org/10.2166/ws.2018.190.

Zhang, Y., Li, H., Xiao, K., Wang, X., Lu, X., Zhang, M., An, A., Qu, W., Wan, L., Zheng, C., Wang, X., Jiang, X., 2017. Improving Estimation of Submarine Groundwater Discharge Using Radium and Radon Tracers: Application in Jiaozhou Bay, China. J. Geophys. Res.-Oceans 122 (10), https://doi.org/10.1002/2017JC013237.

Oceanologia (2020) 62, 126—138

Available online at www.sciencedirect.com

ScienceDirect

journal homepage: www.journals.elsevier.com/oceanologia

ORIGINAL RESEARCH ARTICLE

Indian Ocean wind speed variability and global teleconnection patterns

Mourani Sinha[a,*], **Somnath Jha**[b], **Paromita Chakraborty**[c]

[a] *Department of Mathematics, Techno India University, Saltlake, Kolkata, India*
[b] *Department of Home, Swami Vivekananda State Police Academy, Barrackpore, India*
[c] *National Centre for Medium Range Weather Forecasting, Noida, Uttar Pradesh, India*

Received 23 February 2019; accepted 11 October 2019
Available online 30 October 2019

KEYWORDS
Wind speed;
Sea surface temperature;
Monsoon;
Wavelet coherence;
Indian Ocean;
Global teleconnection

Summary The influence of the local sea surface temperature (SST) and remote ENSO (El Niño-Southern Oscillation) indices on the wind speed (WS) data were explored for the Indian Ocean region. Relationships among the parameters were studied using spatial correlation plots and significant correlation ranges. Two months (July and January) representing opposite monsoon phases were selected for analysis for the period 1950—2016. There was a significant negative correlation between WS and SST over the Bay of Bengal (BOB) during July. Although different ENSO indices correlated differently in different areas of the Indian Ocean, the region off the coast of Sri Lanka was most significantly teleconnected. The southwest monsoon locally impacted the WS and SST relationship and the WS parameter was remotely teleconnected in both the monsoon seasons. Further empirical orthogonal function (EOF) analysis was applied on the 67 years WS data of the BOB region to extract the dominant mode representing maximum variability of the total variance. The temporal pattern of the first principal component (PC1) of WS data was linked to the North Atlantic Oscillations in January and the Atlantic Multidecadal Oscillation in July respectively. The continuous wavelet power spectra of the PC1 of WS showed significant regions in the 2—4-year band resembling the ENSO variability. Wavelet coherence applied between PC1 of WS and the ENSO indices showed greatest values for January in the 8—16-year band and for July in the 0—4-year band. A close relationship was established between the WS variability in BOB and the ENSO indices.

* Corresponding author at: Department of Mathematics, Techno India University, Saltlake, Kolkata 700091, India. Tel.: +91 9350904194
E-mail address: mou510@gmail.com (M. Sinha).
Peer review under the responsibility of the Institute of Oceanology of the Polish Academy of Sciences.

ELSEVIER Production and hosting by Elsevier

https://doi.org/10.1016/j.oceano.2019.10.002

1. Introduction

Several studies reveal the impact of the Indian Ocean in shaping the climate on both regional and, global scales (Dong and McPhaden, 2018; Kug and Kang, 2006; Okomura and Deser, 2010). There are modes of climate variability, ranging from intraseasonal to interannual and, also longer time scales. The ENSO is the most significant interannual mode of tropical coupled ocean-atmosphere phenomenon (McPhaden, 2002). The inverse relationship between Indian summer monsoon rainfall and, ENSO (Kumar et al., 1999) was modulated on decadal timescales and, its changes were linked to Atlantic Multidecadal Oscillation (Chen et al., 2010), aerosol impacts (Azad and Rajeevan, 2016) and, zonal shifts in ENSO's center from eastern Pacific to central Pacific (Fan et al., 2017). The summer variability over the Indo-Northwest Pacific region was studied (Xie et al., 2016) in reference to the occurrence of a large-scale anomalous anticyclone in post-El Niño summers over the tropical Northwest Pacific and North Indian oceans. Li et al. (2017) discussed various theories relating to the formation, development, and maintenance of the western North Pacific anomalous anticyclone that transfers El Niño's impact on East Asian climate. Sun and Wang, (2019) revealed a connection between the summer climate of the Three-River-Source region of China and the global climate system in terms of North Atlantic Oscillation, western Indian Ocean sea surface temperature, El Niño-Southern Oscillation, and the East Asian summer monsoon. During an El Niño event, there were positive SST anomalies over the Indian Ocean from 3 to 6 months after SST anomalies peak in the tropical Pacific (Klein et al., 1999). The interannual Indian Ocean SST variations were positively correlated with the eastern equatorial Pacific Ocean SST anomalies with a lag of about 4 months (Venzke et al., 2000). Li et al. (2001) analyzed that although the eastern Pacific SST affects the monsoon on the ENSO time scale (2—7 year), the Indian monsoon rainfall had significant positive correlations with the Indian Ocean SST on the tropical biennial oscillation time scale (2—3 year). The warming in the Indian Ocean produced an easterly wind stress anomaly over Indonesia and, the western Pacific during the mature phase of El Niño (Kug and Kang, 2006). The easterly wind stress anomaly over the western Pacific, as mentioned above, lead to the rapid termination of El Niño and a fast transition to La Niña by generating upwelling Kelvin waves. The Indian Ocean warming which was effective for relatively strong El Niños resulted in La Niña one year after the mature phase of El Niño (Kug and Kang, 2006). A review was performed based on the climatic importance of Indian Ocean SST and the role of ocean dynamics in their generation (Schott et al., 2009). A possible role of the Indian Ocean was identified in the asymmetric evolution of surface wind anomalies over the western Pacific (Okomura and Deser, 2010). The relationship between sea surface temperature anomaly (SSTA) and, wind energy input in the Pacific Ocean was studied from 1949 to 2003 (Huang and Qiao, 2009). They showed a strong negative correlation between SSTA and, local wind energy input to surface waves in most of the domains at low and middle latitudes. Huang and Qiao (2009) also indicated wind energy input may play an important role in the interannual and decadal variability of the wind parameter in the Pacific Ocean by regulating vertical mixing processes in the upper ocean. The varied wind energy input over the past decades may lead to varied mixing in the upper ocean which may affect the SST and, then the global climate system. The role of the Indian Ocean was observed in initiating El Niño events, their development and fading away (Annamalai et al., 2005). Dong and McPhaden (2018) suggested warm SSTs in the Indian Ocean in 2014 weakened westerly wind anomalies in the Pacific which suppressed the development of the El Niño in 2014. Goswami et al. (2006) identified warm (cold) phases of the Atlantic Multidecadal Oscillation (AMO) producing increased (decreased) Indian summer monsoon rainfall and negative (positive) North Atlantic Oscillation (NAO) events resulting in below (above) normal monsoon rainfall. Through the NAO they established a fundamental link between the North Atlantic and the Indian summer monsoon. Thus the Indian Ocean is connected with the different climatic oscillations around the world.

In this study, the variability of the wind speed parameter in the BOB region was explored for possible teleconnection patterns across the globe. Several statistical tools like empirical orthogonal function analysis, wavelet analysis, wavelet coherence, significant correlation ranges have been used and are discussed in methodology. The wind speed is a major parameter for monitoring and predicting extreme weather patterns. It affects the development of surface waves and storm surges. In this paper, the impact of local SST and remote ENSO indices on the wind speed parameter in the Indian Ocean region was discussed. A connection was explored linking the relationship between WS variability and the ENSO indices in the BOB region.

2. Data and methodology

NCEP/NCAR reanalysis monthly mean surface (0.995 sigma level) WS data were available at 2.5-degree latitude by 2.5-degree longitude global grid. WS data were extracted for July and January for the Indian Ocean region covering the area from 30°E to 120°E and 30°N—70°S for the period 1950—2016. NOAA Extended Reconstructed Sea Surface Temperature V4 data were available at 2.0-degree latitude by a 2.0-degree longitude global grid. SST data were extracted for the above region for the same period. WS and SST data were interpolated to 1.0-degree by 1.0-degree spatial resolution for uniformity in dimension required during the statistical analysis.

For the present work the month of July, representing the southwest monsoon and the month of January, representing the northeast monsoon, have been analyzed for particular years of the period 1950—2016 and classified as normal or El Niño or La Niña months following the Oceanic Nino Index (ONI) standard. The ONI is a three month average of SST anomalies in the Niño 3.4 region (5°N—5°S, 120°—170°W), based on 30-year base periods updated every 5 years. The extended reconstructed sea surface temperature, version 5 (ERSSTv5) has been updated and improved (Huang et al., 2017) and used for the ONI calculation. Average SST for the Niño 3.4 region was calculated for each month, and further averaged using values from previous and following months. This three-month average was compared with the 30-year average and the difference was the ONI value for

the three-month considered. NOAA uses ONI as the primary index for identifying El Niño (warm) and La Niña (cool) events in the tropical Pacific. When the index is 0.5°C or higher, El Niño conditions exist and when the index is −0.5°C or lower, La Niña conditions exist.

Three ENSO indices namely, Southern Oscillation Index (SOI), Multivariate ENSO Index (MEI) and NINO3.4 have been correlated with WS in the present study. Monthly data for the above three indices were accessed from http://www.esrl.noaa.gov/psd/data/climateindices/. The SOI index is the difference between the atmospheric pressure at sea level at Tahiti and Darwin. Prolonged periods of negative (positive) SOI values coincide with El Niño (La Niña) episodes. SST anomalies equal to or greater than ±0.5°C in the Niño 3 region (5°N—5°S,150°W—90°W) are indicative of ENSO warm (cold) phase conditions. The Multivariate ENSO Index (MEI) is based on the six main observed variables over the tropical Pacific. These six variables are sea-level pressure, zonal and meridional components of the surface wind, sea surface temperature, surface air temperature, and total cloudiness fraction of the sky. The MEI integrates more information than SST based indices and thus is more comprehensive.

Spatial correlation plots were generated depicting regions statistically significant for WS, SST and ENSO indices. To identify the significant correlation ranges probability or p-values were calculated at the 0.05 significance level. If the p-value is less than 0.05 then the Pearson correlation coefficient is considered statistically significant (Fisher, 1992).

The NAO index is based on the surface sea-level pressure difference between the subtropical high and the subpolar low. The polar pressure is taken near Iceland and the subtropical pressure is taken near the Azores. The first mode of rotated EOF analysis of monthly mean 500 millibar height anomaly data from 1950 to 2000 over 0—90°N latitude is considered as the NAO pattern (Barnston and Livezey, 1987). The AMO is a 65—80-year cycle of North Atlantic sea surface temperatures for 1856—1999 (Kerr, 2000). AMO warm phases occurred during 1860—1880 and 1940—1960, and cool phases during 1905—1925 and 1970—1990 (Enfield et al., 2001). The NAO index for January and AMO index for July for the period 1950—2016 have been compared with the PC1 of WS.

In the first experiment, spatial correlation plots were generated between WS and SST data for all the 67 years to analyze the local impact. To explore how WS is influenced by remote ENSO indices (SOI, MEI, NINO3.4) respective spatial correlation plots were generated. Instead of all the 67 years together next particular years representing normal, El Niño and La Niña phases were taken into account for analysis. The above experiments were repeated and correlation plots generated for the particular phases.

Empirical orthogonal function (EOF) analysis is a powerful tool for data compression and dimensionality reduction. The EOF technique decomposes the space-time distributed data into spatial modes ranked by their temporal variances. Since EOFs have been introduced in atmospheric science by Lorenz (1956), it has become a statistical tool of fundamental importance in the atmosphere, ocean, and climate science for exploratory data analysis and dynamical mode reduction. Spectral analysis is a tool for extracting embedded structures in a time series. In particular, Fourier analysis has been used extensively by researchers for extracting deterministic structures from time series but is incapable of detecting non-stationary features often present in geophysical time series. Wavelet analysis can extract transient features embedded in time series, with a wavelet power spectrum representing variance (power) of a time series as a function of time and period. Since the work of Torrence and Compo (1998), wavelet analysis has been applied extensively to geophysical time series such as the indices for the North Atlantic Oscillation (Olsen et al., 2012) and Arctic Oscillation (Jevrejeva et al., 2003). The application of wavelet coherence and cross-wavelet analyses (Grinsted et al., 2004), moreover, has proven useful in relating geophysical time series to other time series (Jevrejeva et al., 2003).

Considering July and January representing the southwest and northeast monsoon periods, EOF analysis is applied on WS data for the BOB region (78°E to 98°E and 25°N to 5°N) for the analyzed period. The time series of the first principal components were linked to the NAO and AMO to establish a relationship between the WS variability and the ENSO indices. The localized intermittent periodicities can be identified on the time series data using continuous wavelet transforms, that expands a time series into a time-frequency space. The periodicity of the first principal components (PC1) of WS data was assessed using the wavelet method. Continuous wavelet power spectra were generated for analysis. Finally, wavelet coherence was applied to PC1 of WS and the ENSO indices to examine possible relationships between them. Coherence plots were generated between the two time series in both the time and frequency domain.

3. Results and discussions

3.1. Relationship between WS data, SST data and ENSO indices for IO

WS data were explored for the Indian Ocean region (30°E—120°E and 30°N—70°S) for July and January representing the southwest and northeast monsoons respectively. Spatial correlation plots were generated at a 95% confidence interval to analyze how WS, SST, and ENSO indices were related. To test if the correlation values are statistically significant, p-values were calculated (Table 1) at 0.05 significance level. Figure 1a and b depict significantly correlated regions for January and July representing opposite monsoon phases between WS and SST for all the 67 years. Considering the northern Indian Ocean, there was a negative correlation between WS and SST over BOB during July. It indicated higher (lower) WS at lower (higher) SST values. Figures 2—4 show how WS and SST correlated differently in the study area during the normal, El Niño and La Niña years for the above mentioned period. During the normal years (July) there was a significant negative correlation over BOB which fades away from La Niña to El Niño years. During the El Niño years, there was a significant negative correlation between WS and SST off the west coast of India in January and a positive correlation off the coast of Sri Lanka during July. During the La Niña years, there was a significant negative correlation over parts of BOB during July and a significant positive correlation off the Somali coast during January. Thus during El Niño events, the influence of local SST on the WS value decreased in the northern Indian Ocean in July whereas it increased on the

Table 1 p-values calculated to test if the correlation (r) is significant at 0.05 significance level for the period 1950–2016 (N=67). First all the January (JAN) months and all the July (JUL) months were considered. Then the above period was classified as normal or El Niño or La Niña year and tested.

(r)	All JAN 1950–2016 N=67 p-value	All JUL 1950–2016 N=67 p-value	Normal JAN N=22 p-value	Normal JUL N=33 p-value	El Niño JAN N=25 p-value	El Niño JUL N=17 p-value	La Niña JAN N=20 p-value	La Niña JUL N=17 p-value
1	0.00001	0.00001	0.00001	0.00001	0.00001	0.00001	0.00001	0.00001
0.8	0.00001	0.00001	0.00001	0.00001	0.00001	0.0001	0.00001	0.0001
0.6	0.00001	0.00001	0.0031	0.0002	0.0015	0.0109	0.0052	0.0109
0.5	0.00001	0.00001	0.0178	0.0030	0.0109	0.0409	0.0248	0.0409
0.45	0.00013	0.00013	0.0356	0.0086	0.0240	0.0699	0.0465	0.0699
0.4	0.0008	0.0008	0.0651	0.0211	0.0476	0.1116	0.0805	0.1116
0.35	0.0037	0.0037	0.1103	0.0458	0.0863	0.1684	0.1303	0.1684
0.3	0.0136	0.0136	0.1749	0.0898	0.1451	0.2420	0.1988	0.2420
0.25	0.0413	0.0413	0.2618	0.1606	0.2281	0.3331	0.2878	0.3331
0.2	0.1046	0.1046	0.3722	0.2644	0.3378	0.4415	0.3979	0.4415
0	1	1	1	1	1	1	1	1
−0.2	0.1046	0.1046	0.3722	0.2644	0.3378	0.4415	0.3979	0.4415
−0.25	0.0413	0.0413	0.2618	0.1606	0.2281	0.3331	0.2878	0.3331
−0.3	0.0136	0.0136	0.1749	0.0898	0.1451	0.2420	0.1988	0.2420
−0.35	0.0037	0.0037	0.1103	0.0458	0.0863	0.1684	0.1303	0.1684
−0.4	0.0008	0.0008	0.0651	0.0211	0.0476	0.1116	0.0805	0.1116
−0.45	0.00013	0.00013	0.0356	0.0086	0.0240	0.0699	0.0465	0.0699
−0.5	0.00001	0.00001	0.0178	0.0030	0.0109	0.0409	0.0248	0.0409
−0.6	0.00001	0.00001	0.0031	0.0002	0.0015	0.0109	0.0052	0.0109
−0.8	0.00001	0.00001	0.00001	0.00001	0.00001	0.0001	0.00001	0.0001
−1	0.00001	0.00001	0.00001	0.00001	0.00001	0.00001	0.00001	0.00001

(If the p-value is less than the significance level $\alpha = 0.05$ then r is significant).

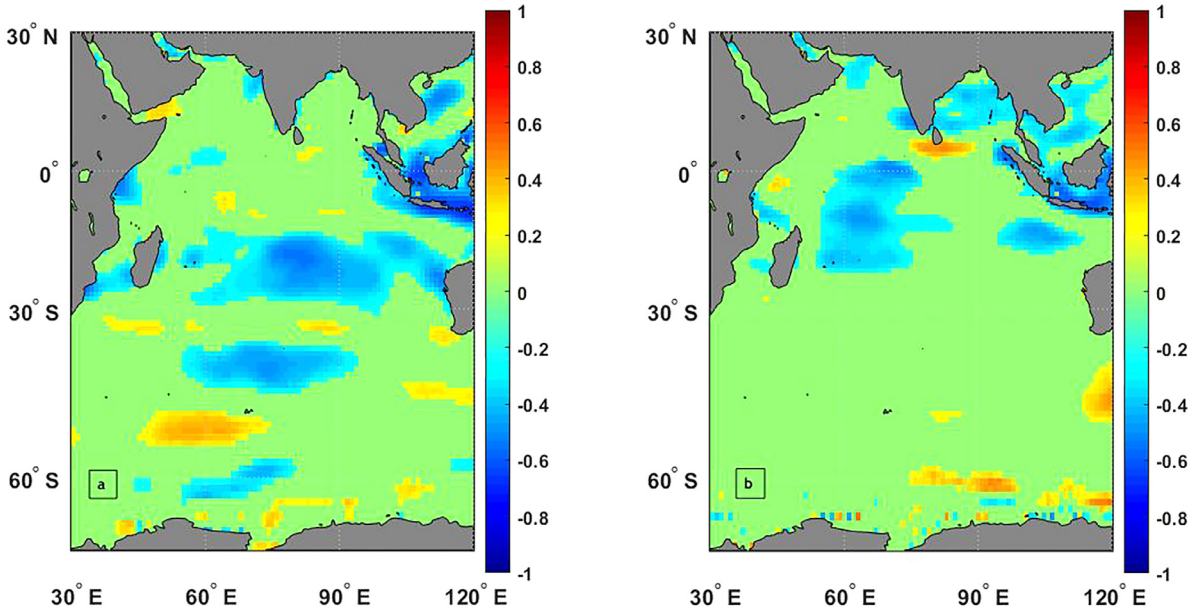

Figure 1 Significantly correlated regions between WS and SST at 95% confidence interval for (a) all January months (1950–2016) and (b) all July months (1950–2016).

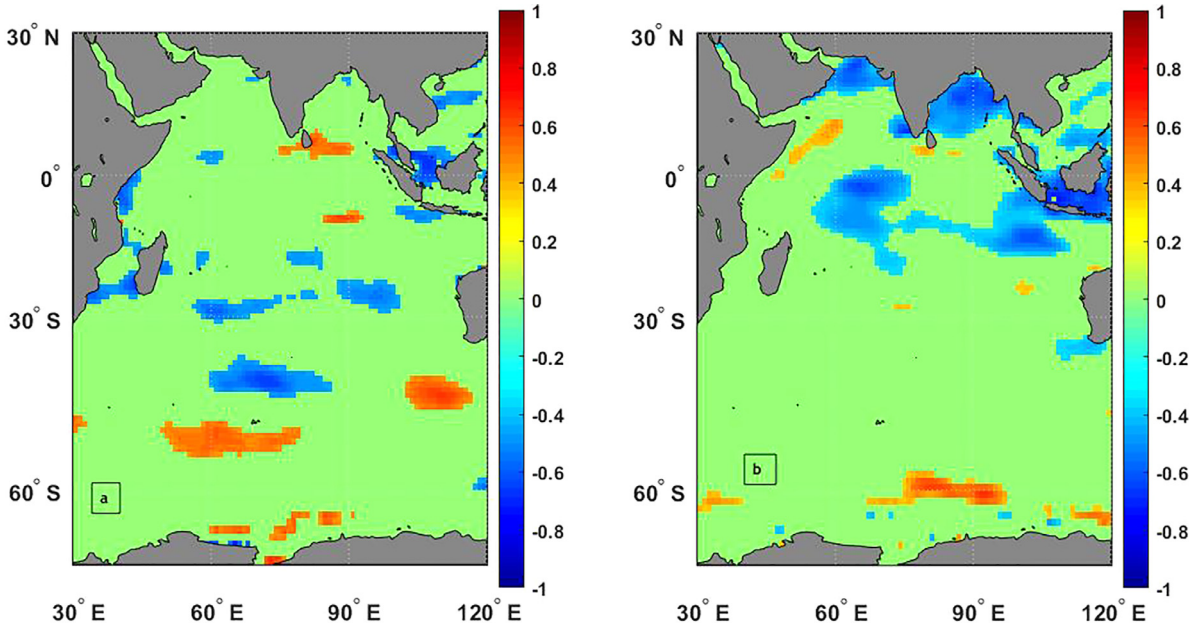

Figure 2 Significantly correlated regions between WS and SST at 95% confidence interval for (a) normal January months (22 years) and (b) normal July months (33 years).

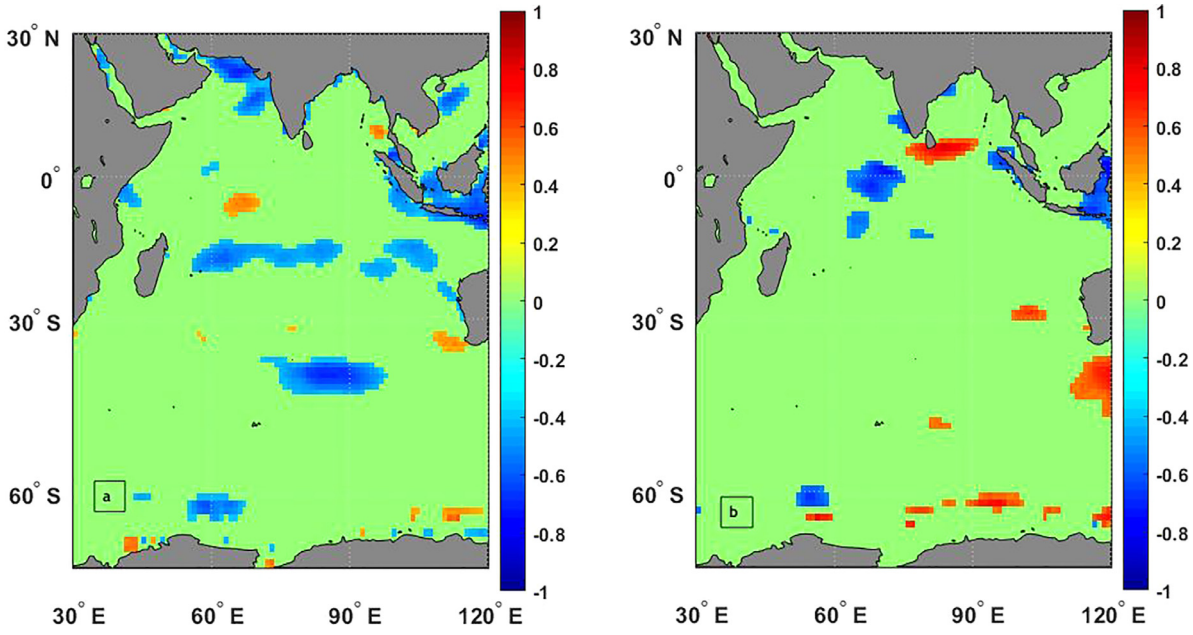

Figure 3 Significantly correlated regions between WS and SST at 95% confidence interval for (a) El Niño January months (25 years) and (b) El Niño July months (17 years).

west coast of India in January. Between 30°S and 60°S, there were both positively and negatively significantly correlated regions in January considering the normal years. These patches of correlated regions again faded away from La Niña to El Niño years. In July the Southern Indian Ocean was however uncorrelated in terms of WS and SST parameters.

The six plots in Fig. 5 depicts significant correlation regions between WS and the ENSO indices namely SOI, MEI and NINO3.4 for the normal January and July months respectively. During January there was a negative correlation between WS and SOI off Sri Lanka and southern part of the west coast of India and positive correlation with MEI and NINO3.4 for the same regions. As per the definitions of the indices opposite correlation signs were justified. The correlation patterns indicated the teleconnection features of the wind parameters with the ENSO indices. Figure 6 gave similar six plots for El Niño years and subsequently Fig. 7 for La Niña years. During the January El Niño episodes, the WS was significantly positively correlated with the MEI and NINO3.4 indices over a large area off Sri Lanka. In July the

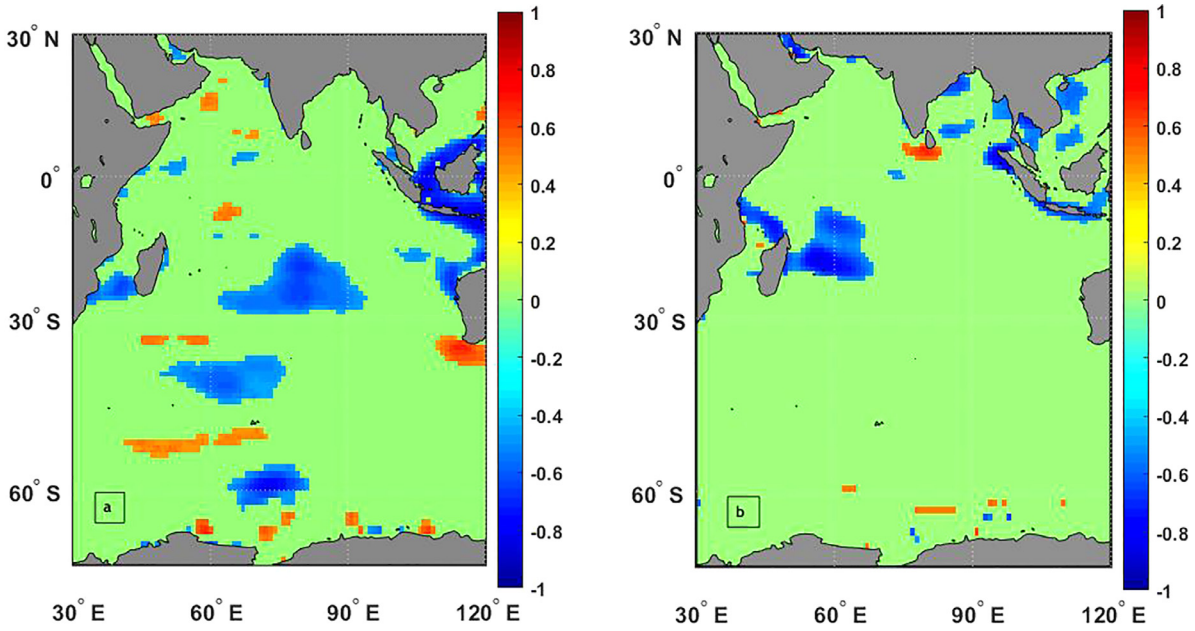

Figure 4 Significantly correlated regions between WS and SST at 95% confidence interval for (a) La Niña January months (20 years) and (b) La Niña July months (17 years).

influence was over a smaller area. However, such an impact was absent during the La Niña years.

3.2. EOF analysis and wavelet analysis for WS data of BOB region

EOF analysis was applied to the WS data of the BOB region (25°N to 5°N and 77.5°E to 100°E) for the analyzed period to extract the dominant mode representing the maximum variability. For January the first eigenmode accounted for 42.9% of the total variability of the WS data for the BOB region. Figure 8c depicts the spatial pattern of the first eigenmode of WS data. The maximum loading at the central BOB may be attributed to the northeast monsoon winds. The other eigenvectors contributed insignificantly and thus were not discussed. The PC1 corresponding to the first eigenmode is given in Fig. 8a, in which the maximum value occurred in 2007, while a deep fluctuation giving a minimum value in 2008. The high (low) peaks in the temporal pattern exhibited by the WS-PC1 corresponds to the negative (positive) NAO events (Fig. 8e). Thus, in general, an inverse relationship (negative correlation) between the NAO and the WS in the BOB region during the winter monsoon was observed, although there were few instances of positive correlation in the late 1960s and the mid-1980s. For July the first eigenmode accounted for 49.1% of the total variability of the WS data and Fig. 8d depicts maximum loading at the head Bay. The corresponding PC1 is given in Fig. 8b. The temporal pattern gave a maximum in 1962, a minimum in 1964. Again an inverse relationship can be established between the July WS-PC1 and the AMO which have a decreasing trend during 1962 and an increasing trend during 1965 (Fig. 8f). Standardized time series were considered in Fig. 8e and f for effective comparison.

The PC1 of WS data corresponding to January and July were normalized by their standard deviation and then were decomposed using the Morlet wavelet function. The Morlet wavelets are non-orthogonal wavelet functions that are useful for time series analysis. The continuous wavelet power spectra were generated with the cone of influence, where edge effects become important. Anything outside it limits the ability to interpret the results. The black contour enclosed regions of greater than 95% confidence for a red-noise process with a lag-1 coefficient of 0.52 (January) and 0.21 (July). The continuous wavelet power spectra generated exhibits significant regions in the 2—4-year band which corresponds to the ENSO oscillations having 2—7-year periodicity. In Fig. 9a representing the power spectrum in January the maximum power occurred during 2007 in the 2—4-year period. This matches the maximum value during 2007 in Fig. 8a representing the PC1 of WS data. Similarly, for July, the maximum power in Fig. 9b matches with the maximum value in Fig. 8b corresponding to the period 1962—64. Thus for the 67 years BOB WS data, the red-noise wavelet power spectra exhibits 2—4-year period oscillations which maybe teleconnected with the ENSO variability occurring in the 2—7-year band.

Wavelet coherence is a measure of the correlation between two time-series in the time-frequency plane. The relative phase relationship between the two time-series is shown with arrows. This can also be interpreted as a lead or a lag. Phase arrows pointing right or left represents an in-phase or anti-phase relationship. For two time-series X and Y phase arrows pointing down say X leading Y by 90 degrees. A lead of 90 degrees can also be interpreted as a lag of 270 degrees or a lag of 90 degrees relative to the anti-phase (opposite sign). Figure 10a and b displays the wavelet coherence between PC1-WS data and SOI index for January and July respectively for the analyzed period. In January and July, WS and SOI were in anti-phase (when one is maximum, the other is minimum and vice versa) in the 32-year period but were very insignificantly. From Fig. 10a,

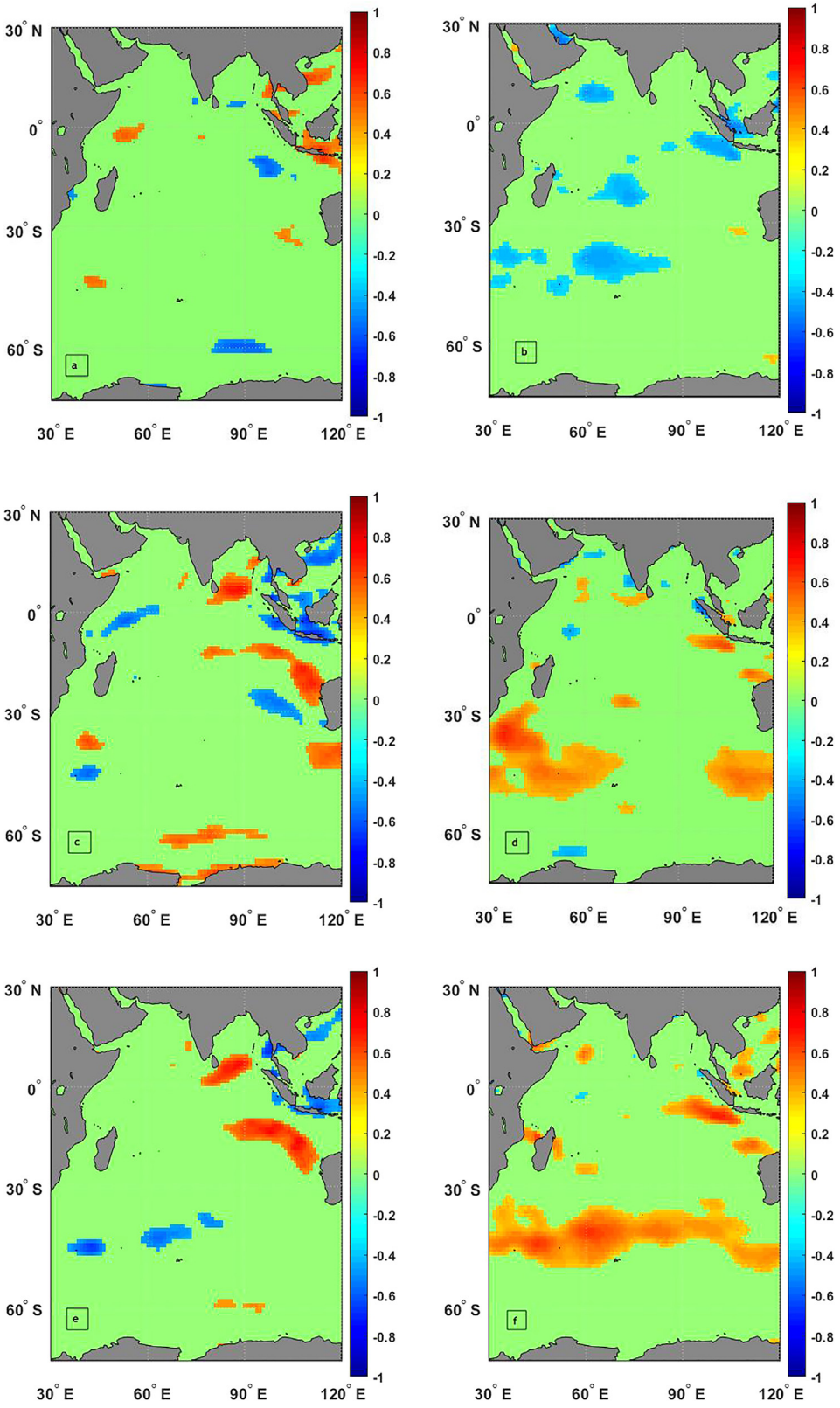

Figure 5 Significantly correlated regions at 95% confidence interval (a) between WS and SOI for 22 normal January months and (b) between WS and SOI for 33 normal July months and (c) between WS and MEI for 22 normal January months and (d) between WS and MEI for 33 normal July months and (e) between WS and NINO3.4 for 22 normal January months and (f) between WS and NINO3.4 for 33 normal July months.

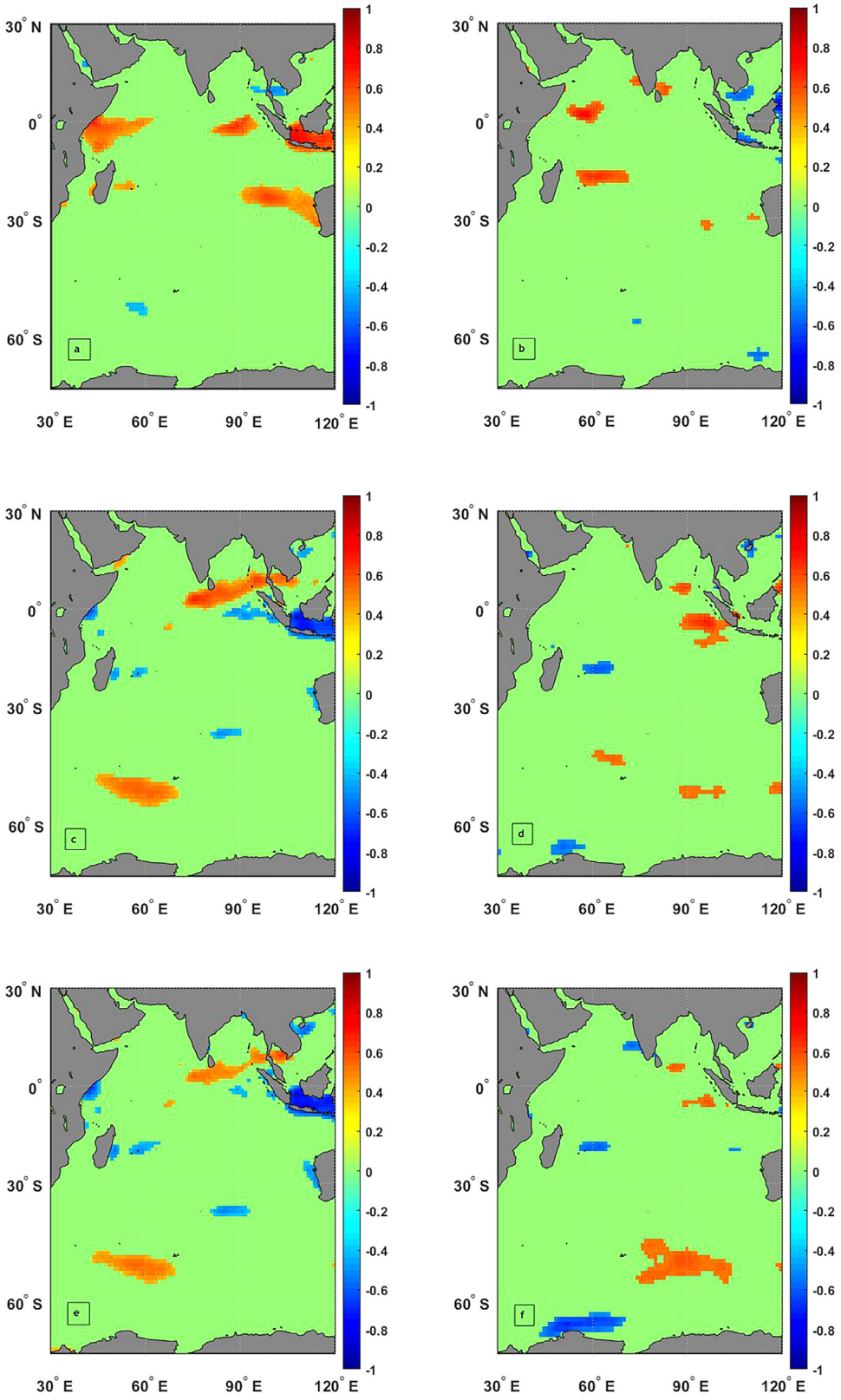

Figure 6 Significantly correlated regions at 95% confidence interval (a) between WS and SOI for 25 El Niño January months and (b) between WS and SOI for 17 El Niño July months and (c) between WS and MEI for 25 El Niño January months and (d) between WS and MEI for 17 El Niño July months and (e) between WS and NINO3.4 for 25 El Niño January months and (f) between WS and NINO3.4 for 17 El Niño July months.

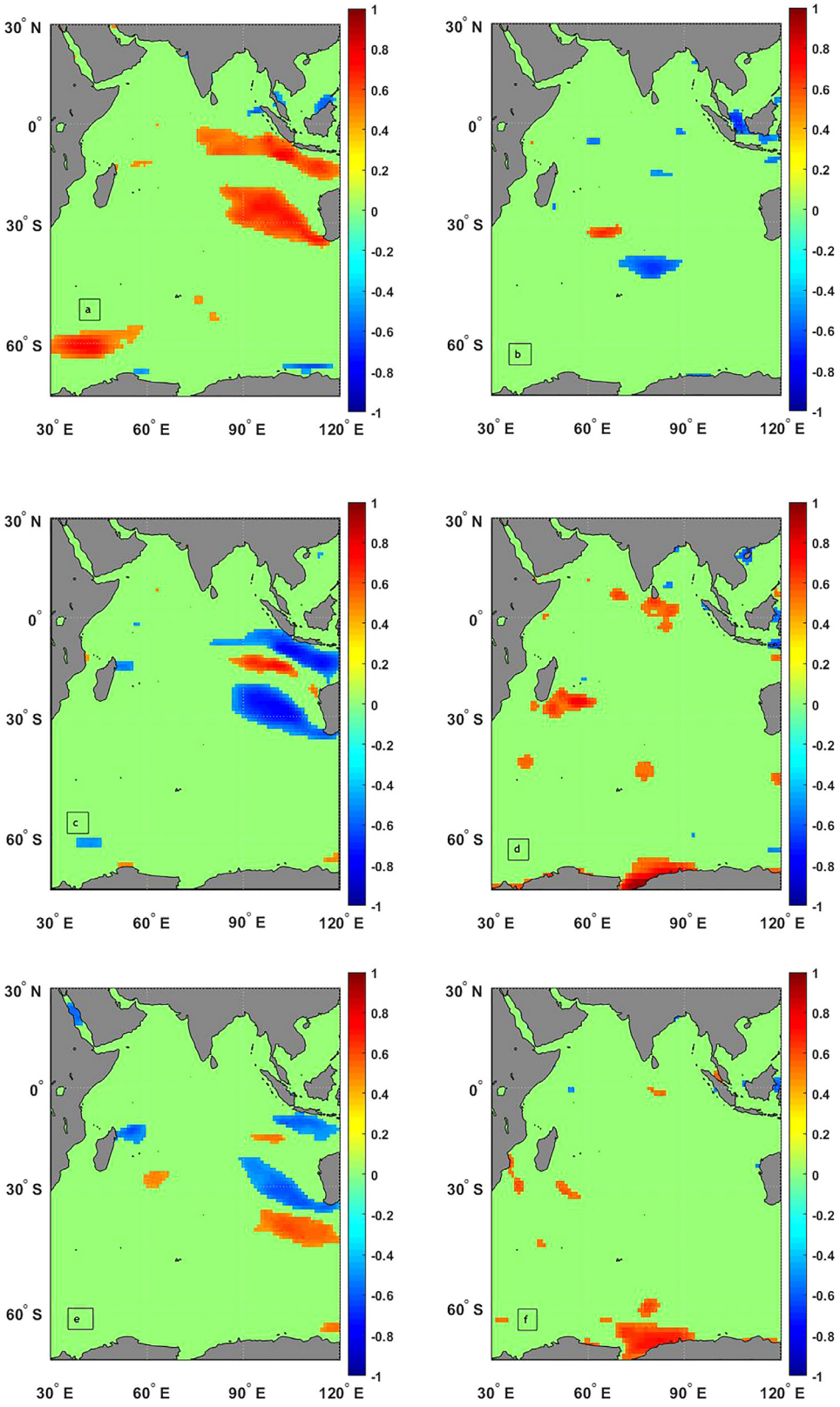

Figure 7 Significantly correlated regions at 95% confidence interval (a) between WS and SOI for 20 La Niña January months and (b) between WS and SOI for 17 La Niña July months and (c) between WS and MEI for 20 La Niña January months and (d) between WS and MEI for 17 La Niña July months and (e) between WS and NINO3.4 for 20 La Niña January months and (f) between WS and NINO3.4 for 17 La Niña July months.

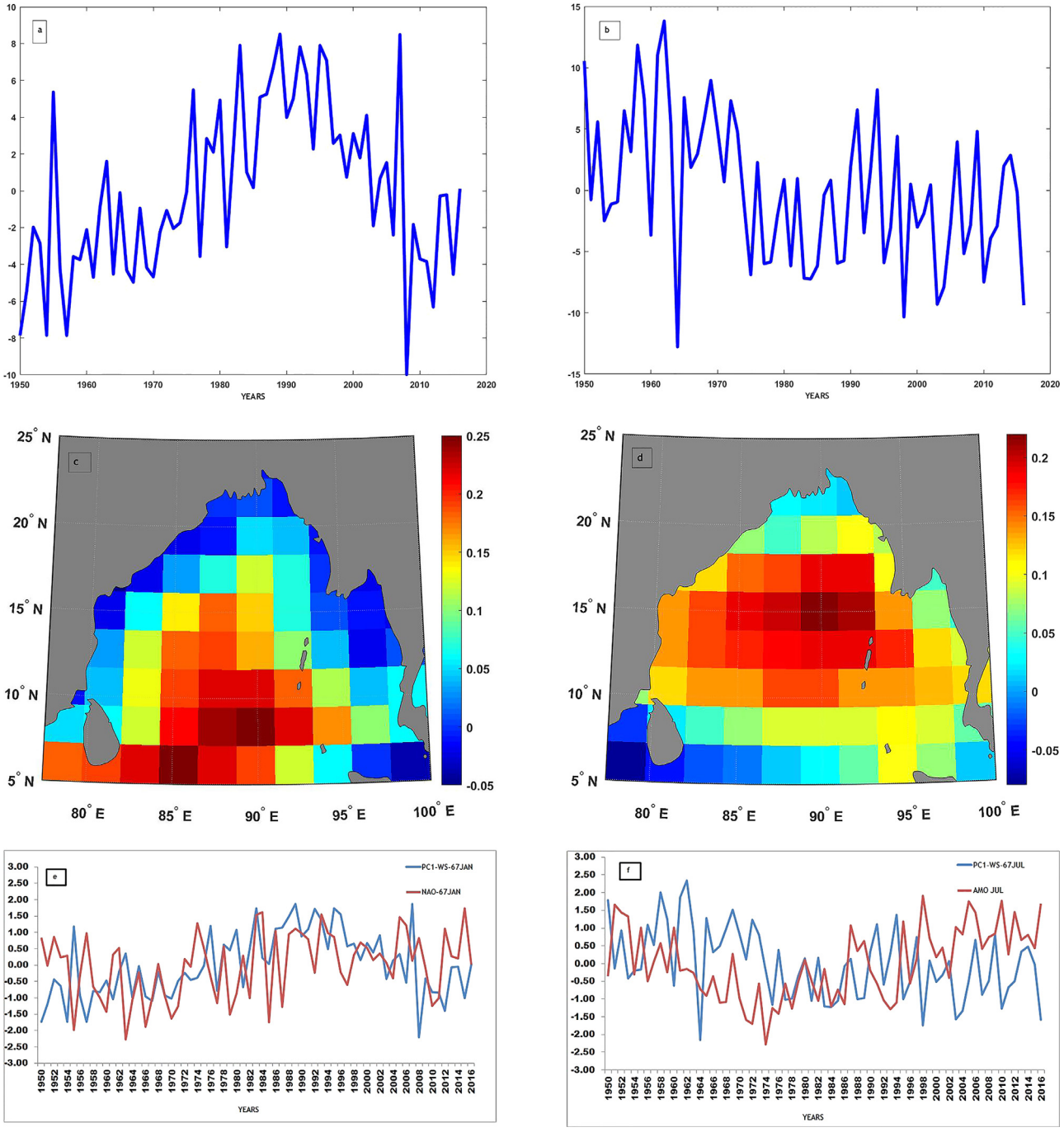

Figure 8 For the BOB WS data (1950—2016) (a) the PC1 for January and (b) the PC1 for July and (c) the first spatial eigenmode (42.9%) for January and (d) the first spatial eigenmode (49.1%) for July and (e) comparison between standardized WS-PC1 and NAO for January and (f) comparison between standardized WS-PC1 and AMO for July.

it can be said, the coherency was greater than 0.8 during 1955—65 (from x-axis) in the 8—16-year band (from y-axis). Figure 10b shows higher coherency regions in the 0—4-year period with both in-phase and anti-phase relationships. Figure 11a and b gave the wavelet coherence between PC1-WS data and MEI index for January and July respectively for the analyzed period with similar periodicities. In Fig. 11a there were again higher coherency regions in the 8—16-year period but with both in-phase and anti-phase relationships. Fig. 11b shows the in-phase relationship in the 0—4-year period along with higher coherency. Figure 12a and b gave similar plots with the NINO3.4 index. In January (Fig. 12a) and July (Fig. 12b) there were regions with higher coherency in the 8—16-year band and 0—4-year period respectively. An 8-year quasi-cyclic behavior of NAO may be the cause of the 8—16-year band coherency of WS variability with the ENSO indices. In July there was an in-phase relationship between WS and the ENSO indices in the 0—4-year band. This may

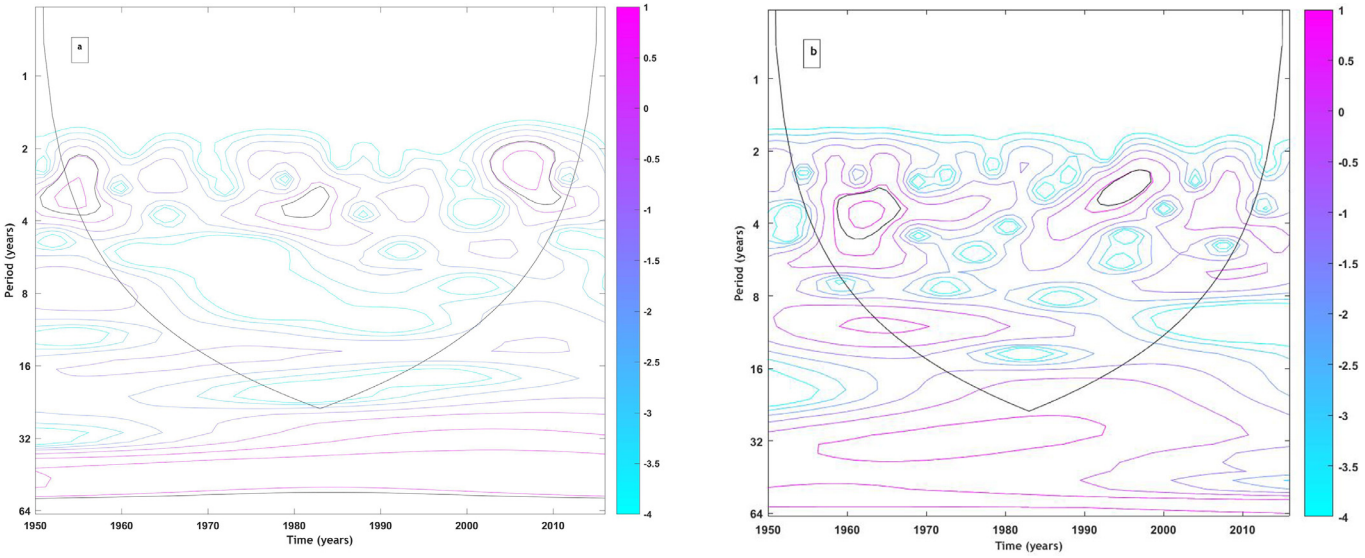

Figure 9 The continuous wavelet power spectrum of WS-PC1 along with the black contours which encircle the 5% significance regions, using a red-noise background spectrum, for (a) January and (b) July.

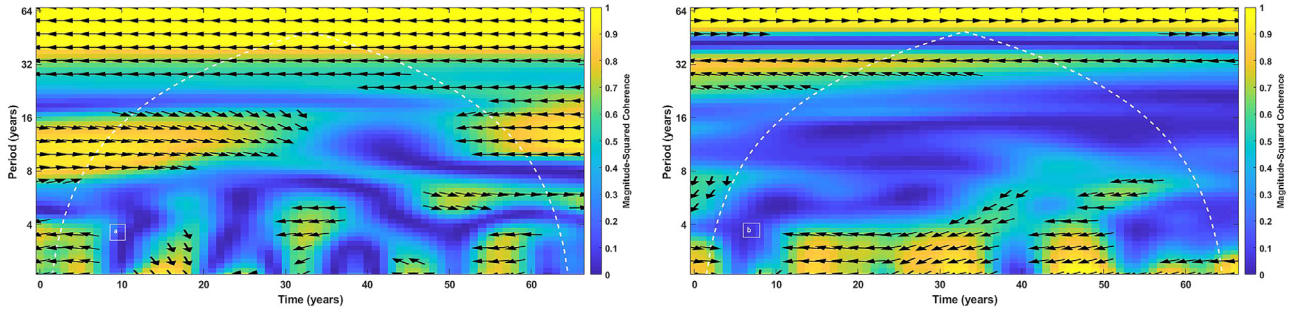

Figure 10 Squared wavelet coherence between PC1-WS and SOI time series for (a) January and (b) July.

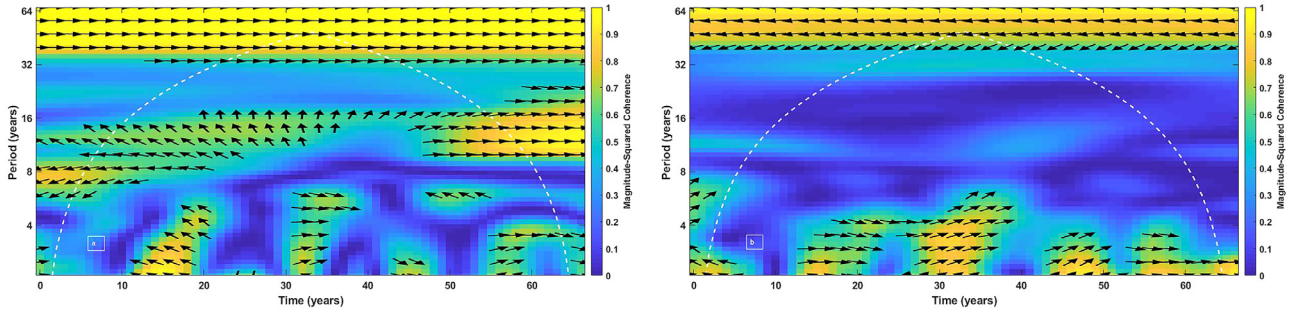

Figure 11 Squared wavelet coherence between PC1-WS and MEI time series for (a) January and (b) July.

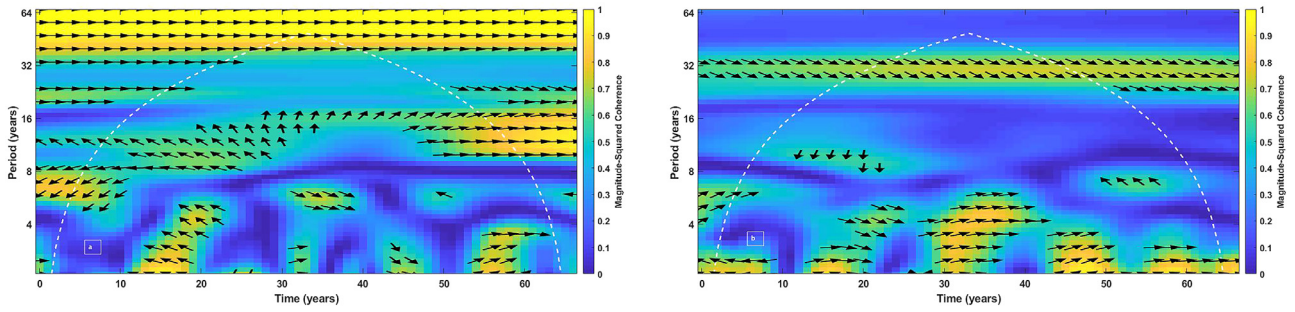

Figure 12 Squared wavelet coherence between PC1-WS and NINO3.4 time series for (a) January and (b) July.

be linked to the warm phases of AMO which are known to strengthen the summer monsoon rainfall over India.

4. Conclusions

An attempt has been made in the present work to explore how WS of the Indian Ocean region were influenced by the local SST and remote ENSO indices. Spatial correlation plots with significance level were generated between WS, SST data and the ENSO indices for July and January representing the southwest and northeast monsoons respectively. During the normal July months, there was a significant negative correlation between WS and SST over BOB which fades during El Niño years. Thus the SW monsoon locally impacted the WS and SST relationship. Next correlation plots were generated at a 95% confidence interval between WS and ENSO indices. Considering the normal January months WS had a significant negative correlation with SOI off the coast of Sri Lanka and south-west coast of India while the significant positive correlation with MEI and NINO3.4 for the same regions. During the El Niño years, WS had a significant positive correlation with MEI and NINO3.4 both, in January and July. Thus during the El Niño episodes, WS data was remotely influenced by the ENSO indices. During the La Niña years, there were no significant correlation patterns.

Further EOF analysis was applied to the WS data of the BOB region. For January the first eigenmode accounted for 42.9% and July 49.1% of the total variability. The January and July wind speed PCs were linked with the NAO and AMO oscillations respectively. The continuous wavelet power spectra of PC1 of WS data were generated for January and July. For both the red-noise wavelet power spectra, the significant regions occurred in the 2—4-year period replicating ENSO like oscillations. In January there were higher coherency values in the 8—16-year band which was related to the 8-year quasi-cyclic behavior of NAO. In July the higher coherency regions in the 0—4 year period were associated with the warm phases of the AMO which were known to strengthen the Indian summer monsoon rainfall. Thus patterns of global climate oscillations were compared to establish a close relationship between the WS variability and the ENSO indices in the BOB region.

Acknowledgments

This study is a part of a project no SR/FTP/ES80/2013 under Science and Engineering Research Board (SERB). It was sponsored by the Department of Science and Technology (DST), Government of India. The authors are grateful to DST for sponsoring the project.

References

Annamalai, H., Xie, S.P., McCreary, J.P., Murtugudde, R., 2005. Impact of Indian Ocean sea surface temperature on developing El Niño. J. Clim. 18, 302—319, http://dx.doi.org/10.1175/JCLI-3268.1.

Azad, S., Rajeevan, M., 2016. Possible shift in the ENSO-Indian monsoon rainfall relationship under future global warming. Nature Sci. Rep. 6 (1), art. no. 20145, 6 pp., http://dx.doi.org/10.1038/srep20145.

Barnston, A.G., Livezey, R.E., 1987. Classification, seasonality and persistence of low-frequency atmospheric circulation patterns. Mon. Weather Rev. 115, 1083—1126, http://dx.doi.org/10.1175/1520-0493(1987)115⟨1083:CSAPOL⟩2.0.CO;2.

Chen, W., Dong, B., Lu, R., 2010. Impact of the Atlantic Ocean on the multidecadal fluctuation of El Niño-Southern Oscillation-South Asian monsoon relationship in a Coupled General Circulation Model. J. Geophys. Res. 115 (D17), art. no. D17109, 12 pp., http://dx.doi.org/10.1029/2009JD013596.

Dong, L., McPhaden, M.J., 2018. Unusually warm Indian Ocean sea surface temperatures help to arrest development of El Niño in 2014. Nature Sci. Rep. 8, art. no. 2249, 10 pp., http://dx.doi.org/10.1038/s41598-018-20294-4.

Enfield, D.B., Mestas-Nunez, A.M., Trimble, P.J., 2001. The Atlantic Multidecadal Oscillation and its relationship to rainfall and river flows in the continental U.S. Geophys. Res. Lett. 28, 2077—2080, http://dx.doi.org/10.1029/2000GL012745.

Fan, F., Dong, X., Fang, X., Xue, F., Zheng, F., Zhu, J., 2017. Revisiting the relationship between the south Asian summer monsoon drought and El Niño warming pattern. Atmos. Sci. Lett. 18 (4), 175—182, http://dx.doi.org/10.1002/asl.740.

Fisher, R.A., 1992. Statistical Methods for Research Workers. In: Kotz, S., Johnson, N.L. (Eds.), Breakthroughs in Statistics. Springer Series in Statistics (Perspectives in Statistics). Springer, New York, 66—70, http://dx.doi.org/10.1007/978-1-4612-4380-9_6.

Goswami, B.N., Madhusoodanan, M.S., Neema, C.P., Sengupta, D., 2006. A physical mechanism for North Atlantic SST influence on the Indian summer monsoon. Geophys. Res. Lett. 33 (2), art. no. L02706, 4 pp., http://dx.doi.org/10.1029/2005GL024803.

Grinsted, A., Moore, J.C., Jevrejeva, S., 2004. Application of the CrossWavelet Transform and Wavelet Coherence to Geophysical Time Series. Nonlinear Proc. Geoph. 11, 561—566, http://dx.doi.org/10.5194/npg-11-561-2004.

Huang, C., Qiao, F., 2009. The relationship between sea surface temperature anomaly and wind energy input in the Pacific Ocean. Progr. Nat. Sci. 19 (10), 1409—1412, http://dx.doi.org/10.1016/j.pnsc.2009.03.004.

Huang, B., Thorne, P.W., Banzon, V.F., Boyer, T., Chepurin, G., Lawrimore, J.H., Menne, M.J., Smith, T.M., Vose, R.S., Zhang, H., 2017. Extended Reconstructed Sea Surface Temperature, Version 5 (ERSSTv5): Upgrades, Validations and Intercomparisons. J. Clim. 30, 8179—8205, http://dx.doi.org/10.1175/JCLI-D-16-0836.1.

Jevrejeva, S., Moore, J.C., Grinsted, A., 2003. Influence of the Arctic Oscillation and El Nino-Southern Oscillation (ENSO) on Ice Conditions in the Baltic Sea: The wavelet Approach. J. Geophys. Res. 108, art. no. D214677, 10 pp., http://dx.doi.org/10.1029/2003JD003417.

Kerr, R.A., 2000. A North Atlantic climate pacemaker for the centuries. Science 288 (5473), 1984—1986, http://dx.doi.org/10.1126/science.288.5473.1984.

Klein, S., Soden, A.B.J., Lau, N.C., 1999. Remote sea surface temperature variations during ENSO: Evidence for a tropical atmospheric bridge. J. Clim. 12, 917—932, http://dx.doi.org/10.1175/1520-0442(1999)012⟨0917:RSSTVD⟩2.0.CO;2.

Kug, J.S., Kang, I.S., 2006. Interactive feedback between ENSO and the Indian Ocean. J. Clim. 19, 1784—1801, http://dx.doi.org/10.1175/JCLI3660.1.

Kumar, K.K., Rajagopalan, B., Cane, M.A., 1999. On the weakening relationship between the Indian monsoon and ENSO. Science 284 (5423), 2156—2159, http://dx.doi.org/10.1126/science.284.5423.2156.

Li, T., Wang, B., Wu, B., Zhou, T., Chang, C.P., Zhang, R., 2017. Theories on formation of an anomalous anticyclone in western North Pacific during El Niño: A review. J. Meteorol. Res. 31 (6), 987—1006, http://dx.doi.org/10.1007/s13351-017-7147-6.

Li, T., Zhang, Y., Chang, C.P., Wang, B., 2001. On the relationship between Indian Ocean sea surface temperature and Asian summer monsoon. Geophys. Res. Lett. 28, 2843—2846, http://dx.doi.org/10.1029/2000GL011847.

Lorenz, E.N., 1956. Empirical orthogonal functions and statistical weather prediction. Statistical Forecast Project Report 1, Dept. of Meteor. MIT Tech. Rep. 49, 52 pp., https://eapsweb.mit.edu/sites/default/files/Empirical_Orthogonal_Functions_1956.pdf.

McPhaden, M.J., 2002. El Niño and La Niña: Causes and global consequences, in Encyclopedia of Global Environmental Change. John Wiley, Chichester, U.K, 353—370, https://www.pmel.noaa.gov/gtmba/files/PDF/pubs/ElNinoLaNina.pdf.

Okumura, M.Y., Deser, C., 2010. Asymmetry in the Duration of El Niño and La Niña. J. Clim. 23 (21), 5826—5843, http://dx.doi.org/10.1175/2010JCLI3592.1.

Olsen, J., Anderson, J.N., Knudsen, M.F., 2012. Variability of the North Atlantic Oscillation over the past 5200 years. Nat. Geosci. 5, 808—812, http://dx.doi.org/10.1038/ngeo1589.

Schott, F.A., Xie, S.P., McCreary Jr., J.P., 2009. Indian Ocean circulation and climate variability. Rev. Geophys. 47, art. no. RG1002, 46 pp., http://dx.doi.org/10.1029/2007RG000245.

Sun, B., Wang, H., 2019. Enhanced connections between summer precipitation over the Three-River-Source region of China and the global climate system. Climate Dynamics 52 (5—6), 3471—3488, http://dx.doi.org/10.1007/s00382-018-4326-9.

Torrence, C., Compo, G.P., 1998. A Practical Guide to Wavelet Analysis. Bull. Am. Meteorol. Soc. 79, 61—78, http://dx.doi.org/10.1175/1520-0477(1998)079⟨0061:APGTWA⟩2.0.CO;2.

Venzke, S., Latif, M., Villwock, A., 2000. The coupled GCM ECHO-2. Part II: Indian Ocean response to ENSO. J. Clim. 13, 1371—1383, http://dx.doi.org/10.1175/1520-0442(2000)013⟨1371:TCGE⟩2.0.CO;2.

Xie, S.P., Kosaka, Y., Du, Y., Hu, K., Chowdary, J.S., Huang, G., 2016. Indo-western Pacific ocean capacitor and coherent climate anomalies in post-ENSO summer: A review. Adv. Atmos. Sci. 33 (4), 411—432, http://dx.doi.org/10.1007/s00376-015-5192-6.

Oceanologia (2020) 62, 139—163

Available online at www.sciencedirect.com

ScienceDirect

journal homepage: www.journals.elsevier.com/oceanologia

ORIGINAL RESEARCH ARTICLE

Element enrichment and provenance of the detrital component in Holocene sediments from the western Black Sea

Vesselin M. Dekov[a,b,*], Valentina Y. Darakchieva[c], Kjell Billström[d], C. Dieter Garbe-Schönberg[e], George D. Kamenov[f], Morgane Gallinari[g], Lyubomir Dimitrov[h], Olivier Ragueneau[g], Ellen Kooijman[d]

[a] *Tokyo University of Marine Science and Technology, Konan, Minato-ku, Tokyo, Japan*
[b] *Department of Marine Geosciences, IFREMER, Plouzané, France*
[c] *Institute of Mineralogy and Crystallography, Bulgarian Academy of Sciences, Sofia, Bulgaria*
[d] *Department of Geosciences, Swedish Museum of Natural History, Stockholm, Sweden*
[e] *Institute of Geosciences, Marine Climate Research, University of Kiel, Kiel, Germany*
[f] *Department of Geological Sciences, University of Florida, Gainesville, FL, USA*
[g] *UMR CNRS/UBO 6539 LEMAR, European Institute for Marine Studies, Technopôle Brest-Iroise, Plouzané, France*
[h] *Institute of Oceanology, Bulgarian Academy of Sciences, Varna, Bulgaria*

Received 12 August 2019; accepted 11 October 2019
Available online 30 October 2019

KEYWORDS
Anoxic;
Black Sea;
Element enrichment;
Sr-Nd-Pb-isotopes;
Holocene

Summary Concentrations of a large set of major and trace elements, and Sr, Nd and Pb isotope ratios were measured in Holocene sediments cored in the western deep Black Sea in order to unravel: (1) the controls of element enrichment, and (2) sources of the detrital component. The transition of the basin from oxic to euxinic resulted in enrichment or depletion in a number of elements in the deep-sea sediments. Authigenic Fe enrichment appears to depend on the amount of Fe mobilized from the sediment through the benthic redox shuttle mechanism and free H_2S in the water column (degree of "euxinization"). Manganese enrichment is controlled by diagenetic reactions within the sediment: the dissolution of Mn minerals, Mn^{2+} diffusion upward and reprecipitation. Barium enrichment is also controlled by diagenetic reactions, sulfate

* Corresponding author at: Tokyo University of Marine Science and Technology, 4-5-7 Konan, Minato-ku, Tokyo 108-8477, Japan; Department of Marine Geosciences, IFREMER, 29280 Plouzané, France; Tel.: +81 03-5463-0642; fax: +81 03-5463-0642.
E-mail address: vdekov0@kaiyodai.ac.jp (V.M. Dekov).
Peer review under the responsibility of the Institute of Oceanology of the Polish Academy of Sciences.

Production and hosting by Elsevier

https://doi.org/10.1016/j.oceano.2019.10.001

reduction and methanogenesis, that take place above and below the sulfate-methane transition, respectively. The major part of V, Co, Ni, Cu, Zn, Cr, Mo, Cd and Sb is inferred to have co-precipitated with Fe in the euxinic deep waters and to have been incorporated into authigenic Fe-sulfides. Basin reservoir effect additionally influences the Mo enrichment. The U enrichment is interpreted to have a different origin in the two organic-rich stratigraphic units (II and I). It is inferred to be: (i) at the expense of the U inventory of the deepwater pool and a result of inorganic reduction of U at euxinic conditions in the lower Unit II; and (ii) at the expense of the U inventory of the surface water pool and a result of biogenic uptake and transfer to the sediment by the plankton in the upper Unit I. The high field strength elements are closely linked to the detrital component and their depletion in the organic-rich sediments reflects a dilution of the detrital component by the biogenic one. The enrichments of REE, Sn and Th are likely controlled by adsorption on clay minerals. Sr-Nd-Pb isotope compositions of the alumino-silicate component of the studied sediments are relatively uniform. They are most likely controlled by riverine suspended matter supplied mainly in the NW Black Sea (Danube Delta) and transported southward by marine currents, and to a lesser degree by suspended matter from the small rivers draining SE Bulgaria and NW Turkey. Wind-blown dust from the Sahara Desert appears to have a minor contribution to the alumino-silicate component of the sediments. The slight shift in the Pb isotopes in Unit I upper layers is possibly caused by the addition of anthropogenic Pb.

1. Introduction

The upper section of the sediment blanketing the Black Sea floor has been increasingly investigated since the first half of 20th century with the major goal to untangle the oceanographic/limnological as well as the geological history of this semi-isolated anoxic basin. The early works (Arkhangel'skii and Strakhov, 1938) subdivided it into three stratigraphic units (from top to bottom): (1) Recent sediments, (2) Old Black Sea layers, and (3) New Euxinian sediments. Later studies (Degens and Ross, 1972; Ross et al., 1970; Ross and Degens, 1974) essentially confirmed the presence of the same units (named as Units I, II and III), dated precisely their boundaries and showed that the stratigraphic units recognized at the shelf (Neveskii, 1967) are difficult to be correlated to those described in the deep Black Sea (Degens and Ross, 1972). Deep probing of the sediment and wide set of applied analytical approaches (Degens and Ross, 1974; Hsü, 1978; Ross, 1978; Ross et al., 1978; Stoffers and Müller, 1978; Stoffers et al., 1978) provided evidence that the distinct sediment alternation (Units I, II and III) records varying oxic lacustrine and anoxic marine conditions produced in the basin by the climatic changes over the Quaternary. Unraveling the Black Sea geological history and the potential implications for the processes in ancient anoxic basins involved the use of geochemical proxies (Calvert and Batchelor, 1978; Hirst, 1974). Geochemical studies of the Quaternary Black Sea sediments revealed that a number of trace elements are enriched (relative to the background detrital sediment or to the average shale) in the sediment layers deposited under anoxic conditions. They suggested that these enrichments may be used for determining the redox conditions in the sediment or in the bottom waters at the time of deposition (Calvert and Pedersen, 1993; Little et al., 2015). Although these studies comprehensively investigated the element enrichments and reasonably interpreted them as results of a range of reactions across redox interfaces (Calvert and Pedersen, 1993; Little et al., 2015) they considered only a limited number of elements (Cd, Cr, Cu, Fe, Mn, Mo, Ni, Re, U, V, Zn) measured in the uppermost (or uppermost + underlying; unclear in Little et al. (2015)) stratigraphic unit.

Challenged by the possibility to explore the environmental potential of a larger element set analyzed across the three Upper Quaternary stratigraphic units we investigated the distribution and enrichment of a large element set (54 elements) in a series of Holocene sediments from the western Black Sea. Since the upper organic-rich stratigraphic units (I and II) were shown to have received almost constant organic flux diluted by fluctuating terrigenous input through time (Calvert and Karlin, 1998) we, additionally, analyzed the Sr-Nd-Pb-isotope composition of the terrigenous component of these sediments in order to determine its provenance. The results of our study are discussed in this contribution.

2. Geologic setting

The Black Sea is the largest permanently anoxic basin in the modern Ocean. Permanent anoxia in the major part of its water body is a result of the combination of restricted water mass exchange with the Mediterranean Sea, positive water balance and moderate bio-production in the euphotic layer. The Black Sea water body is vertically stratified in two layers with contrasting chemistry that are separated by a transition layer (chemocline): oxic surface layer (~0 to 50 m), suboxic intermediate/transition layer (chemocline) (~50 to 100 m) and anoxic (euxinic) deep waters (~100 to 2000 m) (Murray et al., 1989).

The upper part of the Black Sea sedimentary cover, deposited during the Late Pleistocene and Holocene, is composed of three distinct stratigraphic layers (units) spread throughout the deep Black Sea (Degens and Ross, 1972;

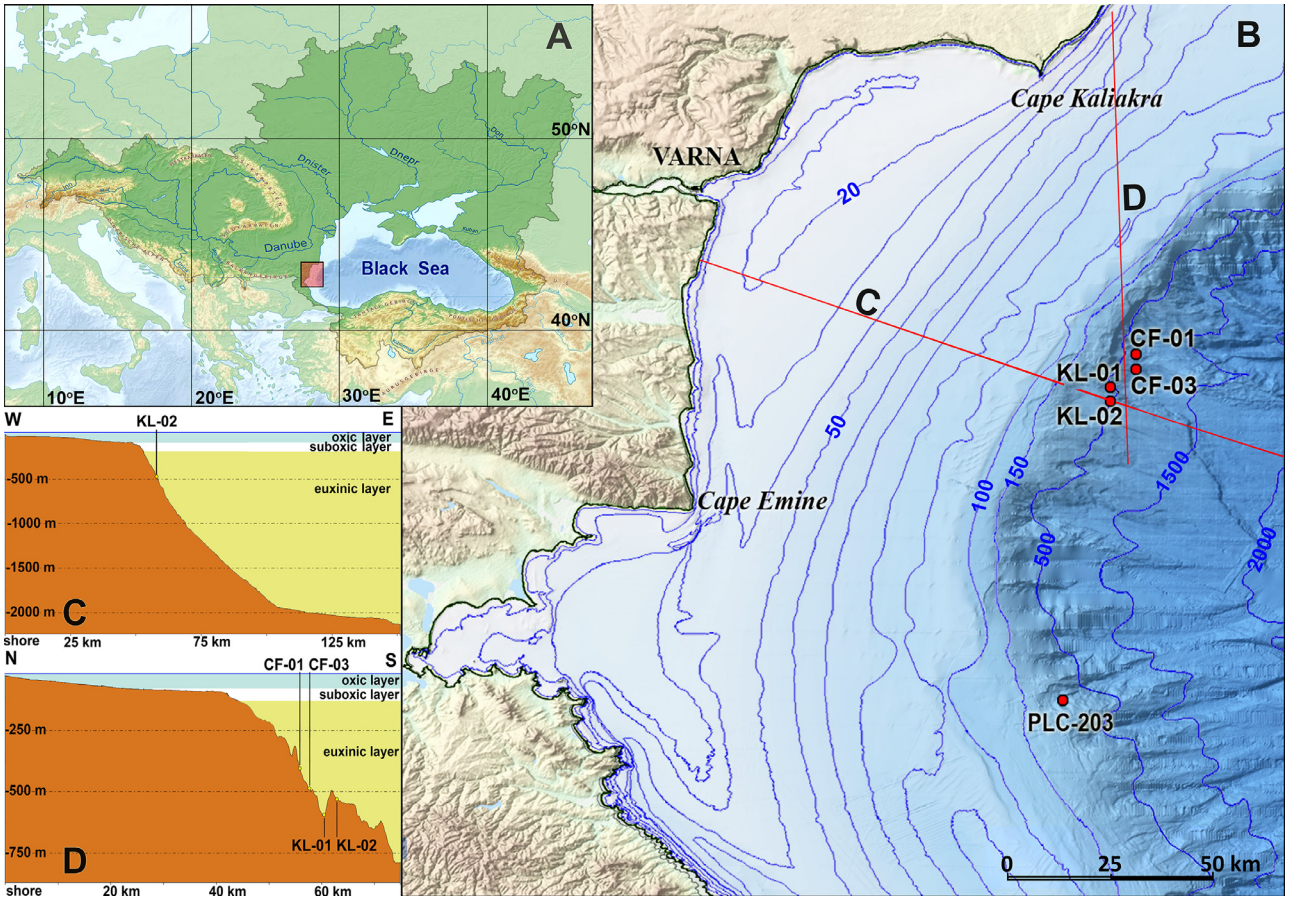

Figure 1 (a) Map of the Black Sea and its catchment area. Highlighted rectangle encircles the area of studies. (b) Western part of the Black Sea with locations of the studied sediment cores (red closed circles). Red lines marked with C and D indicate positions of the cross sections shown at (c) and (d) demonstrating the locations of the studied sediment cores CF-01, CF-03, KL-01 and KL-02 relative to the oxic, suboxic and euxinic water layers.

Ross et al., 1970). The uppermost layer (Unit I) is a modern laminated coccolith ooze that overlies the finely laminated sapropel (Unit II). The boundary between them is sharp and dated at ~3 ka BP (Kwiecien et al., 2008). The transition between Unit II and Unit III, terrigenous mud (lutite; Ross et al., 1970), is distinct and estimated to be at ~9 ka BP (Soulet et al., 2011). The deposition of these three different lithologic units is explained by changes in the environmental conditions, i.e. evolution of the basin from limnic to marine (Degens and Ross, 1972), whereas their impressive correlation along the entire basin is supposed to attest for uniform depositional environment over most of the Black Sea (Ross et al., 1970).

The organic-rich sapropel layer (Unit II) has been the focus of a number of studies (Calvert, 1990; Calvert et al., 1987; Glenn and Arthur, 1985). The high content of organic matter in this layer has been found to be caused by low dilution of the organic fraction by other sediment components (e.g., terrigenous and biogenic) rather than by high preservation of organic matter (Calvert and Karlin, 1998). Therefore, its formation is supposed not to be necessarily characteristic of anoxic basins. However, the anoxic conditions in the Black Sea water body and the deposition of organic-rich sediments (Units I and II) on the Black Sea floor were inferred to be the major controls of enrichment of a number of elements in the sediments (Calvert and Pedersen, 1993; Little et al., 2015).

3. Samples and methods of investigation

3.1. Samples

Five sediment cores recovered from the western deep Black Sea (Fig. 1a,b; Table 1) during two expeditions of the r/v *Akademik* (Institute of Oceanology, Bulgarian Academy of Sciences) in April 2006 and February 2007 were selected for our study. Twenty-nine sediment samples from the three stratigraphic units crossed by these cores (Unit III was not completely penetrated by any core) were washed from pore water salts with distilled water (18.2 MΩ/cm resistivity), freeze-dried and ground to fine powder in agate mortar before the elemental concentrations and isotope ratios measurements. The "red layers" in Unit III (Bahr et al., 2005; Kwiecien et al., 2008; Major et al., 2002) that mark the transition from the last glacial (Late Pleistocene) to Holocene were not reached by any core. Therefore, we can consider that the cored sediments are entirely within the Holocene.

Table 1 Investigated sediment cores sampling and lithology details.

Core ID	Latitude (N)	Longitude (E)	Depth (m)	Sampling device	Lithology description
CF-01	42°55.613′	28°36.405′	614	gravity corer	0–87 cm: finely laminated greenish-gray coccolith ooze (Unit I) 87–204 cm: finely laminated sapropel (Unit II) 204–223 cm: greenish-yellow fine terrigenous mud (Unit III)
CF-03	42°55.125′	28°36.413′	647	gravity corer	0–33 cm: finely laminated green-gray coccolith ooze (Unit I) 33–173 cm: finely laminated brown-green sapropel with sharp upper boundary (Unit II) 173–175 cm: sharp boundary 175–250 cm: grayish-white fine terrigenous mud (Unit III)
KL-01	42°52.505′	28°33.885′	457	gravity corer	0–94 cm: finely laminated greenish-gray coccolith ooze (Unit I) 95–210 cm: finely laminated (alternation of dark-brown organic-rich laminae and light-gray terrigenous laminae) sapropel (Unit II) 210 cm: sharp boundary 210–360 cm: greenish-gray fine terrigenous mud, with black stains (275-360 cm), which becomes compact down core (350–360 cm) (Unit III)
KL-02	42°53.045′	28°33.899′	475	gravity corer	0–115 cm: finely laminated greenish-gray coccolith ooze (Unit I) 115–250 cm: finely laminated brown to gray sapropel (Unit II) 250–320 cm: gray terrigenous mud (Unit III)
PLC-203	42°24.157′	28°27.796′	314	gravity corer	0–115 cm: finely laminated greenish-gray coccolith ooze (Unit I) 115–310 cm: sapropel (fine alternation of dark-brown to olive organic-rich laminae becoming denser towards the catch-corer, greenish-gray terrigenous laminae and rarely aragonite-rich laminae) (Unit II)

3.2. Methods of investigation

3.2.1. Bulk geochemical analyses and enrichment factors (EF) calculations

Major element (Al_2O_3, Fe_2O_3, MnO, MgO, CaO, Na_2O, K_2O, TiO_2, P_2O_5) concentrations of the samples were determined by Inductively Coupled Plasma Optical Emission Spectrometry (ICP-OES) (Spectro Ciros SOP instrument; Institute of Geosciences, University of Kiel) after total sample dissolution performed by pressurised HF-$HClO_4$-aqua regia attack (Garbe-Schönberg, 1993). Total SiO_2 (SiO_{2tot}) was estimated as the difference between the sum of all major elements including loss on ignition (LOI) and 100%. Amorphous SiO_2 (SiO_{2am}) concentrations were measured after sample dissolution following the method of DeMaster (1981) and Koning et al. (2002). About 20 mg of powdered sample was dissolved in 50 mL 0.5*M* NaOH in centrifuge tubes at 85°C for 3 hours (in a water-bath with stirring). After 1, 2 and 3 hours we centrifuged the tubes with dissolved samples (for 3 minutes at 3500 rpm), pipetted 0.5 mL from the solution, diluted this aliquot by 20 with distilled water (18.2 MΩ/cm resistivity) and analyzed it for dissolved silica using a Bran + Luebbe AA3 HR auto-analyzer as described by Aminot and Kérouel (2007). Detrital SiO_2 (SiO_{2det}) concentrations were calculated by subtracting of SiO_{2am} from SiO_{2tot}.

Trace (Li, Sc, V, Cr, Co, Ni, Cu, Zn, Ga, Rb, Sr, Y, Zr, Nb, Mo, Ag, Cd, Sn, Sb, Cs, Ba, Hf, Ta, W, Tl, Pb, Th, U) and rare earth (REE) elements concentrations were analysed by Inductively Coupled Plasma Mass Spectrometry (ICP-MS) (Agilent 7500cs instrument; Institute of Geosciences, University of Kiel) after total sample dissolution following the same protocol as for the major elements (Garbe-Schönberg, 1993). Unfortunately, this dissolution protocol bears the risk of incomplete dissolution of some well-crystallized zircon grains and leaves a possibility that not all Zr and Hf are represented in the analysis. However, Zr, Hf and Nb, Ta, Th in the reference material Marine Sediment GSMS-2 (Jochum et al., 2005) that had been repeatedly analyzed together with our samples were recovered with 90% and 100%, respectively, and the observed perfect correlation between these elements and Al confirmed that a significant fraction of these high-field-strength elements (HFSE) had been dissolved and analyzed, which allowed for correct interpretations. The accuracy of the analytical results was controlled by analyzing international standard reference mate-

rials (AC-E, BE-N, BHVO-1, BHVO-2, BIR-1, MESS-2, GSMS-2) following the same analytical protocols as for the sediment samples. Measured elemental concentrations of the standards were generally within <5% of the recommended values for most elements. The precision of sample duplicates, as well as repeated analyses, was better than 5% for most elements.

Approximately 3–4 mg of each sample were loaded into tin capsules and placed in a 50-position automated Zero Blank sample carousel on a Carlo Erba NA1500 CNHS elemental analyzer for measuring the total carbon (C_{tot}) and nitrogen concentrations. After flash combustion in a quartz column containing chromium oxide and silvered cobaltous/cobaltic oxide at 1020°C in an oxygen-rich atmosphere, the sample gas was transported in a He carrier stream and passed through a hot (650°C) reduction column consisting of reduced elemental copper to remove oxygen. The effluent stream then passed through a chemical [$Mg(ClO_4)_2$] trap to remove water. The stream then passed through a 0.7 meter GC column at 125°C that separates the N_2 and CO_2 gases. Finally, the gases passed through a thermal conductivity detector that measured the size of the pulses of N_2 and CO_2.

Total inorganic carbon (C_{inorg}) was measured coulometrically using a UIC (Coulometrics) 5014 CO_2 coulometer coupled with an AutoMate automated carbonate preparation device (AutoMateFX.com). Approximately 20 mg of each sample was weighed into septum top tubes and placed into the AutoMate carousel. A double needle assembly was used to purge the sample vial of atmospheric gas using CO_2-free nitrogen carrier gas. 10% phosphoric acid was then injected into the sample vial and evolved CO_2 was carried through a silver nitrate scrubber to the coulometer where C content was measured.

Organic carbon (C_{org}) concentrations were calculated as a difference between the measured total carbon and total inorganic carbon concentrations.

LOI (in wt.%) was measured on air-dry powdered samples placed after weighing in a muffle furnace at 950°C for 1 hour.

In order to evaluate the relative enrichment or depletion of the elements in the sediment we calculated the authigenic enrichment factors (Calvert and Pedersen, 1993; Little et al., 2015):

$$EF_{element} = (element/Al)_{sample}/(element/Al)_{reference}.$$

Traditionally, the reference material for normalization was the average shale (Calvert and Pedersen, 1993). Little et al. (2015) argued that the average shale could not be representative of the local background sedimentation and suggested the usage of the proximal oxic sediment as a correct normalizing lithogenic background. Since we have not studied the composition of the proximal shelf sediments (oxic and detrital) contemporaneous with the studied deep-sea stratigraphic units (Unit I, II and III) we normalized our concentration data to those for the upper continental crust (UCC) (Rudnick and Gao, 2003).

3.2.2. Sr-Nd-Pb isotope analysis

Twenty-three sub-samples (out of the entire set of 29) from four of the sediment cores were selected for a combined Sr-Nd-Pb isotope study (Department of Geological Sciences, Swedish Museum of Natural History, Stockholm). According to previous works (Ross et al., 1970; Ross and Degens, 1974) the Upper Pleistocene-Holocene Black Sea sediments (Units III–I) contain a considerable proportion of biogenic carbonate and organic matter. These sediment components are marine-born and their Sr-Nd-Pb-isotope composition is supposed to reflect that of the seawater (Haley et al., 2008; Hedge and Walthall, 1963; Vance and Burton, 1999). Thus, in order to trace the provenance of the non-marine component (e.g., terrigeneous) in the studied sediments we subjected the selected sub-samples to a three-step leaching procedure (Bayon et al., 2002) to eliminate the marine-born components. First, 10% acetic acid was added to ~150 mg of the powdered sample which, after 3 hours in an ultrasonic bath, was left overnight. This treatment step removes the carbonates. After rinsing with distilled water (18.2 MΩ/cm resistivity), centrifugation, and decantation the residue was collected. Second, Fe-Mn-oxyhydroxides were removed from the residue by adding 25% acetic acid, with sample vials left on a hot plate kept at different temperatures (at 90° and 60°C) for a total period of two hours. After rinsing with distilled water, centrifugation and decantation, the residue was recovered. Third, the organic carbon was removed from the residues by adding 5% H_2O_2 to them and keeping the vials for seven hours in an ultrasonic bath. In order to ensure that the organic fraction was fully dissolved, we added aqua regia to the vials. The final residue (after rinsing, centrifugation and decantation) is supposed to represent the alumino-silicate fraction of the sediment. In order to estimate the quantity of different fractions during the treatment, the resulting sample residues were weighed. We found that the alumino-silicates compose ~40–60% of the studied sediment samples.

The alumino-silicate residues were dissolved in a HF-$HClO_4$ acid mixture before the Sr-Nd-Pb-isotope ratio measurements. The sample solutions were left for three days in order to ensure the total dissolution of the alumino-silicate component. Conventional ion-exchange techniques, performed in columns filled with AG50W × 8, H^+ form resin (De Ignacio et al., 2006), were applied to the sample solutions in order to separate and purify the elements whose isotopic composition were to be determined. Sr was further purified in a second pass through the same columns, whereas Nd was isolated in Ln-spec columns (Pin and Zalduegui, 1997). The Pb fractions were re-dissolved in HBr, and treated further in columns with AG1 × 8, Cl^- form resin.

A Thermo-Finnigan Triton thermal ionization mass spectrometry (TIMS) instrument was used for the Sr and Nd isotope analyses and data were normalized to $^{88}Sr/^{86}Sr = 0.1194$ and $^{146}Nd/^{144}Nd = 0.7219$, respectively. Additionally, replicate analyses of the NBS-987 Sr standard analyzed during the course of the study yielded an average $^{87}Sr/^{86}Sr = 0.710221 \pm 0.000011$ (2σ external precision). Corresponding analyses of the La Jolla Nd standard yielded an average $^{143}Nd/^{144}Nd = 0.511848 \pm 0.000009$ (2σ external precision). These standard values are very close to the accepted values and therefore, no additional corrections were applied to the obtained sample Sr or Nd data. Estimated analytical uncertainties amount to ca. ±0.4 and ±0.00002 for the given εNd and Sr isotope values, respectively. Pb isotope analyses were performed with Tl added to allow for an internal correction of the mass bias, and the

measured intensities were corrected for background and Hg interference on mass 204. Two ICP-MS instruments were used: a Micromass Isoprobe multi-collector (core KL-02) and a Nu Plasma II (cores CF-03, KL-01 and PLC-203). For the data produced by the latter instrument (hosted by the Vegacenter facility), the NBS-981 Pb standard was run at regular intervals and all unknowns were analyzed in duplicate. The obtained values for the standard are within the error of those given by Todt et al. (1996), and the external reproducibility is between 0.04% ($^{206}Pb/^{204}Pb$) and 0.08% ($^{208}Pb/^{204}Pb$). The external reproducibility of the unknowns is of a similar order, but in order to account for errors arising during the chemical treatment in the clean laboratory, an overall uncertainty of ±0.10% is adopted.

4. Results

4.1. Geochemistry of the sediments

4.1.1. Elemental concentrations and REE distribution patterns

Vertical distributions of the concentrations of Al, Fe and K co-vary along the studied sediment cores (Table 2; Fig. 2). Titanium and detrital SiO_2 co-vary with them in the upper part of Unit II and in Unit I (Fig. 2). Concentrations of Si (total, detrital and amorphous), Al, Fe and K have maximum values in the sapropel layer (Unit II) and minimum values in the terrigenous mud (Unit III) and coccolith ooze (Unit I) (Table 2). Calcium (as $CaCO_3$) demonstrates opposite behavior with maximum concentrations in both the terrigenous mud and coccolith ooze, and minimum content in the sapropel layer (Table 2; Fig. 2). Although the content of Mn is broadly similar in all the three stratigraphic units (Table 2) it shows a particular vertical distribution with a gradual increase from Unit III towards the boundary between Units II and I, followed by a slight decrease through Unit I (Fig. 2). Unit I has the lowest Mg and the highest P concentrations (Table 2). Organic carbon shows the highest content in the sapropel layer (particularly in its lower part) and lowest concentration in the terrigenous mud (Table 2; Fig. 2). It correlates well with SiO_{2am} (Table 2; Fig. 2).

Silicon, Al and Ca appeared to be the most abundant major elements in these sediments (Table 2). Theoretically, Al is mostly terrigenous (detrital), whereas Si has a dual origin, terrigenous and biogenic, in these sediments (Hay et al., 1990). Biogenic Si concentrations (within the amorphous SiO_2 of diatoms and silicoflagellates (Pilskaln and Pike, 2001)) cluster between 1 and 2% (as SiO_{2am}) and have a maximum in the sapropel layer (Table 2). In order to investigate the terrigenous material deposited in the western Black Sea during the Holocene, we calculated the SiO_{2det}/Al_2O_3 ratio in the studied sediments (Table 2). This ratio spans between 4.5 and 7.8, but clusters around 5 (Table 2). Assuming that the terrigenous material entering the western Black Sea has an average composition close to that of the UCC, we compared the SiO_{2det}/Al_2O_3 ratio of our sediments to that of the UCC: 4.3 (Rudnick and Gao, 2003). This comparison demonstrated that the western Black Sea sediments are enriched in SiO_{2det} relative to the UCC.

Vertical distributions of the concentrations of most trace elements co-vary with those of one or another of the major elements. A large group of trace elements including Li, Co, Ni, Cu, Zn, V, Cr, Ag, Sc, Ga, Sn, Rb, Cs, W, Th, Nb, Ta, Hf and REE correlate positively with Al (Fe and K) (Fig. 2). Similarly, Sr co-varies with $CaCO_3$, Ba with Mn, and Pb, Y with P (Fig. 2). Two pairs of trace elements do not show any correlation with the major elements, but co-vary with each other: Cd with Sb, and U with Mo (Fig. 2). Like most of the major elements a range of trace elements have maximum concentrations in the sapropel layer and minimum contents in the terrigenous mud: V, Cr, Ni, Cu, Zn, Cd, Ga, Mo, Sb, Li, Rb, Cs, Ba, Sn, Sc, Zr, Hf, Ta, W, Tl, Th, U and REE (Tables 2, 3). Co, Pb and Y have maximum concentrations in the coccolith ooze and minimum concentrations in the terrigenous mud (Tables 2, 3). Sr concentrations are also the highest in the coccolith ooze, but lowest in the sapropel layer (Table 2).

Concentrations of the REE (ΣREE) are the highest in the sapropel layer (Unit II) and the lowest in the terrigenous mud (Unit III) (Table 3; Fig. 3a). ΣREE correlates inversely with the SiO_{2det}/Al_2O_3 ratio (Tables 2, 3). The UCC-normalized REE distribution patterns of all the three stratigraphic units are similar (Fig. 3a). They show very weak negative to no Ce anomaly ($Ce/Ce^* \sim 1$), have a weak negative Eu anomaly ($Eu/Eu^* < 1$) and exhibit depletion of light REE relative to heavy REE ($La_{UCCN}/Lu_{UCCN} < 1$) (Fig. 3a; Table 3). The negative Eu anomaly is highest in the terrigenous mud (Fig. 2).

4.1.2. Enrichment factors

Iron is enriched relative to Al in all the three stratigraphic units over the UCC abundance (Table 4). Although the Fe enrichment is, on average, similar in all stratigraphic units (Table 4) it varies along the sediment cores showing a general trend of upward decrease with two maxima at the lower and upper parts of Unit II, which is similar to the vertical profile of the C_{org} concentrations (Figs 2, 4).

Organic-rich sediments are typically enriched in trace elements (Goldschmidt, 1954) and our data largely confirm this observation: most of the analyzed trace elements (Ag, V, Cr, Co, Ni, Cu, Zn, Cd, Ga, Mo, Sb, Li, Rb, Cs, Sr, Ba, Sn, Sc, Nb, Ta, W, Tl, Pb, Th, U, Y and REE) show elevated concentrations in the organic-rich Units I and II (some even in the terrigenous mud, Unit III) (Table 4). Others, such as Mn, Zr and Hf, are depleted in these sediments (Table 4). The sapropel layer (Unit II) is the most enriched in V, Cr, Ni, Cu, Zn, Cd, Mo, Sb, Li, Rb, Cs, Sc, Tl and U, whereas the coccolith ooze (Unit I) is the most enriched in Ag, Co, Ba, Pb, Y and Tm (Table 4). The terrigenous mud (Unit III) is the richest in Mn, Sr, Sn, Zr, Hf, Nb, Ta, W, Th and most of the REE (La, Ce, Pr, Nd, Sm, Eu, Gd, Tb, Dy, Lu) (Table 4). Particularly enriched ($EF > 3$) are Mo, Cd, Ag, Sb, Li and U (Table 4).

The vertical profile of the EF_{Mn} (Fig. 4) shows depletion in the sapropel layer (Unit II) and gradual increase upwards to the coccolith ooze (Unit I). The EF_{Ba} shows a similar profile (Fig. 4), but its absolute minimum and maximum appear earlier than those of the EF_{Mn}: at the base and at the upper part of Unit II, respectively. Sr is strongly depleted in the sapropel layer (Unit II). The vertical profiles of the enrichment factors of Co and Cu co-vary with that of Fe (Fig. 4). The enrichments of Ni, Zn, W, Cr, Ga, Sc, Li and Cs (and Rb, not shown at Fig. 4) demonstrate maxima like that of EF_{Fe} at the base of Unit II, but their upper (and smaller) maxima are displaced upward in Unit I (Fig. 4). EF_V, EF_{Mo},

Table 2 Major and trace elements concentrations (measured using Inductively Coupled Plasma Optical Emission Spectrometry (ICP-OES) and Inductively Coupled Plasma Mass Spectrometry (ICP-MS)) of the studied sediments.

Core ID	Horizon (cm)	Lithology Unit	SiO_{2tot} (wt.%)	SiO_{2am}	SiO_{2det}	Al_2O_3	SiO_{2det}/Al_2O_3	Fe_2O_{3tot}	MnO	MgO	CaO	Na_2O	K_2O	TiO_2	P_2O_5	LOI	C_{inorg}	C_{org}	C_{tot}	N	Si_{am}/C_{org} (mol/mol)	Ag (ppm)	V
CF-01	57–59	I	48.7	0.77	47.9	8.88	5.4	3.58	0.05	1.85	11.3	1.39	1.64	0.37	0.12	22.1	2.80	2.64	5.44	0.26	0.06	0.18	100
	93–95	II	53.0	1.37	51.6	11.0	4.7	4.46	0.06	2.20	4.82	1.58	2.01	0.44	0.14	20.4	1.02	4.36	5.38	0.42	0.06	0.19	120
	124–126	II	52.3	1.27	51.0	10.3	4.9	4.12	0.05	2.28	5.88	1.48	1.89	0.44	0.10	21.2	1.24	3.97	5.21	0.37	0.06	0.17	120
	155–157	II	50.1	5.24	44.9	7.83	5.7	3.14	0.04	1.83	4.16	2.27	1.39	0.30	0.14	28.9	0.99	7.25	8.24	0.60	0.14	0.15	107
	195–197	II	47.8	0.89	46.9	7.77	6.0	3.02	0.03	1.83	7.07	1.24	1.43	0.31	0.13	29.3	2.25	7.05	9.30	0.51	0.03	0.16	159
	218–220	III	50.8	0.84	49.9	8.50	5.9	3.36	0.04	2.45	11.5	1.36	1.60	0.41	0.10	19.8	2.61	1.89	4.50	0.15	0.09	0.12	87.3
CF-03	55–57	II	52.3	1.67	50.6	10.2	5.0	4.09	0.05	2.30	5.52	1.99	1.89	0.42	0.13	21.1	1.24	4.29	5.53	0.39	0.08	0.17	117
	104–106	II	52.0	1.32	50.7	10.6	4.8	4.08	0.04	2.13	5.08	1.47	1.91	0.42	0.13	22.1	1.12	4.87	5.99	0.43	0.05	0.18	128
	133–135	II	49.5	1.91	47.6	8.91	5.3	3.57	0.04	1.96	4.80	1.49	1.61	0.35	0.12	27.6	1.03	7.79	8.82	0.67	0.05	0.17	120
	170–172	II	55.6	0.67	55.0	7.78	7.1	2.93	0.03	2.03	6.28	1.45	1.42	0.35	0.12	22.0	1.34	4.27	5.61	0.28	0.03	0.14	119
	216–218	III	39.1	0.64	38.5	4.91	7.8	1.99	0.04	1.63	21.2	0.62	0.90	0.21	0.07	29.3	6.40	1.10	7.50	0.08	0.12	0.08	55.7
KL-01	165–167	II	51.3	1.42	49.9	9.49	5.3	3.80	0.05	2.10	4.74	1.57	1.73	0.38	0.11	24.7	1.12	6.87	7.99	0.62	0.04	0.17	116
	178–180	II	50.1	1.28	48.9	9.51	5.1	3.88	0.04	2.06	4.85	1.58	1.75	0.37	0.10	25.7	1.03	6.80	7.83	0.54	0.04	0.16	120
	200–202	II	48.4	0.88	47.5	8.66	5.5	3.41	0.03	2.00	7.41	1.39	1.60	0.34	0.10	26.6	1.71	6.13	7.84	0.48	0.03	0.15	131
	250–252	III	40.3	0.59	39.7	5.25	7.5	2.12	0.05	1.69	22.6	0.75	0.98	0.22	0.07	26.0	6.47	1.10	7.57	0.08	0.11	0.08	57.6
	294–296	III	40.9	1.41	39.5	5.82	6.8	2.28	0.04	1.77	16.5	0.72	1.06	0.26	0.09	30.5	4.94	1.31	6.25	0.10	0.21	0.10	65.9
KL-02	58–60	I	47.0	0.80	46.2	8.70	5.3	3.39	0.05	1.72	12.2	1.28	1.58	0.35	0.11	23.6	3.21	2.57	5.78	0.26	0.06	0.16	107
	86–88	I	47.7	1.00	46.7	8.64	5.4	3.44	0.05	1.78	12.1	1.26	1.59	0.35	0.13	22.9	3.23	2.82	6.05	0.28	0.07	0.18	104
	116–118	II	53.2	1.39	51.8	11.5	4.5	4.65	0.06	2.34	4.75	1.43	2.09	0.47	0.11	19.4	0.94	4.03	4.97	0.38	0.07	0.21	136
	153–155	II	52.1	1.55	50.5	10.4	4.8	4.12	0.05	2.28	5.69	1.37	1.91	0.43	0.11	21.5	1.24	4.23	5.47	0.39	0.07	0.18	122
	204–206	II	51.9	7.40	44.5	8.91	5.0	3.51	0.04	2.00	4.73	1.66	1.62	0.36	0.10	25.1	0.92	6.26	7.18	0.53	0.24	0.15	109
	232–234	II	50.5	1.17	49.3	9.43	5.2	3.91	0.04	2.13	4.92	1.66	1.74	0.38	0.11	25.2	1.18	6.66	7.84	0.53	0.04	0.15	130
	270–272	III	50.9	0.88	50.0	8.36	6.0	3.41	0.05	2.44	12.1	1.08	1.55	0.41	0.10	19.6	2.99	1.74	4.73	0.13	0.10	0.12	84.6
PLC-203	65–67	I	49.3	1.73	47.6	9.46	5.0	3.82	0.07	1.94	10.8	1.21	1.73	0.40	0.13	21.2	2.72	2.53	5.25	0.25	0.14	0.16	113
	109–111	I	50.2	1.27	48.9	10.1	4.9	4.00	0.06	2.14	9.12	1.39	1.86	0.42	0.11	20.7	2.35	2.26	4.61	0.22	0.11	0.17	120
	170–172	II	53.4	2.27	51.2	11.3	4.5	4.59	0.06	2.41	4.80	1.26	2.06	0.47	0.12	19.5	0.91	3.34	4.25	0.32	0.14	0.17	126
	218–220	II	52.3	2.62	49.7	10.6	4.7	4.44	0.06	2.33	4.87	1.39	1.96	0.45	0.11	21.4	0.91	3.69	4.60	0.34	0.14	0.16	117
	260–262	II	54.0	1.92	52.1	10.9	4.8	4.40	0.04	2.36	5.46	1.26	1.98	0.45	0.11	19.0	1.06	3.69	4.75	0.35	0.10	0.17	120
	278–280	II	51.0	2.79	48.2	9.66	5.0	4.08	0.06	2.18	5.00	1.25	1.77	0.40	0.11	24.6	0.85	5.11	5.96	0.46	0.11	0.16	112
Average		I	48.6	1.11	47.5	9.15	5.2	3.65	0.06	1.89	11.1	1.30	1.68	0.38	0.12	22.1	2.86	2.56	5.43	0.25	0.09	0.17	109
		II	51.6	2.05	49.6	9.72	5.1	3.91	0.05	2.14	5.31	1.52	1.78	0.40	0.12	23.4	1.16	5.30	6.46	0.45	0.08	0.17	123
		III	44.4	0.87	43.5	6.57	6.6	2.63	0.04	2.00	16.8	0.90	1.22	0.30	0.09	25.0	4.68	1.43	6.11	0.11	0.12	0.10	70.2

(*continued on next page*)

Table 2 (*continued*)

Core ID	Horizon (cm)	Lithology Unit	Cr (ppm)	Co	Ni	Cu	Zn	Cd	Ga	Mo	Sb	Li	Rb	Cs	Sr	Ba	Sn	Sc	Zr	Hf	Nb	Ta	W	Tl	Pb	Th	U
CF-01	57–59	I	80.6	17.0	64.7	38.7	73.9	0.44	13.8	47.1	1.60	51.9	104	7.08	520	573	2.21	11.6	64.8	1.86	8.75	0.61	1.17	0.64	26.6	8.42	9.73
	93–95	II	101	19.1	79.3	54.8	91.2	0.54	17.4	56.7	1.30	65.6	127	8.73	239	720	2.64	15.1	78.1	2.25	10.3	0.72	1.33	0.71	22.5	10.0	6.97
	124–126	II	100	14.0	78.6	41.5	87.0	0.60	16.7	61.9	1.67	60.6	122	8.31	254	560	2.65	13.9	74.9	2.15	10.5	0.73	1.39	0.82	20.9	9.93	12.8
	155–157	II	84.2	14.3	84.3	45.4	77.0	0.64	14.0	41.7	1.17	50.5	101	7.10	218	429	2.20	12.0	55.1	1.64	8.07	0.57	1.20	0.62	17.7	8.09	12.4
	195–197	II	76.9	11.2	77.0	47.6	71.7	0.66	13.8	71.1	1.36	47.6	101	6.76	534	412	2.17	11.2	62.5	1.80	8.22	0.59	1.21	0.89	18.0	8.26	15.1
	218–220	III	76.1	10.4	43.8	26.8	66.2	0.29	13.4	5.15	1.23	43.0	92.2	5.69	303	421	2.31	10.0	62.1	1.83	9.34	0.67	1.21	0.54	15.9	8.33	3.29
CF-03	55–57	II	97.1	15.0	75.3	43.5	87.1	0.63	16.4	55.3	1.64	60.8	125	8.40	241	592	2.63	13.4	66.5	1.91	10.2	0.71	1.33	0.85	20.8	9.64	9.36
	104–106	II	99.7	14.9	84.2	49.7	91.1	0.76	17.1	67.1	1.66	63.9	126	8.84	245	766	2.57	14.1	78.5	2.26	10.1	0.70	1.33	0.80	21.6	9.89	13.9
	133–135	II	93.2	15.2	84.4	49.0	85.2	0.80	15.9	71.5	1.44	57.0	115	8.15	241	754	2.45	13.3	64.5	1.84	9.22	0.65	1.35	0.74	19.7	9.01	13.1
	170–172	II	72.6	9.59	62.4	38.1	61.8	0.62	12.2	34.4	1.31	40.9	85.7	5.42	270	378	2.01	9.61	62.7	1.81	8.38	0.60	1.11	0.86	15.1	7.33	9.31
	216–218	III	46.6	6.69	30.3	18.1	42.1	0.23	8.61	1.04	0.71	29.2	58.8	3.86	451	284	1.45	6.68	35.9	1.13	5.46	0.40	0.75	0.38	10.2	5.38	2.07
KL-01	165–167	II	96.34	14.6	78.9	46.3	84.4	0.60	16.0	62.6	1.23	57.8	121	8.39	203	476	2.56	13.1	62.3	1.81	9.65	0.68	1.32	0.69	20.3	9.37	12.3
	178–180	II	96.75	16.9	83.4	43.7	84.9	0.82	16.3	159	1.81	59.6	124	8.58	220	400	2.58	13.2	59.4	1.74	9.42	0.66	1.32	0.74	20.0	9.30	19.7
	200–202	II	86.34	12.9	83.1	42.6	78.5	0.64	14.9	109	1.78	53.1	110	7.68	682	367	2.36	12.1	60.6	1.76	8.72	0.61	1.24	0.74	18.9	8.80	21.3
	250–252	III	50.29	7.32	32.2	16.7	43.0	0.22	8.89	0.78	0.65	29.5	59.7	4.01	436	231	1.49	6.99	38.2	1.18	5.61	0.40	0.77	0.38	10.4	5.41	1.86
	294–296	III	56.63	7.80	36.1	18.3	49.7	0.24	10.3	0.77	0.62	33.8	69.2	4.44	383	263	1.76	7.92	47.2	1.42	66.86	0.49	0.90	0.42	12.1	6.46	2.42
KL-02	58–60	I	79.0	15.7	64.1	42.2	73.2	0.62	14.0	45.7	1.61	52.2	104	7.04	574	471	2.21	11.6	60.3	1.79	8.39	0.59	1.11	0.70	19.8	8.20	9.40
	86–88	I	80.9	16.3	69.0	41.8	75.2	0.50	14.1	35.7	1.13	52.4	106	7.19	580	551	2.29	11.8	59.8	1.75	8.76	0.61	1.15	0.72	26.4	8.51	7.18
	116–118	II	107	25.0	87.3	60.7	96.5	0.65	18.1	45.3	1.54	67.1	130	9.17	229	856	2.75	15.1	76.1	2.21	10.7	0.75	1.37	0.78	22.6	10.4	6.17
	153–155	II	97.9	15.1	75.1	43.5	86.1	0.59	16.8	46.0	1.27	61.5	126	8.57	249	719	2.63	13.7	72.2	2.11	10.4	0.73	1.34	0.90	21.5	9.87	7.33
	204–206	II	91.9	14.5	72.3	43.3	77.8	0.54	15.2	81.5	1.19	55.1	112	7.91	217	416	2.38	12.6	58.2	1.73	9.05	0.64	1.23	0.68	18.8	8.86	10.3
	232–234	II	96.5	18.7	94.2	42.9	83.2	0.64	16.1	112	1.86	56.5	119	8.23	223	366	2.57	13.1	66.0	1.92	9.61	0.68	1.38	0.70	20.3	9.42	10.6
	270–272	III	73.8	10.8	49.0	23.1	63.4	0.30	13.0	2.62	1.12	42.6	89.3	5.46	310	348	2.25	9.78	60.5	1.79	9.32	0.68	1.18	0.52	15.8	8.14	3.13
PLC-203	65–67	I	91.6	17.7	65.3	38.9	77.8	0.37	15.2	21.3	1.22	55.0	115	7.70	509	501	2.46	12.1	64.9	1.91	9.55	0.67	1.30	0.72	24.8	9.02	4.77
	109–111	I	91.1	17.3	64.9	37.6	81.2	0.35	15.5	20.0	1.40	57.4	116	7.93	396	569	2.52	12.5	60.8	1.81	9.72	0.68	1.27	0.77	23.1	9.07	3.88
	170–172	II	107	21.4	79.3	42.1	92.1	0.53	17.8	33.4	1.74	65.8	133	9.26	215	913	2.83	14.5	74.8	2.17	10.9	0.77	1.40	0.86	21.9	10.4	5.98
	218–220	II	108	20.6	78.1	36.6	92.1	0.43	17.2	33.9	1.16	62.2	131	9.22	200	433	2.73	13.8	69.7	2.03	10.7	0.75	1.39	0.80	21.9	10.0	5.18
	260–262	II	103	17.2	72.0	38.4	91.2	0.40	17.3	37.0	1.25	63.1	128	8.81	219	444	2.75	14.0	70.3	2.08	10.7	0.76	1.41	0.80	21.3	10.2	5.73
	278–280	II	101	18.1	75.4	40.1	88.4	0.45	16.4	55.2	1.59	59.2	120	8.41	205	433	2.64	13.5	70.1	2.05	10.2	0.72	1.42	0.72	20.4	9.73	6.49
Average		I	84.6	16.8	65.6	39.8	76.3	0.46	14.5	34.0	1.39	53.8	109	7.39	516	533	2.34	11.9	62.1	1.82	9.03	0.63	1.20	0.71	24.1	8.64	6.99
		II	95.6	16.2	79.2	44.7	84.6	0.61	16.1	65.0	1.47	58.3	119	8.21	269	549	2.53	13.2	67.5	1.96	9.74	0.69	1.32	0.77	20.2	9.39	10.7
		III	60.7	8.60	38.3	20.6	52.9	0.26	10.8	2.07	0.87	35.6	73.8	4.69	377	309	1.85	8.27	48.8	1.47	19.3	0.53	0.96	0.45	12.9	6.74	2.55

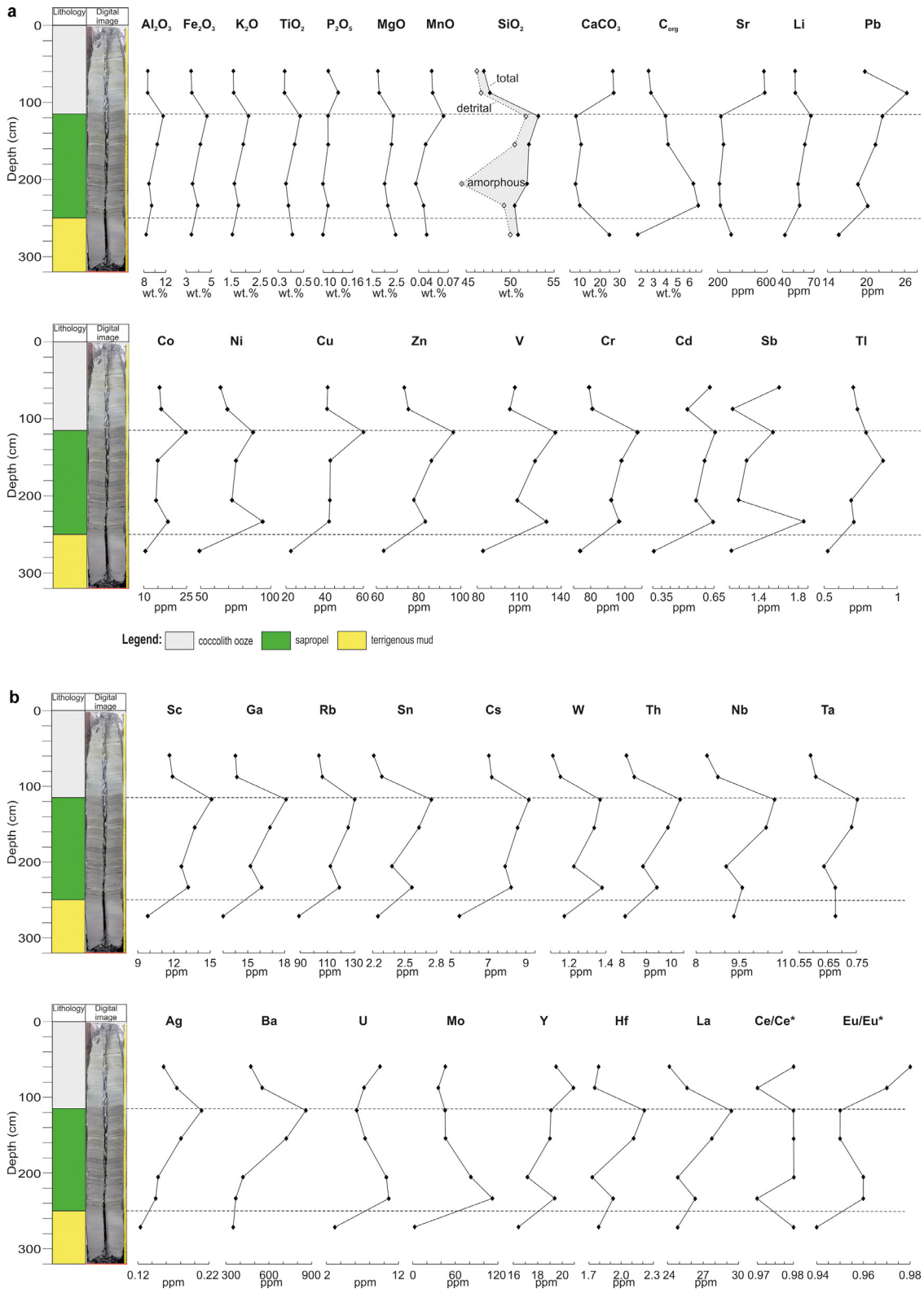

Figure 2 Vertical profiles of selected elements concentrations and selected elements ratios along the sediment core KL-02.

Table 3 Rare earth elements (REE) and Yttrium (Y) concentrations (measured using Inductively Coupled Plasma Mass Spectrometry, ICP-MS) of the studied sediments.

Core ID	Horizon (cm)	Lithology Unit	La (ppm)	Ce	Pr	Nd	Sm	Eu	Gd	Tb	Dy	Ho	Er	Tm	Yb	Lu	Y	ΣREE	(Ce/Ce*)[a]	(Eu/Eu*)[b]	La_{UCCN}/Lu_{UCCN}
CF-01	57–59	I	25.0	50.6	5.97	23.0	4.59	0.98	4.19	0.64	3.72	0.73	2.00	0.30	1.93	0.28	19.9	124	0.98	0.96	0.88
	93–95	II	28.9	58.6	6.83	25.9	5.13	1.07	4.50	0.69	3.98	0.78	2.15	0.32	2.15	0.32	20.5	141	0.98	0.96	0.90
	124–126	II	27.9	56.9	6.70	25.4	5.07	1.04	4.45	0.68	3.88	0.75	2.06	0.31	2.05	0.30	19.8	138	0.98	0.95	0.92
	155–157	II	22.9	46.1	5.45	21.1	4.25	0.90	3.96	0.61	3.56	0.71	1.98	0.30	1.96	0.30	20.1	114	0.97	0.95	0.77
	195–197	II	23.4	46.8	5.59	21.4	4.34	0.92	3.96	0.61	3.59	0.71	1.93	0.29	1.92	0.29	19.9	116	0.96	0.96	0.81
	218–220	III	25.3	51.7	6.10	23.3	4.60	0.93	3.96	0.60	3.38	0.66	1.79	0.26	1.75	0.26	17.4	125	0.98	0.94	0.97
CF-03	55–57	II	27.6	56.2	6.60	25.1	4.97	1.02	4.31	0.65	3.71	0.72	1.97	0.29	1.96	0.29	18.9	135	0.98	0.96	0.96
	104–106	II	27.8	56.1	6.58	24.9	4.90	1.01	4.29	0.66	3.83	0.75	2.09	0.31	2.10	0.31	19.9	136	0.98	0.96	0.89
	133–135	II	25.4	51.3	6.08	23.2	4.63	0.96	4.15	0.64	3.69	0.73	2.00	0.30	1.99	0.30	19.6	125	0.97	0.95	0.86
	170–172	II	22.2	44.4	5.34	20.5	4.08	0.86	3.67	0.56	3.22	0.63	1.74	0.26	1.71	0.25	17.3	109	0.96	0.96	0.88
	216–218	III	15.6	31.7	3.77	14.5	2.86	0.57	2.49	0.37	2.09	0.41	1.11	0.16	1.10	0.16	10.8	77	0.97	0.93	0.96
KL-01	165–167	II	26.4	53.8	6.34	24.1	4.79	1.00	4.19	0.64	3.65	0.71	1.94	0.29	1.91	0.28	18.6	130	0.98	0.96	0.93
	178–180	II	25.9	52.2	6.16	23.4	4.67	0.97	4.08	0.62	3.56	0.69	1.88	0.28	1.86	0.28	18.1	127	0.97	0.96	0.94
	200–202	II	24.7	49.8	5.93	22.7	4.54	0.95	4.11	0.62	3.57	0.69	1.89	0.28	1.85	0.28	18.8	122	0.97	0.95	0.90
	250–252	III	16.0	32.4	3.84	14.7	2.90	0.59	2.49	0.37	2.13	0.41	1.13	0.17	1.11	0.17	10.9	78	0.97	0.95	0.97
	294–296	III	20.1	40.9	4.80	18.3	3.57	0.70	3.05	0.45	2.51	0.48	1.30	0.20	1.29	0.19	12.7	98	0.98	0.92	1.06
KL-02	58–60	I	24.1	48.8	5.75	22.0	4.40	0.95	4.01	0.62	3.62	0.71	1.97	0.29	1.93	0.29	19.6	119	0.98	0.98	0.84
	86–88	I	25.6	51.7	6.10	23.5	4.74	1.01	4.36	0.66	3.86	0.76	2.06	0.30	1.99	0.29	21.0	127	0.97	0.97	0.88
	116–118	II	29.3	59.7	6.95	26.2	5.15	1.04	4.41	0.67	3.77	0.73	2.04	0.31	2.03	0.31	19.1	143	0.98	0.95	0.96
	153–155	II	27.7	56.2	6.61	25.1	4.94	1.01	4.30	0.65	3.72	0.73	1.99	0.30	1.99	0.29	19.0	135	0.98	0.95	0.94
	204–206	II	24.8	50.4	5.95	22.7	4.52	0.94	3.93	0.60	3.42	0.66	1.81	0.27	1.78	0.27	17.2	122	0.98	0.96	0.93
	232–234	II	26.3	52.9	6.28	23.9	4.79	1.00	4.27	0.66	3.75	0.74	2.00	0.30	1.97	0.29	19.4	129	0.97	0.96	0.90
	270–272	III	24.8	50.6	6.00	22.8	4.51	0.91	3.89	0.58	3.24	0.62	1.71	0.25	1.66	0.25	16.5	122	0.98	0.94	1.00
PLC-203	65–67	I	25.9	52.9	6.20	23.7	4.72	0.98	4.21	0.64	3.70	0.73	1.97	0.30	1.95	0.29	19.4	128	0.98	0.95	0.91
	109–111	I	26.0	52.6	6.17	23.6	4.68	0.97	4.08	0.62	3.51	0.68	1.87	0.28	1.82	0.27	18.1	127	0.98	0.96	0.97
	170–172	II	29.0	58.9	6.89	26.2	5.16	1.04	4.49	0.69	3.96	0.78	2.12	0.32	2.12	0.31	20.2	142	0.98	0.94	0.93
	218–220	II	27.9	57.1	6.66	25.4	5.01	1.03	4.32	0.65	3.70	0.72	1.97	0.30	1.98	0.29	18.7	137	0.99	0.96	0.96
	260–262	II	28.7	58.6	6.86	26.0	5.13	1.06	4.47	0.67	3.84	0.74	2.05	0.31	2.05	0.30	19.4	141	0.98	0.96	0.94
	278–280	II	27.1	55.3	6.48	24.6	4.89	1.01	4.33	0.66	3.84	0.75	2.05	0.30	2.03	0.30	19.5	134	0.98	0.96	0.90
Average		I	25.3	51.3	6.04	23.2	4.63	0.98	4.17	0.64	3.68	0.72	1.97	0.29	1.92	0.28	19.6	125	0.98	0.96	0.90
		II	26.5	53.8	6.33	24.1	4.79	0.99	4.22	0.64	3.70	0.72	1.98	0.30	1.97	0.29	19.2	130	0.98	0.96	0.91
		III	20.4	41.5	4.90	18.7	3.69	0.74	3.18	0.47	2.67	0.52	1.41	0.21	1.38	0.21	13.7	100	0.98	0.94	0.99

[a] $Ce/Ce^* = 2Ce_{UCCN}/(La_{UCCN}+Pr_{UCCN})$

[b] $Eu/Eu^* = 2Eu_{UCCN}/(Sm_{UCCN}+Gd_{UCCN})$

Table 4 Calculated enrichment factors (EFs) for some of the analyzed elements in the studied sediments.

Core ID	Horizon (cm)	Lithology Unit	EF_{Fe}	EF_{Mn}	EF_{Ag}	EF_{V}	EF_{Cr}	EF_{Co}	EF_{Ni}	EF_{Cu}	EF_{Zn}	EF_{Cd}	EF_{Ga}	EF_{Mo}	EF_{Sb}	EF_{Li}	EF_{Rb}	EF_{Cs}	EF_{Sr}	EF_{Ba}	EF_{Sn}	EF_{Sc}	EF_{Zr}	EF_{Hf}
CF-01	57–59	I	1.23	0.95	5.89	1.79	1.52	1.70	2.39	2.40	1.91	8.48	1.37	74.2	6.94	4.29	2.15	2.51	2.82	1.59	1.82	1.44	0.58	0.61
	93–95	II	1.24	0.89	5.02	1.73	1.54	1.55	2.36	2.74	1.91	8.41	1.39	72.2	4.55	4.38	2.12	2.50	1.05	1.62	1.76	1.51	0.57	0.59
	124–126	II	1.22	0.71	4.78	1.84	1.62	1.21	2.49	2.21	1.94	9.94	1.42	83.9	6.23	4.30	2.17	2.53	1.18	1.34	1.88	1.48	0.58	0.60
	155–157	II	1.23	0.84	5.57	2.17	1.80	1.63	3.53	3.19	2.26	14.0	1.57	74.6	5.76	4.73	2.37	2.85	1.34	1.35	2.06	1.69	0.56	0.61
	195–197	II	1.19	0.56	5.98	3.25	1.66	1.28	3.25	3.37	2.12	14.5	1.56	128	6.73	4.49	2.38	2.73	3.31	1.31	2.05	1.58	0.64	0.67
	218–220	III	1.21	0.73	4.10	1.63	1.50	1.09	1.69	1.73	1.79	5.84	1.39	8.5	5.57	3.71	1.99	2.10	1.72	1.22	1.99	1.29	0.58	0.63
CF-03	55–57	II	1.23	0.72	4.85	1.83	1.60	1.31	2.42	2.35	1.97	10.6	1.42	76.1	6.20	4.38	2.25	2.59	1.14	1.44	1.89	1.45	0.52	0.55
	104–106	II	1.18	0.57	4.94	1.92	1.58	1.25	2.60	2.58	1.98	12.3	1.42	88.7	6.03	4.42	2.18	2.62	1.11	1.78	1.78	1.46	0.59	0.62
	133–135	II	1.22	0.75	5.55	2.14	1.75	1.52	3.10	3.03	2.20	15.4	1.57	112	6.22	4.69	2.37	2.88	1.30	2.09	2.02	1.64	0.58	0.60
	170–172	II	1.15	0.62	5.23	2.43	1.56	1.10	2.63	2.69	1.83	13.6	1.38	61.9	6.48	3.85	2.02	2.19	1.67	1.20	1.89	1.36	0.64	0.68
	216–218	III	1.24	1.33	4.73	1.80	1.59	1.21	2.02	2.03	1.97	8.01	1.54	3.0	5.56	4.36	2.19	2.47	4.42	1.43	2.16	1.50	0.58	0.67
KL-01	165–167	II	1.22	0.86	5.20	1.94	1.70	1.37	2.72	2.68	2.04	10.8	1.48	92.3	4.99	4.46	2.34	2.78	1.03	1.24	1.98	1.52	0.52	0.55
	178–180	II	1.25	0.72	4.89	2.00	1.70	1.58	2.87	2.53	2.05	14.8	1.51	234	7.33	4.60	2.39	2.84	1.11	1.04	1.99	1.53	0.50	0.53
	200–202	II	1.20	0.52	5.03	2.40	1.67	1.33	3.15	2.71	2.08	12.7	1.51	176	7.92	4.50	2.33	2.79	3.79	1.05	2.00	1.54	0.56	0.59
	250–252	III	1.24	1.52	4.42	1.74	1.60	1.24	2.01	1.75	1.88	7.16	1.49	2.1	4.76	4.12	2.08	2.40	3.99	1.09	2.08	1.46	0.58	0.65
	294–296	III	1.20	1.10	4.99	1.80	1.63	1.19	2.03	1.73	1.96	7.06	1.56	1.9	4.10	4.26	2.18	2.40	3.17	1.12	2.22	1.50	0.65	0.71
KL-02	58–60	I	1.19	0.95	5.34	1.95	1.52	1.61	2.41	2.67	1.93	12.2	1.42	73.5	7.12	4.40	2.19	2.54	3.17	1.34	1.86	1.47	0.55	0.60
	86–88	I	1.22	0.96	6.06	1.91	1.57	1.68	2.62	2.66	2.00	9.91	1.44	57.9	5.04	4.45	2.25	2.62	3.23	1.57	1.94	1.50	0.55	0.59
	116–118	II	1.23	0.86	5.29	1.87	1.55	1.93	2.48	2.89	1.92	9.64	1.38	55.0	5.14	4.27	2.07	2.50	0.96	1.83	1.75	1.44	0.53	0.56
	153–155	II	1.21	0.69	5.01	1.85	1.57	1.29	2.36	2.29	1.89	9.66	1.42	61.6	4.68	4.32	2.21	2.58	1.15	1.70	1.85	1.44	0.55	0.59
	204–206	II	1.20	0.65	4.89	1.94	1.73	1.45	2.66	2.67	2.01	10.4	1.50	128	5.14	4.53	2.30	2.79	1.17	1.15	1.96	1.56	0.52	0.56
	232–234	II	1.27	0.73	4.62	2.19	1.71	1.77	3.27	2.50	2.03	11.6	1.50	166	7.59	4.39	2.31	2.74	1.14	0.96	2.00	1.53	0.56	0.59
	270–272	III	1.25	0.89	4.17	1.61	1.48	1.15	1.92	1.52	1.74	6.14	1.37	4.4	5.16	3.74	1.96	2.05	1.78	1.03	1.97	1.29	0.58	0.62
PLC-203	65–67	I	1.23	1.16	4.92	1.90	1.62	1.67	2.26	2.26	1.89	6.70	1.41	31.5	4.97	4.27	2.23	2.56	2.59	1.31	1.91	1.41	0.55	0.59
	109–111	I	1.21	0.85	4.90	1.89	1.51	1.53	2.11	2.05	1.85	5.94	1.35	27.8	5.35	4.18	2.11	2.47	1.89	1.39	1.83	1.36	0.48	0.52
	170–172	II	1.24	0.77	4.39	1.78	1.59	1.69	2.31	2.06	1.88	8.05	1.39	41.5	5.95	4.28	2.16	2.58	0.92	2.00	1.84	1.42	0.53	0.56
	218–220	II	1.28	0.80	4.38	1.75	1.70	1.73	2.41	1.90	2.00	6.93	1.43	44.7	4.21	4.30	2.26	2.73	0.91	1.01	1.89	1.43	0.52	0.56
	260–262	II	1.24	0.57	4.55	1.76	1.59	1.41	2.17	1.95	1.93	6.31	1.40	47.7	4.43	4.26	2.16	2.55	0.97	1.01	1.86	1.42	0.52	0.56
	278–280	II	1.29	0.96	4.81	1.84	1.75	1.67	2.56	2.28	2.10	7.97	1.49	80.0	6.34	4.50	2.28	2.74	1.02	1.11	2.01	1.54	0.58	0.62
Average		I	1.22	0.97	5.42	1.89	1.55	1.64	2.36	2.41	1.92	8.64	1.40	53.0	5.88	4.32	2.19	2.54	2.74	1.44	1.87	1.44	0.54	0.58
		II	1.23	0.73	5.00	2.03	1.65	1.48	2.70	2.56	2.01	10.9	1.46	96.1	5.89	4.40	2.25	2.66	1.38	1.38	1.92	1.50	0.56	0.59
		III	1.22	1.11	4.48	1.72	1.56	1.18	1.93	1.75	1.87	6.84	1.47	3.95	5.03	4.04	2.08	2.28	3.02	1.18	2.09	1.41	0.59	0.66

(*continued on next page*)

Table 4 (*continued*)

Core ID	Horizon (cm)	Lithology Unit	EF_{Nb}	EF_{Ta}	EF_{W}	EF_{Tl}	EF_{Pb}	EF_{Th}	EF_{U}	EF_{La}	EF_{Ce}	EF_{Pr}	EF_{Nd}	EF_{Sm}	EF_{Eu}	EF_{Gd}	EF_{Tb}	EF_{Dy}	EF_{Ho}	EF_{Er}	EF_{Tm}	EF_{Yb}	EF_{Lu}	EF_{Y}
CF-01	57–59	I	1.26	1.18	1.07	1.23	2.71	1.39	6.25	1.40	1.39	1.46	1.48	1.69	1.70	1.82	1.59	1.65	1.52	1.51	1.73	1.67	1.57	1.64
	93–95	II	1.20	1.12	0.98	1.11	1.85	1.33	3.62	1.31	1.30	1.35	1.34	1.53	1.50	1.58	1.38	1.43	1.32	1.31	1.49	1.51	1.45	1.37
	124–126	II	1.30	1.21	1.09	1.36	1.83	1.41	7.07	1.34	1.35	1.41	1.40	1.61	1.55	1.66	1.45	1.48	1.35	1.34	1.54	1.53	1.44	1.41
	155–157	II	1.32	1.25	1.24	1.36	2.05	1.52	9.04	1.45	1.44	1.51	1.54	1.78	1.77	1.95	1.71	1.80	1.68	1.69	1.97	1.93	1.90	1.88
	195–197	II	1.36	1.30	1.26	1.96	2.10	1.56	11.1	1.50	1.47	1.56	1.57	1.83	1.82	1.96	1.73	1.82	1.69	1.66	1.91	1.90	1.85	1.88
	218–220	III	1.41	1.35	1.15	1.09	1.69	1.44	2.21	1.48	1.49	1.56	1.56	1.77	1.68	1.79	1.55	1.57	1.44	1.41	1.57	1.59	1.52	1.50
CF-03	55–57	II	1.29	1.19	1.06	1.43	1.85	1.39	5.25	1.35	1.35	1.41	1.41	1.60	1.54	1.63	1.40	1.44	1.31	1.30	1.46	1.48	1.42	1.36
	104–106	II	1.22	1.13	1.02	1.29	1.85	1.37	7.49	1.30	1.29	1.35	1.34	1.52	1.47	1.56	1.37	1.43	1.31	1.32	1.50	1.53	1.45	1.38
	133–135	II	1.33	1.25	1.23	1.42	2.00	1.48	8.39	1.42	1.41	1.48	1.49	1.70	1.66	1.79	1.58	1.64	1.52	1.50	1.73	1.72	1.67	1.61
	170–172	II	1.38	1.32	1.16	1.89	1.76	1.38	6.82	1.42	1.39	1.49	1.50	1.72	1.70	1.82	1.58	1.63	1.50	1.50	1.72	1.69	1.60	1.63
	216–218	III	1.43	1.39	1.24	1.32	1.88	1.61	2.40	1.58	1.58	1.66	1.68	1.91	1.79	1.95	1.66	1.68	1.55	1.51	1.67	1.72	1.62	1.61
KL-01	165–167	II	1.30	1.23	1.13	1.24	1.94	1.45	7.39	1.38	1.39	1.45	1.45	1.65	1.62	1.70	1.48	1.52	1.39	1.37	1.57	1.55	1.47	1.44
	178–180	II	1.27	1.19	1.13	1.33	1.91	1.43	11.8	1.35	1.34	1.41	1.40	1.61	1.57	1.65	1.43	1.48	1.35	1.32	1.51	1.51	1.46	1.40
	200–202	II	1.29	1.21	1.16	1.46	1.98	1.49	14.0	1.42	1.41	1.49	1.50	1.72	1.69	1.83	1.58	1.63	1.48	1.46	1.66	1.65	1.61	1.59
	250–252	III	1.37	1.30	1.19	1.24	1.79	1.51	2.02	1.51	1.51	1.59	1.60	1.81	1.73	1.82	1.55	1.60	1.45	1.44	1.66	1.63	1.61	1.52
	294–296	III	14.8	1.44	1.25	1.24	1.88	1.63	2.37	1.72	1.72	1.79	1.79	2.01	1.85	2.02	1.70	1.70	1.53	1.50	1.76	1.71	1.62	1.60
KL-02	58–60	I	1.24	1.16	1.03	1.38	2.06	1.38	6.16	1.38	1.37	1.43	1.44	1.66	1.68	1.77	1.57	1.64	1.51	1.52	1.71	1.71	1.65	1.65
	86–88	I	1.30	1.21	1.08	1.43	2.77	1.45	4.74	1.47	1.46	1.53	1.55	1.80	1.80	1.94	1.68	1.77	1.63	1.60	1.78	1.77	1.67	1.78
	116–118	II	1.19	1.11	0.96	1.16	1.78	1.32	3.05	1.26	1.27	1.31	1.30	1.46	1.39	1.47	1.28	1.29	1.17	1.18	1.38	1.36	1.34	1.21
	153–155	II	1.28	1.20	1.04	1.47	1.86	1.39	4.00	1.32	1.32	1.37	1.37	1.55	1.49	1.58	1.37	1.41	1.30	1.28	1.47	1.47	1.38	1.33
	204–206	II	1.30	1.23	1.12	1.31	1.91	1.46	6.59	1.38	1.38	1.45	1.45	1.66	1.62	1.70	1.48	1.52	1.37	1.36	1.56	1.54	1.50	1.42
	232–234	II	1.31	1.23	1.19	1.27	1.95	1.47	6.41	1.39	1.37	1.44	1.45	1.66	1.63	1.74	1.54	1.57	1.46	1.42	1.63	1.61	1.53	1.51
	270–272	III	1.43	1.39	1.14	1.06	1.71	1.43	2.13	1.47	1.48	1.56	1.55	1.77	1.68	1.79	1.53	1.53	1.38	1.37	1.53	1.53	1.48	1.45
PLC-203	65–67	I	1.30	1.21	1.11	1.30	2.38	1.40	2.88	1.36	1.37	1.42	1.43	1.64	1.60	1.71	1.49	1.55	1.43	1.39	1.63	1.59	1.52	1.50
	109–111	I	1.24	1.15	1.02	1.31	2.08	1.32	2.20	1.28	1.28	1.33	1.34	1.52	1.48	1.56	1.35	1.38	1.25	1.24	1.43	1.39	1.33	1.32
	170–172	II	1.24	1.17	1.01	1.31	1.76	1.35	3.03	1.28	1.28	1.33	1.33	1.50	1.42	1.53	1.35	1.39	1.28	1.26	1.46	1.45	1.37	1.32
	218–220	II	1.29	1.21	1.06	1.29	1.87	1.38	2.78	1.31	1.32	1.36	1.37	1.55	1.49	1.57	1.35	1.38	1.26	1.24	1.45	1.44	1.36	1.29
	260–262	II	1.27	1.20	1.05	1.26	1.78	1.38	3.01	1.31	1.32	1.37	1.37	1.55	1.50	1.59	1.36	1.40	1.27	1.26	1.47	1.45	1.37	1.31
	278–280	II	1.36	1.28	1.19	1.28	1.91	1.48	3.83	1.39	1.40	1.46	1.45	1.66	1.61	1.73	1.50	1.57	1.44	1.42	1.59	1.62	1.54	1.48
Average		I	1.27	1.18	1.06	1.33	2.40	1.39	4.44	1.38	1.37	1.43	1.45	1.66	1.65	1.76	1.54	1.60	1.47	1.45	1.66	1.63	1.55	1.58
		II	1.29	1.21	1.11	1.38	1.89	1.42	6.56	1.36	1.36	1.42	1.42	1.62	1.58	1.69	1.47	1.52	1.39	1.38	1.58	1.57	1.51	1.46
		III	4.08	1.38	1.20	1.19	1.79	1.52	2.23	1.55	1.55	1.63	1.64	1.85	1.75	1.88	1.60	1.62	1.47	1.45	1.64	1.63	1.57	1.54

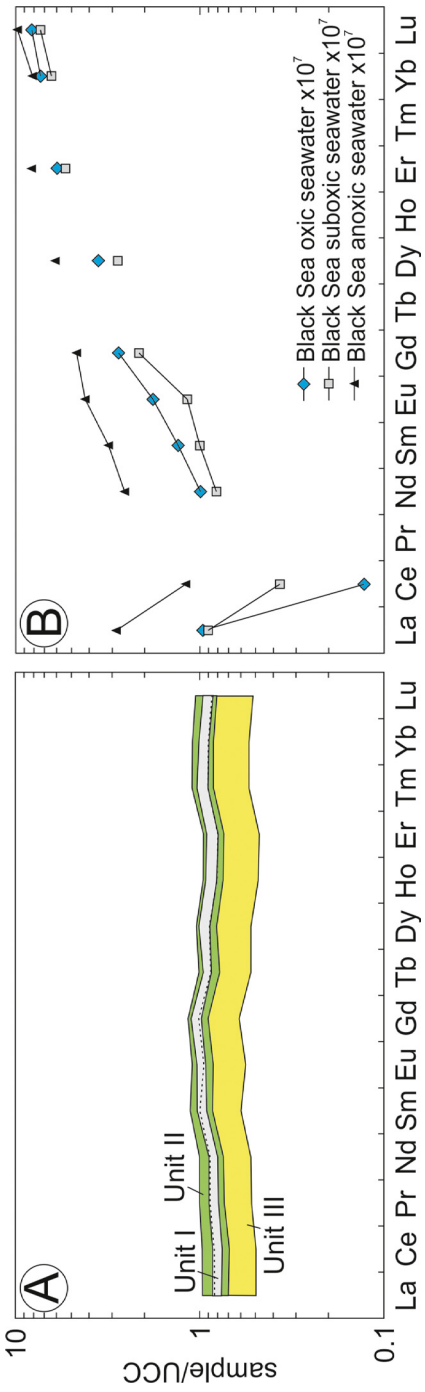

Figure 3 UCC-normalized (Rudnick and Gao, 2003) REE distribution patterns of: (A) studied Black Sea Quaternary sediments from Unit I (coccolith ooze), Unit II (sapropel) and Unit III (terrigenous mud); (B) oxic (50 m water depth), suboxic (100 m water depth) and anoxic (2185 m water depth) seawater from Black Sea (German et al., 1991).

EF_U, EF_{Cd} and EF_{Sb} exhibit similar vertical profiles (Fig. 4) with strong enrichments at the base of Unit II, decrease in the enrichment towards Unit I and a following increase towards the upper part of Unit I. The general upward trend (from Unit III to Unit I) in the enrichment factors of Sn, Th, La (representative for the light REE), Lu (representative for the heavy REE), Nb and Ta is a decrease through Units III and II, and a sharp increase in Unit I (Fig. 4). These elements are enriched (relative to the UCC) in all the three stratigraphic units (Fig. 4). Vertical profiles of the enrichment factors of Pb and Ag are similar to upward increases and maxima in Unit I (Fig. 4). The EF_{Zr} and EF_{Hf} co-vary, but both elements are depleted (relative to the UCC) in all the three stratigraphic units, particularly in the sapropel layer (Fig. 4).

4.2. Sr-Nd-Pb-isotope composition of the terrigenous component of the sediments

The Sr-Nd-Pb-isotope composition of the terrigenous component of the studied sediments (Table 5) is relatively uniform and there are only minor differences between samples from different sites and between those from different stratigraphic units. Strontium isotope composition ($^{87}Sr/^{86}Sr$) of this component is generally quite radiogenic compared to the Black Sea water signature ($^{87}Sr/^{86}Sr_{Last\ Glacial\ Maximum} = 0.70865–0.70875$, $^{87}Sr/^{86}Sr_{modern} = 0.709133$; Major et al., 2006) and has a total range from ~0.7196 to 0.7224. Both the lowest and highest values were measured in the sapropel samples: from cores CF-03 and PLC-203, respectively (Table 5). Furthermore, there is a general tendency of $^{87}Sr/^{86}Sr$ variation across the boundaries between the stratigraphic units, but there is no simple relationship between the Sr isotope ratios and Sr concentration as exemplified by data from core Kl-02 (Fig. 5). The overall Nd isotope pattern is similar to that observed for the Sr isotope system: εNd values are relatively homogeneous and range from −8.0 to −10.2, with one lower value (−12.5) in core PLC-203 (Table 5). Although the variations are overall small, $^{206}Pb/^{204}Pb$ decreases upward (from Unit III to Unit I) along each sediment core (Table 5; Fig. 5), and this vertical distribution is also observed for the Nd isotopes for the same profile (Fig. 5). However, the other two Pb isotope ratios show similar values for all samples irrespective of their lithology although data from core PLC-203 generally are somewhat more radiogenic (Table 5). The binary relations of Sr-Pb, Sr-Nd and Nd-Pb isotopes (not shown) do not indicate any obvious linear trends related to stratigraphic position within a core.

5. Discussion

5.1. Element enrichment in organic-rich sediments

5.1.1. Iron

The Fe enrichment observed in the Black Sea organic-rich sediments (Units II and I) is inferred to be of neither diagenetic origin (Eckert et al., 2013; Lyons and Severmann, 2006) nor is it a result of preferential physical transport of reactive Fe-rich detrital component to the deep basin

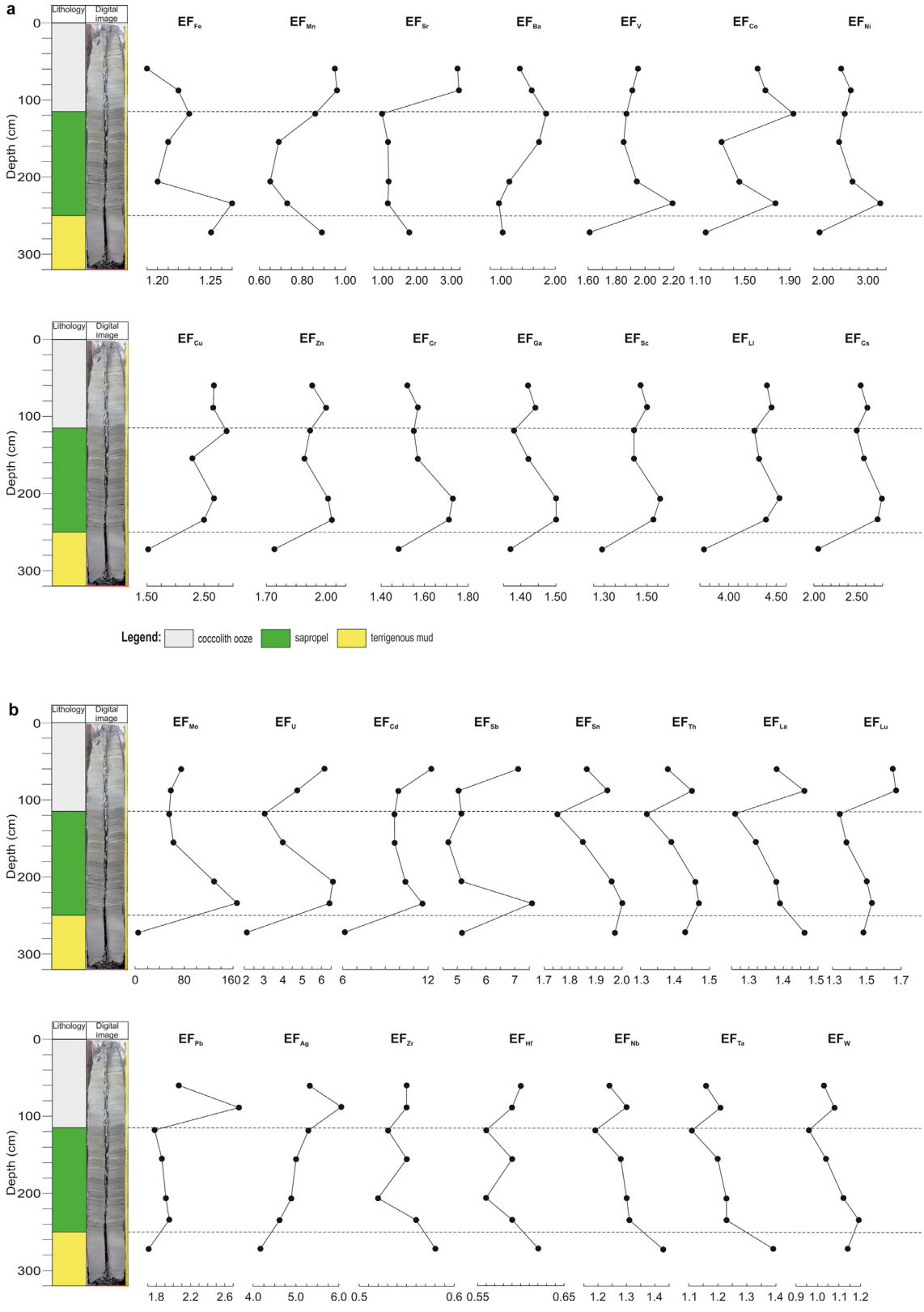

Figure 4 Vertical profiles of enrichment factors (EFs) of some elements along the sediment core KL-02.

Table 5 Isotope composition of the terrigenous component of the studied sediments.

Core ID	Horizon (cm)	Lithology Unit	$^{87}Sr/^{86}Sr$	$\pm 2\sigma_m$	$^{143}Nd/^{144}Nd$	$\pm 2\sigma_m$	$\varepsilon_{Nd(0)}$	$^{206}Pb/^{204}Pb$	$^{207}Pb/^{204}Pb$	$^{208}Pb/^{204}Pb$
CF-03	55–57	II	0.720946	9	0.512113	14	-10.24	18.893	15.669	38.918
	104–106	II	0.719618	10	0.512157	3	-9.38	18.877	15.659	38.895
	133–135	II	0.720269	8	0.512163	3	-9.27	18.875	15.667	38.895
	170–172	II	0.719619	8	0.512175	5	-9.03	18.906	15.671	38.871
	216–218	III	0.721602	9	0.512168	5	-9.17	19.008	15.682	38.927
KL-01	165–167	II	0.721683	10	0.512194	3	-8.66	18.886	15.669	38.908
	178–180	II	0.722007	9	0.512213	6	-8.29	18.874	15.670	38.907
	200–202	II	0.720938	6	0.512147	5	-9.58	18.914	15.669	38.923
	250–252	III	0.722410	7	0.512230	19	-7.96	19.010	15.683	38.947
	294–296	III	0.721951	8	0.512129	10	-9.93	19.120	15.697	39.177
KL-02[a]	58–60	I	0.721513	9	0.512171	4	-9.11	18.814	15.666	38.901
	86–88	I	0.721241	9	0.512169	3	-9.15	18.801	15.661	38.887
	116–118	II	0.720371	8	0.512175	4	-9.03	18.834	15.663	38.914
	153–155	II	0.721124	12	0.512162	4	-9.29	18.838	15.664	38.893
	204-206	II	0.722097	9	0.512162	3	-9.29	18.838	15.666	38.909
	232–234	II	0.721857	6	0.512168	3	-9.17	18.844	15.666	38.895
	270–272	III	0.721258	9	0.512137	5	-9.77	18.892	15.675	38.985
PLC-203	65–67	I	0.722630	13	0.512168	27	-9.17	18.907	15.680	39.053
	109–111	I	0.722593	8	0.512137	6	-9.77	18.977	15.692	39.062
	170–172	II	0.722119	8	0.512164	18	-9.25	18.978	15.691	39.054
	218–220	II	0.722543	9	0.511995	8	-12.54	18.981	15.691	39.062
	260–262	II	0.722696	8	0.512126	41	-9.99	19.018	15.696	39.082
	278–280	II	0.722809	8	0.512135	6	-9.81	18.981	15.694	39.045
BCR-2[b]			-		0.512620	7		18.751	15.624	38.719
BCR-2[b]			0.705017	6	0.512663	10		18.777	15.616	38.755

[a] Pb isotope data were partly obtained by a Micromass Isoprobe, the others by a Nu Plasma II instrument. The $^{87}Sr/^{86}Sr$ values of the samples were corrected to $^{87}Sr/^{86}Sr = 0.710245$ for the NIST SRM-987 Sr standard. No external corrections were required for the Nd runs.

[b] Unleached data.

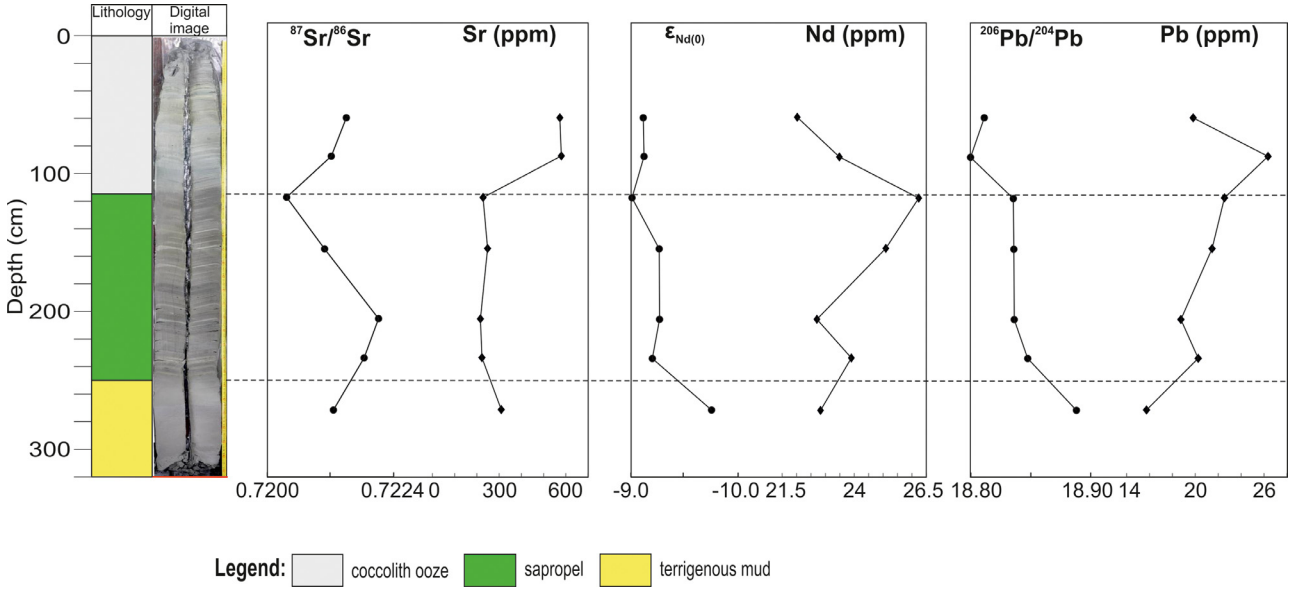

Figure 5 Vertical profiles of Sr, Nd, Pb isotope ratios and elemental concentrations along the sediment core KL-02.

(Lyons and Severmann, 2006). The reactive Fe enrichment of these sediments has been recognized (Anderson and Raiswell, 2004; Canfield et al., 1996; Lyons and Severmann, 2006; Raiswell and Anderson, 2005) as a uniquely euxinic phenomenon. Dissolved Fe supply to the euxinic pool has been attributed to the operation of a benthic Fe redox shuttle. According to this model (Lyons and Severmann, 2006), in oxic to suboxic sediments (now at the Black Sea shelf) with organic matter content high enough to produce anoxia, but not enough to create H_2S production by SO_4^{2-} reduction, the deposited Fe-oxyhydroxides are dissolved in the sediment. Produced Fe^{2+} is mobile in the anoxic pore fluids and diffuses into the bottom seawater. Then it can be transported into the euxinic deep waters of the basin where it reacts with dissolved H_2S and forms sulfides that settle down on the seafloor (Lyons and Severmann, 2006). This process strips almost completely the dissolved Fe out of the euxinic deep seawater.

This general model was further developed by Eckert et al. (2013) in their attempt to explain the variations of Fe enrichment in the Holocene Black Sea sediments. A key point of this model, based on the evolution of euxinia in the Black Sea, is the temporal fluctuation of the chemocline which is the primary contributor of dissolved Fe to the enxinic pool. In our endeavor to explain the observed vertical distribution of the Fe enrichment in the studied sediments (Fig. 4) we employ this model (Eckert et al., 2013) with two new assumptions: (1) the establishment of euxinia in the deep Black Sea started with onset of suboxia that gradually evolved to euxinia; (2) the chemocline, developed during the evolution of the deep water from oxic to euxinic, has not undergone substantial fluctuations during its rise up to the shelf.

The last ingression of Mediterranean seawater into the Black Sea through the narrow and shallow Bosporus Strait started at ~9 ka BP (Bahr et al., 2005, 2008; Soulet et al., 2011). The inflow of saline marine waters marks the last transition of the Black Sea from oxic lacustrine to the euxinic marine basin (Fig. 6a). The Black Sea deep waters evolved from oxic to suboxic as a result of oxygen depletion due to saline stratification of the water column, incurred reduced vertical ventilation and oxygen consumption due to respiration of organic matter (Murray et al., 1991). The sediment at vast areas of the abyssal plain and the lower continental slope produced high Fe^{2+} flux to the bottom water as a result of the benthic Fe redox shuttle mechanism (Lyons and Severmann, 2006) (Fig. 6a). Progressively increasing concentration of the dissolved H_2S due to microbial SO_4^{2-} reduction increased the amount of precipitated dissolved Fe^{2+} as Fe-sulfides recorded as a peak in the Fe enrichment at the base of Unit II (Fig. 6b). Further development of the euxinia resulted in an increase of the volume of the deep euxinic waters and a rise of the chemocline (suboxic zone) formed between euxinic (deep) and oxic (surface) waters upward the continental slope. Seafloor overlaid by euxinic waters did not produce dissolved Fe anymore because the released Fe^{2+} within the sediment was sulfidized *in situ* by dissolved H_2S. Thus, the narrow band where the chemocline impinged the continental slope became the major source of Fe^{2+} to the euxinic pool. Since the magnitude of released Fe^{2+} flux is a function of the source area (Lyons and Severmann, 2006) the Fe^{2+} supply and consequently Fe-sulfide deposition during this stage was reduced. This is recorded as a decrease of the EF_{Fe} in the middle part of Unit II (Fig. 6c). We interpret the next maximum of the Fe enrichment at the upper part of Unit II (Fig. 4) as a result of a further rise of the chemocline and its impingement on the continental shelf: i.e., a further increase in the source area and related increase in the dissolved Fe^{2+} flux, and consequent Fe-sulfide burial in the deep basin (Fig. 6d). According to previous estimates (Eckert et al., 2013) the rising chemocline reached the shelf at ~5.3 ka BP. The second maximum of the EF_{Fe} in our cores is before the transition between Units II and I (Fig. 4) dated at ~3 ka BP (Kwiecien et al., 2008). However, the increase of the EF_{Fe} begins earlier (Fig. 4) which may be interpreted as the beginning of the chemocline incursion into the shelf (Fig. 6d). It may roughly be estimated at ~5 ka BP, which is in line with the previous studies (Eckert et al., 2013). The following decrease in the Fe enrichment towards the middle of Unit I (Fig. 4) may be explained by an exhaustion of the source shelf sediments in Fe and a related decrease in the dissolved Fe flux to the euxinic pool. We may speculate that this situation has not evolved dramatically up to now when the chemocline (span from ~ 50 to 100 m water depth; Murray et al., 1989) impinges at the shelf (shelf edge at ~150 m water depth; Degens and Ross, 1974) (Fig. 1c,d).

5.1.2. Manganese

A benthic redox shuttle similar to that for Fe is supposed to operate for Mn as well (Lyons and Severmann, 2006). However, the enrichment profile of Mn differs from that of Fe (Fig. 4), which means that the mechanisms of enrichment/depletion of reactive Mn and Fe in the studied euxinic sediments differ from each other. The key details are that the Mn is, in general, depleted in these euxinic sediments (Units II and I; Table 4, Fig. 4) and it is most depleted in the sapropel layer (Unit II). This general Mn depletion (against UCC) is in accord with a previous suggestion (Konovalov et al., 2007) that Mn is not accumulated in sediments of the Black Sea anoxic zone where all our cores are located (Fig. 1c,d; Table 1).

The euxinic sediments (Units I and II) of the Black Sea sedimentary cover have a high content of organic matter (Calvert, 1990; Calvert et al., 1987; Degens and Ross, 1972; Glenn and Arthur, 1985; Ross et al., 1970) (Fig. 2). The organic matter degradation is the principal process that drives the dissolution and reprecipitation of a number of mineral phases within the sediment and provides both sources and sinks (respectively) of global importance to the geochemical mass balance of trace metals in the ocean (Emerson and Hedges, 2003). Therefore, a diagenetic (caused by organic matter degradation) redistribution of the redox-sensitive elements across the organic-rich Units I and II may be anticipated.

Manganese is a redox-sensitive element and therefore when interpreting the vertical profile of EF_{Mn} (Fig. 4) we considered the vertical distribution of Mn^{2+} concentrations in the Black Sea sediment pore fluids (Konovalov et al., 2007). The $[Mn^{2+}]_{pore\ fluid}$ profile shows an upward Mn^{2+} flux (Konovalov et al., 2007) indicating a diagenetic Mn_{solid} dissolution and Mn^{2+} diffusion towards the bottom seawater. The similarity of this profile to that of the EF_{Mn} we observed in the studied sediments (Fig. 4) implies that the vertical distribution of the reactive Mn in these sediments is primar-

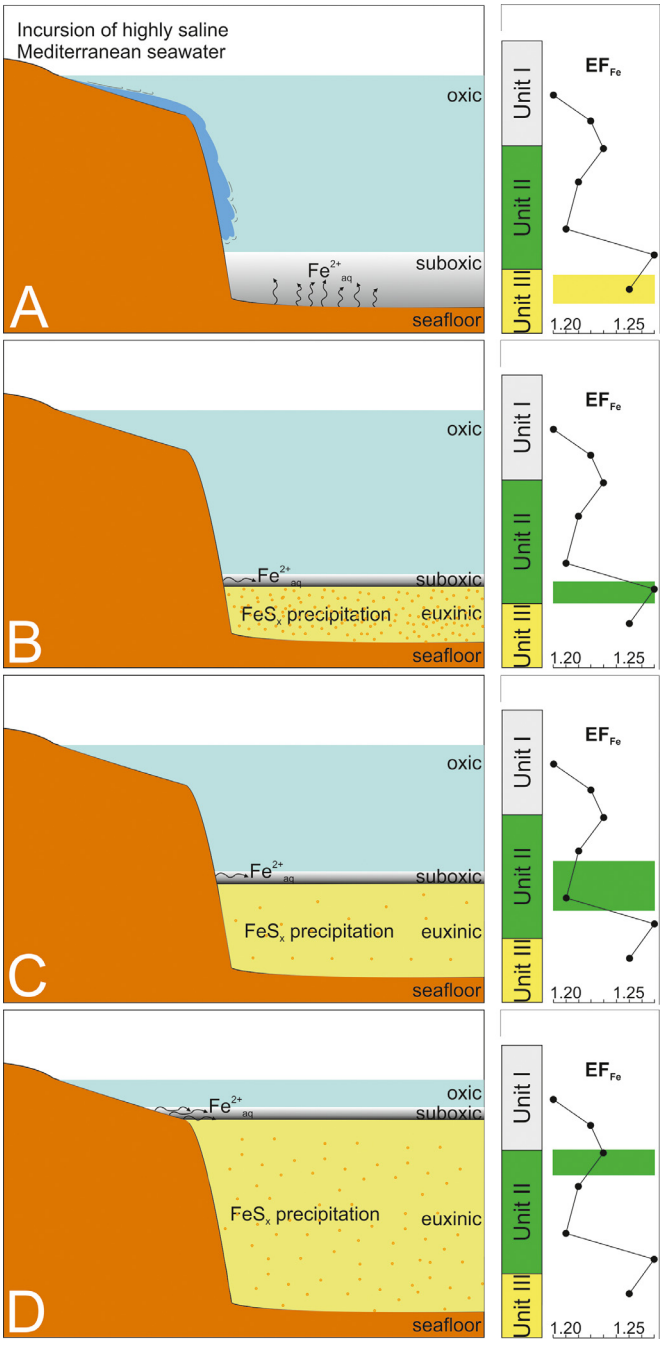

Figure 6 Schematic representation of Fe enrichment (as EF_{Fe}) in the Holocene sediments of the western Black Sea as a result of euxinia development and migration of suboxic layer (chemocline) upward the continental slope. (a) As a result of the incursion of Mediterranean saline waters in the Black Sea at ~9 ka BP the Black Sea deep waters evolved from oxic to suboxic. The sediment overlain by the suboxic waters produced high Fe^{2+}_{aq} flux to the bottom water as a result of the benthic Fe redox shuttle mechanism. The small fraction of the dissolved Fe^{2+}_{aq} was reprecipitated as sulfides due to reaction with H_2S, which started appearing as a result of microbial SO_4^{2-} reduction. (b) Deep suboxic waters evolved to euxinic with the progressive increase of H_2S concentration. This led to a quantitative removal of the accumulated Fe^{2+}_{aq} as Fe-sulfides that settled at the seafloor. Fe(-sulfide) deposition was recorded as a peak in the Fe enrichment at the base of Unit II. A thin suboxic layer developed as a transition zone (chemocline) between the deep euxinic waters and oxic water above them. (c) Development of the euxinia resulted in an increase of the volume of the deep euxinic waters and a rise of the suboxic layer upward the continental slope. Sediment overlain by euxinic waters did not produce Fe^{2+}_{aq}. The narrow band where the suboxic layer impinged the continental slope became the major source of Fe^{2+}_{aq} to the euxinic pool. Reduced Fe^{2+}_{aq} supply led to a reduced Fe-sulfide deposition recorded as a decrease of the EF_{Fe} in the middle part of Unit II. (d) Further increase of the volume of euxinic deep pool led to a rise of the chemocline (suboxic layer) and its impingement on the continental shelf. This resulted in an increase in the source area, related increase in the Fe^{2+}_{aq} flux to the deep euxinic basin, and consequent high Fe-sulfide precipitation. This is recorded as a second maximum of the Fe enrichment at the upper part of Unit II. (For more explanations see the text.)

ily controlled by diagenetic processes: dissolution in Unit II, diffusion to and reprecipitation in Unit I (Fig. 4). While we agree with the previous observations that Mn is not accumulated in sediments of the Black Sea anoxic zone (Konovalov et al., 2007) ($EF_{Mn}<1$; Table 4) the maximum of EF_{Mn} in Unit I (Fig. 4) suggests for some Mn_{solid} accumulation there. If we suppose the diagenetic dissolution of Mn_{solid} in Unit II and upward Mn diffusion, the Mn reprecipitation in Unit I has to be controlled by the solubility of Mn solid phases. Pore fluids in the Black Sea anoxic sediments are anoxic (Konovalov et al., 2007) and we cannot expect Mn-oxide precipitation in the Unit I. Konovalov et al. (2007) measured high flux of dissolved sulfide from Unit I to the bottom seawater and concluded that the sulfide source is in Unit II from where it diffuses upward. We may speculate that Mn dissolved from Unit II diffuses upward along with sulfide and its precipitation in Unit I is controlled by the solubility of Mn-sulfides.

5.1.3. Barium

A major part of Ba in marine sediments was found to be in the biogenic barite, $BaSO_4$ (Goldberg and Arrhenius, 1958). Barite is highly refractory under oxic conditions, but under anoxic conditions, it dissolves and may further re-precipitate (Henkel et al., 2012). Previous studies suggest that a significant fraction of non-detrital Ba deposited at the seafloor is recycled during diagenesis within the sediment and may even be released back to the seawater (McManus et al., 1994, 1998). Diagenetic reactions related to the organic matter decomposition play a certain role in the dissolution and diffusive flux of Ba back into the ocean (Monnin et al., 2001). Thus, the Ba cycling in the sediment is primarily controlled by the content of organic matter. In the presence of organic matter microbially-mediated reduction of seawater-derived SO_4^{2-} consumes it (SO_4^{2-}) from the pore fluids progressively downward. When the SO_4^{2-} is totally consumed, methanogenesis takes over as the dominant process of organic matter decomposition and the CH_4 content increases further downward the sediment (Henkel et al., 2012). The zone in the sediment where the SO_4^{2-} disappears and CH_4 appears in the pore fluids is termed sulfate-methane transition (SMT). The SMT is an important redox boundary with respect to the Ba cycle. Above it, the $BaSO_4$ is stable because of the presence of SO_4^{2-}. Below it, the absence of SO_4^{2-} results in $BaSO_4$ dissolution and diffusion of Ba^{2+} towards the above sulfate-containing zone where it may re-precipitate as $BaSO_4$. The high-resolution studies of pore fluids and sediments from the NW Black Sea (Henkel et al., 2012) revealed that the SMT in this area is located within the lower part of Unit II. Solid Ba_{xs} (Ba enrichment) was documented to gradually decrease upward Unit III and reaches minimum values below or slightly above the Unit III/Unit II boundary (Henkel et al., 2012). Diagenetic Ba enrichment was found at and slightly above the SMT (Henkel et al., 2012). Ba_{xs} is high in the upper part of Unit II and decreases upward in Unit I (Henkel et al., 2012).

Ba enrichment profile (expressed as EF_{Ba}) recorded in our sediments (Fig. 4) is similar to that (expressed as Ba_{xs}) described in the sediments cored in the NW Black Sea (Figs 2 and 3 in Henkel et al., 2012). Ba depletion in the upper part of Unit III and lower part of Unit II, and Ba enrichment in the upper part of Unit II (Fig. 4) suggests that the SMT in the studied area of the western deep Black Sea (Fig. 1a,b) is localized within the middle part of Unit II. This interpretation is supported by the location of the maximum of $C_{org.}$ concentration in the lower part of Unit II (Fig. 2). The EF_{Ba} peak just at the Unit II/Unit I boundary (Fig. 4) likely represents the current authigenic $BaSO_4$ front.

5.1.4. Copper, Co, Ni, Zn, Cr, W, Mo, V, Cd and Sb

In the presence of free H_2S in the seawater column and in the sediment pore fluids the excess reactive Fe precipitates as Fe-sulfide. Fe-sulfides found in the Black Sea sediments include pyrite (FeS_2) and Fe-monosulfides (disordered FeS, mackinawite (FeS_{1-x}), and greigite (Fe_3S_4)) (Franke et al., 2009). It has been shown that at high H_2S concentrations the Fe-monosulfides transform into pyrite in euxinic marine sediments (Hurtgen et al., 1999). Thus, pyrite appears to be one of the major authigenic minerals found to form in anoxic-euxinic sediments (Berner, 1981). Pyrite can be an important sink for a range of trace elements (Boulègue et al., 1982). Investigations of trace element incorporation in authigenic pyrite in a variety of redox environments (Huerta-Diaz and Morse, 1992) revealed that co-precipitation is the mechanism of incorporation of these elements into pyrite. The magnitude of this incorporation is a function of both the amount of precipitated pyrite and the concentrations of trace elements in the reactive fluid (Huerta-Diaz and Morse, 1992). Thus, the authigenic pyrite appears to be an important sink for Mo, moderately important for Co, Cu and Ni, and of less importance for Cr, Zn and Cd. The highest values of the degree of trace metal pyritization were found in anoxic-euxinic environments (Huerta-Diaz and Morse, 1992).

The co-variation of Cu and Co enrichments with that of Fe along the entire cored sediments, and the co-variation of Ni, Zn, Cr, W, Mo, V, Cd and Sb enrichments with that of Fe in the upper Unit III and lower Unit II (Fig. 4) suggest that these trace elements might have been incorporated into authigenic Fe-sulfides (e.g., pyrite) in the respective sediments. Co-precipitation may have been a possible mechanism of their incorporation in the Fe-sulfides. Nickel, Zn, Cr, W, Mo, V, Cd and Sb decouple from Fe in the Unit I (Fig. 4) and this implies that the major part of these elements in this sediment layer may not be co-precipitated with Fe within Fe-sulfides. This series of elements can be divided in two groups according to their vertical distribution in Unit I: Ni, Zn, Cr, W, and Mo, V, Cd, Sb. The enrichments of Ni, Zn, Cr and W co-vary with that of Mn and it is possible that like Mn these elements were subjected to diagenetic redistribution in Unit I: dissolution in the upper part of Unit II, diffusion to and reprecipitation in Unit I (Fig. 4).

The enrichments of Mo, V, Cd and Sb co-vary in the upper part of Unit II and Unit I (Fig. 4) and this implies that they might have had a similar mechanism of precipitation. Although the precise mechanisms of Mo sequestration from euxinic waters and its transfer to sediment are debatable (Little et al., 2015), the strong correlation of Mo enrichment with that of Fe in the upper Unit III and lower Unit II (Fig. 4) suggests that Fe-sulfides played a major role as host for Mo (as well as for V, Cd and Sb) at the onset of Holocene marine stage of the Black Sea evolution. The

strong decrease in EF_{Mo} towards upper Unit II and Unit I (Fig. 4) can be explained by the "basin reservoir effect" (Algeo and Lyons, 2006): Mo enrichment has decreased in the increasingly stagnant Black Sea water body due to Mo removal to the sediment without adequate resupply by deep water renewal. In a similar way the "basin reservoir effect" seems to be responsible for the vertical distribution of the V, Cd and Sb enrichments in Unit I (Fig. 4). Weak enrichments in the topmost studied sample (Fig. 4) may be due to a recent increase in the element supply.

5.1.5. Uranium

Uranium is enriched under anoxic conditions (Morford and Emerson, 1999) and it is not surprising that the Holocene organic-rich sediments in the Black Sea are about one order of magnitude richer in U than the average marine sediment (Degens et al., 1977). Spatial (basin-wide) and temporal (along the sediment cores) variations of the U enrichment in the Black Sea sediments (Barnes and Cochran, 1991) imply that there may be several controls on this enrichment. Degens et al. (1977) provided evidence that the planktonic organic matter is the principal carrier of enhanced content of U and concluded that this was the reason for U enrichment in the coccolith ooze (Unit I). However, the C_{org} concentrations across the studied coccolith ooze layer (Unit I) decrease upwards (Fig. 2) whereas the EF_U increases (Fig. 4). This rules out the possibility that the planktonic organic matter is responsible for the U enrichment in Unit I. Studies of Barnes and Cochran (1991) showed that authigenic U (excess over the lithogenic background) is supplied to the uppermost sediment (<38 cm) via diffusion from the bottom seawater. Although we are not aware of any high-resolution studies of the pore fluid U distribution across the coccolith ooze layer (Unit I) down to the Unit I/Unit II boundary we may speculate that the U enrichment in the upper Unit I (Fig. 4) is a result of the influence of the bottom seawater U flux. Low EF_U in the terrigenous mud (Unit III; Fig. 4) is likely due to both low organic matter content in it (Fig. 2; see also Degens et al., 1977) and oxic conditions in the basin (lacustrine stage) during the deposition of this layer in which U is highly mobile. Explanation of the U enrichment distribution across Unit II is challenging. High U enrichment in the lower Unit II (Fig. 4) coincides with a peak of organic matter content (Fig. 2; see also Degens et al., 1977). However, this organic matter was found to be mostly land-derived and not rich in U (Degens et al., 1977). EF_U maximum right after the transition from oxic to euxinic conditions in the deep Black Sea (above the boundary Unit III/Unit II) (Fig. 4) can be explained by continuous reduction of U dissolved in oxic lake water and its quantitative (complete) removal to the sediment in euxinic brackish-marine water. The upward decrease of the EF_U towards the Unit II/Unit I boundary (Fig. 4) is interpreted as a "basin reservoir effect": U removal without resupply by deep water renewal. Thus, the two U enrichments, at the base of Unit II and in Unit I (Fig. 4), likely have different genesis and neither of them is directly related to the C_{org} content. We hypothesize that the enrichment at the base of Unit II is at the expense of the U inventory of the deepwater pool and is a result of inorganic reduction of U in euxinic environment. The enrichment in Unit I is supposed to be a result of the bottom seawater U influx.

5.1.6. Zirconium, Hf, Nb, Ta and Li, Rb, Cs, Ga, Sc

The high field strength elements Zr, Hf, Nb and Ta are closely linked to the detrital component in marine sediments and their concentrations are primarily controlled by the proportion of detrital and biogenic phases (Plank and Langmuir, 1998). Therefore, the depletion of Zr and Hf in the organic-rich Units II and I (Fig. 4) obviously reflects a significant dilution of the detrital component with biogenic component (C_{org} and $CaCO_3$; Fig. 2). Similarly, the weak enrichment of Nb and Ta over the UCC abundance in Unit III (Fig. 4) suggests low biogenic dilution of the detrital background. According to previous estimates (Calvert and Karlin, 1998) the accumulation rate of lithogenic matter in Unit II is lower than that in Unit I, which accounts for the higher depletion of Zr and Hf in Unit II (Fig. 4). In addition to the dilution effect of the biogenic component on the detrital component, the values of the enrichment factors of these elements are affected by (probably) the slight difference between the chemistry of the local detrital component and that of the UCC (grand average values).

Enrichments of Li, Rb, Cs, Ga and Sc co-vary with those of Ni, Zn, Cr and W (Fig. 4), but it is challenging to suppose that these elements may have been subjected to diagenetic redistribution in Units II and I like Ni, Zn, Cr and W (e.g., *5.1.4*). Lithium, Rb, Cs, Ga and Sc are considered to be mostly detrital in the marine sediments (Goldberg, 1954; 1961), but their EFs do not show clear correlation with those of the other detrital elements (e.g., Zr, Hf, Nb and Ta) (Fig. 4). The only assumption we can make is that the values of the EF of these elements are affected by the difference between the chemistry of their carrier (local detrital component) and that of the UCC.

5.1.7. Rare earth elements, Sn and Th

REE distribution patterns of the studied sediments (Fig. 3) indicate that their REE composition is principally controlled by the lithogenic matter. No detectable influence of seawater-derived components (e.g., organic matter, biogenic $CaCO_3$) (Fig. 3b) is observed. Thus, the weak REE enrichments estimated in all the three stratigraphic units (Table 4; Fig. 4) must be controlled by the lithogenic matter. A possible mechanism of enrichment of the lithogenic matter in REE over the UCC values is the adsorption on clay minerals. A large body of evidence demonstrates that the REE adsorption on clay minerals is of great importance in the sedimentary geochemistry of the REE (Aagaard, 1974; Bruque et al., 1980; Takahashi et al., 2004; Tertre et al., 2005; Wan and Liu, 2005). The lowest REE enrichment in Unit II (Fig. 4) likely reflects the lowest accumulation rate of the lithogenic matter in this sediment layer (Calvert and Karlin, 1998).

The inverse correlation between ΣREE and SiO_{2det}/Al_2O_3 ratio (Tables 2, 3) is in accord with the suggestion that SiO_{2det}/Al_2O_3 ratio of the studied sediments is higher than that of the UCC due to high quartz content in the former (see *5.1.9*). Quartz is known to contain very low amounts of REE (McLennan, 1989). Hence, the high SiO_{2det}/Al_2O_3 ratio means high quartz content, which in turn implies low ΣREE (dilution effect of low-REE quartz). Therefore, SiO_{2det}/Al_2O_3 and ΣREE correlate inversely.

The enrichments of Sn and Th co-vary with those of the REE (Fig. 4) and, similarly, are interpreted to be related to adsorption on clay minerals.

5.1.8. Calcium and Sr

In marine sediments Sr is mostly held in the $CaCO_3$ crystal lattice and therefore, its variations are controlled by the relative proportions of $CaCO_3$, clays and biogenic opal (Goldberg and Arrhenius, 1958; Plank and Langmuir, 1998). Perfect co-variation of $CaCO_3$ and Sr in the studied sediments (Figs 2, 4) suggests that the biogenic $CaCO_3$ is the main carrier of Sr. Strontium depletion in Unit II and enrichment in Units III and I confirm the well-known decrease and increase, respectively, of the $CaCO_3$ content across the succession of these sediment units (Ross and Degens, 1974).

5.1.9. Silicon

The observed excess of detrital SiO_2 in the studied sediments over the UCC [$(SiO_{2det}/Al_2O_3)_{samples} = 4.5–7.8$, $(SiO_2/Al_2O_3)_{UCC} = 4.3$] (see *4.1.1*) can be explained with local enrichment in SiO_2 of the detrital material supplied to the western Black Sea. We may speculate that this detrital material might have been enriched in quartz (SiO_2). The SiO_2/Al_2O_3 ratio is considered as an indicator of mineralogical and textural maturity of the sediments (Pettijohn et al., 1972). The higher the ratio the greater the maturity, which in turn implies the sediments have undergone a larger sedimentary cycle. We infer that the major part of the detrital component in the western Black Sea sediments might have been delivered from a distal source that has resulted in detrital material refinement and its slight enrichment in quartz.

SiO_{2am} maximum in the sapropel layer (Unit II) and its covariation with C_{org} (Fig. 2; Table 2) confirms the biogenic origin of both components (Pilskaln and Pike, 2001). As the studied sediments are located at the continental slope (Table 1; Fig. 1b–d) there is a probability that the biogenic silica (SiO_{2am}) and C_{org} in them may have not originated from the pelagic sedimentation, but may have come from the continental shelf through downward transport along the slope (e.g., Ragueneau et al., 2009). In order to investigate this potential source of SiO_{2am} and C_{org} in the sediments, we calculated the Si_{am}/C_{org} molar ratio in our samples (Table 2). This ratio (0.09 in Unit I, 0.08 in Unit II and 0.12 in Unit III, in average) is lower than that of the continental shelf sediments (~0.6) and open ocean siliceous oozes (20–60) (DeMaster et al., 1991), and comparable to that of most living marine diatoms grown under replete nutrient conditions: 0.13 (Brzezinski, 1985). It suggests that the SiO_{2am} and C_{org} in the studied sediments have not originated at the shelf and transported afterward to the continental slope, but are likely a result of pelagic sedimentation. It also implies that there has been no preferential preservation of Si_{am} relative to C_{org} after burial (usually observed, with Si_{am}/C_{org} ratios increasing typically up to 0.5–1 in the Atlantic deep-sea sediments and up to 10 in equatorial Pacific sediments; Ragueneau et al., 2002) and both biogenic components have remarkably been preserved likely due to the anoxic conditions in the basin. Thus, Si_{am}/C_{org} molar ratio appears to be a good indicator for C_{org} preservation.

5.2. Sr-Nd-Pb isotope constraints on the source and type of terrigenous component

Sr-Nd-Pb isotope data, inferred to represent the isotope composition of the terrigenous component of the studied sediments in the western Black Sea, show quite homogenous values (Table 5). Although some intra-core isotope variations exist, particularly noted for the Nd component in sample PLC-203 (260–262), neither of the sediment cores have isotopic values that are clearly distinct from any of the others. These minor isotopic differences are not unexpected given that the studied sites occupy a small geographic area, and they are in agreement with the recognized uniform depositional environment within the entire deep Black Sea during the Late Quaternary (Ross et al., 1970). Yet, this isotope homogeneity is quite remarkable considering that the studied sediments were deposited during variable climatic conditions, implying variations in both erosion rates and wind regimes over the sediment supplying provenances. Fluctuations in the riverine and aeolian sediment supplies are known to cause variations in the isotope composition of sapropel-containing sedimentary successions (e.g., Eastern Mediterranean Sea; Weldeab et al., 2002).

Basically, the terrigenous component of marine sediments can be supplied in two major ways: riverine (river flux) and aeolian (wind-blown flux). Five potential sources of this component might be considered given the location of the studied sediment cores (Fig. 1a,b): (A) material supplied to the NW Black Sea by the Danube (and possibly by the Dniester, Bug and Dnieper) River that may further be dispersed southward by marine currents; (B) continental run-off from the closest landmasses (SE Bulgaria and NW Turkey); (C) wind-blown loess particles from the Danube Plain, Carpathian Mountains and Ukraine; (D) wind-blown dust from the Sahara Desert; (E) volcanic ash from Quaternary eruptions around the Black Sea. Two main scenarios may be considered for explaining the isotopic composition of the studied sediments: either there was a supply from a single source that has a somewhat heterogeneous isotopic character that fits the minor isotopic variations among the sediments deposited at different times and sites; or mixing occurred between two, or more, isotopically different components supplied from different provenances. This implies a thorough mixing of the components that must be delivered at quite constant proportions over time. Uniform isotope compositions can also be reached if one of the components is either much more abundant, or it has much higher element (Sr, Nd and Pb) concentrations compared to the other components, or both. From an isotopic point of view, it appears that the observed combination of radiogenic Sr ($^{87}Sr/^{86}Sr \sim 0.719–0.722$), intermediate Nd ($\varepsilon Nd(0) \sim -8$ to -10), and fairly evolved Pb ($^{206}Pb/^{204}Pb$ ~18.8–19.1) is difficult to reconcile with a known, single source, and the presence of both felsic and more mafic crustal components seems logical. Nardone and Faure (1978) analyzed the detrital fraction of sediments from the central Black Sea and suggested that their variable Sr isotope composition being clearly different from our Black Sea data could be explained by a binary mixing of a felsic (originating from areas north of the Black Sea) and a mafic (from areas south of the Black Sea) rock component. It

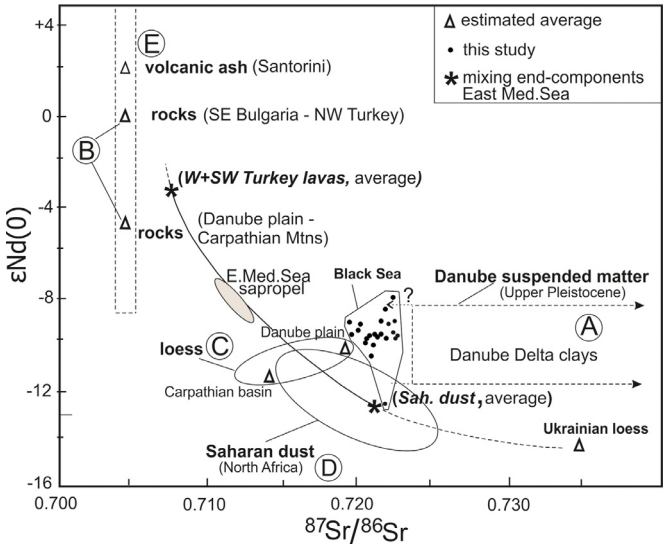

Figure 7 Correlation between $^{87}Sr/^{86}Sr$ versus $\varepsilon Nd(0)$ of the alumino-silicate component of the western Black Sea sediments. Sr-Nd-isotope composition of the rocks, clays, loess and dust from the possible provenances of this component are shown with letters. The solid hyperbolic curve, based on data from the Eastern Mediterranean Sea; the shaded area represents sapropels (Weldeab et al., 2002), refers to a binary mixing involving two end-components (W+SW Turkey lavas and Saharan dust) marked by stars. The uncertainties of the total isotopic range for potential source components with bearing on Black Sea data arise due to the limited amount of published data. Stippled boxes are likely to cover most of the isotopic variation for rocks (and clays) in the potential source areas. Encircled fields represent larger geographical regions and are designed to encompass average values of loess and dust sources. Data for the clays from the Danube Delta from Major et al. (2006); for the rocks from the SE Bulgaria and NW Turkey from Alici et al. (2002), Georgiev et al. (2009), Ruskov et al. (2006); for the rocks from the Danube plain and Carpathian mountains from Bojar et al. (2013), Dupont et al. (2002), Seghedi et al. (2007); for the ash from recent eruptions of the Santorini Volcano from Juul Petersen (2004); for the loess from the Danube plain and Carpathian basin from Schatz et al. (2015), Újvari et al. (2012); for the loess from Ukraine from Schatz et al. (2015); for the Saharan dust from North Africa from Grousset et al. (1998).

must be noted that their studied samples covered a much longer time span, including deposition during both glacial and inter-glacial periods, than what is the case in the present study. Weldeab et al. (2002) studied Late Pleistocene sapropels (S5 and S6 stages) and non-sapropels from the Eastern Mediterranean Sea. They argued that a binary mixing (cf. the hyperbolic mixing curve in Fig. 7) involving a Saharan dust component and a component representing Aegean basalts and/or Nile Delta sediments were consistent with the obtained Sr-Nd data. However, their sapropel data are distinctly different from our results from the Black Sea.

It remains speculative to assign realistic Sr (and Nd) isotope ratios to potential source components available during the appropriate time interval in the Black Sea. One feature illustrating this is that reported Sr-Nd isotope data from a geographical area may vary as a function of the material analyzed as shown by e.g., data from rocks, suspended matter and loess from the Danube plain (Fig. 7). Although quite limited, the variability in Sr-Nd isotope sapropel data indicates a mixing of different types of source components, and initially two riverine components (one from SE Bulgaria/NW Turkey and another one from the NW Black Sea) need to be considered. This is suggested for reasons of proximity (SE Bulgaria/NW Turkey) and because the rivers emptying in the NW Black Sea, in particular, the Danube River, are known to have supplied huge amounts of suspended material into the Black Sea that could further be carried southwards by surface currents (Murray et al., 2007). Four clay fractions separated from the sediments of the Danube Delta (Major et al., 2006), covering the time span 19–11 ka BP, have variable radiogenic compositions with $^{87}Sr/^{86}Sr$ ranging between 0.723 and 0.751, whereas the other samples are much less radiogenic. These shifts to higher isotopic values may be related to short-lived inputs from a high $^{87}Sr/^{86}Sr$ source associated with anomalous run-off into the Black Sea (Major et al., 2006). Although there are no $^{87}Sr/^{86}Sr$ data available for the suspended matter in the NW Black Sea during the ~9 to 3 ka BP interval, it appears possible that a radiogenic component (schematically constrained to the box indicated by letter A in Fig. 7) was available at this time period. Its Nd isotope composition may be similar to data known for the Danube plain (Fig. 7). To the best of our knowledge, no corresponding Sr isotope data are available for the suspended matter entering the SW Black Sea (run-off from SE Bulgaria/NW Turkey). However, the isotope composition of the bedrock in this landmass (Alici et al., 2002; Georgiev et al., 2009; Ruskov et al., 2006) suggests that released riverine suspended matter is expected to have quite unradiogenic Sr and relatively radiogenic Nd values (cf. component B in Fig. 7). A NW (Black Sea) riverine suspended matter component could possibly also carry loess soils known to cover large parts of the Danube drainage basin and its surroundings. Its average Sr-Nd isotope composition (cf. component C in Fig. 7) is fairly similar to the published data from the Danube

plain, but extends to somewhat less radiogenic Sr isotope compositions. For the given assumptions, a mixing involving a predominant NW riverine component diluted with a SW riverine component can apparently produce data that are largely consistent with the Sr-Nd isotope composition of the studied sediments, which were deposited over a time span of ~6 ka. Besides, given that deposition of Saharan dust has been recognized in many areas of the northern hemisphere, including the Eastern Mediterranean (Papayannis et al., 2005), this type of source (component D in Fig. 7) must also be considered. Actually, the spread in Nd isotope ratios could indicate a mix between an aeolian (average) Saharan and a combined (NW+SW Black Sea) riverine component and, in particular, the unradiogenic Nd isotope value for the PLC-203 (260–262) sample (εNd(0) = −12.5) argues for a Saharan dust contribution. Moreover, one cannot reject the possibility of certain air-borne transportation of material from loess-covered landmasses north-west of the basin.

It may also be mentioned that tephra from the large Santorini eruption in ~3300 BP has been identified in Unit II of the Black Sea sediments (Guichard et al., 1993), but not in the other units sampled in the present study. However, the tephra occupies only a ca 1cm thick layer and the Sr-Nd isotope compositions of the Santorini volcanic products (Juul Petersen, 2004) and those of the hypothetical ash-fall related to the Quaternary volcanism in western Anatolia (Alici et al., 2002 and references therein) exhibit average values far from our data (cf. component E in Fig. 7). Therefore, in the light of the Sr-Nd isotope systematics being uniform for all the three stratigraphic units, we infer that the possible effect of any kind of ash-fall was insignificant.

Due to the lack of information about the prehistoric Pb isotopic composition of the riverine input to the Black Sea we cannot provide a detailed discussion about the sources of the Pb isotopes. Generally, the obtained Pb isotope compositions are relatively evolved and the similarity in data indicates a continuous supply from a crustal source that did not change significantly during the ongoing sedimentation. It is important to note that Pb in modern and even historical riverine input in the region likely will be influenced to a variable extent by anthropogenic Pb. In general, anthropogenic Pb addition to lake or marine sediments in the European region causes a shift in the Pb isotopes to lower ratios (e.g., Kamenov et al., 2009; Shotyk et al., 1998). Environmental archives show that the onset of Pb pollution in Europe began around 3000 years ago, with particular strong anthropogenic Pb input around 2000 years ago during the Roman Empire (Shotyk et al., 1998). Although we do not have exact dates for the analyzed sediment samples in Unit I, the boundary between Units I and II is dated to ~3000 BP (Kwiecien et al., 2008). Therefore, it is quite possible that the slight decrease in $^{206}Pb/^{204}Pb$ at the upper levels of Unit I (Fig. 5) can be a result of the incorporation of anthropogenic Pb in these sediments.

6. Conclusions

The last transition of the Black Sea from an oxic limnic to anoxic-euxinic marine basin at the beginning of the Holocene Epoch had a significant impact on the enrichment (or depletion) of a range of elements in the deep-sea sediments. At the onset of this transition, the deep waters evolved from oxic through suboxic to euxinic. Large amounts of Fe were remobilized through a benthic redox shuttle mechanism from the sediment when the suboxic conditions were established and prevailed over the abyssal plain and lower continental slope. With increasing euxinia in the deep pool, the mobilized Fe^{2+} was quantitatively removed to the sediment, which was recorded as Fe enrichment at the base of the lower Holocene Unit II. Sediment beneath the euxinic pool could not further release dissolved Fe and the only Fe^{2+} supply came from the narrow zone where the suboxic transition layer between the euxinic (deep) and oxic (surface) waters impinged the continental slope. The reduced Fe flux to the euxinic pool (recorded as weak Fe enrichment in the sedimentary archive) sharply increased when the rising suboxic layer impinged the continental shelf. The increased Fe supply was recorded as a second peak of the Fe enrichment at the top of Unit II. The vertical distribution of the Mn enrichment in the sediments seems to be principally controlled by the diagenetic dissolution of solid Mn phases in Unit II, Mn^{2+} upward diffusion to and reprecipitation in Unit I. Barium enrichment (depletion) in the studied sediments is controlled by diagenetic reactions: sulfate reduction and methanogenesis. Vertical Ba profile suggests that the sulfate-methane transition (important redox boundary for the Ba cycle) in the studied area is localized within the middle part of Unit II and the current authigenic $BaSO_4$ front is at the Unit II/Unit I boundary. The major part of Cu and Co, and partly Ni, Zn, Cr, W, Mo, V, Cd and Sb (in the upper Unit III and lower Unit II) are interpreted to have co-precipitated with Fe in the euxinic deep waters and been incorporated into authigenic Fe-sulfides. Nickel, Zn, Cr and W distributions in the upper Unit I are controlled by diagenetic processes. Vertical enrichment profiles of Mo, V, Cd and Sb are affected by basin reservoir effect. The U enrichment at the base of Unit II is inferred to be at the expense of the U inventory of the deepwater pool and a result of inorganic reduction of U at euxinic conditions. The U enrichment in Unit I is supposed to be a result of the bottom seawater U influx. The high field strength elements (Zr, Hf, Nb and Ta) are closely linked to the detrital component and their depletion in the organic-rich Units II and I reflects dilution of the detrital component with biogenic. The weak enrichments of REE, Sn and Th in all the three stratigraphic units are seemingly controlled by adsorption on clay minerals. Strontium depletion and enrichment are controlled by the decrease and increase of the biogenic $CaCO_3$ content.

According to the Sr-Nd-Pb-isotope studies, the aluminosilicate fraction (terrigenous component) of the studied sediments is best explained by a relatively stable influx of a dominant Danube plain component admixed with lesser amounts of material delivered as dust from the Sahara Desert and suspended matter from rivers draining the SE Bulgaria and NW Turkey.

Acknowledgments

This research was supported by a Marie Curie Intra-European Fellowship (7th European Community Framework Program; grant #253182, IsoBAB) and a Renewed Research Stay Fellowship (Alexander von Humboldt Foundation) to V. M. Dekov. V. Y. Darakchieva acknowledges the support from the Deutsche Bundesstiftung Umwelt and from the

SYNTHESYS program (7th European Community Framework). We appreciate the analytical help of U. Westernströer (Institut für Geowissenschaften, Universität Kiel) for the ICP-MS analyses and J. Curtis (University of Florida) for the C and N analyses. This is a Vegacenter contribution #021.

References

Aagaard, P., 1974. Rare earth elements adsorption on clay minerals. Bull. Groupe Franç. Argiles 26 (2), 193—199.

Algeo, T.J., Lyons, T.W., 2006. Mo-total organic carbon covariation in modern anoxic marine environments: Implications for analysis of paleoredox and paleohydrographic conditions. Paleoceanography 21 (1). art. no. PA1016, 23 pp., https://doi.org/10.1029/2004PA001112 .

Alici, P., Temel, A., Gourgaud, A., 2002. Pb-Nd-Sr isotope and trace element geochemistry of Quarternary extension-related alkaline magmatism: a case study of Kula region (western Anatolia, Turkey). J. Volcanol. Geoth. Res. 115 (3—4), 487—510, https://doi.org/10.1016/S0377-0273(01)00328-6.

Aminot, A., Kérouel, R., 2007. Dosage automatique des nutriments dans les eaux marines: méthodes en flux continu. Ed. Ifremer, Méthodes d'analyse en milieu marin, 188 pp.

Anderson, T.F., Raiswell, R., 2004. Sources and mechanisms for the enrichment of highly reactive iron in euxinic Black Sea sediments. Am. J. Sci. 304 (3), 203—233, https://doi.org/10.2475/ajs.304.3.203.

Arkhangel'skii, A.D., Strakhov, N.M., 1938. Geologicheskoe stroenie i istoriya razvitiya Chernogo morya (Geological structure and history of the evolution of the Black Sea). Izv. Akad. Nauk S.S.S.R. 10, 3—104.

Bahr, A., Lamy, F., Arz, H.W., Kuhlmann, H., Wefer, G., 2005. Late glacial to Holocene climate and sedimentation history in the NW Black Sea. Mar. Geol. 214 (4), 309—322, https://doi.org/10.1016/j.margeo.2004.11.013.

Bahr, A., Lamy, F., Arz, H.W., Major, C., Kwiecien, O., Wefer, G., 2008. Abrupt changes of temperature and water chemistry in the late Pleistocene and early Holocene Black Sea. Geochem. Geophy. Geosy. 9 (1). art. no. Q01004, 16 pp., https://doi.org/10.1029/2007GC001683 .

Barnes, C.E., Cochran, J.K., 1991. Geochemistry of uranium in Black Sea sediments. Deep-Sea Res. 38, S1237—S1254.

Bayon, G., German, C.R., Boella, R.M., Milton, J.A., Taylor, R.N., Nesbitt, R.W., 2002. An improved method for extracting marine sediment fractions and its application to Sr and Nd isotopic analysis. Chem. Geol. 187 (3—4), 179—199, https://doi.org/10.1016/S0009-2541(01)00416-8.

Berner, R.A., 1981. Authigenic mineral formation resulting from organic matter decomposition in modern sediments. Fortschrit. Mineral. 59 (1), 117—135.

Bojar, A.-V., Dodd, J., Seghedi, I., 2013. Isotope geochemistry (O, H and Sr) of Late Cretaceous volcanic rocks, Haţeg basin, South Carpathians, Romania. J. Geol. Soc. London Spec. Publ. 382, 203—211, https://doi.org/10.1144/SP382.10.

Boulègue, J., Lord III, C.J., Church, T.M., 1982. Sulfur speciation and associated trace metals (Fe, Cu) in the porewaters of Great Marsh, Delaware. Geochim. Cosmochim. Acta 46 (3), 453—464, https://doi.org/10.1016/0016-7037(82)90236-8.

Bruque, S., Mozas, T., Rodriguez, A., 1980. Factors influencing retention of lanthanide ions by montmorillonite. Clay Miner. 15 (4), 413—420, https://doi.org/10.1180/claymin.1980.015.4.08.

Brzezinski, M.A., 1985. The Si:C:N ratio of marine diatoms: interspecific variability and the effect of some environmental variables. J. Phycol. 21 (3), 347—357, https://doi.org/10.1111/j.0022-3646.1985.00347.x.

Calvert, S.E. , 1990. Geochemistry and origin of the Holocene sapropel in the Black Sea. In: Ittekkot, V., Kempe, S., Michaelis, W., Spitzy, A. (Eds.), Facets of Modern Biogeochemistry. Springer-Verlag, Berlin, 326—352.

Calvert, S.E., Batchelor, C.H. , 1978. Major and minor element geochemistry of sediments from Hole 379A, Leg 42B, Deep Sea Drilling Project. In: Usher, J.L., Supko, P. (Eds.), Initial Reports of the Deep Sea Drilling Project. U.S. Government Printing Office, Washington, 527—541.

Calvert, S.E., Pedersen, T.F., 1993. Geochemistry of Recent oxic and anoxic marine sediments: Implications for the geological record. Mar. Geol. 113 (1—2), 67—88, https://doi.org/10.1111/10.1016/0025-3227(93)90150-T.

Calvert, S.E., Karlin, R.E., 1998. Organic carbon accumulation in the Holocene sapropel of the Black Sea. Geology 26 (2), 107—110, https://doi.org/10.1130/0091-7613(1998)026⟨0107:OCAITH⟩2.3.CO;2.

Calvert, S.E., Vogel, J.S., Southon, J.R., 1987. Carbon accumulation rates and the origin of the Holocene sapropel in the Black Sea. Geology 15 (10), 918—921, https://doi.org/10.1130/0091-7613(1987)15⟨918:CARATO⟩2.0.CO;2.

Canfield, D.E., Lyons, T.W., Raiswell, R., 1996. A model for iron deposition to euxinic Black Sea sediments. Am. J. Sci. 296 (7), 818—834, https://doi.org/10.2475/ajs.296.7.818.

De Ignacio, C., Muñoz, M., Sagredo, J., Fernández-Santín, S., Johansson, Å, 2006. Isotope geochemistry and FOZO mantle component of the alkaline-carbonatitic association of Fuerteventura, Canary Islands, Spain. Chem. Geol. 232 (3—4), 99—113, https://doi.org/10.1016/j.chemgeo.2006.02.009.

Degens, E.T., Ross, D.A., 1972. Chronology of the Black Sea over the last 25,000 years. Chem. Geol. 10 (1), 1—16, https://doi.org/10.1016/0009-2541(72)90073-3.

Degens, E.T., Ross, D.A., 1974. The Black Sea — Geology, chemistry, and biology. In: Degens, E.T., Ross, D.A. (Eds.), American Assoc. Petroleum Geolog. Mem. 20. Tulsa, OK, 633 pp.

Degens, E.T., Khoo, F., Michaelis, W., 1977. Uranium anomaly in Black Sea sediments. Nature 269 (5629), 566—569, https://doi.org/10.1038/269566a0.

DeMaster, D.J., 1981. The supply and accumulation of silica in the marine environment. Geochim. Cosmochim. Acta 45 (10), 1715—1732, https://doi.org/10.1016/0016-7037(81)90006-5.

DeMaster, D.J., Nelson, T.M., Harden, S.L., Nittrouer, C.A., 1991. The cycling and accumulation of biogenic silica and organic carbon in Antarctic deep-sea and continental margin environments. Mar. Chem. 35 (1—4), 489—502, https://doi.org/10.1016/S0304-4203(09)90039-1.

Dupont, A., Auwera, J.V., Pin, C., Marincea, S., Berza, T., 2002. Trace element and isotope (Sr, Nd) geochemistry of porphyry- and skarn mineralising Late Cretaceous intrusions from Banat, western South Carpathians. Romania. Miner. Deposita 37 (6—7), 568—586, https://doi.org/10.1007/s00126-002-0274-7.

Eckert, S., Brumsack, H.-J., Severmann, S., Schnetger, B., März, C., Fröllje, H., 2013. Establishment of euxinic conditions in the Holocene Black Sea. Geology 41 (4), 431—434, https://doi.org/10.1130/G33826.1.

Emerson, S., Hedges, J. , 2003. Sediment diagenesis and benthic flux. In: Elderfield, H. (Ed.), The Oceans and Marine Geochemistry. Treatise on Geochemistry, 1st edn.. Elsevier, Amsterdam, 293—319.

Franke, C., Robin, E., Henkel, S., Kasten, S., Bleil, U., 2009. Iron sulfide minerals in Black Sea sediments. In: EGU General Assembly 2009, Vienna 19—24.04.2009, 10672.

Garbe-Schönberg, C.-D., 1993. Simultaneous determination of thirty-seven trace elements in twenty-eight international rock standards by ICP-MS. Geostandard Newslett 17 (1), 81—97, https://doi.org/10.1111/j.1751-908X.1993.tb00122.x.

Georgiev, S., Marchev, P., Heinrich, C.A., Von Quadt, A., Peytcheva, I., Manetti, P., 2009. Origin of nepheline-normative high-K ankaramites and the evolution of Eastern Srednogorie Arc in SE Europe. J. Petrol. 50 (10), 1899—1933, https://doi.org/10.1093/petrology/egp056.

German, C.R., Holliday, B.P., Elderfield, H., 1991. Redox cycling of rare earth elements in the suboxic zone of the Black Sea. Geochim. Cosmochim. Acta 55 (12), 3553–3558, https://doi.org/10.1016/0016-7037(91)90055-A.

Glenn, C.R., Arthur, M.A., 1985. Sedimentary and geochemical indicators of productivity and oxygen contents in modern and ancient basins: The Holocene Black Sea as the "type" anoxic basin. Chem. Geol. 48 (1–4), 325–354, https://doi.org/10.1016/0009-2541(85)90057-9.

Goldberg, E.D., 1954. Marine geochemistry 1. Chemical scavengers of the sea. J. Geol. 62 (3), 249–265, https://www.jstor.org/stable/30080120.

Goldberg, E.D., 1961. Chemical and mineralogical aspects of deep-sea sediments. Phys. Chem. Earth 4, 281–302, https://doi.org/10.1016/0079-1946(61)90009-X.

Goldberg, E.D., Arrhenius, G.O.S., 1958. Chemistry of Pacific pelagic sediments. Geochim. Cosmochim. Acta 13 (2–3), 153–212, https://doi.org/10.1016/0016-7037(58)90046-2.

Goldschmidt, V.M., 1954. Geochemistry. The Clarendon Press, Oxford, 730 pp.

Grousset, F.E., Parra, M., Bory, A., Martinez, P., Bertrand, P., Shimmield, G., Ellam, R.M., 1998. Saharan wind regimes traced by the Sr-Nd isotopic composition of the subtropical Atlantic sediments: last glacial maximum vs. today. Quat. Sci. Rev. 17 (4–5), 395–409, https://doi.org/10.1016/S0277-3791(97)00048-6.

Guichard, F., Carey, S., Arthur, M.A., Sigurdsson, H., Arnold, M., 1993. Tephra from the Minoan eruption of Santorini in sediments of the Black Sea. Nature 363 (6430), 610–612, https://doi.org/10.1038/363610a0.

Haley, B.A., Frank, M., Spielhagen, R.F., Fietzke, J., 2008. Radiogenic isotope record of Arctic Ocean circulation and weathering inputs of the past 15 million years. Paleoceanography 23 (1). art. no. PA1S13, 16 pp., https://doi.org/10.1029/2007PA001486 .

Hay, B.J., Honjo, S., Kempe, S., Ittekkot, V.A., Degens, E.T., Konuk, T., Izdar, E., 1990. Interannual variability in particle flux in the southwestern Black Sea. Deep Sea Res. 37 (6), 911–928, https://doi.org/10.1016/0198-0149(90)90103-3.

Hedge, C.E., Walthall, F.G., 1963. Radiogenic strontium-87 as an index to geologic processes. Science 140 (3572), 1214–1217, https://doi.org/10.1126/science.140.3572.1214-a.

Henkel, S., Mogollón, J.M., Nöthen, K., Franke, C., Bogus, K., Robin, E., Bahr, A., Blumenberg, M., Pape, T., Seifert, R., März, C., de Lange, G.J., Kasten, S., 2012. Diagenetic barium cycling in Black Sea sediments – A case study for anoxic marine environments. Geochim. Cosmochim. Acta 88, 88–105, https://doi.org/10.1016/j.gca.2012.04.021.

Hirst, D.M., 1974. Geochemistry of sediments from eleven Black Sea cores. In: Degens, E.T., Ross, D.A. (Eds.), The Black Sea – Geology, Chemistry, and Biology. American Assoc. Petroleum Geolog. Mem. 20, Tulsa, OK, 430–455.

Hsü, K.J. , 1978. Correlation of Black Sea sequences. In: Usher, J.L., Supko, P. (Eds.). Initial Reports of the Deep Sea Drilling Project. Vol. 42, pt. 2. U.S. Gov. Printing Office, Washington, 489–497.

Huerta-Diaz, M.A., Morse, J.W., 1992. Pyritization of trace metals in anoxic marine sediments. Geochim. Cosmochim. Acta 56 (7), 2681–2702, https://doi.org/10.1016/0016-7037(92)90353-K.

Hurtgen, M.T., Lyons, T.W., Ingall, E.D., Cruse, A.M., 1999. Anomalous enrichments of iron monosulfide in euxinic marine sediments and the role of H_2S in iron sulfide transformations: Examples from Effingham Inlet, Orca Basin, and the Black Sea. Am. J. Sci. 299 (7), 556–588, https://doi.org/10.2475/ajs.299.7-9.556.

Jochum, K.P., Nohl, U., Herwig, K., Lammel, E., Stoll, B., Hofmann, A.W., 2005. GeoReM: A new geochemical database for reference materials and isotopic standards. Geostand. Geoanal. Res. 29 (3), 333–338, https://doi.org/10.1111/j.1751-908X.2005.tb00904.x.

Juul Petersen, A.D., 2004. A geological and petrological study of dikes in the Megalo Vouno volcano complex, Santorini. Department of Geology, Copenhagen Univ., 142 pp.

Kamenov, G.D., Dekov, V.M., Willingham, A.L., Savelli, C., Belucci, L.G., 2009. Anthropogenic Pb in recent hydrothermal sediments from the Tyrrhenian Sea: Implications for seawater Pb control on low-temperature hydrothermal systems. Geology 37 (2), 111–114, https://doi.org/10.1130/G25104A.1.

Koning, E., Epping, E., Van Raaphorst, W., 2002. Determining biogenic silica in marine samples by tracking silicate and aluminium concentrations in alkaline leaching solutions. Aquat. Geochem. 8 (1), 37–67, https://doi.org/10.1023/A:1020318610178.

Konovalov, S.K., Luther III, G.W., Yücel, M., 2007. Porewater redox species and processes in the Black Sea sediments. Chem. Geol. 245 (3–4), 254–274, https://doi.org/10.1016/j.chemgeo.2007.08.010.

Kwiecien, O., Arz, H.W., Lamy, F., Wulf, S., Bahr, A., Röhl, U., Haug, G.H., 2008. Estimated reservoir ages of the Black Sea since the Last Glacial. Radiocarbon 50 (1), 99–118, https://doi.org/10.1017/S0033822200043393.

Little, S.H., Vance, D., Lyons, T.W., McManus, J., 2015. Controls on trace metal authigenic enrichment in reducing sediments: Insights from modern oxygen-deficient settings. Am. J. Sci. 315 (2), 77–119, https://doi.org/10.2475/02.2015.01.

Lyons, T.W., Severmann, S., 2006. A critical look at iron paleoredox proxies: New insights from modern euxinic marine basins. Geochim. Cosmochim. Acta 70 (23), 5698–5722, https://doi.org/10.1016/j.gca.2006.08.021.

Major, C., Ryan, W., Lericolais, G., Hajdas, I., 2002. Constraints on Black Sea outflow to the Sea of Marmara during the last glacial-interglacial transition. Mar. Geol. 190 (1–2), 19–34, https://doi.org/10.1016/S0025-3227(02)00340-7.

Major, C.O., Goldstein, S.L., Ryan, W.B.F., Lericolais, G., Piotrowski, A.M., Hajdas, I., 2006. The co-evolution of Black Sea level and composition through the last deglaciation and its paleoclimatic significance. Quat. Sci. Rev. 25 (17–18), 2031–2047, https://doi.org/10.1016/j.quascirev.2006.01.032.

McLennan, S.M. , 1989. Rare earth elements in sedimentary rocks: Influence of provenance and sedimentary processes. In: Lipin, B.R., McKay, G.A. (Eds.). Geochemistry and Mineralogy of Rare Earth Elements. Reviews in Mineralogy, 21, 169–200.

McManus, J., Berelson, W.M., Klinkhammer, G.P., Kilgore, T.E., Hammond, D.E., 1994. Remobilization of barium in continental margin sediments. Geochim. Cosmochim. Acta 58 (22), 4899–4907, https://doi.org/10.1016/0016-7037(94)90220-8.

McManus, J., Berelson, W.M., Klinkhammer, G.P., Johnson, K.S., Coale, K.H., Anderson, R.F., Kumar, N., Burdige, D.J., Hammond, D.E., Brumsack, H.J., McCorkle, D.C., Rushdi, A., 1998. Geochemistry of barium in marine sediments: Implications for its use as a paleoproxy. Geochim. Cosmochim. Acta 62 (21–22), 3453–3473, https://doi.org/10.1016/S0016-7037(98)00248-8.

Monnin, C., Wheat, C.G., Dupre, B., Elderfield, H., Mottl, M.M., 2001. Barium geochemistry in sediment pore waters and formation waters of the oceanic crust on the eastern flank of the Juan de Fuca Ridge (ODP Leg 168). Geochem. Geophy. Geosy. 2. (1), art. no. 2000GC000073, 15 pp., https://doi.org/10.1029/2000GC000073 .

Morford, J.L., Emerson, S., 1999. The geochemistry of redox sensitive trace metals in sediments. Geochim. Cosmochim. Acta 63 (11–12), 1735–1750, https://doi.org/10.1016/S0016-7037(99)00126-X.

Murray, J.W., Jannasch, H.W., Honjo, S., Anderson, R.F., Reeburgh, W.S., Top, Z., Friederich, G.E., Codispoti, L.A., Izdar, E., 1989. Unexpected changes in the oxic/anoxic interface in the Black Sea. Nature 338 (6214), 411–413, https://doi.org/10.1038/338411a0.

Murray, J.W., Top, Z., Özsoy, E., 1991. Hydrographic properties and ventilation of the Black Sea. Deep-Sea Res. 38 (S2), S663–S689, https://doi.org/10.1016/S0198-0149(10)80003-2.

Murray, J.W., Stewart, K., Kassakian, S., Krynytzky, M., DiJulio, D. , 2007. Oxic, suboxic, and anoxic conditions in the Black Sea. In: Yanko-Hombach, V., Gilbert, A.S., Panin, N., Dolukhanov, P.M. (Eds.), The Black Sea Flood Question: Changes in Coastline, Climate, and Human Settlement. Springer, Dordrecht, 1—21.

Nardone, C.D., Faure, G., 1978. A study of sedimentation at DSDP Hole 379A, Black Sea, based on the isotopic composition of strontium. In: Usher, J.L., Supko, P. (Eds.), Initial Reports of the Deep Sea Drilling Project. Vol. 42, pt. 2. U.S. Government Printing Office, Washington, 607-615.

Neveskii, E.N., 1967. Protsessy osadkoobrazovaniya v pribrezhnoy zone morya (Processes of sediment formation in the near-shore zone of the sea). Nauka, Moscow, 255 pp.

Papayannis, A., Balis, D., Amiridis, V., Chourdakis, G., Tsaknakis, G., Zerefos, C., Castanho, D.A., Nickovic, S., Kazadzis, S., Grabowski, J., 2005. Measurements of Saharan dust aerosols over the Eastern Mediterranean using elastic backscatter — Raman lidar, spectrophotometric and satellite observations in the frame of the EARLINET project. Atmos. Chem. Phys. 5 (8), 2065—2079, https://doi.org/10.5194/acpd-5-2075-2005.

Pettijohn, F.J., Potter, P.E., Siever, R., 1972. Sand and Sandstone. Springer, New York, 618 pp.

Pilskaln, C.H., Pike, J., 2001. Formation of Holocene sedimentary laminae in the Black Sea and the role of the benthic flocculent layer. Paleoceanography 16 (1), 1—19, https://doi.org/10.1029/1999PA000469.

Pin, C., Zalduegui, J.F.S., 1997. Sequential separation of light rare-earth elements, thorium and uranium by miniaturized extraction chromatography: Application to isotopic analyses of silicate rocks. Anal. Chim. Acta 339 (1—2), 79—89, https://doi.org/10.1029/1999PA000469.

Plank, T., Langmuir, C.H., 1998. The chemical composition of subducting sediment and its consequences for the crust and mantle. Chem. Geol. 145 (3—4), 325—394, https://doi.org/10.1016/S0009-2541(97)00150-2.

Ragueneau, O., Dittert, N., Pondaven, P., Tréguer, P., Corrin, L., 2002. Si/C decoupling in the world ocean: is the Southern Ocean different? Deep-Sea Res. Pt. II 49 (16), 3127—3154, https://doi.org/10.1016/S0967-0645(02)00075-9.

Ragueneau, O., Regaudie-de-Gioux, A., Moriceau, B., Gallinari, M., Vangriesheim, A., Baurand, F., Khripounoff, A., 2009. A benthic Si mass balance on the Congo margin: Origin of the 4000 m DSi anomaly and implications for the transfer of Si from land to ocean. Deep-Sea Res. Pt. II 56 (23), 2197—2207, https://doi.org/10.1016/j.dsr2.2009.04.003.

Raiswell, R., Anderson, T.F., 2005. Reactive iron enrichment in sediments deposited beneath euxinic bottom waters: constraints on supply by shelf recycling. Geol. Soc. London, Spec. Publ. 248 (1), 179—194, https://doi.org/10.1144/GSL.SP.2005.248.01.10.

Ross, D.A. , 1978. Black Sea stratigraphy. In: Usher, J.L., Supko, P. (Eds.). Initial Reports of the Deep Sea Drilling Project. Vol. 42, pt. 2. U.S. Gov. Printing Office, Washington, 17—26.

Ross, D.A., Degens, E.T. , 1974. Recent sediments of the Black Sea. In: Degens, E.T., Ross, D.A. (Eds.). The Black Sea — Geology, Chemistry, and Biology. Vol. 20. American Association of Petroleum Geologists Memoir, Tulsa, Oklahoma, 183—199.

Ross, D.A., Degens, E.T., MacIlvaine, J., 1970. Black Sea: Recent sedimentary history. Science 170 (3954), 163—165, https://doi.org/10.1126/science.170.3954.163.

Ross, D.A., Stoffers, P., Trimonis, E.S. , 1978. Black Sea sedimentary framework. In: Usher, J.L., Supko, P. (Eds.). Initial Reports of the Deep Sea Drilling Project. Vol. 42, pt. 2. U.S. Gov. Printing Office, Washington, 359—372.

Rudnick, R.L., Gao, S. , 2003. Composition of the continental crust. In: Rudnick, R.L. (Ed.). The Crust. Treatise on Geochemistry, Vol. 3, 1st edn.. Elsevier, Amsterdam, 1—64.

Ruskov, K., von Quadt, A., Peytcheva, I., Georgiev, S., Strashimirov, S., 2006. Geochemical and Sr-Nd isotope constraints on the Late Cretaceous magmatism in the area of the Zidarovo ore field. In: Annual of the University of mining and geology "St. Ivan Rilski", Vol. 49, Pt. I, Geology and Geophysiscs, 1—6.

Schatz, A.-K., Qi, Y., Siebel, W., Wu, J., Zöller, L., 2015. Tracking potential source areas of Central European loess; examples from Tokaj (HU), Nussloch (D) and Grub (AT). Open Geosci. 7 (1), 678—720, https://doi.org/10.1515/geo-2015-0048.

Seghedi, I., Bojar, A.-V., Downes, H., Roşu, E., Tonarini, S., Mason, P., 2007. Generation of normal and adakite-like calc-alkaline magmas in a non-subductional environment: An Sr-O-H isotopic study of the Apuseni Mountains neogene magmatic province, Romania. Chem. Geol. 245 (1—2), 70—88, https://doi.org/10.1016/j.chemgeo.2007.07.027.

Shotyk, W., Weiss, D., Appleby, P.G., Cheburkin, A.K., Frei, R., Gloor, M., Kramers, J.D., Reese, S., Van Der Knaap, W.O., 1998. History of atmospheric lead deposition since 12,370 ^{14}C yr BP from a peat bog, Jura Mountains, Switzerland. Science 281 (5383), 1635—1640, https://doi.org/10.1126/science.281.5383.1635.

Soulet, G., Ménot, G., Lericolais, G., Bard, E., 2011. A revised calendar age for the last reconnection of the Black Sea to the global ocean. Quat. Sci. Rev. 30 (9—10), 1019—1026, https://doi.org/10.1016/j.quascirev.2011.03.001.

Stoffers, P., Müller, G. , 1978. Mineralogy and lithofacies of Black Sea sediments Leg 42B Deep Sea Drilling Project. In: Usher, J.L., Supko, P. (Eds.), Initial Reports of the Deep Sea Drilling Project. U.S. Government Printing Office, Washington, 373—411.

Stoffers, P., Degens, E.T., Trimonis, E.S. , 1978. Stratigraphy and suggested ages of Black Sea sediments cored during Leg 42B. In: Usher, J.L., Supko, P. (Eds.), Initial Reports of the Deep Sea Drilling Project. U.S. Government Printing Office, Washington, 483—487.

Takahashi, Y., Tada, A., Shimizu, H., 2004. Distribution pattern of rare earth ions between water and montmorillonite and its relation to the sorbed species of the ions. Anal. Sci. 20 (9), 1301—1306, https://doi.org/10.2116/analsci.20.1301.

Tertre, E., Berger, G., Castet, S., Loubet, M., Giffaut, E., 2005. Experimental sorption of Ni^{2+}, Cs^{+} and Ln^{3+} onto a montmorillonite up to 150°C. Geochim. Cosmochim. Acta 69 (21), 4937—4948, https://doi.org/10.1016/j.gca.2005.04.024.

Todt, W., Cliff, R.A., Hanser, A., Hofmann, A.W. , 1996. Evaluation of a ^{202}Pb-^{205}Pb double spike for high-precision lead isotopic analysis. In: Basu, A., Hart, S.R. (Eds.), Earth Processes: Reading the Isotopic Code. Geophys. Monogr. Ser. Vol. 95. American Geophys. Union, 429—437.

Újvári, G., Varga, A., Ramos, F.C., Kovács, J., Németh, T., Stevens, T., 2012. Evaluating the use of clay mineralogy, Sr-Nd isotopes and zircon U-Pb ages in tracking dust provenance: An example from loess of the Carpathian Basin. Chem. Geol. 304—305, 83—96, https://doi.org/10.1016/j.chemgeo.2012.02.007.

Vance, D., Burton, K., 1999. Neodymium isotopes in planktonic foraminifera: a record of the response of continental weathering and ocean circulation rates to climate change. Earth Planet. Sci. Lett. 173 (4), 365—379, https://doi.org/10.1016/S0012-821X(99)00244-7.

Wan, Y.X., Liu, C.Q., 2005. Study on adsorption of rare earth elements by kaolinite. J. Rare Earths 23 (3), 377—381.

Weldeab, S., Emeis, K.-C., Hemleben, C., Vennemann, T.W., Schulz, H., 2002. Sr and Nd isotope composition of Late Pleistocene sapropels and nonsapropelic sediments from the Eastern Mediterranean Sea: Implications for detrital influx and climatic conditions in the source areas. Geochim. Cosmochim. Acta 66 (20), 3585—3598, https://doi.org/10.1016/S0016-7037(02)00954-7.

Oceanologia (2020) 62, 164—172

Available online at www.sciencedirect.com

ScienceDirect

journal homepage: www.journals.elsevier.com/oceanologia

ORIGINAL RESEARCH ARTICLE

Influence of climate change on the ice conditions of the Curonian Lagoon

Darius Jakimavičius*, **Diana Šarauskienė**, **Jūratė Kriaučiūnienė**

Laboratory of Hydrology, Lithuanian Energy Institute, Kaunas, Lithuania

Received 28 June 2019; accepted 17 October 2019
Available online 31 October 2019

KEYWORDS
Curonian lagoon;
Ice indices;
Ice duration;
Ice thickness;
Ice breakup;
RCP scenarios

Summary The Curonian Lagoon is a shallow freshwater lagoon of significant environmental value in the south-eastern part of the Baltic Sea. The objective of the study was to evaluate changes of ice indices (duration, thickness and breakup dates) of this lagoon and to assess their possible tendencies in the 21st century. A methodology was developed combining the assessment of past changes (1960—2017) of ice indices and their projections in the near (2021—2040) and far (2081—2100) future periods using a hydrometeorological database, statistical methods and regression analysis as well as regional climate models and RCP scenarios. Climate change has a considerable impact on ice conditions in the Curonian Lagoon. During the historical period of 1960—2017, the Curonian Lagoon was covered with ice for 72 days a year, ice thickness reached 23 cm, whereas ice breakup was observed in the middle of March on average. According to the different scenarios, in the near and far future periods, ice duration will last 35—45 and 3—34 days, respectively. Ice thickness is projected to be 13—15 cm in the near future, whereas, at the end of the century, it is expected to decline to 0—13 cm. In the past, the lagoon ice cover remained until the middle of the third decade of February. At the end of the 21st century, RCP8.5 scenario projects the most drastic shifts: the permanent ice cover might be absent, whereas short-term ice cover is expected to melt already in the beginning of January.

* Corresponding author at: Laboratory of Hydrology, Lithuanian Energy Institute, Breslaujos st. 3, LT444003 Kaunas, Lithuania. Tel.: +370 8 37 401901.
E-mail address: darius.jakimavicius@lei.lt (D. Jakimavičius).
Peer review under the responsibility of the Institute of Oceanology of the Polish Academy of Sciences.

Production and hosting by Elsevier

https://doi.org/10.1016/j.oceano.2019.10.003

1. Introduction

Sea-ice is considered as one of the most sensitive and obvious indicators of climate change. In nature, the formation and melting of sea-ice are conventional processes, but in recent years, acceleration of their changes is intimidating. It was estimated that the Arctic sea-ice area shrank by $\sim 2 \times 10^6$ km^2 or by 17.5% over the last 40 years (Olonscheck et al., 2019). As sea-ice areas diminish, the albedo of the Earth's surface decreases, therefore less and less sunlight is reflected and more and more of it is absorbed. As a result, the air temperature rises even faster resulting in an even more rapid increase of sea-ice melting (Stroeve et al., 2012).

Ice regime changes are not only accelerating climate change but can lead to various ecological crises, as the ice cover (and the snow layer on it) limits the penetration of light into deeper layers of water bodies as well as the gas exchange between water and atmosphere. The shortening of the ice cover period has a significant impact on the biogeochemical processes and functioning of the aquatic ecosystem (Beall et al., 2016; Lindenschmidt et al., 2018; Woodward et al., 2010). It has been found that the shorter ice duration leads to losses of time required for settling and consolidation of suspended particles into sediments, thereby reducing the extent of re-suspension following ice thaw and thus increasing the concentration of nutrients (Kleeberg et al., 2013).

Global-scale changes are particularly well reflected in the ice regime of water bodies in northern latitudes. It was estimated that 14,800 lakes currently experience intermittent winter ice cover around the Northern Hemisphere and this number will increase by a dozen times at rising air temperatures (Sharma et al., 2019). Significant impacts of future climatic changes on lake ice phenology were identified for northern temperate lakes in the Laurentian Great Lakes region of North America (Hewitt et al., 2018). Alarming shifts in ice extent and timing based on past trends are projected for the Bering and Chukchi Seas (Douglas, 2010). A study of ice seasons in the Baltic Sea during the 20th century also revealed a vulnerability of the ice formation process to the observed climate changes (Jevrejeva et al., 2004). The projections reveal that the Baltic Sea ice will significantly decrease during this century as well (Jylhä et al., 2008; Luomaranta et al., 2014). The Climatological Ice Atlas (Sztobryn and Przygrodzki, 2012) provides detailed information about the western and southern parts of the Baltic Sea in 1961—2010. It shows trends in reducing ice duration and earlier ice breakup dates in the Baltic Sea lagoons and bays. Ice conditions in the largest coastal lagoon of the Baltic Sea — the Curonian Lagoon — are also of great interest and attract attention from research teams (Baukšys, 1978; Rukšėnienė et al., 2015). Baukšys (1978) analysed ice regime data of the Curonian Lagoon in 1948—1972 and estimated that this lagoon froze up at the beginning of December, while ice breakup occurred at the beginning of April. Ice duration continued for 110 days on average, ranging from 12 to 169 days. Rukšėnienė et al. (2015) identified a relation between ice phenomena and air temperature, SST and salinity in the Curonian Lagoon using ice data of 1993—2013. However, no publications can be found that discuss future changes of ice indices of this unique brackish lagoon while using regional climate models and RCP scenarios recommended by the IPCC's Fifth Assessment Report (AR5) for their projections.

The objective of this paper is to evaluate the changes of ice indices of the Curonian Lagoon and to assess their possible tendencies in the 21st century using a hydrometeorological database, regional climate models, RCP scenarios and statistical analysis methods.

2. Material and methods

2.1. Study area

The Curonian Lagoon is a shallow freshwater lagoon in the south-eastern part of the Baltic Sea (Fig. 1). The Nemunas River supplies about 90% of its inflows. The Curonian Lagoon has a significant international environmental value. The Nemunas delta is a regional park and is included in the list of Ramsar Convention sites. The lagoon itself is considered as a very valuable and important bird area preserved by the Bonn Convention. Since 1929, in the Ventė Cape ornithology station based in the headland of the Nemunas delta, about 60—80 thousand birds are ringed each year. The Curonian Lagoon is also well-known for the richness and abundance of its fish species. The Curonian Spit National Park is included in the UNESCO World Heritage List.

The surface area of the lagoon is 1584 km^2 in total. 381.6 km^2 of its northern part belong to Lithuania. The volume of the Curonian Lagoon is 6.2 km^3, the mean depth is 3.8 m, while the maximum depth is 5.8 m (Gailiušis et al., 2001). A 98 km long Curonian Spit separates the lagoon from the Baltic Sea coast. Water exchange with the sea is possible only through the Klaipėda Strait, where the port of Klaipėda is located. Due to the geographic location and local climate conditions, the Curonian Lagoon is ice-covered for an average of 72 days. However, due to intensive shipping, even in severe winters, ice cover in the territory of the Klaipėda port is being broken by vessels entering or leaving the port. The rest of the lagoon usually remains covered with ice, the thickness of which varies between 10 and 70 cm (Baukšys, 1978).

2.2. Methodology and data

A methodology was developed combining the assessment of past changes (1960—2017) of ice indices (ice duration, thickness and breakup date) and their projections in the near (2021—2040) and far (2081—2100) future. Changes in the past were evaluated using statistical analysis methods, whereas projections were carried out according to the created methodology covering two main steps (Fig. 2).

The first step was an assessment of the statistical relationship between the ice indices (ice duration, thickness and breakup date) in the Curonian Lagoon and different hydrometeorological parameters such as air and water temperatures, wind speed and atmospheric circulation indices (NAO, AO, SCAND) (Fig. 2). Data of the reference period of 1986—2005 (recommended by IPCC, 2013). Meteorological

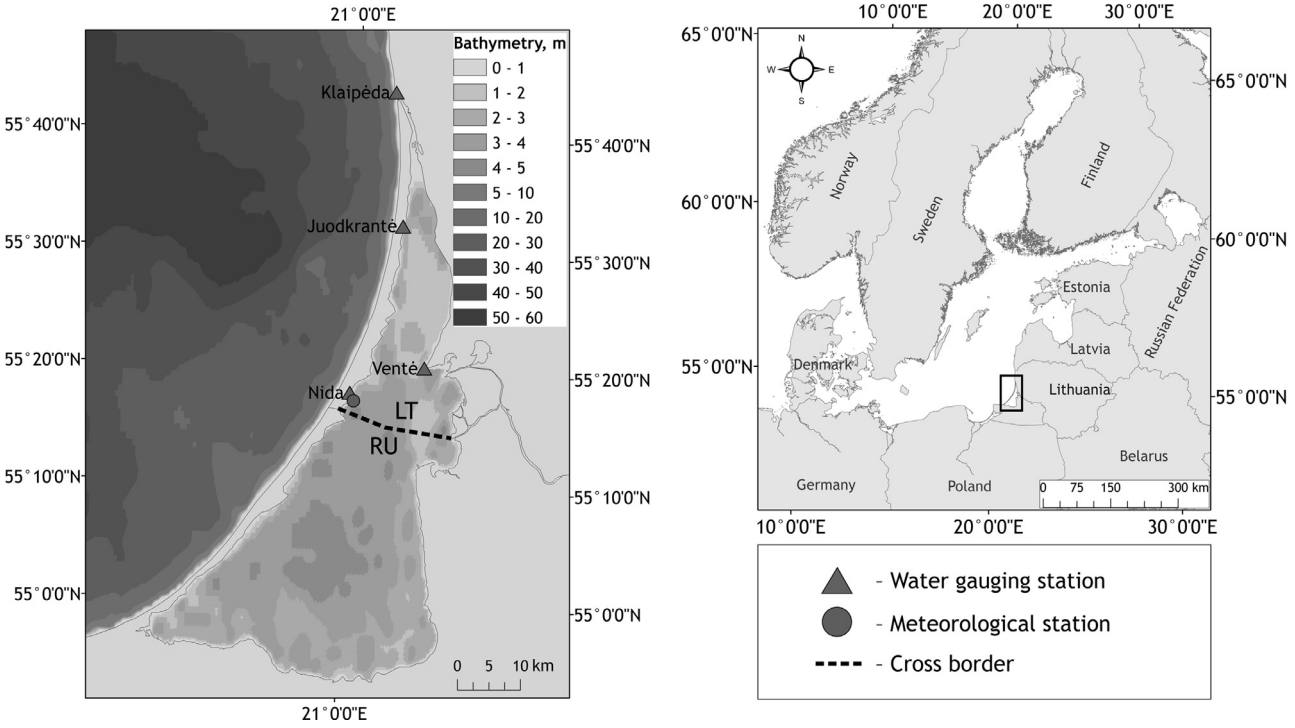

Figure 1 Location of the Curonian Lagoon and monitoring stations (MSs).

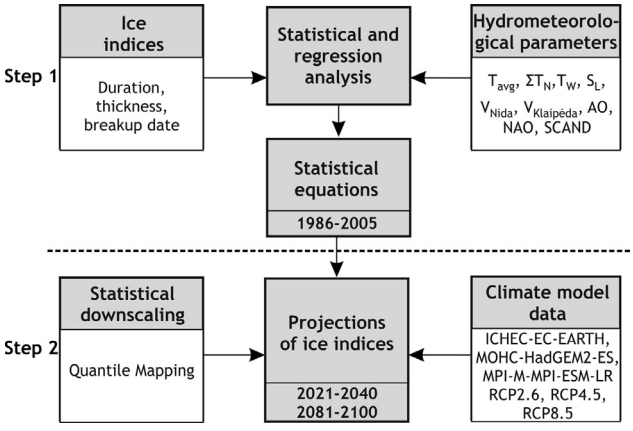

Figure 2 Methodological scheme for projection of ice indices. T_{avg} — mean air temperature in December–February at Nida MS, T_W — water temperature of the winter season in the Curonian Lagoon, ΣT_N — sum of negative air temperatures at Nida MS, V_{Nida} and $V_{Klaipėda}$ — wind speed at Nida and Klaipėda, S_L — salinity of the Curonian Lagoon in winter season, NAO, AO and SCAND — atmospheric circulation indices.

parameters having the most significant impact on ice formation were identified. Statistical relationships (equations) were created between the identified meteorological parameters and the selected ice indices. These equations were intended to be used for projections.

In the second step, in order to make projections of ice indices, future changes of meteorological parameters according to three regional climate models and three scenarios called representative concentration pathways (RCPs) were determined (Fig. 2). RCPs were used to create projections based on various factors, including demographic data, economic activity, lifestyle, energy use, technology and climate policy. They describe four different pathways of greenhouse gas concentration (GHG) emissions and atmospheric concentrations, air pollutant emissions and land use in the 21st century (IPCC, 2013). In this study, the three most common RCPs were applied: RCP2.6, RCP4.5 and RCP8.5. RCP2.6 is representative of scenarios that lead to very low GHG levels: the projected peak in radiative forcing is at about 3 W/m^2 by mid-century and declines to 2.6 W/m^2 by 2100 (van Vuuren et al., 2011). RCP4.5 is considered as a stabilisation scenario in which the total radiative forcing (4.5 W/m^2) is stabilised shortly after 2100, without overshooting the long-run radiative forcing target level (Thomson et al., 2011). RCP8.5 is characterised by rising GHG emissions over time, representative of scenarios that lead to high GHG concentration levels (Riahi et al., 2011). A grid cell of the selected regional models (ICHEC-EC-EARTH (thereafter EARTH, the Norwegian Earth System Model), MOHC-HadGEM2-ES (thereafter HAD, Hadley Centre Global Environmental Model, UK) and MPI-M-MPI-ESM-LR (thereafter MPI, the Max Planck Institute for Meteorology)) is 11 × 11 km (https://www.euro-cordex.net). We used one of the model output statistics methods (MOS) for recalculation of the values from the regional climate model (RCM) cell to the location of the meteorological station. The selected method of Quantile mapping (QM) is suitable not only for statistical downscaling of air temperature but for the data of other meteorological parameters as well (Gudmundsson et al., 2012; Sunyer et al., 2015). The main equation of this method is the following:

$$P_0 = h(P_s) = F_0^{-1}(F_s(P_s)), \quad (1)$$

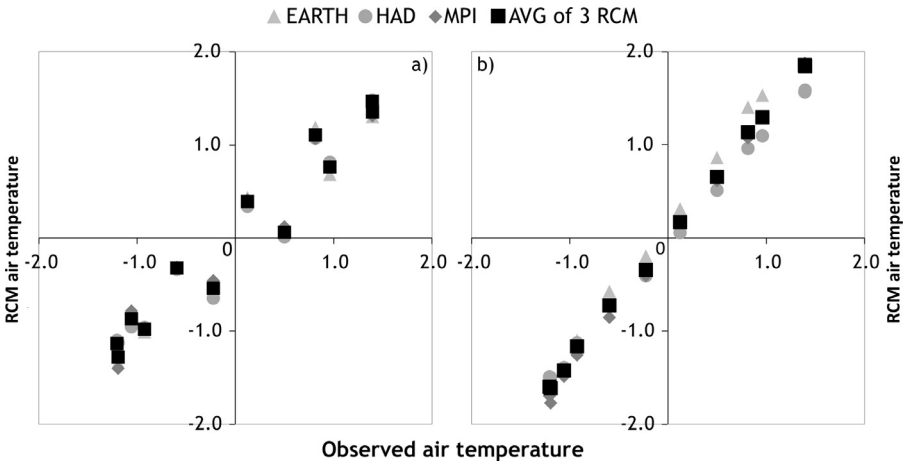

Figure 3 A normal Q—Q plot projections of Nida MS air temperature data in the reference period according to regional climate models without (a) and using (b) Quantile mapping method.

where P_0 — observed meteorological parameter, P_s — meteorological parameter of climate model, F_s — cumulative distribution function (CDF) of P_s, F_0^{-1} — inverse CDF of P_0.

All calculated results are assessed with respect to the reference period (1986—2005).

A specific example of the application of the QM method for air temperature data at Nida MS is provided in Fig. 3. A normal Q—Q plot was prepared comparing average monthly air temperature standard data (*y*-axis) of regional climate models (RCMs) to a standard observed air temperature data (*x*-axis) in the reference period (1986—2005). Considerable differences between the observed data and its projections according to RCMs were identified (Fig. 3a). For a more accurate estimate of future changes in air temperature patterns, the reference temperature data should correspond to the climate model projections for the reference period as much as possible. Recalculated air temperature data of the reference period according to the RCMs and using the QM method was almost identical to the observed temperature data at Nida MS (Fig. 3b). Thus it can be concluded that the selected regional climate models and downscaling technique are suitable for air temperature projections and can be used to project ice indices as well.

According to the created statistical equations between ice cover indices and hydrometeorological parameters, projections of ice cover duration, thickness and breakup dates were made using three regional climate scenarios under three RCP scenarios for the near (2021—2040) and far future (2081—2100) periods. The results of the projections were compared with ice indices calculated using the same climate models for the reference period (1986—2005).

Ice data (days with ice (duration), thickness and breakup dates) of 1960—2017 from Klaipėda, Juodkrantė (closed in 2012), Nida, Ventė and Uostadvaris (opened in 2013) water gauging stations (WGS) (Fig. 1) were used for ice regime analysis in the past.

Equations for projections of ice cover indices were created according to air temperature at Nida meteorological station (MS), wind speed at Klaipėda and Nida MS, lagoon water temperature near Nida, water salinity near Juodkrantė and atmospheric circulation indices (NAO, AO, SCAND). Air temperature data of regional climate models EARTH, HAD and MPI according to RCP2.6, RCP4.5 and RCP8.5 scenarios were obtained from the EURO-CORDEX database (https://www.euro-cordex.net). Atmospheric circulation indices were derived from the NOAA database (www.cpc.ncep.noaa.gov).

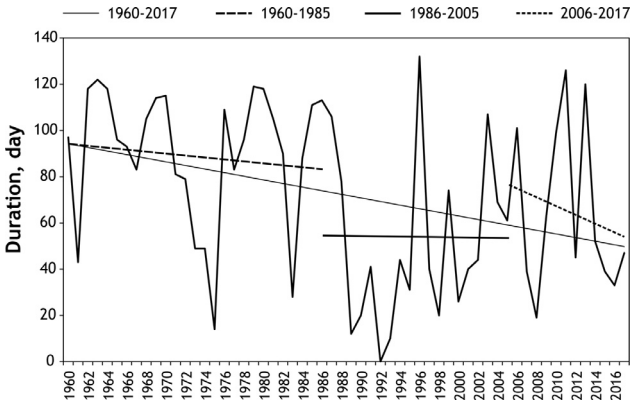

Figure 4 Duration of the Curonian Lagoon ice cover in 1960—2017.

3. Results

3.1. Ice conditions in the historical period

The analysis of mean annual ice indices (duration, thickness and breakup dates) according to data of Klaipėda, Juodkrantė, Nida and Ventė WGS identified change patterns and trends of these indices in the historical period of 1960—2017 (Fig. 4—6).

The Curonian Lagoon is covered with ice for 72 days a year, on average. The duration of ice cover in different years varied from 10 (1993) to 132 days (1996). The relations between the mentioned ice data and the mean winter temperature (T_{winter}) of Nida MS were determined. Permanent ice cover may not form at all if T_{winter} is above 2.4°C (as in

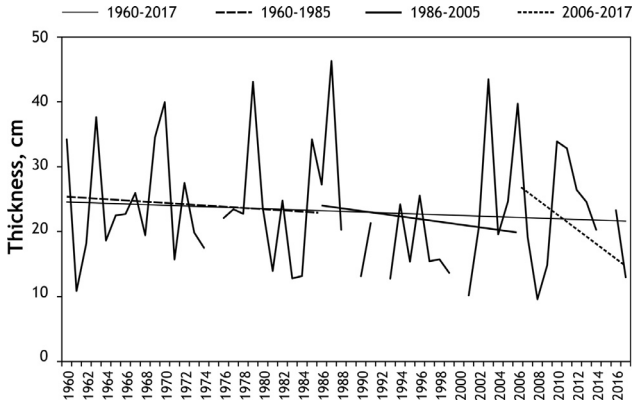

Figure 5 The mean thickness of the Curonian Lagoon ice in 1960–2017.

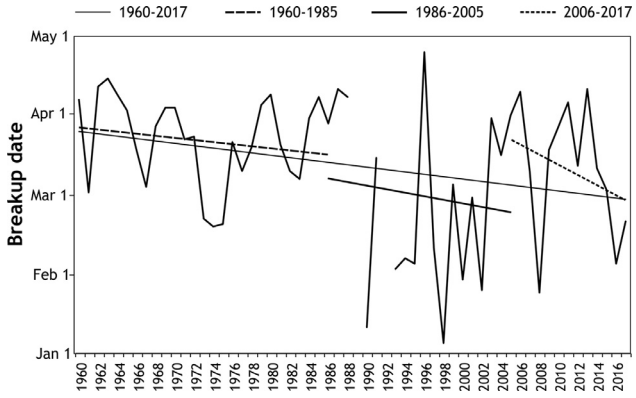

Figure 6 Ice breakup dates in the Curonian Lagoon in 1960–2017.

1992). The permanent ice cover lasts up to 20 days when 1°C $< T_{winter} <$ 2.4°C, 20–60 days – when −1.3°C $< T_{winter} <$ 1°C, 60–100 days – when −3.6°C $< T_{winter} <$ −1.3°C and the lagoon ice cover remains for 100–140 days if T_{winter} decreases down to −3.6°C.

Figure 4 reveals a steady decline in ice duration in the historical period. In 1960–2017, permanent ice of the Curonian Lagoon decreased by 0.8 day/yr. However, the decrease rate was different in separate periods: in 1986–2005 (during the reference period used for projections) it changed only slightly, while in 1960–1985 (before the reference period) it declined to 0.4 day/yr. In 2006–2017 (after the reference period) it fell to 1.9 days/yr.

Ice thickness is another critical index which was analysed over the historical period. Strong variation of the annual ice thickness of the Curonian Lagoon is presented in Figure 5. In certain years with cold winters, the mean thickness of ice cover exceeded 40 cm (in 1979, 1987 and 2003). However, in the case of warm winters, the constant ice cover did not form or was too thin to allow safe measurements (1975, 1989, 1992, 2000, and 2015). The detected trends revealed an unsubstantial but steady decline of the analysed index. Over the entire period of 1960–2017, ice thickness decreased by 3 cm. Until 1986, the average thickness of ice decreased by 0.1 cm/yr. It decreased by 0.2 cm/yr during the reference period and by 1.0 cm/yr since 2006.

The last analysed ice index of the Curonian Lagoon was the ice breakup date (Fig. 6). During the entire observation period, the earliest date of the ice breakup was in the first decade of January, while the latest date was in the last decade of April. A significant negative trend in ice breakup dates was identified (Fig. 6). At the beginning of the observation period, on average, the Curonian Lagoon ice broke up in the third decade of March, while at the end of this period it broke up in the third decade of February. Therefore, the records reveal that ice breakup has advanced by one month (every second year it is reduced by one day). Over the observation period, ice broke up earlier in a different speed: until 1986, this process started earlier by 0.2 day/yr, during the reference period – by 0.6 day/yr and since 2006 – by 1.9 days/yr.

The data showcased in Figures 4–6 revealed that in the period of 2006–2017, considerable tendencies of decreasing ice duration and thickness as well as the earlier beginning of ice breakup process in the Curonian Lagoon were being observed.

3.2. Evaluation of hydrometeorological parameters with the greatest impact on ice formation

Local hydrometeorological conditions (air and water temperatures and wind speed) and atmospheric circulation indices (NAO, AO, SCAND) determine ice indices (its duration, thickness and breakup date). Hydrometeorological parameters having the greatest impact on ice formation in the Curonian Lagoon were identified applying correlation analysis. The estimated correlation coefficients are provided in Table 1.

Mean air temperature in December–February at Nida MS (T_{avg}), sum of negative air temperatures at Nida MS (ΣT_N) and water temperature of the winter season in the Curonian Lagoon (T_W) were identified as best correlating with ice indices. A very weak correlation existed between ice indices and atmospheric circulation indices. The rest of the studied parameters (wind speed (V_{Nida}, $V_{Klaipėda}$) and salinity (S_L) in winter season) did not show a significant relationship.

Therefore, T_{avg}, ΣT_N and T_W were used for further analysis. Equations describing the dependence of ice indices on the selected hydrometeorological parameters were developed using polynomial regression analysis (Eqs. 2–4):

$$D = -0.0003\Sigma T_N^2 + 0.3701\Sigma T_N - 5.0079, \quad (2)$$

$$T = -0.00001\Sigma T_N^2 + 0.0479\Sigma T_N + 9.9040, \quad (3)$$

$$B = -0.0003\Sigma T_N^2 + 0.3797\Sigma T_N + 9.0662, \quad (4)$$

where D – ice duration, days, T – average thickness of ice cover, cm, B – date of complete ice breakup, days, ΣT_N – the sum of negative air temperatures at Nida from December to April, °C.

Correlation coefficients between the observed ice indices and those calculated according to equations varied from 0.89 to 0.94. This indicates that the created equations are suitable to project future changes of ice indices. These developed equations were based on statistical relations between the sum of negative air temperatures and ice indices

Table 1 Linear correlation coefficients between ice indices and hydrometeorological parameters.

Ice indices	Hydrometeorological parameters								
	T_{avg}	T_W	ΣT_N	V_{Nida}	$V_{Klaipėda}$	S_L	NAO	AO	SCAND
Duration	−0.93	−0.71	−0.91	0.09	−0.10	−0.20	−0.24	−0.48	0.28
Thickness	−0.83	−0.46	−0.90	0.20	0.04	0.12	−0.02	−0.24	−0.07
Breakup date	−0.93	−0.55	−0.91	0.13	−0.11	−0.22	−0.25	−0.49	0.25

where T_{avg} – mean air temperature in December–February at Nida MS, T_W – water temperature of the winter season in the Curonian Lagoon, ΣT_N – sum of negative air temperatures at Nida MS, V_{Nida} and $V_{Klaipėda}$ – wind speed at Nida and Klaipėda, S_L – salinity of the Curonian Lagoon in winter season, NAO, AO and SCAND – atmospheric circulation indices.

of the period of 1986–2005. They can be applied only if $\Sigma T_N \leq -60°C$. Otherwise, if $\Sigma T_N > -60°C$, it is assumed that a permanent ice cover is absent.

3.3. Ice conditions in the near and far future

Projections of ice indices in the Curonian Lagoon for the near (2021–2040) and far future (2081–2100) periods were assessed as the mean of three regional climate models (RCMs) according to a different RCP. The results were compared with the values of ice indices calculated using the same RCMs for the historical period (1986–2005). The findings revealed that in both future periods the ice regime in the lagoon is going to change significantly. In the near future, these changes will be negligible, whereas. at the end of the century (especially according to RCP8.5), ice phenology and thickness are expected to change substantially (Fig. 7).

According to the data of RCMs, ice duration on the Curonian Lagoon during the winter season is on average 55 days in the reference period. This number can vary from 17 to 87 days in different years depending on climate conditions (i.e. air temperature). The analysis of future projections shows that the dispersal of values of ice indices in the range of 25–75% quartiles decreases when climate scenarios get extreme (Fig. 7a), but the gap between the extreme values and the mean increases. According to the scenarios, ice duration will last from 35 to 45 days on average in the near future, while only lasting for 3–34 days in the far future (Fig. 7a).

According to the data of RCMs, the mean ice thickness of the lagoon varied from 9 to 27 cm (19 cm on average) in the reference period (Fig. 7b). No drastic trends in ice thinning were identified for the near future period: ice thickness is projected to be 13–15 cm depending on the used scenario (Fig. 7b). However, in case of the most extreme RCP8.5 scenario, in the far future ice cover will form only once every five years and its thickness will reach 4–11 cm. At the end of the century, ice thickness is expected to be 13 cm and 9 cm according to RCP2.6 and RCP4.5 scenarios respectively. This index is projected to decline by 32% and 53% according to RCP2.6 and RCP4.5 scenarios respectively relative to the reference period.

The index of ice phenology in the Curonian Lagoon was its breakup date. During the reference period, the lagoon ice cover remained until the middle of the third decade of February. However, the statistical relationship between ice

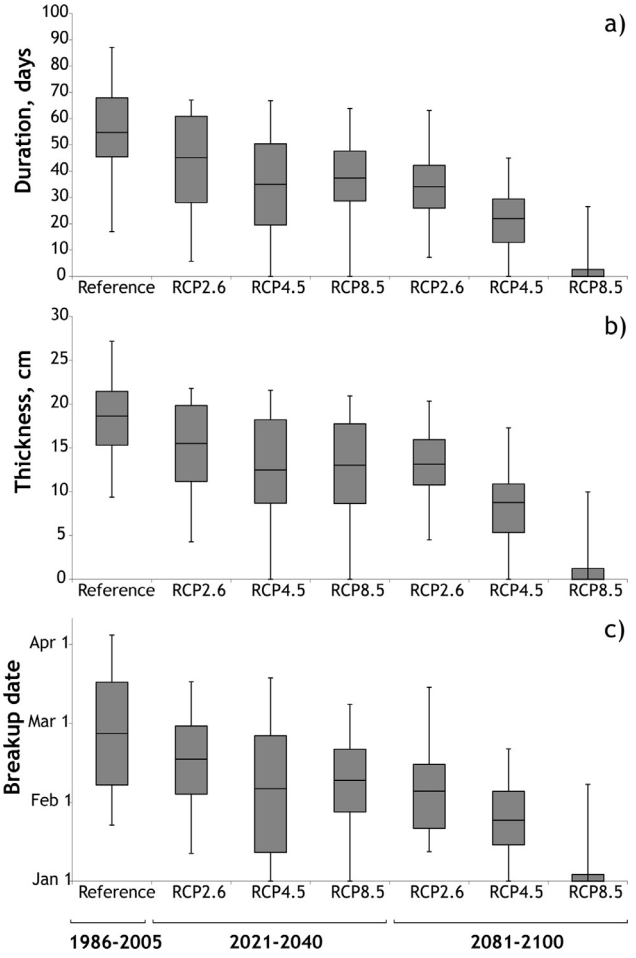

Figure 7 Ice indices in the near (2021–2040) and far future (2081–2100) relative to the reference period: a) duration, b) thickness, c) breakup date.

breakup dates and the sum of negative air temperatures as well as the regional climatic data revealed that this date advanced both in the near and far future (Fig. 7c). During the first period, in case of RCP2.6 scenario, the breakup will be observed in the middle of the second decade of February, while according to the most pessimistic scenario it will occur at the end of the first decade of this month (i.e. by 8 days later). In the far future period, the breakup will advance even more: it might begin in the first days of February (according to RCP2.6) or even at the end of the third decade of January (according to RCP4.5). RCP8.5 scenario projects

the most drastic shifts: at the end of the 21st century, the long-term ice cover might be absent, whereas short-term ice cover is expected to melt at the beginning of January.

4. Discussion

The present study was intended to assess the impact of climate change on ice conditions of the Baltic Sea's Curonian Lagoon. Many authors confirm that climatic factors (such as air temperature, wind speed, etc.) have the greatest influence on the sea-ice regime (Baukšys, 1978; Kļaviņš et al., 2016; Stroeve et al., 2012; Sztobryn et al., 2012). As it was expected, the results showed an obvious influence of rising air temperatures on the lagoon ice regime both in the past and future, i.e. ice duration and thickness will continue to decrease, while ice breakup is expected to begin earlier.

Other studies and observation data show that lagoons of the Baltic Sea have different ice regimes, although they are located in similar geographical and climate conditions. According to the Climatological Ice Atlas (Sztobryn and Przygrodzki, 2012), in 1961–2010, in the southern part of the Baltic Sea, the average number of days with ice in the Vistula Lagoon was 83 days, while in the western and eastern parts of the Szczecin Lagoon it was 60 and 61 respectively. A recent study by Chubarenko et al. (2019) generalised the data of the Vistula Lagoon from 1946 and confirmed a decreasing trend of the number of days with ice coverage. According to Dailidienė et al. (2012), the duration of the ice season in the Baltic Sea itself (at Nida) decreased by 50% during the period of 1961–2005 due to continuously warming winters and today the duration of ice season is approximately one month. Further north, in the Gulf of Riga, which has a direct connection with the Baltic Sea, the estimated average number of days with ice cover for the period of 1949–2013 was 64 (at Salacgriva) (Kļaviņš et al., 2016). The authors of the current study estimated that according to the data of 1960–2017, the Curonian Lagoon is covered with ice for 72 days per year on average; this number varies from 10 to 132 days and is in line with the mentioned findings.

The estimated rate of decrease of ice duration in the Curonian Lagoon was 2.0 days/10 years over the observation period (1960–2017) and was similar to the ones estimated in the Szczecin Lagoon (in 1889–1995) (Kozuchowski and Girjatowicz, 1997), the Gulf of Riga (in 1949–2013) (Kļaviņš et al., 2016) and the Vistula Lagoon (in 1961–2010) (Sztobryn and Przygrodzki, 2012): 2.6, 2.7 and 3.2 days/10 years respectively.

Due to climate change, ice cover breakup dates in the Baltic Sea and its lagoons are getting earlier as well. It was estimated that in the Gulf of Riga ice disappears earlier by 5.2 days/10 years (1949–2012) (Kļaviņš et al., 2016), while in the lagoons of Vistula and Szczecin ice melts earlier by 3.7 and 3.6 days/10 years (1961–2010) respectively (Sztobryn and Przygrodzki, 2012). According to the current study, ice on the Curonian Lagoon breaks up 4.4 days earlier every 10 years.

According to Jevrejeva et al. (2004), 100 year-long time series of ice data from the coastal observation stations in the Baltic Sea provide evidence of a general trend toward easier ice conditions; the largest change is in the length of the ice season, which is decreasing by 14–44 days per century. The trends of a reduction of about 8–20 days per century to the earliest ice breakup detected in this study are in agreement with a warming trend in the winter air temperature over Europe. Other studies by Tarand and Nordli (2001) and Jaagus (2006) in Finland, by Jevrejeva (2001) in Latvia and by Sztobryn (1994) in Poland are also in accord with the current study, indicating negative trends in the ice cover duration and thickness in the Baltic Sea coastal waters.

Ice regime changes are recorded not only in the Baltic Sea and its lagoons but also in other lagoons and lakes of the world. A similar pattern of results was obtained by Shirasawa et al. (1994) in the Saroma Lagoon (Hokkaidō, Japan), where the estimated average duration of ice cover of 110 days in 1963–1978 declined to 72 days in 1979–1992. In Canada, in the period of 1951–2000, trends toward earlier ice breakup dates were detected for many lakes during the latter part of the 20th century (Brown and Duguay, 2010; Duguay et al., 2006; Latifovic and Pouliot, 2007). Long-term records of winter ice duration, formation, and breakup dates (1869–1996) and maximum thickness (1950–1995) on the World's deepest Lake Baikal revealed highly significant trends of decreasing ice duration and thickness over the period, associated with later ice formation and earlier breakup dates, and these trends are broadly in line with those of winter air temperatures in the region (Todd and Mackay, 2003).

Ice regime changes are related to the water body thermal regime, which in turn has a major role in the water ecosystem and its biochemical processes. Due to climate change, expected changes in ice conditions are going to have considerable consequences for aquatic systems, which is the reason why the projection of these negative effects is of great importance. Therefore, investigation of the ice regime of large water bodies should also encompass projections of its changes using climate models based on different future scenarios. However, while reviewing the available literature, no such scientific studies were found about the projection of ice indices in the Curonian Lagoon or other lagoons of the Baltic Sea. Projections based on simulations produced with seven regional climate models under two greenhouse gas emissions scenarios (A2 and B2) for the period of 2071–2100 made by Jylhä et al. (2008) showed a drastic decrease of ice in the Baltic Sea. A similar investigation which used climate models and emission scenarios recommended by the IPCC's Fourth Assessment Report (AR4) (2007) was carried out for Lake Ontario (Canada) (Minns et al., 2014). It was found that in the middle of the 21st century, lake ice will break up 7–8 days earlier relative to the reference period. The duration of the ice cover on Lake Ontario will reduce from 14 (according to the mildest scenario) to 17 days (according to the most drastic scenario), while the maximum ice cover thickness will decrease from 7.5 to 9.0% compared to the reference period (Minns et al., 2014). Luomaranta et al. (2014) estimated future changes in the Baltic Sea ice indices under the RCP4.5 and RCP8.5 scenarios based on temperature responses produced by 28 CMIP5 GCMs. According to both studied RCP scenarios, the annual maximum ice extent was found to decrease markedly. As expected, the decline in mean maximum sea ice thickness in coastal areas is faster in the RCP8.5 scenario than in the RCP4.5 scenario. According to RCP8.5, in a conventional winter of the 2080s, sea

ice would only occur in the Bay of Bothnia, with a maximum ice thickness of 30—40 cm, and in the north-eastern parts of the Gulf of Finland, with an ice thickness of 0—10 cm. Consistent with the available literature, the current research identified similar tendencies of ice regime changes due to climate change in the future. Projections showed that in the near future, ice duration will reduce to 35—45 days in the Curonian Lagoon, while in the far future, it will last only for 3—34 days. Significant shifts in ice thickness were identified only in the second future period, when changes projected under the RCP8.5 scenario may even lead to ice loss. Ice breakup will advance almost by a month according to the extreme scenario relative to the reference period.

Tendencies of changes of ice indices are similar in the Curonian Lagoon and the mentioned water bodies around the World. The intensity of changes of ice indices depends on morphometric characteristics of water bodies (such as volume, surface area, and depth) as well as local geographical—climatic conditions.

5. Conclusions

Climate change has a considerable impact on ice conditions of the investigated Curonian Lagoon as it was well demonstrated using both historical data and the future projections. During the historical period of 1960—2017, the Curonian Lagoon was covered with ice on average for 72 days a year, permanent ice cover decreased by 0.8 day/yr, ice thickness declined by 3 cm, whereas ice breakup has advanced by one month.

According to different scenarios, in the near future (2021—2040), ice duration will last 35—45 days, while in the far future (2081—2100), it will remain only for 3—34 days. In the reference period of 1986—2005, ice duration was 55 days on average.

In the near future, ice thickness is projected to be 13—15 cm, whereas at the end of the century, it is expected to decline to 13 (under RCP2.6) or even 9 (under RCP4.5) cm. While during the reference period, the mean ice thickness of the lagoon was 21 cm.

The lagoon ice cover remained until the middle of the third decade of February; this date will advance both in the near and far future. RCP8.5 scenario projects the most drastic shifts: at the end of the 21st century, the long-term ice cover might be absent, whereas short-term ice cover is expected to melt at the beginning of January.

Similar trends of changes of ice indices are expected to occur in other unexplored water bodies since the identified changes are closely in line with the described studies. Future research should further develop and confirm these initial findings by using numerical ice sheet models and the newest climate scenarios data.

Acknowledgement

The authors are grateful to the Department of Marine Research of the Environmental Protection Agency of Lithuania, which kindly facilitated the ice indices observation data necessary for this study.

References

Baukšys, J., 1978. Ice regime. In: Rainys A. (Ed.), The Curonian Lagoon. Vol. II. Vilnius, 34—49, (in Lithuanian).

Beall, B.F.N., Twiss, M.R., Smith, D.E., Oyserman, B.O., Rozmarynowycz, M.J., Binding, C.E., Bourbonniere, R.A., Bullerjahn, G.S., Palmer, M.E., Reavie, E.D., Waters, M.K., Woityra, W.C., McKay, R.M.L., 2016. Ice cover extent drives phytoplankton and bacterial community structure in a large north-temperate lake: implications for a warming climate. Environ. Microbiol. 18 (6), 1669—2079, https://dx.doi.org/10.1111/1462-2920.12819.

Brown, L.C., Duguay, C.R, 2010. The response and role of ice cover in lake-climate interactions. Prog. Phys. Geog. 34 (5), 671—704, http://dx.doi.org/10.1177/0309133310375653.

Chubarenko, B., Chechko, V., Kileso, A., Krek, E., 2019. Hydrological and sedimentation conditions in a non-tidal lagoon during ice coverage — The example of Vistula Lagoon in the Baltic Sea. Estuar. Coast. Shelf. Sci. 216, 38—53, http://dx.doi.org/10.1016/j.ecss.2017.12.018.

Dailidienė, I., Davulienė, L., Kelpšaitė, L., Razinkovas, A., 2012. Analysis of the Climate Change in Lithuanian Coastal Areas of the Baltic Sea. J. Coastal. Res. 28 (3), 557—569, http://dx.doi.org/10.2112/JCOASTRES-D-10-00077.1.

Douglas, D.C., 2010, Arctic sea ice decline: Projected changes in timing and extent of sea ice in the Bering and Chukchi Seas: U.S. Geological Survey Open-File Report 2010—1176, 32 pp., https://doi.org/10.3133/ofr20101176.

Duguay, C.R., Prowse, T.D., Bonsal, B.R., Brown, R.D., Lacroix, M.P., Ménard, P., 2006. Recent trends in Canadian lake ice cover. Hydrol. Process. 20, 781—801, http://dx.doi.org/10.1002/hyp.6131.

Gailiušis, B., Jablonskis, J., Kovalenkovienė, M., 2001. Lithuanian rivers: hydrography and runoff, Lithuanian Energy Inst., Kaunas, 792 pp., (in Lithuanian).

Gudmundsson, L., Bremnes, J.B., Haugen, J.E., Engen—Skaugen, T., 2012. Technical Note: Downscaling RCM precipitation to the station scale using statistical transformations — a comparison of methods. Hydrol. Earth Syst. Sci. 16, 3383—3390, https://dx.doi.org/10.5194/hess-16-3383-2012.

Hewitt, B.A., Lopez, L.S., Gaibisels, K.M., Murdoch, A., Higgins, S.N., Magnuson, J.J., Paterson, A.M., Rusak, J.A., Yao, H., Sharma, S., 2018. Historical Trends, Drivers, and Future Projections of Ice Phenology in Small North Temperate Lakes in the Laurentian Great Lakes Region. Water Sci. 10 (1), Art. no. 70, 16 pp., https://dx.doi.org/10.3390/w10010070.

IPCC, 2007. Climate Change 2007: Synthesis Report, Contribution of Working Groups I, II and III to the Fourth Assessment Report of the Intergovernmental Panel on Climate Change. In: Pachauri, R.K., Reisinger, A. (Eds.), Climate Change 2007: Synthesis Report, Contribution of Working Groups I, II and III to the Fourth Assessment Report of the Intergovernmental Panel on Climate Change. IPCC, Geneva, Switzerland, 104 pp.

IPCC, 2013. Climate Change 2013: The Physical Science Basis. Contribution of Working Group I to the Fifth Assessment Report of the Intergovernmental Panel on Climate Change. In: Stocker, T.F., Qin, D., Plattner, G.—K., Tignor, M., Allen, S.K., Boschung, J., Nauels, A., Xia, Y., Bex, V., Midgley, P.M. (Eds.), Climate Change 2013: The Physical Science Basis. Contribution of Working Group I to the Fifth Assessment Report of the Intergovernmental Panel on Climate Change. Cambridge Univ. Press, Cambridge, UK, New York, USA, 1535 pp., https://dx.doi.org/10.1017/CBO9781107415324.

Jaagus, J., 2006. Trends in sea ice conditions in the Baltic Sea near the Estonian coast during the period 1949/1950-2003/2004 and their relationship to large-scale atmospheric circulation. Boreal Environ. Res. 11, 169—183.

Jevrejeva, S., 2001. Severity of winter seasons in the northern Baltic Sea between 1529 and 1990: reconstruction and analysis. Clim. Res. 17, 55—62, https://dx.doi.org/10.3354/cr017055.

Jevrejeva, S., Drabkin, V.V., Kostjukov, J., Lebedev, A.A., Leppäranta, M., Mironov, Ye.U., Schmelzer, N., Sztobryn, M., 2004. Baltic Sea ice seasons in the twentieth century. Clim. Res. 25, 217—227, https://dx.doi.org/10.3354/cr025217.

Jylhä, K., Fronzek, S., Tuomenvirta, H., Carter, T.R., Ruosteenoja, K., 2008. Changes in frost, snow and Baltic sea ice by the end of the twenty-first century based on climate model projections for Europe. Climatic Change 86, 441—462, https://dx.doi.org/10.1007/s10584-007-9310-z.

Kļaviņš, M., Avotniece, V., Rodinovs, Z., 2016. Dynamics and Impacting Factors of Ice Regimes in Latvia Inland and Coastal Waters. Proc. Latvian Acad. Sci. 70 (6), 400—408, https://dx.doi.org/10.1515/prolas-2016-0059.

Kleeberg, A., Freidank, A., Jöhnk, K., 2013. Effects of ice cover on sediment resuspension and phosphorus entrainment in shallow lakes: combining in situ experiments and wind-wave modeling. Limnol. Oceangr. 58, 1819—1833, https://dx.doi.org/10.4319/lo.2013.58.5.1819.

Kozuchowski, K., Girjatowicz, J., 1997. Variation of the Ice Cover on the Szczecin Lagoon versus Contemporary Climatic Fluctuations. Unpublished manuscript, https://www.researchgate.net/publication/295565026_variation_of_the_ice_cover_on_the_szczecin_lagoon_versus_contemporary_climatic_fluctuations.

Latifovic, R., Pouliot, D., 2007. Analysis of climate change impacts on lake ice phenology in Canada using the historical satellite data record. Remote Sens. Environ. 106, 492—507, https://dx.doi.org/10.1016/j.rse.2006.09.015.

Lindenschmidt, K.E., Baulch, H.M., Cavaliere, E., 2018. River and Lake Ice Processes—Impacts of Freshwater Ice on Aquatic Ecosystems in a Changing Globe, Water 10, Art. no. 1586, 9 pp., https://doi.org/10.3390/w10111586.

Luomaranta, A., Ruosteenoja, K., Jylhä, K., Gregow, H., Haapala, J., Laaksonen, A., 2014. Multimodel estimates of the changes in the Baltic Sea ice cover during the present century. Tellus A, 66 (1) Art. no. 22617, 18 pp., http://dx.doi.org/10.3402/tellusa.v66.22617.

Minns, C.K., Shuter, B.J., Fung, S.R., 2014. Regional Projections of Climate Change Effects on Ice Cover and Open-Water Duration for Ontario Lakes Using Updated Ice-Date Models, CLIMATE CHANGE RESEARCH REPORT CCRR-40, Sci. Res. Branch, Ontario Forest Res. Inst. Ministry of Natural Resources, 52 pp.

Olonscheck, D., Mauritsen, T., Notz, D., 2019. Arctic sea-ice variability is primarily driven by atmospheric temperature fluctuations. Nat. Geosci. 12 (6), 430—434, https://dx.doi.org/10.1038/s41561-019-0363-1.

Riahi, K., Rao, S., Krey, V., Cho, C., Chirkov, V., Fisher, G., Kindermann, G., Nakicenovic, N., Rafaj, P., 2011. RCP8.5: a scenario of comparatively high greenhouse gas emissions. Climatic Change 109, 33—57, https://dx.doi.org/10.1007/s10584-011-0149-y.

Rukšėnienė, V., Dailidienė, I., Myrberg, K., Dučinskas, K., 2015. A simple approach for statistical modelling of ice phenomena in the Curonian Lagoon, the south-eastern Baltic Sea. Baltica 28 (1), 11—18, https://dx.doi.org/10.5200/baltica.2015.28.02.

Sharma, S., Blagrave, K., Magnuson, J.J., O'Reilly, C.M., Oliver, S., Batt, R.D., Magee, M.R., Straile, D., Weyhenmeyer, G.A., Winslow, L., Woolway, R.I., 2019. Widespread loss of lake ice around the Northern Hemisphere in a warming world. Nat. Clim. Change 9 (3), 227—231, https://dx.doi.org/10.1038/s41558-018-0393-5.

Shirasawa, K., Ikeda, M., Takatuka, T., Ishikawa, M., Aota, M., Ingram, G., Belanger, C., Peltora, P., Takahashi, S., Matsuyama, M., Hudier, E., Fujiyoshi, Y., Kodama, Y., Ishikawa, N., 1994. Atomospheric and Oceanographic data report for Saromako lagoon of the SARES (Saroma-Resolute Studies) Project, 1992. Low Temperature Sci., Ser. A 52, 69—167, http://hdl.handle.net/2115/18791.

Stroeve, J.C., Serreze, M.C., Holland, M.M., Jennifer, E., Kay, J.E., Malanik, J., Barret, A.P., 2012. The Arctic's rapidly shrinking sea ice cover: a research synthesis. Climatic Change 110 (3—4), 1005—1027, https://dx.doi.org/10.1007/s10584-011-0101-1.

Sunyer, M.A., Hundecha, Y., Lawrence, D., Madsen, H., Willems, P., Martinkova, M., Vormoor, K., Burger, G., Hanel, M., Kriaučiūnienė, J., Loukas, A., Osuch, M., Yucel, I., 2015. Inter—comparison of statistical downscaling methods for projection of extreme precipitation in Europe. Hydrol. Earth Syst. Sci. 19, 1827—1847, https://dx.doi.org/10.5194/hess-19-1827-2015.

Sztobryn, M., 1994. Long-term changes in ice conditions at the Polish coast of the Baltic Sea. In: Proc. IAHR Ice Symposium. Norwegian Inst. Tech., 345—354.

Sztobryn, M., Przygrodzki, P., 2012. Climatological ice atlas for the western and southern. Baltic sea (1961—2010). In: Schmelzer, N., Holfort, J. (Eds.), Hamburg and Rostock: Bundesamt für Seeschifffahrt und Hydrographie. (BSH), 88 pp.

Sztobryn, M., Wójcik, R., Miętus, M., 2012. Occurrence of ice in the Baltic Sea — current state and expected changes in the future. In: Wibig, J., Jakusik, E. (Eds.), Climatic and oceanographic conditions in Poland and south Baltic Sea. IMGW PIB, Warsaw, 189—215, (in Polish).

Tarand, A., Nordli, P.Ø., 2001. The Tallinn temperature series reconstructed back half a millennium by use of proxy data. In: Ogilvie, A.E.J., Jónsson, T. (Eds.), The Iceberg in the Mist: Northern Research in pursuit of a "Little Ice Age". Springer, Dordrecht, 189—199, https://dx.doi.org/10.1007/978-94-017-3352-6_9.

Thomson, A.M., Calvin, K.V., Smith, S.J., Kyle, G.P., Volke, A., Patel, P., Delgado-Arias, S., Bond-Lamberty, B., Wise, M.A., Clarke, L.E., Edmondset, J.A., 2011. RCP4.5: a pathway for stabilization of radiative forcing by 2100. Climatic Change 109, 77—94, https://dx.doi.org/10.1007/s10584-011-0151-4.

Todd, M.C., Mackay, A.W., 2003. Large-Scale Climatic Controls on Lake Baikal Ice Cover. J. Climate 16 (19), 3186—3199, https://doi.org/10.1175/1520-0442(2003)016⟨3186:LCCOLB⟩2.0.CO;2.

van Vuuren, D.P., Edmonds, J., Kainuma, M., Riahi, K., Thomson, A., Hibbard, K., Hurtt, G.C., Kram, T., Krey, V., Lamarque, J.-F., Masui, T., Meinshausen, M., Nakicenovic, N., Smith, S.J., Rose, S.K., 2011. The representative concentration pathways: an overview. Climatic Change 109, 5—31, https://dx.doi.org/10.1007/s10584-011-0148-z.

Woodward, G., Perkins, D.M., Brown, L.E., 2010. Climate change and freshwater ecosystems: impacts across multiple levels of organization. Philos. Trans. R. Soc. Lond. B. Biol. Sci. 365 (1549), 2093—2106, https://dx.doi.org/10.1098/rstb.2010.0055.

Oceanologia (2020) 62, 173—189

Available online at www.sciencedirect.com

ScienceDirect

journal homepage: www.journals.elsevier.com/oceanologia

ORIGINAL RESEARCH ARTICLE

Simulating tropical storms in the Gulf of Mexico using analytical models

Mehdi Yaghoobi Kalourazi[1], **Seyed Mostafa Siadatmousavi**[1,*], **Abbas Yeganeh-Bakhtiary**[1], **Felix Jose**[2]

[1] *School of Civil Engineering, Iran University of Science and Technology, Narmak, Tehran, Iran*
[2] *Department of Marine & Earth Sciences, Florida Gulf Coast University, Fort Myers, FL, USA*

Received 12 June 2019; accepted 7 November 2019
Available online 25 November 2019

KEYWORDS
Analytical wind model;
H*Wind;
Buoy data;
Optimization;
Hurricanes;
Gulf of Mexico

SUMMARY Different analytical models have been evaluated for estimating wind speed of the tropical storm, where the storm-induced wind velocity is calculated as a function of distance from the center of the hurricane. For these models, different parameters such as maximum wind speed, a radius of the maximum wind, hurricane shape parameter, hurricane translation speed and the orientation of the trajectory, etc., affect the shape of a hurricane. Hurricanes Lili (2002), Ivan (2004), Katrina (2005), Gustav (2008) and Ike (2008) from the Gulf of Mexico were used for skill assessment. The maximum wind radius was calculated using significant wind radii (R_{34}, R_{50} and R_{64}) reported by the National Hurricane Center. Different formulas for calculating the radius of maximum wind speed were evaluated. The asymmetric wind field for each hurricane was generated using analytic methods and compared with in situ data from buoys in the Gulf of Mexico and the H*Wind data. Analytical models were able to predict high wind speed under tropical cyclone conditions with relatively high precision. Among the analytical models evaluated in this research, the model proposed by Holland et al. (2010) showed excellent results. Dynamical wind models such as NCEP/NARR provide wind speed with the coarse spatial resolution which is acceptable for far-field locations away from the hurricane eye. In contrast, analytical models were able to produce sufficiently reliable wind speed within a particular radius from the center of the hurricane. Therefore blending of dynamical and analytical models can be used to provide accurate wind data during hurricane passage in the Gulf of Mexico.

* Corresponding author at: School of Civil Engineering, Iran University of Science and Technology, Narmak, Tehran, Iran.
E-mail address: siadatmousavi@iust.ac.ir (S.M. Siadatmousavi).
Peer review under the responsibility of the Institute of Oceanology of the Polish Academy of Sciences.

Production and hosting by Elsevier

https://doi.org/10.1016/j.oceano.2019.11.001

1. Introduction

A tropical cyclone (TC) is a rapidly rotating storm system characterized by a low-pressure center and strong winds. TC might be called a hurricane, typhoon, tropical storm, tropical depression, or a cyclone depending on their intensity over different locations around the world. In general, a tropical cyclone generates high energy winds, incredible waves, torrential rain, and coastal flooding from storm surge. When it approaches the coast making landfall, the huge waves and storm surge are major threats to human life and property in coastal regions of the world. Among such susceptible coasts, one may refer to the northern Gulf of Mexico; where enormous property damage, and loss of life are ubiquitously associated with TC landfalls each year. As a result, simulation and prediction of tropical storms are of paramount importance.

Depperman (1947) adopted a model called Rankine vortex based on the rotation of the current around a rigid body to simulate the hurricane. This model was then modified by Hughes (1952) who presented the modified Rankine vortex model (MRV). Jelesniansky (1992) proposed a model called Sea, Lake, and Overland Surges from Hurricanes (SLOSH) for simulating hurricanes and its impact along the coast. Houston et al. (1999) evaluated the differences between Hurricane Research Division (HRD) surface wind analysis data and results of SLOSH model. There are several analytical relationships for modeling surface wind velocity of a hurricane, based on the radial distance from the hurricane center (e.g. DeMaria and Kaplan, 1994; Holland, 1980; Holland et al., 2010; Jelesniansky, 1967; Knaff et al., 2007; Willoughby et al., 2006; Wood et al., 2013). Considering Holland (1980) model and Advanced Coastal Circulation (ADCIRC) model for simulating a hurricane in the symmetrical and asymmetrical conditions, Mattocks and Forbes (2008) developed a deterministic prediction system for hurricanes and corresponding floods induced by storm surge along the North Carolina coast. The results led to National Weather Service (NWS) models such as NWS8 and NWS19, for simulating symmetrical and asymmetrical hurricanes in the Surface-Water Modeling Solution. Harper (2002), Atkinson and Holliday (1977), Dvorak (1975), Knaff and Zehr (2007), and Holland (2008) evaluated the relationships between the maximum wind velocity, V_{max}, and central pressure of the hurricane. In Holland (1980), the centeral pressure of the hurricane decreases with an increase in maximum sustained wind speed. Given the fact that the Holland (1980) method assumes a symmetric hurricane, while an actual hurricane is asymmetric in its core, recent studies improved the Holland (1980) model for asymmetric hurricane condition (e.g. Chen et al., 2003; Xie et al., 2006).

Several empirical formulations have been focused on calculating the maximum wind radius (R_{max}) in asymmetric conditions (e.g. Graham and Nunn, 1959; Kawai et al., 2005; Knaff et al., 2007; Takagi et al., 2012). Xie et al. (2006) employed the significant wind radii (R_{34}, R_{50} and R_{64}) at four quadrants of the hurricane to estimate R_{max}). Phadke et al. (2003) used existing analytical wind models to evaluate performance of the wind field resulted from Hurricane Iniki. Emanuel (2004) derived a model for the outer region of the hurricane, based on the combination of free-tropospheric thermodynamic balance and boundary-layer Ekman dynamic balance. He used angular entropy and the momentum balance in the boundary layer and for the inner convective region of the hurricane. In these solutions, the absolute temperature of the outflow is assumed nearly constant; whereas Emanuel and Rotunno (2011) showed this assumption is flawed in most of the cases. They argued that the thermal stratification of the outflow was set by small-scale turbulences which would limit the Richardson Number; implying the variation of outflow temperature with angular momentum. Such variation leads to a realistic prediction of the vortex structure of a hurricane.

Wind structure in a hurricane is based upon two components in the northern hemisphere: a counter-clockwise rotation of the surface background wind and the storm translation speed. Lin and Chavas (2012), and later Chavas et al. (2015) have mathematically merged existing theoretical solutions for the radial wind structure on the top of the boundary layer in the inner ascending region of the hurricane. It was based on the solution of Emanuel and Rotunno (2011) in which convective transfer of moisture and heat was persistent. In the outer descending region, the solution of Emanuel (2004) was employed in which the convection was absent. Hu et al. (2012) proposed a parametric hurricane wind model based on the asymmetric Holland-type vortex models. They included the impact of Coriolis deflection on the hurricane shape parameter. They also excluded the forward velocity of hurricane before applying the Holland vortex model to avoid unnecessary exaggeration of the wind asymmetry.

In general, analytical wind models are suitable for simulating wind field up to a specific radius from the center of hurricane, and beyond which prediction would go wrong as hurricane may be affected by other global weather systems. Wood et al. (2013) showed that central pressure deficit in an axisymmetric vortex core is strongly related to the choice of free parameters that control the shape of the radial profiles of the tangential velocity. A new model to represent TC wind velocity field is developed by Wijnands et al. (2016) consisting three components fit to the maximum wind velocities in the eye to capture the extent of gale-force winds around the TC, and the construction of the wind profile using a cubic spline approach.

Another method for simulating hurricane wind is to use long-term reanalysis wind data such as data provided by the National Centers for Environmental Prediction (NCEP), the European Centre for Medium-Range Weather Forecasts (ECMWF), and the Cross-Calibrated Multi-Platform (CCMP). Such wind data have also been extensively used for

hindcasting and predicting the hydrodynamics in various ocean basins. However, studies have shown that the use of such coarse-resolution reanalyzed data for forcing wave models led to underestimation of wave height. The quality of wind data is always blamed for such an underestimation (e.g. Brenner et al., 2007; Cavaleri and Sclavo, 2006; Mazaheri et al., 2013; Moeini et al., 2010; Signell et al., 2005). Combining two data sources, i.e., Holland (1980) model and CCMP data, Pan et al. (2016) reported improvement in wind field hindcast for two TCs, i.e., Fanapi and Meranti, which made landfall in China. They evaluated the effect of different TC models on hindcasting V_{max}. Combining wind data from different sources have been used extensively for improving hurricane wave modeling in the Gulf of Mexico (e.g. SiadatMousavi et al., 2009).

This study quantitatively evaluates the wind fields calculated using different parametric models for several hurricanes traversed across the Gulf of Mexico. Given that R_{max} is an important parameter contributing to the storm-induced wind velocity, its influences on the wind field is compared among different analytic methods and the most appropriate method is selected for calculating R_{max} in the Gulf of Mexico. All evaluations were based on in situ data from National Data Buoy Center (NDBC) buoys. Finally, most appropriate analytical model data were compared against H*Wind model in terms of hurricane forward motion, angle of the maximum wind velocity, V_{max} and the range in which analytical model is applicable. The results of analytical models were also compared with NCEP/NARR (North American Regional Reanalysis) dynamical model to determine whether it is possible to merge both datasets to produce an optimized wind data for the study area.

2. Parametric tropical storm-induced wind velocity

Wind vector, V, of a TC is composed of rotational velocity of the hurricane and the translational motion of the hurricane eye, and can be expressed as follows:

$$V = k_m V_r + \delta_m V_m, \tag{1}$$

where V_r is velocity over a distance r from the hurricane center, V_m is the hurricane translation velocity, k_m can be considered as 0.8 according to Powell (1980); however, his later observational studies (e.g. Powell et al., 1991, 1998) have showed its variability over the range 0.7 to 0.9, due to variations in the vertical stability. The asymmetry coefficient δ_m is equal to zero for a symmetric hurricane and 0.5 for an asymmetric one.

Numerous methods have been proposed for calculating V_r. Schloemer (1954) proposed a radial relationship for calculating the pressure based on the difference between the central surface pressure of the hurricane (P_c) and the ambient pressure (P_n). Later on, Holland (1980, hereafter H80) modified the Schloemer's theory and presented a rectangular hyperbola radial relationship between pressure and wind velocity as follows:

$$P(r,\theta) = P_c + (P_n - P_c)\exp\left[\left(-\frac{R_{\max(\theta)}}{r}\right)\right]^B, \tag{2}$$

$$V_r(r,\theta) = \left[\frac{B}{\rho_a}\left(\frac{R_{\max(\theta)}}{r}\right)^B (P_n - P_c)\exp\left[\left(-\frac{R_{\max(\theta)}}{r}\right)\right]^B + \left(\frac{rf}{2}\right)^2\right]^{0.5} - \frac{rf}{2}, \tag{3}$$

where ρ_a is the density of air, $P(r, \theta)$ is the surface pressure at a distance of r from the hurricane center, B is a hurricane shape parameter, f is the Coriolis parameter $f = 2\Omega\sin(\phi)$, Ω is the rotational frequency of the earth and φ is the latitude. The parameter "B" is used to relate the pressure to the wind field and it plays an important role in estimating V_{max} in a hurricane. Indeed, B controls the hurricane eye diameter and fastness of the maximum wind velocity, and varies from 1 to 2.5. It has been shown that B has high correlation with several parameters, such as pressure drop, R_{max}, and the latitude of hurricane center; e.g., the following relationship can be used to calculate hurricane aspect ratio (Levinson et al., 2010):

$$B = \frac{V_{max}^2 \rho_a e}{100(P_n - P_c)}, \tag{4}$$

where e is the base of natural logarithms.

Jelesniansky (1967) suggested a parametric equation to calculate V_r. This formula led to development of the US Weather Service SPALASH storm surge prediction model (Jelesnianski et al., 1973) and the SLOSH model (Jelesnianski, 1992, hereafter S92) as the following relationship:

$$V_r = \begin{cases} V_{max}\left(\dfrac{r}{R_{max}}\right)^{\frac{3}{2}}, & r < R_{max} \\ V_{max}\left(\dfrac{2\,R_{max} r}{r^2 + R_{max}^2}\right), & r \geq R_{max} \end{cases}. \tag{5}$$

Willoughby et al. (2006, hereafter W06) divided the hurricane structure into three parts such that the wind velocity inside the eye of a hurricane increases with increasing the radius from the center. Far from the hurricane eye, it decreases exponentially. A transition area exists between those mentioned areas. On this basis, the wind velocity in each part can be calculated from the following relationships.

$$V_r = \begin{cases} V_i = V_{max}\left(\dfrac{r}{R_{max}}\right)^n, & r < R_1 \\ V_i(1-w) + V_o, & R_1 \leq r < R_2 \\ V_o = V_{max}\left(-\dfrac{r - R_{max}}{X_1}\right), & r \geq R_2 \end{cases}, \tag{6}$$

where V_i and V_o are the tangential wind component in the eye and beyond the transition zone, which lies between $r = R_1$ and $r = R_2$; and permits velocity of V_{max} at the distance of R_{max}; X_1 is the exponential decay length in the outer vortex and n is the exponent for the power law inside the eye; w is the weighted function in the transitional zone. The values of R_{max}, X_1 and n are suggested as a function of V_{max} and φ, using the regression analysis:

$$\begin{cases} R_{max} = 46.4\exp(-0.0155V_{max} + 0.016\phi) \\ X_1 = 270.5 - 4.78V_{max} + 6.17\phi \\ n = 0.431 + 0.136V_{max} - 0.006\phi \end{cases}. \tag{7}$$

The weight function, w, is expressed based on the non-dimensional ξ which is defined as follows:

$$\xi = \frac{r - R_1}{R_2 - R_1}, \tag{8}$$

$$w(\xi) = \begin{cases} 0, & \xi \le 0 \\ 126\xi^5 - 420\xi^6 + 540\xi^7 - 315\xi^8 + 70\xi^9, & 0 \le \xi \le 1. \\ 1, & \xi \ge 1 \end{cases} \tag{9}$$

Knaff et al. (2007, hereafter K07) used MRV model as well as a statistical-parametric model to predict TC wind radii in the Atlantic Ocean, the East Pacific, and the Western North Pacific. They proposed a parametric equation to calculate V_r as follows:

$$V(r,\theta) = \begin{cases} (V_{max} - a)\left(\frac{R_{max}}{r}\right)^x + a\cos(\theta - \theta_0), & r \ge R_{max} \\ (V_{max} - a)\left(\frac{R_{max}}{r}\right) + a\sin(\theta - \theta_0), & r < R_{max} \end{cases} \tag{10}$$

in which x is the size parameter, a is the asymmetry coefficient, and θ_0 is the angle between V_{max} and the storm translation vector. In this equation, using the wind radii (R_{34}, R_{50} and R_{64}) in each quadrant and multiple linear regressions, four parameters (V_{max}, R_{max}, a, θ) can be calculated.

Holland et al. (2010, hereafter H10) retained the rectangular hyperbolic form of previously proposed H80 model and further refined wind velocity relationship at all levels and matched the wind velocity with the data beyond the rotational part of the hurricane. The proposed relationship in H10 is as follows:

$$\left[\frac{b_s}{\rho_a}\left(\frac{R_{\max(\theta)}}{r}\right)^{b_s}(P_n - P_c)\exp\left[\left(-\frac{R_{\max(\theta)}}{r}\right)\right]^{b_s} + \left(\frac{rf}{2}\right)^2\right]^x - \frac{rf}{2}, \tag{11}$$

where the subscript s refers to the surface value (at a nominal height of 10 m). Parameter b_s is the hurricane shape coefficient which can be related to the original b value in H80 by $b_s = bg_s^x$, where g_s is the reduction factor for gradient to-surface wind. If $x = 0.5$ is set, and b_s is assumed to be a constant value, as used in H80, then:

$$\begin{cases} b_s = -4.4 \times 10^{-5}\Delta P^2 + 0.01\Delta P + 0.03\frac{\partial P_c}{\partial t} \\ \quad - 0.014\phi + 0.15\, V_m + 1.0\phi \\ x = 0.6\left(1 - \frac{\Delta P}{215}\right) \end{cases}, \tag{12}$$

where $\Delta P = P_n - P_c$ is in hPa and $\partial P_c/\partial t$ is the rate of change of pressure in hPa/h. Emanuel and Rotunno (2011) extended the Emanuel (2004) model to areas beyond the hurricane eyewall by considering a constant (critical) Richardson Number which is determined based on temperature gradient across the hurricane. This model (hereafter E11) performs well near R_{max}, while becomes less accurate as one gets farther from the center of the hurricane. This model takes into account the Coriolis effect and may turn into Jelesnianski model upon ignoring those effects. E11 suggested the following model for simulating wind surface velocity in a TC:

$$V_r = \frac{2r\left(R_{max}V_{max} + \frac{1}{2}fR_{max}^2\right)}{R_{max}^2 + r^2} - \frac{fr}{2}. \tag{13}$$

Wood et al. (2013, hereafter W13) improved the existing parametric tangential wind profile model of Wood and White (2011) for a better fit to a TC. W13 model has five key parameters controlling the radial profile of tangential wind: V_{max}, R_{max}, and three shape velocity parameters η, λ and κ to control different portions of the profile:

$$\begin{cases} V_r(\rho; m) = V_{max}\phi(\rho; \kappa; \eta; \lambda) \\ \phi(\rho; \kappa; \eta; \lambda) = \frac{\eta^\kappa \rho^\lambda}{\left(\eta - \kappa + \kappa\rho^{\frac{\eta}{\lambda}}\right)^\lambda} \end{cases}, \tag{14}$$

where $\rho = r/R_{max}$ is a dimensionless radius. Note that $0 \le \kappa < \eta$ and $\lambda > 0$.

As discussed in this section, host of models have been proposed to simulate the wind structure of a TC. These formulations will be assessed in the following sections for understanding the complex structure of hurricane wind field in the Gulf of Mexico.

2.1. The radius of the maximum wind

The radius of the maximum wind refers to the distance from the center of the hurricane to the location within its structure where V_{max} occurs. R_{max} plays a significant role in hurricane characteristics. Numerous relationships have been proposed for calculating R_{max} in the literature. In this respect, Graham and Nunn (1959, hereafter G59) suggested Eq. (15) in which R_{max} is a function of latitude, difference between the central surface pressure and the ambient pressure, and translation speed of the tropical storm.

$$R_{max} = 28.25\tanh[0.0873(\phi - 28)] + 12.22\exp\left(\frac{\Delta P}{33.86}\right) + 0.2\, V_m + 37.2. \tag{15}$$

Kawai et al. (2005, hereafter K05) have proposed exponential formulas for R_{max} (km) based on the central pressure:

$$R_{max} = 94.89\exp\left(\frac{P_c - 967}{61.5}\right). \tag{16}$$

K07 suggested the following relationship where m_0, m_1, and m_2 are empirical parameters:

$$R_{max} = m_0 + m_1V_m + m_2(\phi - 25). \tag{17}$$

Takagi et al. (2012, hereafter T12) used the following empirical formula developed by the National Institute for Land and Infrastructure Management (NILIM) to estimate the R_{max}:

$$R_{max} = 80 - 0.769(950 - P_c), \tag{18}$$

where R_{max} and P_c are in km and hPa respectively, and $P_c < 950$ hPa.

Note that the National Hurricane Center (NHC) forecast advisories and the Automated Tropical Cyclone Forecasting (ATCF) product provide parameters such as geographic coordinates of hurricane center, V_{max}, V_m, surface wind forecasts etc., and the hurricane structure is provided by the radii of specified wind velocities (34, 50, 64, and 100 kn) in four quadrants. Figure 1 illustrates the asymmetric wind structure for Hurricane Ivan at 0900 UTC on 15 September 2004. At this time, the center of hurricane was located at 26.1°N, 87.8°W. The 1-min averaged maximum sustained

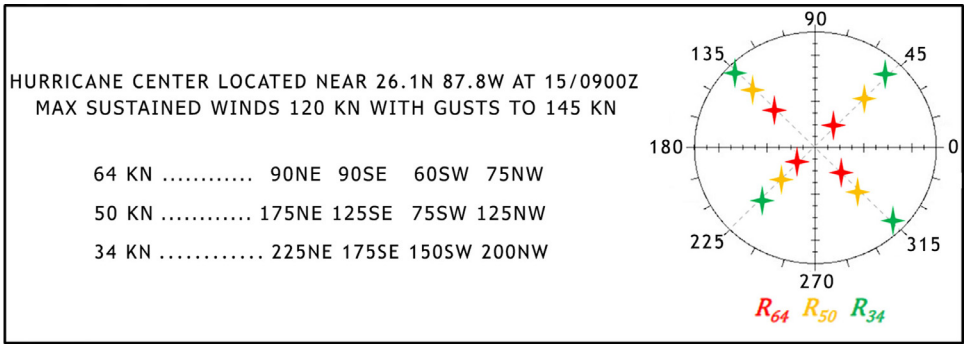

Figure 1 Tropical cyclone parameters provided by the National Hurricane Center (NHC) for Hurricane Ivan at 0900 UTC 09/15/2004.

surface wind speed was 120 kn with gusts up to 145 kn. The 64 kn wind in four quadrants (NE, SE, SW, NW) was located at distances of (90, 90, 60, 75 NM) from the center of the hurricane; Similar information is also provided for the location of 34 and 50 kn winds. Those distances in different quarters are shown as R_{34}, R_{50} and R_{64}. As proposed by Xie et al. (2006, hereafter X06), R_{max} can be set to different values in each quadrant. By solving Eq. (3), based on given information in each direction, curve fitting provides two solutions for R_{max} where the smaller value is the most appropriate solution. Details are presented in the Appendix 1.

3. Methodology

3.1. Selecting tropical storms for analyzing wind field in the Gulf of Mexico

The major hurricanes in the Gulf of Mexico during 2002–2016 include: Lili (2002), Ivan (2004), Katrina (2005), Alberto (2006), Dolly (2008), Gustav (2008), Ike (2008), Ida (2009), Alex (2010), Don (2011), Isaac (2012), Karen (2013) and Colin (2016). Due to non-availability of R_{64} values for some of the TCs, Hurricanes Lili, Ivan, Katrina, Gustav and Ike were selected for detailed study of their complex wind structure. The time period from the entry of tropical storms into the Gulf of Mexico until its landfall along northern Gulf coast was considered for each hurricane. The best hurricane track, geographic coordinates, central pressure, V_{max}, V_m, etc. were retrieved on a six-hourly basis from NHC and ATCF. Moreover, for model validation purpose, corresponding wind data have been extracted from NDBC buoy network from the Gulf of Mexico. The hurricane tracks and available buoys are shown in Figure 2.

3.2. Reconstructing the wind fields of a tropical storm

In order to estimate wind field using analytical models, polar coordinate system was employed. In this study, radius, r, was calculated from 1 to 1000 by steps of 1 km and started from the hurricane center. The azimuthal angle from x-axis, θ, was considered from 1° to 360° by steps of 1°.

4. Results and discussions

4.1. Effect of hurricane shape parameter (B) on the tropical storm-generated wind field

As it was mentioned in section 2, hurricane shape parameter (B) serves as a control parameter for the hurricane shape. It establishes a balance between V_{max} and P_c. H80 proposed a range from 1 to 2.5 for B. In this section the effect of B on wind velocity and the hurricane shape was investigated. In Figure 3, the wind fields of Hurricane Ivan on 15 September 2004, at 0900 UTC was demonstrated for different values of B (0.5–2.5). In this case, $V_{max} = 120$ kn $= 61.73$ m/s, $R_{max} = 40.21$ km and $P_c = 932$ hPa, and the wind velocity was calculated using H80's model. Increasing B would also increase V_{max} at R_{max} and decrease the wind speed away from R_{max}. In case of $B = 1.5$, the corresponding wind velocity at $R_{max} = 40.21$ km was ~60 m/s, indicating that the most appropriate value for B at this instance is ~1.5. It is in agreement with actual hurricane conditions reported by NHC in Figure 1.

4.2. Assessment of different models for calculating R_{max}

Different analytical models such as G59, K05, X06, K07 and T12 can be employed to calculate R_{max}, and the key question is, which method is consistent for the hurricanes traversing across the Gulf of Mexico. In order to address this question, the values of R_{max} calculated using different models and R_{max} derived from H*Wind are compared in Figure 4 for the time interval when Hurricane Ivan was churning across the Gulf of Mexico; i.e. from 1500 UTC on 14 September 2004 to 0300 UTC 16 September 2004. H*Wind is a product of NOAA/Hurricane Research Division which integrates data from all available surface weather platforms and aircraft data within 1000 km from hurricane's eye. The root mean square error (RMSE), scattering index (SI) and BIAS presented in Figure 4 were used to assess the models. It can be concluded that T12, K07 and K05 methods tend to overestimate R_{max} throughout the time period when the Hurricane was active in the Gulf of Mexico until it leaves the Gulf of Mexico. In fact, according to Eq. (16) and Eq. (18), R_{max} in the K05 and T12 methods only depends on P_c which provides limited flexibility to produce realistic values. In contrast, R_{max} in the G59

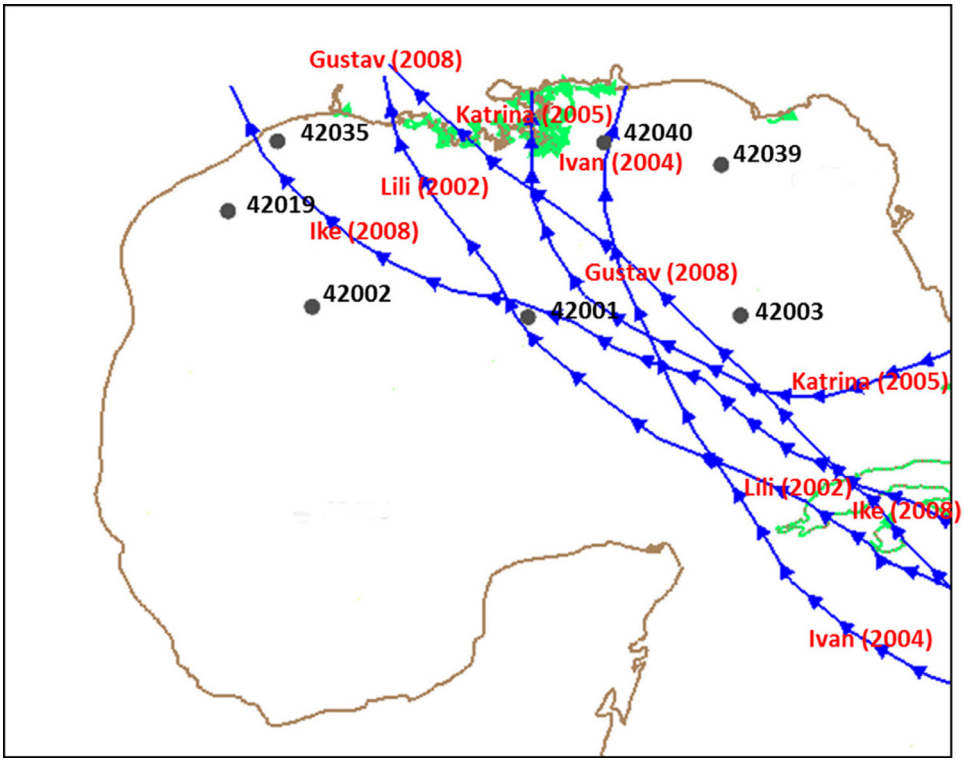

Figure 2 Tracks of five major hurricanes that made landfall along the northern Gulf of Mexico and locations of National Data Buoy Center (NDBC) buoys used for models assessment in the study.

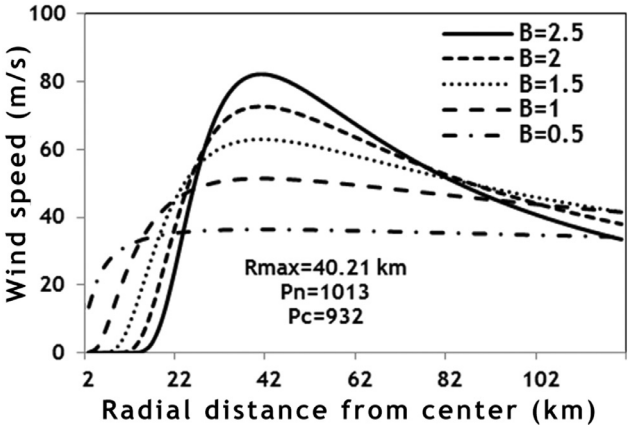

Figure 3 The effect of varying the parameter B on wind velocity for Hurricane Ivan at 0900 UTC 09/15/2004.

and X06 methods is also dependent on the V_m and the geographical location of the tropical cyclone. Therefore, these methods give more desirable results for calculating R_{max}. Based on the statistics presented in Figure 4, X06 was the most successful method in reproducing R_{max}.

4.3. Assessment of different parametric models for calculating the wind field of a tropical storm

Different models can be used to simulate a tropical storm in the Gulf of Mexico including H80, S92, W06, K07, H10, E11 and W13 models as presented in section 2. In all of these models, R_{max} serves as a key parameter, and the formula proposed by X06 was selected as the most appropriate method for calculating R_{max} in the Gulf of Mexico as shown in section 4.2. For assessment, the wind velocities calculated via the analytical approaches were compared to the measured data from NDBC buoys.

4.3.1. Hurricane Lili

Hurricane Lili was one of the strongest hurricanes passing through large areas across the Atlantic Ocean and the Gulf of Mexico and made its landfall along the northern Gulf of Mexico on October 4th, 2002. Comparison between the model-generated wind velocity using H80, S92, W06, K07, H10, E11 and W13 models and the measured data from buoys in the Gulf of Mexico are illustrated in Figure 5. In general, the storm-induced wind velocity was maximum at $r = R_{max}$ while lower velocities were observed in both $r < R_{max}$ (inside the hurricane eyewall) and $r > R_{max}$ (far from the hurricane center). According to Figure 2, this hurricane passed near buoy 42001 on October 2nd when $R_{max} = \sim$23 km and the radial distance between the buoy and the hurricane center $r = \sim$27 km. Since $r \approx R_{max}$, the buoy 42001 was expected to measure V_{max}. As shown in Figure 5, there is a fair agreement between measured data at all buoys and the analytical models.

In order to evaluate the analytical models in more detail, some statistics were presented in Table 1. The BIAS values indicate that, almost all models tend to underestimate the wind velocity at most of the buoys locations. Based on statistics, H10 and W13 models produced better results at most of the buoys compared to other models.

A comparison of wind structure generated by symmetric and asymmetric models for Hurricane Lili at 2100 UTC

Table 1 Statistical parameters characterizng wind velocity obtained using different parametric methods at buoys locations in the Gulf of Mexico during different hurricanes.

Hurricane Lili (2002)

	NDBC-42001							NDBC-42002							NDBC-42003						
	H80	S92	W06	K07	H10	E11	W13	H80	S92	W06	K07	H10	E11	W13	H80	S92	W06	K07	H10	E11	W13
RMSE (m/s)	2.7	3.9	3.0	2.8	2.4	3.6	2.6	2.4	3.1	2.1	2.9	2.0	2.9	1.8	1.9	3.5	3.4	2.2	1.6	3.0	1.5
SI (%)	15	15	20	15	15	18	13	38	32	37	20	33	37	28	18	18	30	14	15	19	12
BIAS (m/s)	−1.5	−3.2	−0.8	1.1	−1.1	−2.4	1.8	−1.3	−2.6	1.0	1.6	−1.0	−2.2	1.0	0.4	−2.9	−1.3	−1.7	0.2	−2.2	0.7

Hurricane Ivan (2004)

	NDBC-42001							NDBC-42002							NDBC-42003						
	H80	S92	W05	K07	H10	E11	W13	H80	S92	W05	K07	H10	E11	W13	H80	S92	W05	K07	H10	E11	W13
RMSE (m/s)	2.2	2.9	3.3	3.7	2.3	3.7	2.9	2.7	1.7	2.5	1.5	2.5	1.4	1.6	2.6	2.9	1.8	2.8	2.6	2.6	1.6
SI (%)	17	19	17	24	19	24	19	44	41	39	41	46	37	38	9	10	8	7	8	10	5
BIAS (m/s)	1.4	−1.4	0.4	−0.6	−0.2	−2.8	−1.3	2.2	0.8	−2.0	1.4	2.0	−0.3	0.9	0.9	−2.0	−0.6	−1.6	2.0	−1.6	1.1

Hurricane Katrina (2005)

	NDBC-42001							NDBC-42002							NDBC-42019						
	H80	S92	W06	K07	H10	E11	W13	H80	S92	W06	K07	H10	E11	W13	H80	S92	W06	K07	H10	E11	W13
RMSE (m/s)	2.3	4.5	3.4	3.8	3.1	5.2	3.1	1.5	2.6	4.1	2.4	2.1	3.0	1.8	2.0	1.7	2.1	2.3	1.8	2.0	2.1
SI (%)	17	27	27	22	32	27	24	27	38	35	25	36	37	30	39	39	47	41	37	43	42
BIAS (m/s)	−0.8	−2.6	−1.5	−0.9	−1.3	−3.1	−1.3	0.3	−1.0	−2.0	−1.2	−0.2	−1.3	−0.1	1.0	0.4	0.5	−1.0	1.1	0.1	1.2

Hurricane Gustav (2008)

	NDBC-42001							NDBC-42019							NDBC-42040						
	H80	S92	W06	K07	H10	E11	W13	H80	S92	W06	K07	H10	E11	W13	H80	S92	W06	K07	H10	E11	W13
RMSE (m/s)	3.3	7.6	2.3	3.1	3.3	7.0	3.4	2.4	3.4	2.3	2.2	1.5	3.8	1.8	3.4	5.7	3.4	2.2	2.8	7.0	2.2
SI (%)	25	20	18	15	21	19	17	37	13	27	13	13	18	15	22	13	21	12	10	13	13
BIAS (m/s)	−1.6	−7.2	−0.8	−2.1	−2.2	−6.6	−2.1	−0.5	−3.3	−1.4	−1.2	−1.2	−3.7	−1.5	0.2	−5.3	−0.8	−1.3	−2.2	−6.7	1.1

Hurricane Ike (2008)

	NDBC-42002							NDBC-42019							NDBC-42040						
	H80	S92	W06	K07	H10	E11	W13	H80	S92	W06	K07	H10	E11	W13	H80	S92	W06	K07	H10	E11	W13
RMSE (m/s)	2.6	3.9	3.6	3.8	2.3	3.3	3.0	2.7	4.1	3.8	3.1	1.7	4.5	2.2	2.9	4.0	3.8	3.2	1.5	4.0	2.9
SI (%)	18	21	28	24	12	27	26	24	12	22	30	17	15	21	20	11	22	26	11	11	20
BIAS (m/s)	1.6	−2.9	−2.2	−1.6	−1.5	−0.3	0.3	1.4	−2.8	−3.1	−0.4	−0.5	−3.0	−0.3	1.7	−2.9	−1.2	−1.5	−0.4	−2.9	−0.9

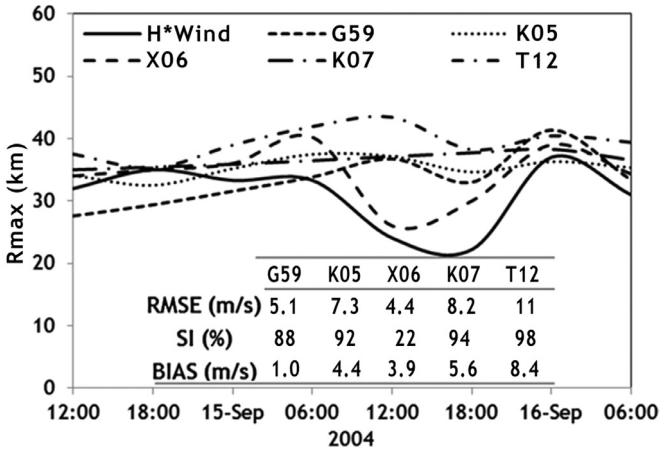

Figure 4 Comparison of the performance of different models applied for calculating R_{max} for Hurricane Ivan (2004).

on 01 October 2002 is provided in Figure 6. The amount of asymmetry depends on V_{max}, R_{max}, V_m and the direction of the hurricane movement (β). The center of hurricane was located near 22.7°N, 85°W at this time, and $V_{max} = 90$ kn, $\beta = 305°$, $V_m = 15$ kn, $P_C = 970$ hPa. Since W13 and H10 methods produced higher wind velocity compared to other models, their corresponding asymmetric structure for the hurricanes are also higher. Increasing the asymmetric amount affect the θ_{max} (the angle of maximum wind velocity). According to the direction of the hurricane movement, the wind surface velocity on the right side of the hurricane is larger than the left side.

4.3.2. Hurricane Ivan

Hurricane Ivan, the strongest hurricane during the 2004 Atlantic hurricane season, resulted in a widespread damage in the Caribbean and United States, and reached Category 5 strength on the Saffir-Simpson scale. It passed across the Gulf of Mexico during 14–16 September. It is evident from Figure 2 that Hurricane Ivan trajectory passed close to buoys 42001, 42003 and 42040. Since wind velocity is higher on the right of the hurricane rather than its left side, higher wind velocity was measured at buoy 42003 than the buoys 42001 on September 15th (see Figure 5). A comparison between the results of parametric models and the measured wind velocity data by buoys shows that the models performances were better during peak hours.

Statistical indices based on data from different buoys presented in Table 1 indicate that E11 underestimated the wind velocity; while H80 tended to overestimate the wind velocity at most of the buoys. The RMSE values at all buoy locations show that all analytical models provided fairly realistic estimation of Hurricane Ivan. In general, H80, H10 and W13 models outperformed the rest of models, especially close to high speed regions of the hurricane. Figure 6 illustrates the wind field simulated by the symmetric and asymmetric models for Hurricane Ivan at 0900 UTC on 15 September 2004. At this time, the hurricane center was located at 26.1°N, 87.8°W, and $V_{max} = 120$ kn, $\beta = 340°$, $V_m = 10$ kn, $P_C = 938$ hPa. Among the analytical models, the wind field and the wind field asymmetry were maximum for H10 model. As an example, at the same radial distances from hurricane center and in the direction of θ_{max}, higher surface wind velocities were estimated by H80 and H10 models and the smallest wind speeds were simulated by S92 and E11. Table 2 illustrates a comparison between wind radii (R_{34}, R_{50} and R_{64}) reported by NHC and H80, H10, E11 models for Hurricane Ivan at 0900 UTC on 15 September 2004. There is relatively good agreement between NHC report and analytical models in terms of the shape of hurricane and the values of wind surface velocity; however, H80 and H10 models overestimated the wind radius, while the E11 underestimated the wind radius.

4.3.3. Hurricane Katrina

Hurricane Katrina was one of the most destructive natural disasters occurred in the United States during the last decades. The hurricane landfall occurred on August 29th along the Mississippi coast as an upper Category 3 Hurricane. As shown in Figure 2, the buoys 42001, 42003 and 42040 were close to the hurricane track. A comparison between the analytical models and measured data in Figure 5 reveals that the performance of analytical models were acceptable; however, the performance was better at buoys 42001 and 42040, compared to other buoys. It can be inferred that the analytical models tend to estimate wind velocity more accurately close to the area of maximum wind speed of a hurricane.

4.3.4. Hurricane Gustav

Hurricane Gustav caused serious destruction in parts of Haiti, the Dominican Republic, Jamaica, the Cayman Islands, Cuba and the United States. As shown in Figure 2, the buoys 42003, 42039 and 42040 were located on the right flank of the hurricane track. The eyeball observation of results presented in Figure 5 and the statistical indices presented in Table 1 show that in most of the buoy locations wind velocity was underestimated by all models. Moreover, K07, H10 and W13 models produced more realistic results when compared to other parametric models for simulating the Hurricane Gustav.

4.3.5. Hurricane Ike

Hurricane Ike entered the Gulf of Mexico during 10–13 September 2008 and passed close to the buoy 42001 on

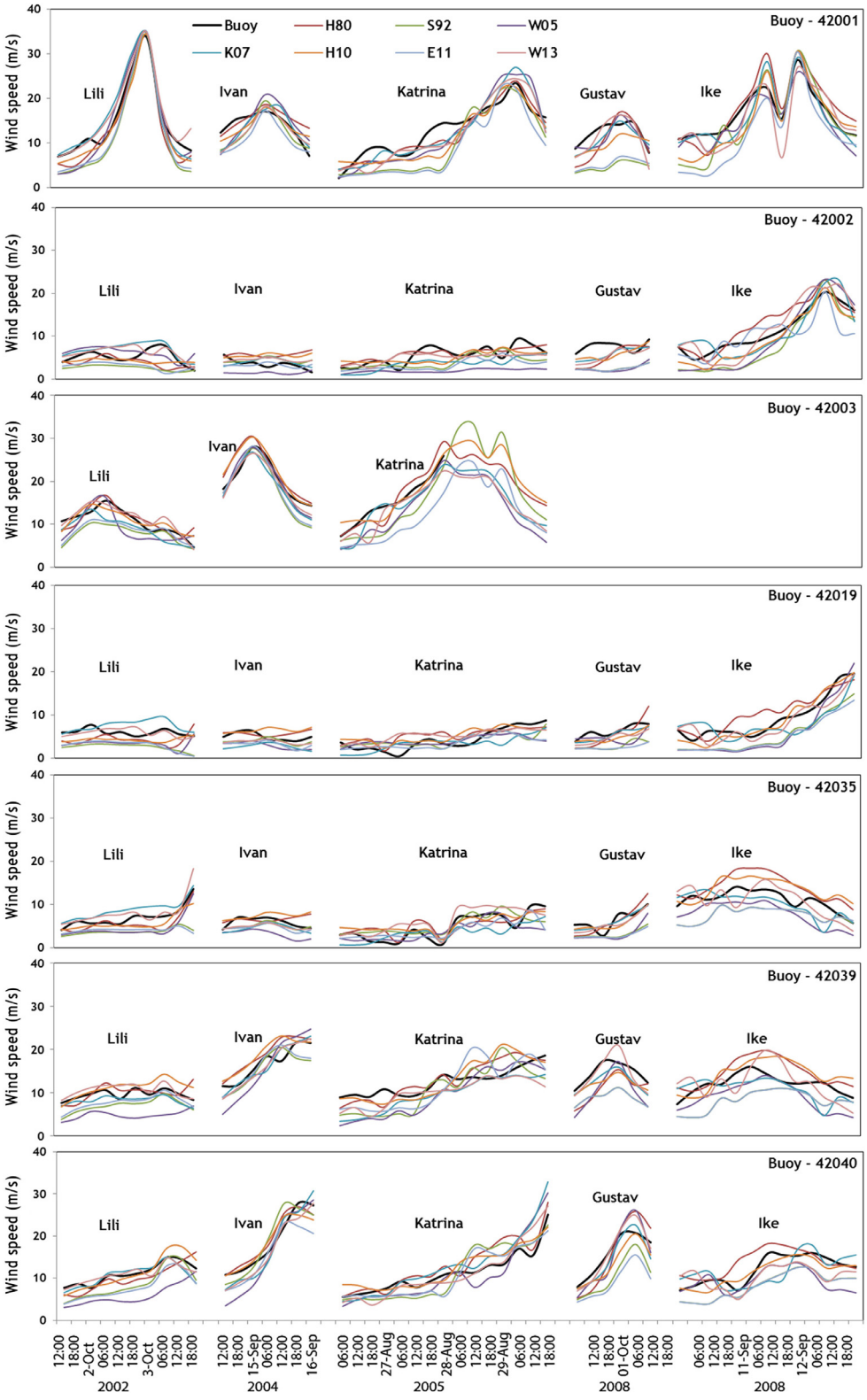

Figure 5 Performance of different methods applied for calculating wind velocity as compared to buoys wind velocity measurements in the Gulf of Mexico during Hurricanes Lili, Ivan, Katrina, Gustav and Ike.

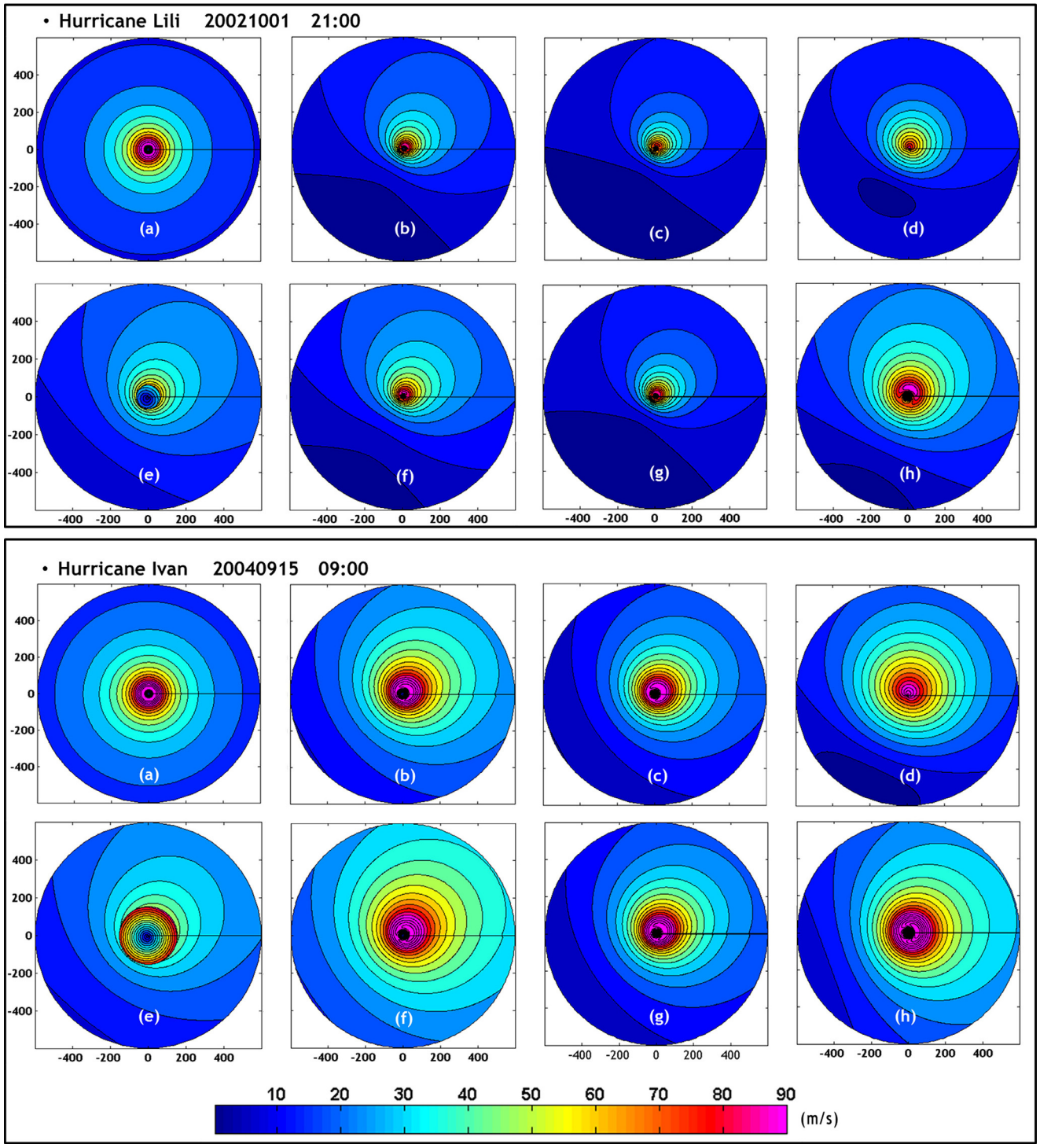

Figure 6 Comparison of the wind fields produced by (a) symmetric, (b) H80, (c) S92, (d) W06, (e) K07, (f) H10, (g) E11, (h) W13, models for the Hurricane Lili at 21:00 10/01/2002 and for the Hurricane Ivan at 09:00 09/15/2004 in the Gulf of Mexico.

September 11th when $R_{max} = \sim 25$ km and the radial distance of the buoy from the center of hurricane was calculated as $r = \sim 5$ km. The storm-induced wind velocity at this buoy, as shown in Figure 5, reduced suddenly when buoy was inside the eye ($r \ll R_{max}$). As summarized in Table 1, S92, W06, K07 and E11 models underestimated the wind velocity at most of the buoys locations. The models proposed by H10 and W13 showed better performance for simulating the Hurricane Ike compared to other analytical models.

4.3.6. Calibrating k_m to improve models' performance

As discussed in the previous section, among different analytical models, the models proposed by S92, W06, K07, and E11 relatively underestimated the wind velocity, while those proposed by H80, H10 and W13 tend to overesti-

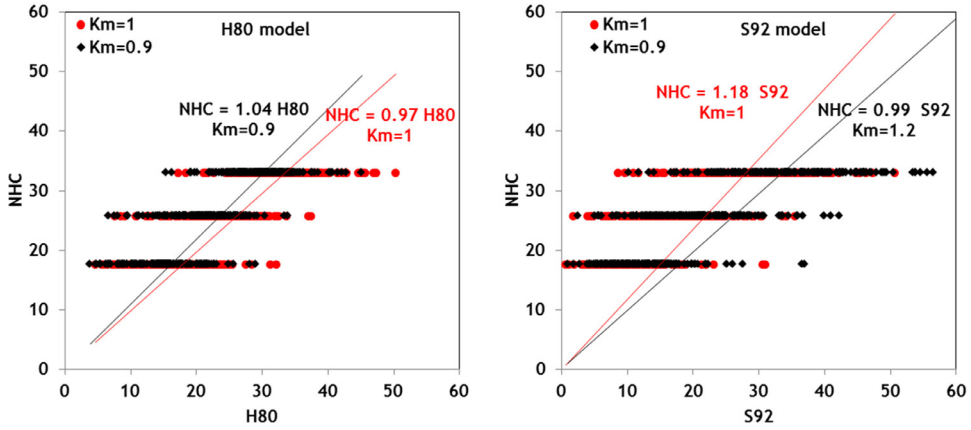

Figure 7 Scatter plot and linear regression of wind velocities (m/s) produced by NHC versus H80 (left panel) and S92 (right panel) models for all tracks of the Hurricanes Lili, Ivan, Katrina, Gustav and Ike.

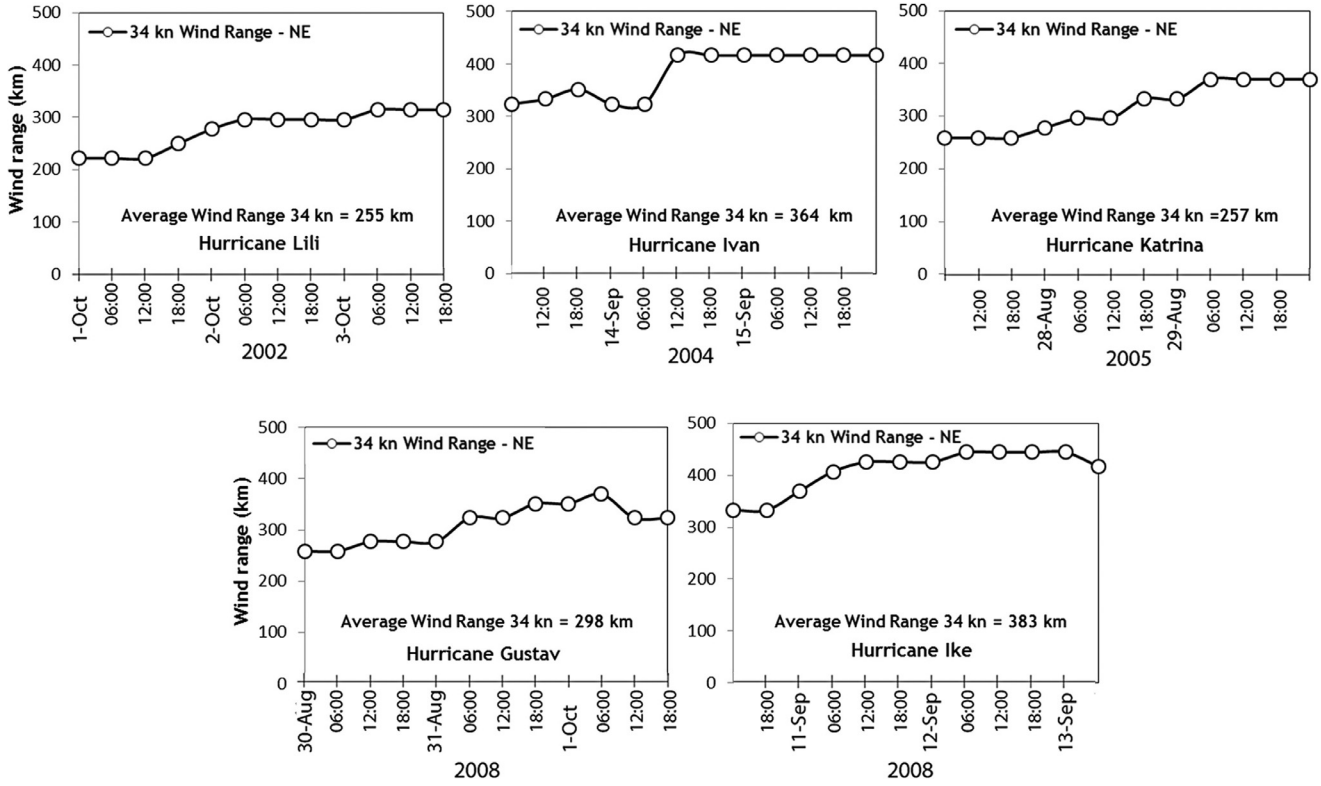

Figure 8 Values of R_{34} produced by NHC for the northeast quarter in 12 snapshots during the Hurricanes Lili, Ivan, Katrina, Gustav and Ike passage over the Gulf of Mexico.

Table 2 Comparison between wind radii (R_{34}, R_{50} and R_{64}) reported by NHC and obtained using H80, H10, E11 models for Hurricane Ivan at 09:00 09/15/2004.

	NHC				H80				H10				E11			
	NE	SE	SW	NW	NE	SE	SW	NW	NE	SE	SW	NW	NE	SE	SW	NW
64 kn	90	90	60	75	96	68	50	76	122	85	61	94	89	71	48	65
50 kn	175	125	75	125	139	95	69	110	184	121	89	146	122	96	63	86
34 kn	225	175	150	200	244	122	109	191	303	213	143	272	182	142	88	122

mate the storm-induced wind velocity. It is possible to calibrate hurricane models by adjusting k_m in Eq. (1) which is 0.7 ~ 0.9 by default (Powell et al., 1991, 1998). Along the track of each hurricane 12 points were selected, and the R_{34}, R_{50} and R_{64} in four quadrants (NE, SE, SW, and NW) reported by NHC were used in models to estimate the wind speed. These estimates from analytical relations were compared with NHC reported speeds (34, 50 and 64 kn) for all aforementioned hurricanes. Figure 7 provides the scatter plots for the H80 and S92 models. To calculate the calibration coefficient, $k_m = 1$ were used in all models and the linear regression provided the ratio of wind velocity between NHC and each analytical model. As shown in Figure 7, the ratio was equal to 0.97 and 1.18 for the H80 and S92 models, respectively. It means that S92 requires k_m value higher than 1 in Eq. (1) while vice versa is true for the H80 model. By trial and error process, $k_m = 1.2$ and $k_m = 0.9$ were found suitable for S92 and H80 models. Similarly, using a linear regression for other analytical models, the values of k_m for each model were estimated as presented Table 3. The BIAS values presented in Table 3 show the improvement of models in reproducing wind velocities at NDBC buoys when calibrated values of k_m were used in analytical models.

4.4. Combining parametric models with numerical models

A comparison between analytical models and observed data from NDBC buoys shows that these models produce relatively appropriate wind velocity within a particular radius to the center of hurricane (R_{he} = radius of the hurricane effect), and the accuracy of simulations degrade as one gets beyond that threshold radius. The *SI* and *RMSE* values were lower at buoys within shorter distance to the hurricane track (i.e. close to R_{max}), as compared to those located farther from the track. R_{he} value depends on R_{max}, V_{max}, and P_c; which may differ for different hurricanes. Since high wind speeds are more important in hurricane modeling, and the fact that the least reported speed by NHC is 34 kn, it is wise to assume that the maximum of R_{he} can be equal to ~R_{34}. Values of R_{34} in 12 snapshots of the Hurricanes Lili, Ivan, Katrina, Gustav and Ike are illustrated in Figure 8. As an example, for Hurricane Ivan, the values of R_{34} varied from 300 to 400 km; hence R_{he} in Hurricane Ivan can be selected as 400 km. With an average of R_{34} from all snapshots, it is possible to determine R_{he} for each hurricane. The values of R_{he} for the Hurricanes Lili, Ivan, Katrina, Gustav and Ike during the time period that these hurricanes were active in the Gulf of Mexico are selected as 300, 400, 350, 350 and 450 km. The Hurricanes Ivan and Ike have the largest range of effect, while hurricanes Lili and Gustav have the least impacted range in the Gulf of Mexico.

In Figure 9, the wind speeds extracted from NCEP/NARR and H*Wind at certain times for different hurricanes were compared with wind speeds calculated by the H10 model. NCEP/NARR is an atmospheric dynamical model which employs regional data for assimilation.

Resolution of wind data for NCEP/NARR, H*Wind and analytical models are 0.3°, 0.0542° and 0.01° respectively (an arbitrary value for the analytical model used here). NCEP/NARR was less accurate than H*Wind data and analytical models during high speeds, most likely due to its

Table 3 Bias values corresponding to different k_m values in analytical models at locations of buoys in the Gulf of Mexico during all hurricanes.

	NDBC-All buoys – Hurricane Lili						NDBC-All buoys – Hurricane Ivan						NDBC-All buoys – Hurricane Katrina					
	H80	S92	W06	K07	H10	E11	W13	H80	S92	W06	K07	H10	E11	W13	H80	S92	W06	K07	H10	E11	W13
k_m	1.0	1.0	1.0	1.0	1.0	1.0	1.0	1.0	1.0	1.0	1.0	1.0	1.0	1.0	1.0	1.0	1.0	1.0	1.0	1.0	1.0
BIAS (m/s)	1.1	−3.7	−3.4	−1.2	0.9	−3.3	1.8	2.2	−1.2	−2.8	−1.6	2.5	−2.3	1.2	1.3	−2.7	−2.5	−2.3	0.8	−3.3	0.6
Calibrated k_m	0.9	1.2	1.2	1.2	0.9	1.2	0.9	0.9	1.2	1.2	1.2	0.9	1.2	0.9	0.9	1.2	1.2	1.2	0.9	1.2	0.9
BIAS	−0.6	−2.8	−2.5	0.4	−0.3	−2.4	0.9	1.2	−0.6	−1.7	−1.0	1.3	−1.6	−0.1	0.4	−1.5	−1.4	−1.2	0.02	−2.0	−0.5
	NDBC-All buoys – Hurricane Ike							NDBC-All buoys – Hurricane Gustav													
	H80	S92	W06	K07	H10	E11	W13	H80	S92	W06	K07	H10	E11	W13							
k_m	1.0	1.0	1.0	1.0	1.0	1.0	1.0	1.0	1.0	1.0	1.0	1.0	1.0	1.0							
BIAS	3.6	−3.9	−3.5	−2.1	0.8	−4.1	0.6	−1.4	−6.2	−4.3	−3.1	−1.4	−6.5	−0.4							
Calibrated k_m	0.9	1.2	1.2	1.2	0.9	1.2	0.9	0.9	1.2	1.2	1.2	0.9	1.2	0.9							
BIAS (m/s)	2.2	−2.6	−2.0	−0.9	−0.2	−2.7	−0.1	−1.7	−4.9	−3.0	−1.6	−1.7	−5.1	−1.2							

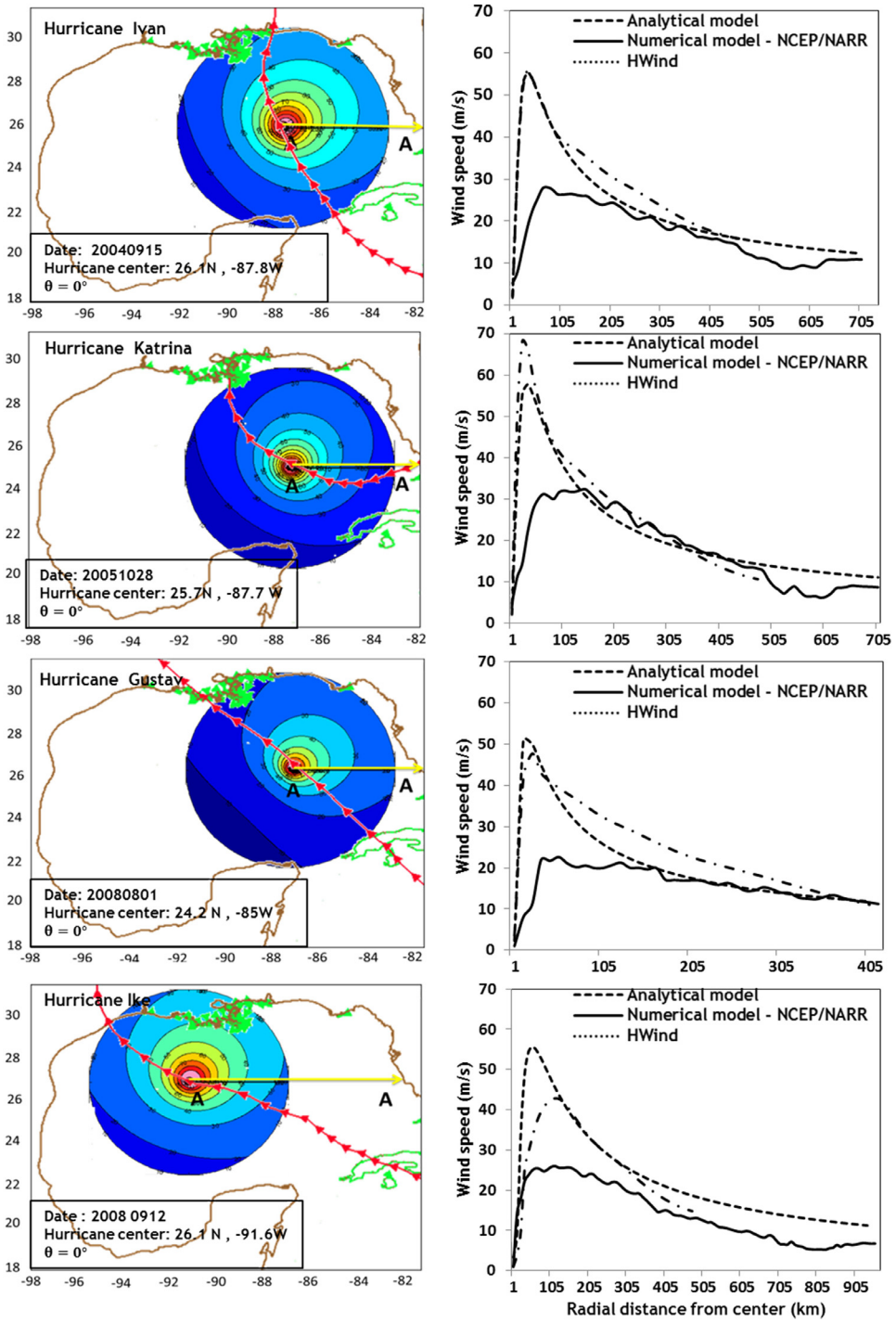

Figure 9 Comparison of the wind velocities produced by the analytical model (H10), numerical model (NCEP/NARR) and H*Wind during at 09/15/2004 (Hurricane Ivan), 10/25/2005 (Hurricane Katrina), 08/31/2008 (Hurricane Gustav) and 09/12/2008 (Hurricane Ike).

coarser spatial resolution; e.g. the V_{max} of H10 and H*Wind for Hurricane Ivan at 0900 UTC 15 September 2004 was 120 kn and 116 kn while corresponding value from NCEP/NARR was 100 kn. Therefore, NCEP/NARR data are not suitable close to R_{max}. There is also a fair agreement between calibrated H10 model and high resolution H*Wind data. Note that H*Wind data are available up to a radius of 480 km from the center of the hurricane, which is roughly equivalent to the value of R_{he}. This figure shows that when the high quality wind field is desired during a hurricane passage, e.g. for a wave simulation, one might adopt an analytical relationship or H*Wind from the center of hurricane up to $r = R_{he}$, and blend it with wind velocity values from model simulations such as *NCEP/NARR* or *ECMWF* database when $r > R_{he}$ to capture the effect of wind dynamics close to the hurricane center.

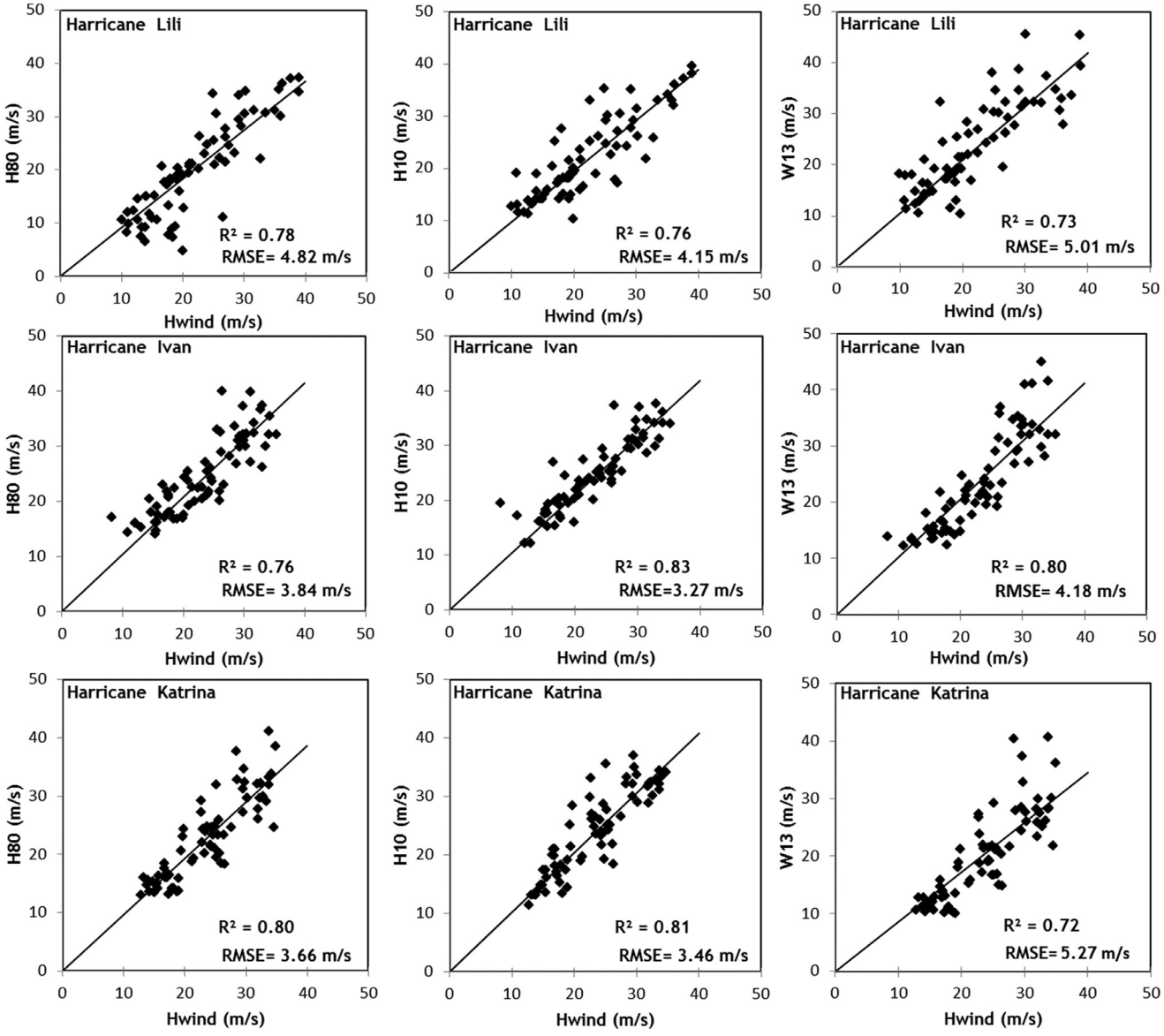

Figure 10 Scatter plot of wind velocities produced by H*Wind versus H80, H10 and W13 models for 12 points along the tracks of Hurricanes Lili, Ivan and Katrina.

4.5. Assessment of analytical models using H*Wind data

H*Wind is one of the most reliable data to describe the wind structure during tropical storm. Atlantic Oceanographic and Meteorological Laboratory combines all surface wind data measured from sea, land, and air (using by either a satellite or an airplane) during the course of a hurricane to produce H*Wind. A moving box with the center located at the center of the hurricane and side length of 2°, 4°, or 8° can be extracted including storm-induced wind velocity data with spatial resolution of 0.0542° and temporal resolution of at least six-hour (Powell and Houston, 1998; Powell et al., 1998). In section 4.3, it has been shown that the analytical models H80, H10 and W13 can better simulate the tropical storm-induced wind field in the Gulf of Mexico compared to other analytical models. To select the most appropriate analytical models in the Gulf of Mexico, the simulated wind speed data from the models H80, H10 and W13 were compared with the H*Wind data. For this purpose, 12 points along the track of each hurricane were selected in four quadrants (NE, SE, SW, NW). Then, wind velocities at different wind radii were extracted from H*Wind corresponding to each point from the center of the hurricane, and compared to wind speed predicted by analytical models. Scatter plots including coefficient of determination (R^2) and RMSE for the Hurricanes Lili, Ivan and Katrina are shown in Figure 10. There is a good agreement between the results of the analytical models and H*Wind model for all hurricanes; however the H10 model outperforms other models when compared to the H*Wind data. For instance, in the case of Hurricane Ivan, RMSE values for H80, H10 and W13 models were 3.84, 3.27 and 4.18 m/s and R^2 values were 0.76, 0.83 and 0.83, respectively.

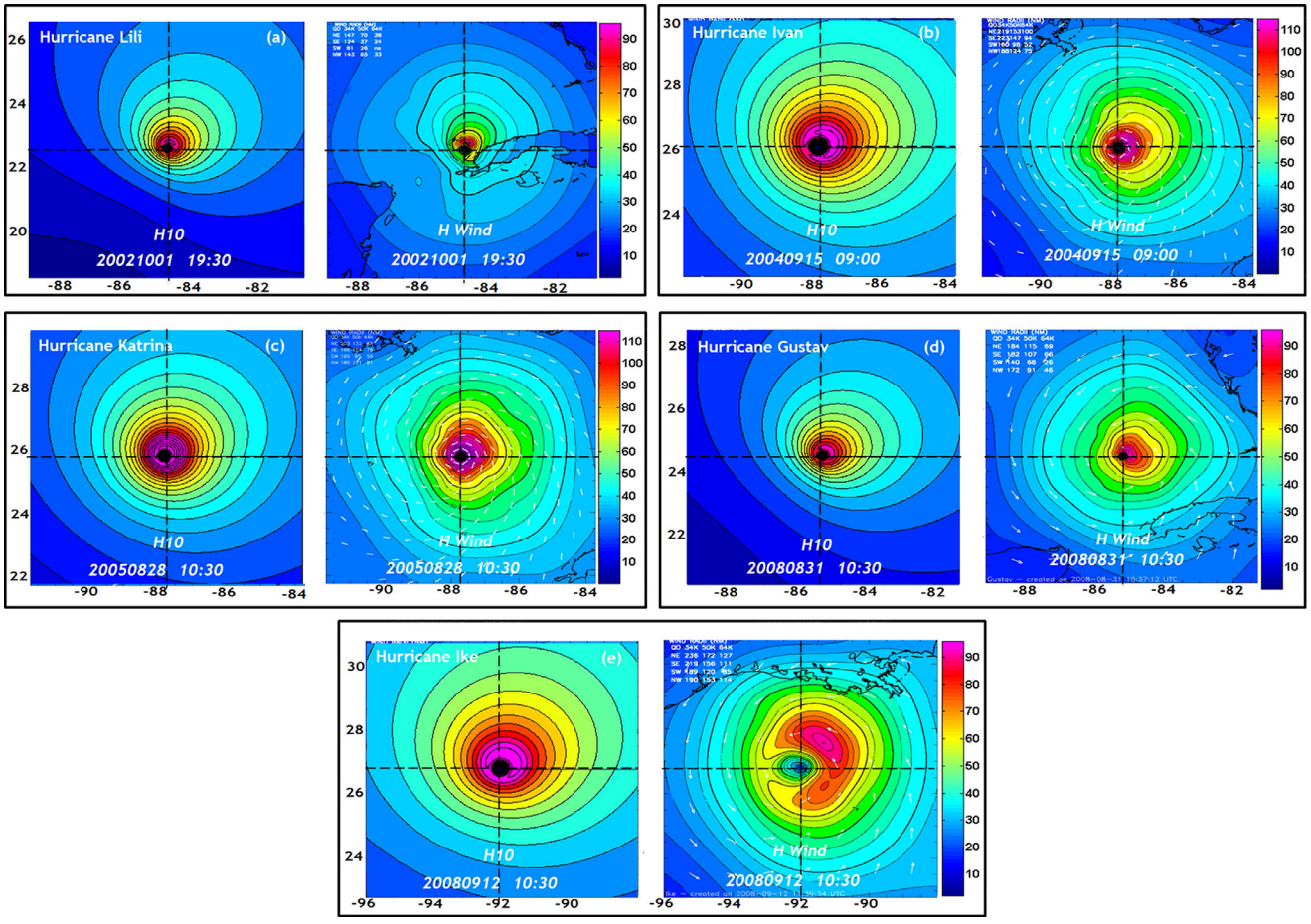

Figure 11 Comparisons of H*Wind distributions and H10 model wind fields during (a) Hurricane Lili at 19:30 UTC, 10/01/2002 (b) Hurricane Ivan at 09:00 UTC, 09/15/2004 (c) Hurricane Katrina at 12:00 UTC, 10/28/2005 (d) Hurricane Gustav at 10:30 UTC, 08/31/2008 (e) Hurricane Ike at 10:30 UTC, 09/12/2008.

Figure 11 displays surface wind fields computed using H10 model as the most appropriate analytical models when compared to H*Wind during different hurricanes. Note that analytical models such as H10 are calibrated based on NHC observed data at four points across the hurricane at limited number of radii (R_{34}, R_{50} and R_{64}), while the H*Wind model is developed based on data measured across the entire hurricane. Hence, a more detailed shape of a hurricane is expected from H*Wind model rather than from parametric models such as H10. A fair agreement was observed between results of H10 model and those of H*Wind model in all hurricanes. In general, for locations across the hurricane, where $r > R_{max}$, the wind velocity obtained from H*Wind model was higher than that estimated by H10 model. V_{max} is one of the most important parameters when comparing an analytical model like H10 to the H*Wind model. Table 4 shows the values of V_{max} were close for both methods during different hurricanes.

Table 4 Comparison of the maximum wind velocity produced by H*Wind and H10 model at times shown in Figure 11.

Hurricane	Model	V_{max} (kn)
Hurricane	H*Wind	94
Lili	H10	92
Hurricane	H*Wind	116
Ivan	H10	115
Hurricane	H*Wind	139
Katrina	H10	138
Hurricane	H*Wind	99
Gustav	H10	96
Hurricane	H*Wind	92
Ike	H10	98

5. Conclusions

Hurricane-generated wind field in the Gulf of Mexico was simulated using a series of analytical models. The B parameter and R_{max} are considered as control parameters for simulating a hurricane; and as a first step, the different methods for determining R_{max} have been compared to determine the most appropriate model for the region. Seven different analytical models, viz., H80, S92, W06, K07, H10,

E11 and W13 have been assessed based on buoys' observations and H*Wind data. The important findings of this research are summarized as follows:

- Increasing B would also increase V_{max} at R_{max} and decrease the wind speed away from R_{max}; hence, at every instant along a hurricane track and having distinct P_c, V_{max} and R_{max}, there is a unique value for B parameter, which provides a more realistic illustration of the wind field in the hurricane. Note that H80 proposed 1 to 2.5 as an acceptable range for B parameter.
- Five analytical models including G59, K05, X06, K07 and T12 were evaluated to calculate R_{max}. Among these methods, the X06 formulation provided the best performance when compared with H*Wind data. Therefore, X06 method is recommended for calculating R_{max} in the Gulf of Mexico.
- Comparison between the results of analytical models and the observed wind velocity data at seven buoy locations across Gulf of Mexico showed that there is a fair agreement between the analytical models and observed data. The models proposed by S92, W06, K07, and E11 relatively underestimated the wind velocity, while those proposed by H80, H10 and W13 slightly overestimated the storm-induced wind velocity. The linear regression was used between NHC and analytical data to calibrate k_m coefficient in the analytical model (see Eq. (1)). Hence, the value of k_m can be set to 1.2 in S92, W06, K07, E11 methods and 0.9 in H80, H10 and W13 methods, respectively.
- The results presented in this study suggested that the H10 model outperformed other methods in estimating wind field in the Gulf of Mexico.
- Comparison between analytical models with H*Wind data revealed that analytical models are able to produce sufficiently reliable wind velocity within a particular radius from the center of the hurricane (R_{he}). Based on the results of this study, R_{he} is estimated between 300 and 450 km.
- Dynamic wind models such as NCEP/NARR are not suitable for calculating high wind speeds close to hurricane eye due to their relatively coarse spatial resolution. On the other hand, the accuracy of the wind field estimated by analytical models degrades beyond R_{he}. Therefore, one might adopt an analytical model or H*Wind from the center of hurricane up to R_{he}, and blend it with wind velocities from dynamic models such as NCEP/NARR for $r > R_{he}$.
- It was found that there is a very good agreement between the results of the wind fields from the H10 and the H*Wind data. However; it underestimates the wind velocity when $r \gg R_{max}$.

Appendix 1: Algorithm to calculate the radius of the maximum wind

It was stated that R_{max} is the most important parameter affecting the results of analytical models. The stronger a hurricane, the larger its maximum wind radius will be. As stated in section 4.2, the method proposed by X06 is selected as a base for calculating R_{max} in this study. Note that Eq. (3) can be decomposed into two parts y_1 and y_2 as follows:

$$\begin{cases} y_1 = \left(V_r + \frac{rf}{2}\right)^2 - \frac{\rho_a}{B(P_n - P_c)}\left(\frac{rf}{2}\right)^2 \\ y_2 = \left(\frac{R_{\max(\theta)}}{r}\right)^B \exp\left[\left(-\frac{R_{\max(\theta)}}{r}\right)\right]^B \end{cases}. \quad (18)$$

In the above equations, the term $(y_1 - y_2)^2$ would be minimized at a particular R_{max} for each pair of r and V_r in dataset. Substituting the values of 34, 50, 64 kn as V_r (1 kn = 0.5144 m/s) and R_{34}, R_{50} and R_{64} as r (1 nm = 1.85 km), the R_{max} can be obtained in each of the four quadrants of the hurricane. For example, the R_{max} values computed at four quadrants in Hurricane Ivan at 0900 UTC 15 September 2004 were 47.12, 38.72, 28.65 and 43.67 n mi for NE, SE, SW and NW. These values should be interpolated to determine R_{max} at any point around the center of the hurricane. Following X06, a polynomial function was used (see Eq. (19)). The R_{max} values at angles of 45°, 135°, 225° and 335°, and the condition of R_{max} (0) = R_{max} (360) can be used to determine the coefficients ($i = 1–5$, Pi)

$$R_{max}(\theta) = P_1\theta^{n-1} + P_2\theta^{n-2} + \ldots + P_{n-1}\theta + P_n. \quad (19)$$

References

Atkinson, G.D., Holliday, C.R., 1977. Tropical cyclone minimum sea level pressure/maximum sustained wind relationship for the western North Pacific. Mon. Weather Rev. 105, 421–427.

Brenner, S., Gertman, I., Murashkovsky, A., 2007. Preoperational ocean forecasting in the southeastern Mediterranean Sea: Implementation and evaluation of the models and selection of the atmospheric forcing. Mar. Sys. 65, 268–287.

Cavaleri, L., Sclavo, M., 2006. The calibration of wind and wave model data in the Mediterranean Sea. Coast. Eng. 53, 613–627.

Chavas, D.R., Lin, N., Emanuel, K., 2015. A model for the complete radial structure of the tropical cyclone wind field. Part I: Comparison with observed structure. J. Atmos. Sci. 72, 3647–3662.

Chen, Y., Brunet, G., Yau, M., 2003. Spiral bands in a simulated hurricane. Part II: Wave activity diagnostics. J. Atmos. Sci 60, 1239–1256.

DeMaria, M., Kaplan, J., 1994. A statistical hurricane intensity prediction scheme (SHIPS) for the Atlantic basin. Weather Forecast 9, 209–220.

Depperman, R.C.E., 1947. Notes on the origin and structures of Philippine typhoons. B. Am. Meteorol. Soc. 28, 399–404.

Dvorak, V.F., 1975. Tropical cyclone intensity analysis and forecasting from satellite imagery. Mon. Weather Rev. 103, 420–430.

Emanuel, K. , 2004. Tropical cyclone energetics and structure. In: Fedorovich, E., Rotunno, R., Stevens, B. (Eds.), Atmospheric Turbulence and Mesoscale Meteorology 165–192.

Emanuel, K., Rotunno, R., 2011. Self-Stratification of Tropical Cyclone Outflow. Part I: Implications for Storm Structure. J. Atmos. Sci. 68, 2236–2249.

Graham, H.E., Nunn, D.E. , 1959. Meteorological Considerations Pertinent to. Standard Project Hurricane, Atlantic and Gulf Coasts of the United States. Weather Bureau, U.S. Department of Commerce, Washington, D.C., 317 pp.

Harper, B., 2002. Tropical cyclone parameter estimation in the Australian region: wind pressure relationships and related issues for engineering planning and design, Rep. no. J0106-PR003E, Woodside Energy, Ltd., 92 pp.

Holland, G., 2008. A revised hurricane pressure—wind model. Mon. Weather Rev. 136, 3432—3445.
Holland, G.J., 1980. An analytic model of the wind and pressure profiles in hurricanes. Mon. Weather Rev. 108, 1212—1218.
Holland, G.J., Belanger, J.I., Fritz, A., 2010. A revised model for radial profiles of hurricane winds. Mon. Weather Rev. 138, 4393—4401.
Houston, S.H., Shaffer, W.A., Powell, M.D., Chen, J., 1999. Comparisons of HRD and SLOSH surface wind fields in hurricanes: Implications for storm surge modeling. Weather Forecast 14, 671—686.
Hu, K., Chen, Q., Kimball, S.K., 2012. Consistency in hurricane surface wind forecasting: an improved parametric model. Nat. Hazards 61, 1029—1050.
Hughes, A.L., 1952. On the low level wind structure of tropical cyclones. J. Meteaor. 9, 422—428.
Jelesnianski, C.P., Taylor, A.D., 1973. A preliminary view of storm surges before and after storm modifications. In: Environmental Research Laboratories. Weather Modification Program Office, Boulder, C.O., p. 33.
Jelesniansky, C.P., 1967. Numerical Computations of Storm Surges With Bottom Stress. Mon. Weather Rev. 95, 740—756.
Jelesniansky, C.P., 1992. SLOSH: Sea, lake, and overland surges from hurricanes. NOAA Technical Rep. NWS 48, US Dept. Commerce, NOAA, NWS, Alice Springs MD, 73 pp.
Kawai, H., Honda, K., Tomita, T., Kakinuma, T., 2005. Characteristic of Typhoons in 2004 and Forecasting and Hindcasting of Their Storm Surges. Tech. Note Port and Airport Res. Inst., No 1103, 34 pp.
Knaff, J.A., Sampson, C.R., DeMaria, M., Marchok, T.P., Gross, J.M., McAdie, C.J., 2007. Statistical tropical cyclone wind radii prediction using climatology and persistence. Weather Forecast 22, 781—791.
Knaff, J.A., Zehr, R.M., 2007. Reexamination of tropical cyclone wind—pressure relationships. Weather Forecast 22, 71—88.
Levinson, D., Vickery, P., Resio, D., 2010. A review of the climatological characteristics of landfalling Gulf hurricanes for wind, wave, and surge hazard estimation. Ocean Engin. 37, 13—25.
Lin, N., Chavas, D., 2012. On hurricane parametric wind and applications in storm surge modeling. J. Geophys. Res.-Atmos. 117, art. no D09120, 19 pp., https://doi.org/10.1029/2011JD017126.
Mattocks, C., Forbes, C., 2008. A real-time, event-triggered storm surge forecasting system for the state of North Carolina. Ocean Model 25, 95—119.
Mazaheri, S., Kamranzad, B., Hajivalie, F., 2013. Modification of 32 years ECMWF wind field using QuikSCAT data for wave hindcasting in Iranian Seas. J. Coast. Res. 65, 344—350.
Moeini, M., Etemad-Shahidi, A., Chegini, V., 2010. Wave modeling and extreme value analysis off the northern coast of the Persian Gulf. Appl. Ocean Res. 32, 209—218.
Pan, Y., Chen, Y.-P., Li, J.-X., Ding, X.-l., 2016. Improvement of wind field hindcasts for tropical cyclones. Water Sci. Eng. 9, 58—66.
Phadke, A.C., Martino, C.D., Cheung, K.F., Houston, S.H., 2003. Modeling of tropical cyclone winds and waves for emergency management. Ocean Eng. 30, 553—578.
Powell, M.D., 1980. Evaluations of diagnostic marine boundary-layer models applied to hurricanes. Mon. Weather Rev. 108, 757—766.
Powell, M.D., Dodge, P.P., Black, M.L., 1991. The landfall of Hurricane Hugo in the Carolinas: Surface wind distribution. Weather Forecast 6, 379—399.
Powell, M.D., Houston, S.H., 1998. Surface wind fields of 1995 hurricanes Erin, Opal, Luis, Marilyn, and Roxanne at landfall. Mon. Weather Rev. 126, 1259—1273.
Powell, M.D., Houston, S.H., Amat, L.R., Morisseau-Leroy, N., 1998. The HRD real-time hurricane wind analysis system. J. Wind Eng. Industrial Aerodynam. 77—78, 53—64.
Schloemer, R.W., 1954. Analysis and synthesis of hurricane wind patterns over Lake Okeechobee, Florida. Hydrometeorological Rep. 31, Department of Commerce and U.S. Army Corps of Engineers, U.S. Weather Bureau, Washington, DC, 49 pp.
Siadatmousavi, S., Jose, F., Stone, G., 2009. Simulating Hurricane Gustav and Ike wave fields along the Louisiana inner shelf: Implementation of an unstructured third-generation wave model, SWAN. In: Proc. Oceans 2009 Conf., 873—880.
Signell, R.P., Carniel, S., Cavaleri, L., Chiggiato, J., Doyle, J.D., Pullen, J., Sclavo, M., 2005. Assessment of wind quality for oceanographic modelling in semi-enclosed basins. J. Mar. Syst. 53, 217—233.
Takagi, H., Nguyen, D., Esteban, M., Tran, T., Knaepen, H.L., Mikami, T., 2012. Vulnerability of coastal areas in Southern Vietnam against tropical cyclones and storm surges. In: The 4th International Conference on Estuaries and Coasts (ICEC2012), 8 pp.
Wijnands, J.S., Qian, G., Kuleshov, Y., 2016. Spline-based modelling of near-surface wind speeds in tropical cyclones. Appl. Math. Model. 40, 8685—8707.
Willoughby, H., Darling, R., Rahn, M., 2006. Parametric representation of the primary hurricane vortex. Part II: A new family of sectionally continuous profiles. Mon. Weather Rev. 134, 1102—1120.
Wood, V.T., White, L.W., 2011. A new parametric model of vortex tangential-wind profiles: Development, testing, and verification. J. Atmos. Sci. 68, 990—1006.
Wood, V.T., White, L.W., Willoughby, H.E., Jorgensen, D.P., 2013. A new parametric tropical cyclone tangential wind profile model. Mon. Weather Rev. 141, 1884—1909.
Xie, L., Bao, S., Pietrafesa, L.J., Foley, K., Fuentes, M., 2006. A real-time hurricane surface wind forecasting model: Formulation and verification. Mon. Weather Rev. 134, 1355—1370.

Oceanologia (2020) 62, 190—199

Available online at www.sciencedirect.com

ScienceDirect

journal homepage: www.journals.elsevier.com/oceanologia

ORIGINAL RESEARCH ARTICLE

Influence of the climatic variations in the wind waves parameters on the alongshore sediment transport

Boris V. Divinsky*, **Ruben D. Kosyan**

Shirshov Institute of Oceanology RAS, Moscow, Russia

Received 9 September 2019; accepted 25 November 2019
Available online 7 December 2019

KEYWORDS
Black Sea;
Sediment transport;
Wind waves;
Swell;
Numerical modeling

Summary The purpose of this work was to analyze the influence of climatic variability of wind waves and swell parameters in the coastal zone on the sediment transport and to assess the contribution of the swell to the formation of alongshore fluxes. The object of research is the Anapa bay-bar (the Black Sea). Mathematical modeling has shown that in the Anapa bay-bar area the average annual wind waves and swell powers have significant interannual variability. For the period from 1979 to 2017, in the southern part of the bay-bar, there was a statistically significant decrease in the share of swell in the alongshore transport, directed from NW to SE, in the central part — an increase in the contribution of swell to the total sediment flow from SE to NW, in the northern part — probable increase in flows to NW and decrease — to SE. Such a dynamic is consistent, in general, with experimental observations of the processes of erosion and accumulation of beach-forming material along the Anapa bay-bar coastline. A separate description of the bottom sediment fluxes under the influence of wind waves and swell made it possible to explain the fluctuations of the coastline over a climatic period.

1. Introduction

The hydrodynamic regime of coastal waters forms significant alongshore sediment flows responsible for erosion or accumulation of sediments in the coastal zone, as well as the transformation of the coastline. The main element of the hydrodynamic effect is wind waves, and a common practice is to present the characteristics of the wave field as a set of integral parameters (significant wave height, mean period, general direction of propagation). Such an approach is justified in the conditions of a uniform wave

* Corresponding author at: Shirshov Institute of Oceanology Russian Academy of Sciences, 117997, 36 Nakhimovskiy pr., Moscow, Russia, Tel.: +7 918 4567922.
E-mail address: divin@ocean.ru (B.V. Divinsky).
Peer review under the responsibility of the Institute of Oceanology of the Polish Academy of Sciences.

Production and hosting by Elsevier

https://doi.org/10.1016/j.oceano.2019.11.002

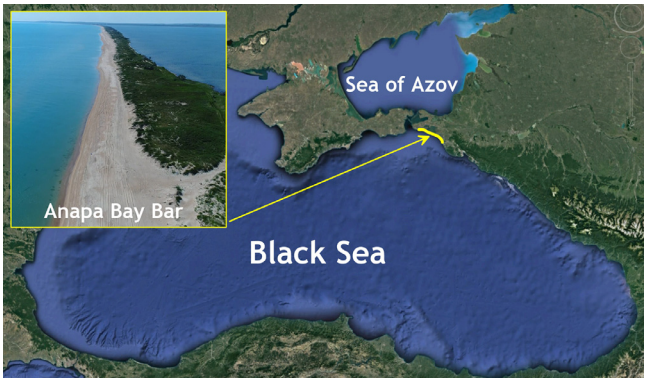

Figure 1 Geographic location of the Anapa bay-bar.

field. If the wave spectrum is formed as a result of the interaction of several wave systems (pure wind waves and swell), then it seems quite natural to obtain separate wave statistics for each of them. The division of the wave-field into separate components allows us to more correctly describe the spatial-temporal structure of the surface waves, and significantly clarify the patterns of redistribution and transport of bottom sediments in the shelf zone.

An analysis of the alongshore sediment transport under the influence of wind waves and swell has attracted the attention of several research groups. Note some publications. In the work (Chowdhury and Behera, 2017) for the western coast of India, long-period fluctuations in the parameters of surface waves and the associated alongshore fluxes of bottom sediments are analyzed. The dominant role of swell waves in the formation of these fluxes is shown. Similar results were obtained in (Almar et al., 2015) for the conditions of the Gulf of Guinea (West Africa). The paper (Bertin et al., 2008) showed that an incorrect description of the initial wave climate (in particular, neglect of swell) can lead to significant distortions in the estimates of multidirectional alongshore flows.

The main goal of this work is to analyze the climatic variability of wind waves and swell parameters, as well as alongshore sediment flows in the coastal zone.

The object of research is the Anapa bay-bar, located in the northeastern part of the Black Sea and representing an open section of the coast with a total length of about 40 km (Fig. 1). The bottom is almost uniformly sloped in the seaward part and with a pronounced system of underwater bars at depths less than 6 m. The general trend in the dynamics of the Anapa bay-bar beaches is the almost universal reduction of their width caused by both natural and anthropogenic factors (Kosyan et al., 2011; Krylenko et al., 2011).

Natural factors include climatic fluctuations of wind-wave parameters, which determine the strength and duration of hydrodynamic effects. Based on this, we define the objectives of this study: analysis of the variability of the main parameters of wind waves and swell from 1979 to 2017 in the coastal zone of Anapa bay-bar; calculation of alongshore fluxes of bottom material caused by wind waves and swell; evaluation of the contribution of swell to the formation of alongshore fluxes.

2. Material and methods

2.1. Spectral wave model

A modern tool for studying the parameters of surface waves is mathematical modeling, which makes it possible to calculate the parameters of sea waves for any period of time from the initial wind fields. For modeling the transformation of the wave field, the modern spectral model DHI MIKE SW (DHI, 2007) has been used, which is successfully used both in open water areas and in the coastal zone. The model was successfully verified for the conditions of the Black Sea (Divinsky and Kosyan, 2017) and configured to automatically separate the components of surface waves (Divinsky and Kosyan, 2018).

As a result of the calculations, we obtained time series of the main parameters of wind waves and swell in the coastal zone of Anapa bay-bar (significant wave heights, peak periods of the spectrum, directions of propagation) for the period from January 1979 to December 2017 (time resolution – 1 hour). In addition to the basic parameters, wind waves and swell have been calculated. In deep water, the power of irregular wind waves is estimated by the expression (Boyle, 2004):

$$E = \frac{\rho g^2}{64\pi} h_s^2 t_e \approx \left(0.5 \frac{kW}{m^3 \cdot s}\right) h_s^2 t_e, \quad (1)$$

where h_s is a significant wave height; t_e is the energy period of the waves, which is equal to the peak period of the spectrum; ρ is the density of water; g is the acceleration of gravity. If a significant wave height is represented in meters, the period is in seconds, then the power of the waves will be expressed in kilowatts per meter of a wavefront. Since significant wave heights and periods are determined through the moments of the energy spectrum, the assessment of wind power, of course, completely depends on the correctness and adequacy of the spectral model when reproducing all stages of wave development. Power, as a function of height and period, can be considered as an integral characteristic of storm waves.

2.2. Mathematical model of sediment transport

Studies of sediment transport in the coastal zone are carried out using a mathematical model that allows calculation of the flow of non-cohesive material under the influence of currents and wind waves. Sediment transport is presented in the form:

$$Q = \frac{l}{\rho} \int_0^h U_{mean} C(z) dz, \quad (2)$$

where l is the length of the profile under consideration, ρ is the sediment particles density, U_{mean} is the depth-averaged velocity of the alongshore flow, C is the concentration of suspended substances (g/l), h is the depth. The averaged velocity of the coastal current is estimated by the formula (Longuet-Higgins, 1970):

$$U_{mean} = 0.25 k_v \sqrt{\gamma_b g H_b} \sin 2\alpha_b, \quad (3)$$

where k_v is a constant, γ_b is the breaking parameter, H_b is the height of waves at the point of wave breaking, α_b is the

angle between the normal to the coast and the wavefront at the point of wave breaking.

Some simplification of the considered approach is the neglect of the main (background) currents. Calculation of the parameters of sea currents is a separate big task and requires setting additional characteristics of both the atmosphere (temperature, humidity, radiation, etc.) and the sea (temperature, salinity). In addition, questions arise for the verification of such a model. Thus, in this study, we focus on the issues of wave impact on the coastal zone.

The parameters of the waves at the point of wave breaking are estimated by the method outlined in (Larson et al., 2009). The vertical concentration profile of suspended sediment is described by the formula:

$$C(z) = C(z_0)exp\left(-w_s \int_{z_0}^{h} \frac{dz}{\varepsilon(z)}\right), \quad (4)$$

where $C(z_0)$ is a concentration of suspended substances at a level z_0, z_0 is a roughness parameter, w_s is a grain settling velocity, $\varepsilon(z)$ is a generalized diffusion coefficient. The vertical profile is determined at the point of wave collapse, located, as a rule, above the underwater bar. At the lower limit of z_0, the suspension concentration is determined by the function of local suspension emission (Zou at al., 2005):

$$C(z_0) = 3.3\left(\frac{\theta - \theta_{cr}}{\theta_{cr}}\right)^{1.5} \frac{(s-1)^{0.6} g^{0.6} d_{50}}{\nu^{0.2}}, \quad (5)$$

where $s = \frac{\rho_s}{\rho}$ – relative sediment density, g – acceleration of gravity (m/s^2), ν – kinematic viscosity of water (m^2/s), d_{50} – median diameter of sand particles (m), θ – Schilds parameter, θ_{cr} – critical meaning of the Schields parameter, ε_z is a generalized diffusion coefficient. The value of the Schields parameter reflects the balance of the shear and holding forces:

$$\theta = \frac{u_*^2}{(\rho_s - \rho_s/\rho))gd_{50}}, \quad (6)$$

where u_* – maximum shear rate calculated by the method described in (Walton, 2002).

The sediment diffusion coefficient is considered variable vertically and is presented as (Kosyan, 1985):

$$\varepsilon(z) = \varepsilon_1(z) + \varepsilon_2(z). \quad (7)$$

The components of the right part of Eq. (7) determine the contribution: $\varepsilon_1(z)$ – of the orbital wave motion, $\varepsilon_2(z)$ – of the turbulent diffusion in the bottom layer. The contribution of the orbital wave motion is found from the relationship:

$$\varepsilon_1(z) = \frac{\pi H^2 \sin h^2 kz}{2\sqrt{2}T \sin h^2 kh}, \quad (8)$$

where H, T are height and wave period, k – wave number. Diffusion in the bottom layer is determined as follows:

$$\varepsilon_2(z) = \frac{b(u_g - w_s)\frac{z}{\delta}}{1 + 0.06\frac{z}{\delta}exp(\frac{z}{\delta})}, \quad (9)$$

where $b = 116(\frac{\rho}{\rho_s - \rho})(\frac{\nu^2}{g})^{\frac{1}{3}}$, u_g – maximum value of the bottom orbital velocity, δ – boundary layer thickness determined from the Johnson equation (Jonsson, 1966):

$$\frac{\delta}{z_0} lg\left(\frac{\delta}{z_0}\right) = 0.6\frac{H}{z_N \sinh(kh)}, \quad (10)$$

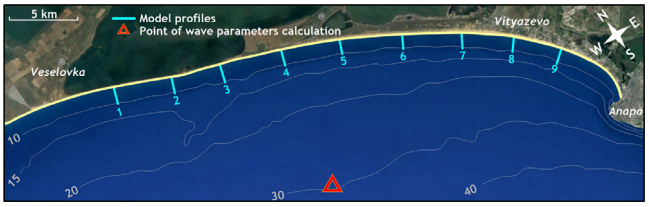

Figure 2 Position of the profiles normal to the shore and the point of calculation of wave parameters

where z_N is the effective roughness of the bottom, which is assumed to be $z_N = 2.5d_{50}$.

The main results of the calculations are the volumes of the along-shore sediment flows both within the selected storm event and integrated for the time interval of interest (a specific calendar year). The calculations were performed separately for the two main components of surface waves: wind waves and swell. The position of the normal to the coast profiles, for which the calculation of the along-shore flows is carried out, as well as the wave parameters calculation point, are shown in Fig. 2. Local bottom profiles for selected profiles are shown in Fig. 3.

The series of significant wave heights, average periods and directions of wave propagation (separately for wind waves and swell) serve as initial wave conditions for the model of transport of bottom sediments.

3. Modeling results

3.1. Wave climate

The wave climate of the coastal zone of Anapa bay-bar is characterized, in general, by the predominance of surface waves in two main directions: the north-east and south-west. Fig. 4 shows the wind waves, swell and mixed (summary) waves for the period 1979–2017.

The geographic location of the spit defines some peculiarities of the wave regime that facilitate the sediment transport: the openness of the coast for wind waves of southern and western points. Storm WSW and SW of directions cause heavy along-shore sediment fluxes, directed from NW to SE; the propagation of swell waves is limited to a wave sector between the southeast and southwest directions.

Based on this, for further analysis we will limit ourselves to 45-degree sectors: for wind waves – SSE (with the direction of waves from 135° to 180°), SSW (180°–225°), WSW (225°–270°), WNW (270°–315°); for swell – SSE, SSW, WSW.

For each wave sector for the period from 1979 to 2017, the average values of significant wave heights, the repeatability of the directions of the sector within the annual cycle, the average and maximum values of wave powers were calculated.

The resulting interannual variability of significant wave heights (averaged for each specific direction), frequency of propagation directions, average and maximum wind waves and swell capacities are presented in Figures 5 and 6.

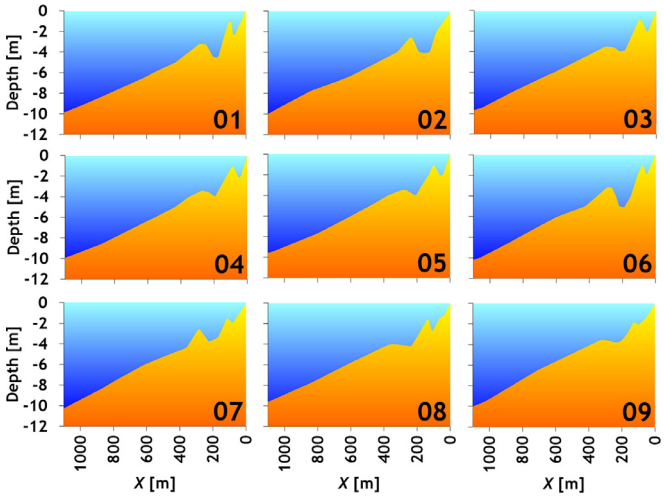

Figure 3 Local bottom profiles of the control sections.

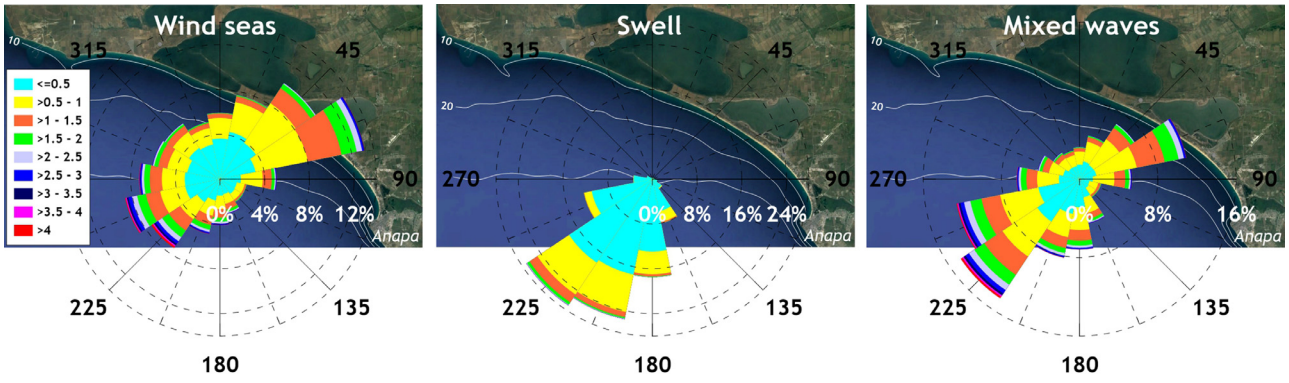

Figure 4 Roses of wind waves (in terms of significant wave heights, m) in the area of Anapa bay-bar for the last 39 years.

Table 1 Analysis of trends in the fluctuations of the parameters of wind waves and swell over a period 1979–2017.

Direction		Wind Waves				Swell		
		SSE	SSW	WSW	WNW	SSE	SSW	WSW
Test	**Occurrence**	Stable	Stable	Stable	No trend	**Increasing**	**Prob. De-creasing**	**Decreasing**
Interpretation								
	h_s	No trend	**Prob. in-creasing**	**Prob. in-creasing**	No trend	No trend	**Prob. in-creasing**	**Prob. in-creasing**
	P_{mean}	No trend	No trend	**Prob. in-creasing**	No trend	No trend	**Increasing**	No trend
	P_{max}	Stable	No trend	No trend	No trend	No trend	No trend	Stable

Let's note the following detail. Practically for all directions from 1979 to 2017, a decrease in the frequency of occurrence is observed along the directions of propagation, with a simultaneous increase in significant wave heights (averaged for specific directions). The only exception is the increased frequency of swell for the SSE sector, and this growth is not related to the local conditions of wave formation, but is determined by the overall strengthening of the eastern wind component for the entire Black Sea. The average power of wind waves in the coastal zone of the Anapa bay-bar is a few kW/m, which is quite a bit compared to other water bodies of the World Ocean. However, in some years, extreme storms with powers exceeding 300 kV/m were observed.

Since we are interested in the climatic characters of fluctuations in the characteristics of surface waves, we pose the question as follows: Are there any interannual stable trends in the variability of the parameters of wind waves and swell? To answer this question, we use the procedure detailed in (Aziz et al., 2003). This procedure implements

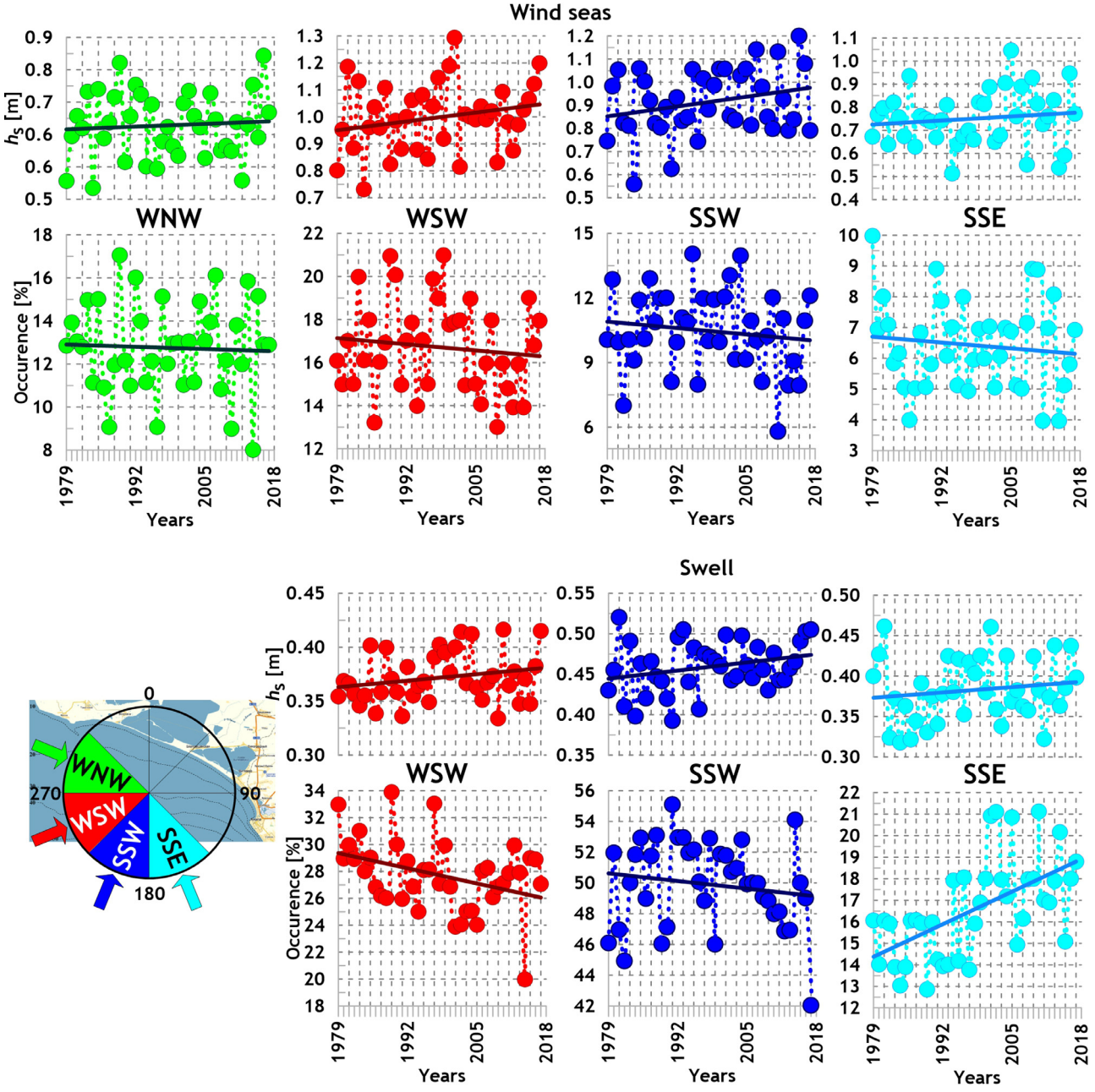

Figure 5 Interannual variations of averaged significant wave heights and the frequency of occurrence of wind waves and swell directions.

the non-parametric Mann-Kendall test. The method does not require knowledge of the law of distribution of initial values, and can also take into account the unevenness of the time scale and gaps in the data. The method considers three main statistical metrics:

- Mann-Kendall statistics (S). It is the sum of the differences in signs between consecutive values;
- confidence level (CF, Confidence Factor);
- coefficient of variation (COV, Coefficient of Variation).

The combination of these three metrics makes it possible to identify trend components in the initial data, as well as to evaluate the sign and statistical significance of trends. The final result is presented in terms of:

- increasing — S> 0 and CF> 95%;
- probably increasing — S> 0 and 90% <CF <95%;
- no trend — (S> 0 and CF <90%) or (S≤0 and CF <90% and COV≥1);
- stable — S≤0 and CF <90% and COV <1;
- probably decreasing — S <0 and 90% <CF <95%;
- decreasing — S <0 and CF> 95%.

Note that the differences between the terms “no trend” and “stable” relate only to the degree of data scatter in the absence of obvious trends. The results of the study of

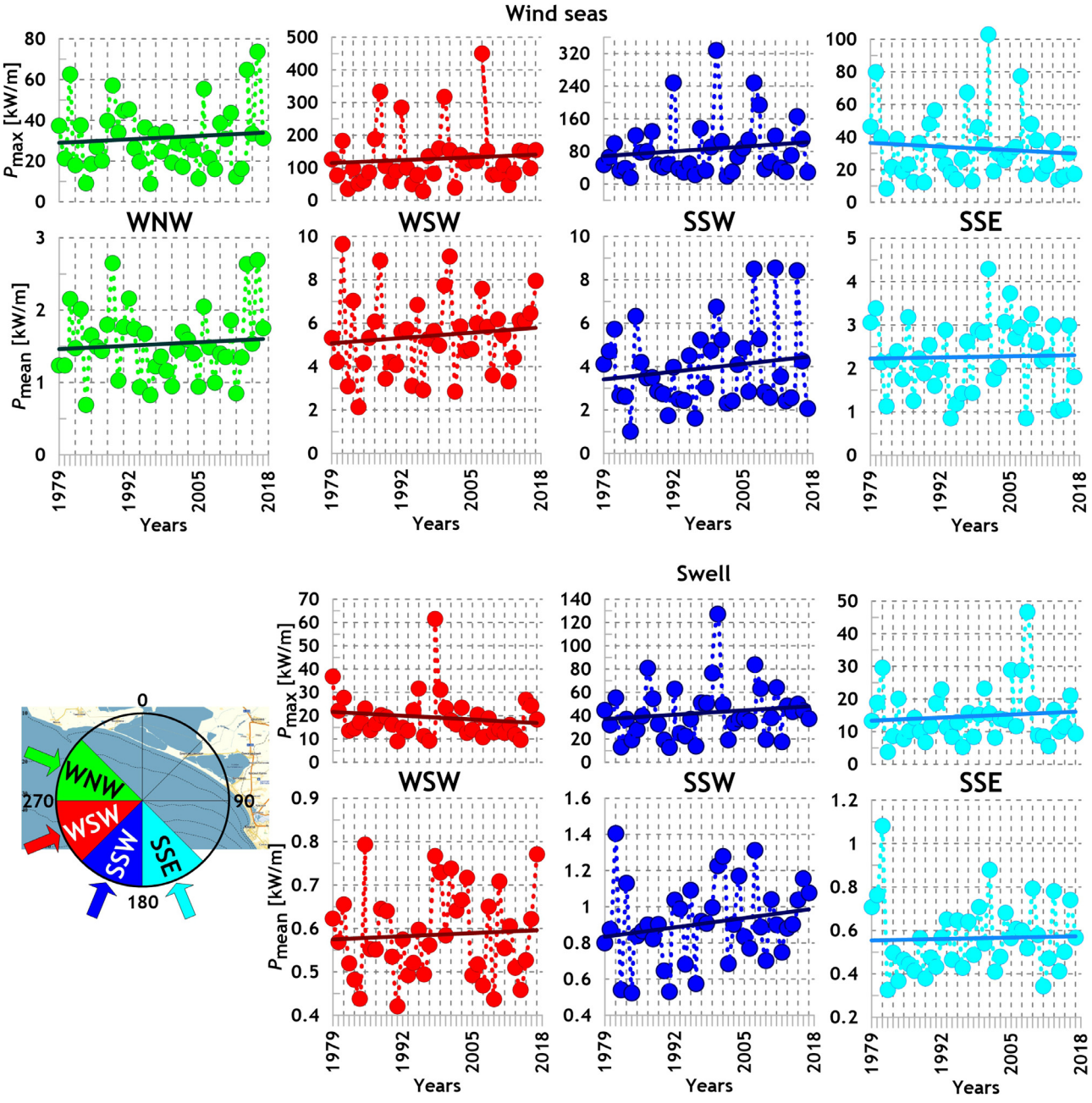

Figure 6 Interannual variations of the average annual and maximum values of the power of wind waves and swell.

possible trends in the interannual fluctuations of significant wave heights, wave frequency, average and maximum wave power are presented in Table 1.

As it follows from Table 1, the role of swell has been increasing in the coastal zone of Anapa bay-bar over the past 39 years. There are stable trends to an increase in the frequency of swelling of the SSE direction and a decrease — of the WSW directions. For the period from 1979 to 2017, an average power of swell of SSE directions increased. Note that the waves of this direction affect practically along the normal to the coast, reinforcing the transverse component of the transport of bottom sediments. Wind wave parameters show (in the climatic sense) greater stability; with some probability, one can speak only about an increase in the average heights of waves in the storms of the SSW and WSW directions, as well as the average power of the WSW sector. Linear climate trends are not revealed on the graphs of the maximum wind waves power and swell.

Next, we will try to assess the impact of the noted features of the wave climate on the bottom sediments transport.

3.2. Climatic flows of sand sediments along the Anapa Bay-bar

The result of the modeling was the integral annual estimates of the alongshore sandy flows in the coastal zone of Anapa bay-bar for the period from 1979 to 2017:

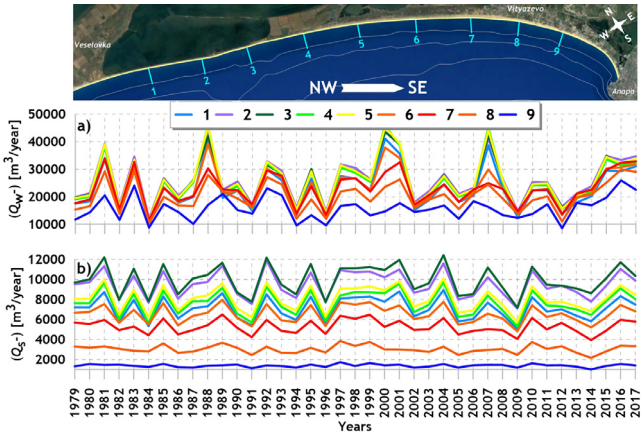

Figure 7 Alongshore flows (m^3/year) under the influence of wind waves (a) and swell (b), directed from NW to SE.

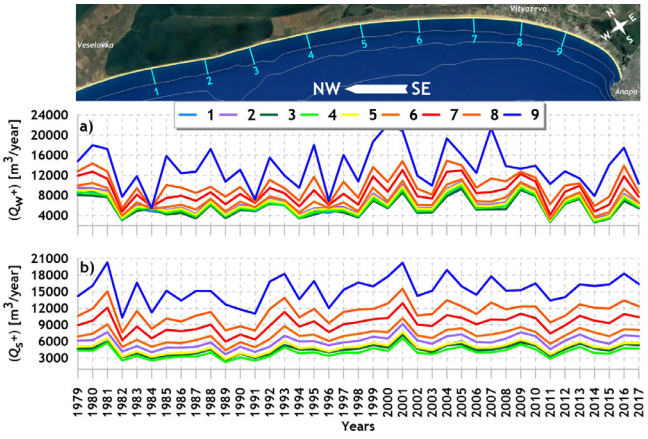

Figure 8 Alongshore flows (m^3/year) under the influence of wind waves (a) and swell (b), directed from SE to NW.

- average annual flows under the influence of wind waves (Qw-) and swell (Qs-), directed from the NW to the SE — Fig. 7;
- average annual flows under the influence of wind waves (Qw+) and swell (Qs+), directed from SE to NW — Fig. 8.

The strongest alongshore fluxes, caused by both wind waves and swell, were simulated for 1981, 1992, 2000, 2001, 2007 and 2016. At the same time, not only the power of storm waves but also the duration (repeatability) of storm conditions play a significant role in the formation of significant fluxes. For example, the streams of 1981, 1992, 2000 and 2017 were determined by extreme storms, the 2001 stream was their recurrence, and the 2016 stream was the recurrence of moderate power storms. Note also that the contribution of individual storms (as, for example, in January 2000 and November 2007) can be a quarter of the total annual sediment flow. As a result of one January 2000 storm, a swell formed, which transferred almost a third of the bottom material from the 2000 total balance. The average (i.e., characterizing the order of magnitude) volumes of material, moving along the coast, are: from the NW to the SE — 30000 m^3/year, from the SE to the NW — 12000 m^3/year.

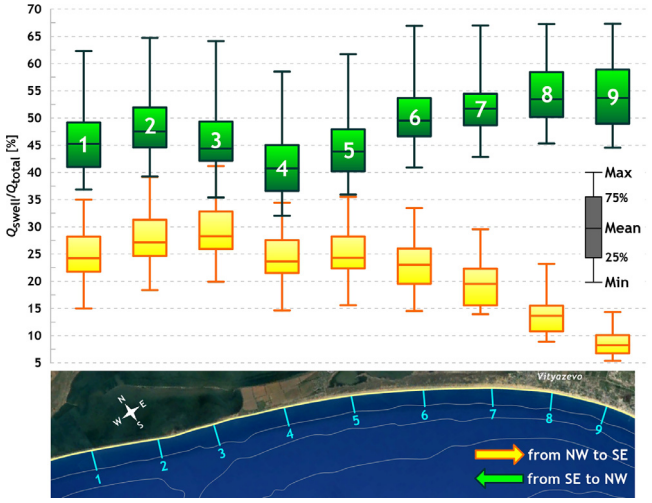

Figure 9 Contribution of swell to the formation of alongshore flows.

In some years, flows can increase (or decrease) by 2–2.5 times. A predominance of the sediment flow directed from the NW to SE is observed practically along the entire length of the bar. The exception is the southern part of the bar, adjacent to Anapa, which is characterized, on average, by the prevalence of flow from the SE to NW. A change in the sign of the general transfer is observed south of Vityazevo (Fig. 2). Strong interannual variability of flows is observed. In the northern part of the bar, the range of the interannual variations of the flows directed from NW to SE can reach about 30000 m^3/year. As moving south, the amplitude of the interannual fluctuations of these flows is significantly reduced.

For flows directed from SE to NW, the picture is reversed: the maximum interannual fluctuations appear in the southern part of the bay-bar and decrease as they move to the north.

4. Discussion

Thus, as a result of the modeling, estimates of the trend components in the fluctuations of the parameters of wind waves in the coastal zone over the climatic period of time. The values of the coastal fluxes of bottom sediments caused by wind waves and swell were obtained as well.

Let us estimate the contribution of swell waves to the formation of alongshore sediment flows. In Fig. 9, the statistical characteristics of the ratios of swell waves flows (Q_{swell}) to general flows (Q_{total}) are presented.

As it follows from Fig. 9, the influence of wind waves dominates in the fluxes directed from the NW to the SE. The contribution of the swell is ˜ 25% in the NW part of the coast and decreases to 6–7% in the SE part. For fluxes directed from SE to NW, the situation is reversed. In the SE part, the contribution of the swell, on average, exceeds 50% and only slightly decreases in NW direction. In some years, the alongshore flows directed from SE to NW can be almost completely determined by the swell impact (up to 67%). Under the conditions of the coastal zone of Anapa bay, the effect of wind waves and swell on the

Table 2 Analysis of linear trends in the share of swell in long-coastal transport of bottom sediments for the period 1979—2017.

Direction	Profiles								
	1	2	3	4	5	6	7	8	9
From NW to SE	**Probably decreas.**	Stable	Stable	Stable	Stable	**Decreas.**	**Decreas.**	**Decreas.**	**Probably decreas.**
From SE to NW	**Probably increas.**	**Probably increase.**	**Increas.**	**Increas.**	**Increas.**	No trend	No trend	No trend	No trend

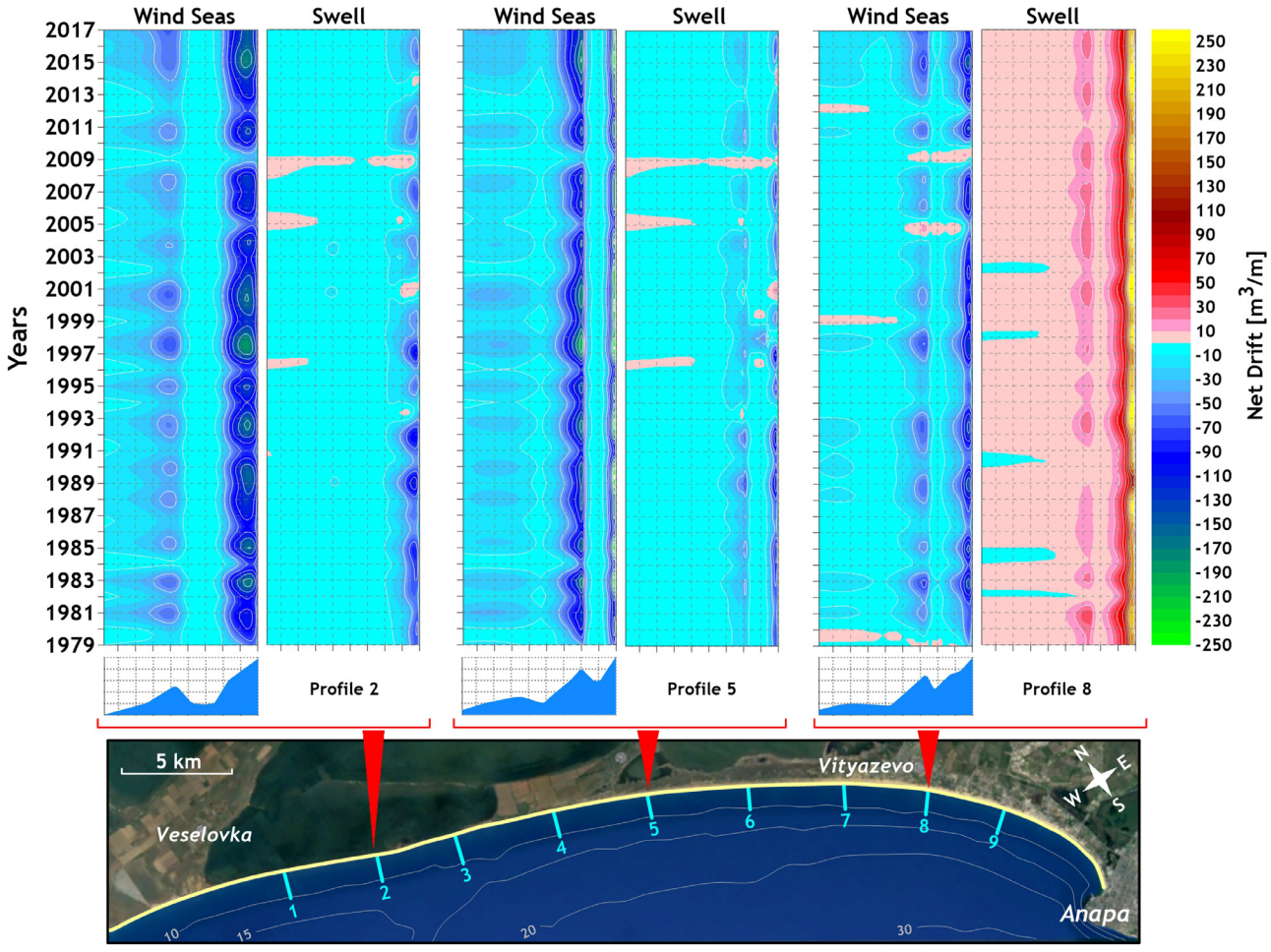

Figure 10 Average annual alongshore sediment flows for selected profiles.

underwater eroded slope is somewhat different. As a rule, the height of wind waves is 2—3 times greater than the height of swell waves. The breaking of wind waves leads to an increase in transverse transport of bottom material with the formation (transformation) of underwater bars and the removal of material towards the sea. The swell dissipates in the near wateredge zone and contributes to the sediments accumulation. Fig. 10 shows the average annual estimates of the resultant alongshore flows for three sections: in the northern part of the bay-bar (Section 2), central (Section 5) and southern (Section 8).

Positive values of flows correspond to flows directed from south-east to north-west, negative values — in the opposite direction. As follows from Fig. 10, sediment flows are confined to local peculiarities of underwater reliefs. In the northern part of the Anapa bay-bar, the main stream caused by wind waves develops in the near-edge zone, in the central one — in the area of the underwater bar, in the south - both in the bar area and in the splash zone. Fluxes under the influence of swell are formed, as a rule, in the near wateredge-zone.

Under the influence of wind waves, the resulting flows are almost always directed from NW to SE with a small exception: in 2005 and 2009, in the southern part of the bay-bar, the stream was directed to NW. The flows formed by the swell in the northern and central parts of the bar

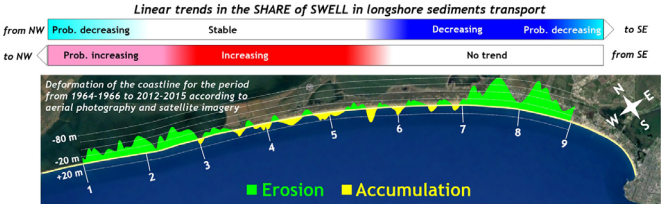

Figure 11 Deformation of the coastline of Anapa bay-bar for the period from 1964—1966 to 2012—2015 according to Krylenko (2015) and linear trends in the share of swell in longshore sediments transport.

are directed to the SE, in the southern — in the opposite direction. Using the Mann-Kendall test described above, we estimate whether the share of swell in the coastal sediment transport changed from 1979 to 2017. The test results are shown in Table 2.

As follows from Table 2, in the southern part of the bar there is a decrease in the share of swell in the alongshore transport, directed from NW to SE, in the central — increase in the contribution of swell to the total sediment flow from SE to NW, in the northern — likely increase inflows to the NW and weakening to SE. Using the data from Krylenko (2015), we reconstruct an averaged picture of the deformation of the Anapa shoreline over the last 50 years (Fig. 11).

Fig. 11 reflects the processes of the coastline erosion and accumulation, which occurred from the mid-1960s to the 2010s. During this period, the southern part of the bar has lost up to 80 meters of the beach, the northern part slightly less, about 20 m. Comparing Fig. 11 and data in Table 2 (and taking into account the uncertainties in both the processing of surface maps and modeling results), it can be noted that in the area of maximum coastal erosion in the southern part, there is a decrease in the percentage of swell in the alongshore transport. The central part of the bar is subject to the increasing influence of swell, which, possibly, is a factor of some stabilization. The stability of the beaches in the central part of the bay-bar can also be facilitated by the fact that the production of mass bivalve mollusks *Chamelea gallina* here has relatively higher values than in the northern part (Kosyan and Divinsky, 2019). Despite the fact that the maximum biomass of mollusks is noted in the southern part of the bar, the here produced carbonates can also be transported along the coastal sediment flow from SE to NW and serve as a source of the replenishment in the central part of the beaches. Linear climatic trends (of different signs) for the northern region of the burrs (Sections 1, 2) are present, although they are not so clearly expressed. Unambiguous interpretation of the results is hardly possible, but note that the erosion of the beaches in the northern region is not as catastrophic as in the southern.

5. Conclusions

The purpose of this work was to analyze the climatic variability of the parameters of wind waves and swell in the coastal zone of Anapa bay-bar, alongshore transport of bottom sediments, and to assess the contribution of swell to the formation of alongshore flows.

Main results:

1. In the Anapa bay-bar area, the average annual wind wave and swell powers experience fairly significant interannual variability. In this case, the average annual values of the wind wave power are 3—4 kW/m, swell — about 0.6—0.8 kW/m.
2. Over the past 39 years, the role of the swell has been increasing. There are steady trends to an increase in the frequency of swell of the SSE direction and a decrease in its frequency of occurrence of the WSW direction. For the period from 1979 to 2017, an average power of swell of SSE directions also increased.
3. In the alongshore flows of bottom material directed from NW to SE, the influence of wind waves dominates. The contribution of swell is ~25% in the NW part of the coast and significantly decreases in the SE part (up to 6—7%). For flows directed from SE to NW, the contribution of swell is rather stable. In the SE part, the contribution of swell, on average, exceeds 50% and somewhat decreases in the NW direction. Note that in some years, alongshore flows directed from SE to NW can be almost completely dominated by the impact of the swell waves (up to 67%).
4. For the period from 1979 to 2017, in the southern part of the bay-bar, there was a statistically significant decrease in the share of swell in the alongshore transport, directed from NW to SE; in the central part — an increase in the contribution of swell to the total sediment flow from SE to NW; in the northern part — probable increase inflows to NW and decrease to SE. Such dynamics is consistent, in general, with experimental observations of the processes of erosion and accumulation of beach-forming material along the Anapa bay-bar coastline.

Note that the conducted studies do not claim to be complete. In the general balance of sediments, many natural and anthropogenic factors play a significant role (depletion of natural sources of bottom material, removal of sand, development of dune space). Nevertheless, the obtained results allowed us to estimate climatic changes in the surface wave structure, as well as the effect of these changes on the characteristics of the coastal sediment transport.

We note one more important point. Obtained results concerning the role of swell waves in the formation of sediment transport features are obviously not universal. The open ocean coasts, for example, are accessible to swell formed at a considerable distance from the coast and not related to local atmospheric conditions. In this case, the swell power can be comparable and even exceed the power of wind waves. The impact of swell waves can determine both the amplitude and the resulting sign of the coastal currents. Perhaps our results, to some extent, will be characteristic

of other enclosed water areas (the Baltic Sea, for example), as further studies will show. One circumstance, perhaps, is undeniable: it is useful (and important) to know not only the parameters of surface waves, but also its structure.

Acknowledgments

This work was initialized by the Russian Foundation for Basic Research (RFBR), project no. 18-05-80035. The computer calculations were supported by the RFBR (projects no. 19-45-230002). The processing of experimental data, used for this paper, was supported by the RFBR, projects no. 19-05-00041 and 18-55-34002. Analysis of the results was carried out within the framework of the program 0149-2019-0014.

References

Almar, R., Kestenare, E., Reyns, J., Jouanno, J., Anthony, E.J., Laibi, R., Hemer, M., Du Penhoat, Y., Ranasinghe, R., 2015. Response of the Bight of Benin (Gulf of Guinea, West Africa) coastline to anthropogenic and natural forcing, Part1: Wave climate variability and impacts on the longshore sediment transport. Cont. Shelf Res. 110, 48—59, https://doi.org/10.1016/j.csr.2015.09.020.

Aziz, J.J., Ling, M., Rifai, H.S., Newell, C.J., Gonzales, J.R., 2003. MAROS: A Decision Support System for Optimizing Monitoring Plans. Ground Water 41 (3), 355—367, https://doi.org/10.1111/j.1745-6584.2003.tb02605.x.

Bertin, X., Castelle, B., Chaumillon, E., Butel, R., Quique, R., 2008. Longshore transport estimation and inter-annual variability at a high-energy dissipative beach: St. Trojan beach, SW Oleron Island, France. Cont. Shelf Res. 28 (10—11), 1316—1332, https://doi.org/10.1016/j.csr.2008.03.005.

Boyle, G. , 2004. Renewable Energy: Power for a Sustainable Future, 2nd edn Oxford Univ. Press, Oxford 566 pp.

Chowdhury, P., Behera, M.R., 2017. Effect of long-term wave climate variability on longshore sediment transport along regional coastlines. Prog. Oceanogr. 156, 145—153, https://doi.org/10.1016/j.pocean.2017.06.001.

DHI Water & Environment, 2007. MIKE 21, Spectral Wave Module.

Divinsky, B.V., Kosyan, R.D., 2017. Spatiotemporal variability of the Black Sea wave climate in the last 37 years. Cont. Shelf Res. 136, 1—19, https://doi.org/10.1016/j.csr.2017.01.008.

Divinsky, B., Kosyan, R., 2018. Parameters of wind seas and swell in the Black Sea based on numerical modeling. Oceanologia 60 (3), 277—287, https://doi.org/10.1016/j.oceano.2017.11.006.

Jonsson, J.G. , 1966. On the existence of universal velocity distributions in an oscillatory, turbulent boundary layer. Coast. Eng. Lab/Hydraul. Lab., Tech. Univ., Denmark, 2—10 Report No. 12.

Kosyan, A.R., Divinsky, B.V., 2019. *Chamelea gallina* in the coastal waters of the Anapa bay bar (the Black Sea) as a carbonate sediment producer. Oceanologia 61 (4), 471—483, https://doi.org/10.1016/j.oceano.2019.04.003.

Kosyan, R., 1985. Vertical distribution of suspended sediment concentrations seawards of the breaking zone. Coast. Eng. 9, 171—187.

Kosyan, R.D., Divinskiy, B.V., Krylenko, V.V., Krylenko, M.V., Kuklev, S.B., Kosyan, A.R. , 2011. The forecast of Anapa bay-bar coast evolution and sand body thickness change. In: Coastal Engineering Practice — Proceedings of the 2011 Conference on Coastal Engineering Practice. San Diego, CA. 21—24.08.2011, 42—55.

Krylenko, V.V., Kosyan, R.D., Kochergin, A.D., 2011. Regularities of the formation of the granulometric composition of the bottom and beach deposits of the Anapa bay-bar. Oceanology 51 (6), 1061—1071, https://doi.org/10.1134/S0001437011060099.

Krylenko, V.V., 2015. Seashore dynamics of the Anapa bay-bar. Oceanology 55 (5), 742—749, https://doi.org/10.1134/S0001437015050070.

Larson, M., Hoan, L.X., Hanson, H., 2009. Direct formula to compute wave height and angle at incipient breaking. J. Waterway, Port, Coast, Ocean Eng. 136 (2), 119—122, https://doi.org/10.1061/(ASCE)WW.1943-5460.0000030.

Longuet-Higgins, M.S., 1970. Alongshore currents generated by obliquely incident sea waves. J. Geophys. Res. 75, 6788—6801.

Walton, T. , 2002. Coastal Engineering Manual, Part III, Coastal Sediment Processes, Chapter III-6, Eng. Manual 1110-2-1100. In: U.S. Army Corps of Engineers. Washington, DC, 72 pp.

Zou, S., Dalrymple, R., Asce, F., Rogers, B., 2005. Smoothed particle hydrodynamics simulation on sediment suspension under breaking waves. Ocean Waves Measurement and Analysis, Fifth Int. In: Symposium Waves — 2005, Madrid, Spain, 186—192.

Oceanologia (2020) 62, 200—213

Available online at www.sciencedirect.com

ScienceDirect

journal homepage: www.journals.elsevier.com/oceanologia

ORIGINAL RESEARCH ARTICLE

Evaluation of carbon stock in the sediment of two mangrove species, *Avicennia marina* and *Rhizophora mucronata*, growing in the Farasan Islands, Saudi Arabia

Ebrahem M. Eid[a,b,*], Khaled M. Khedher[c,d], Hamdi Ayed[c,e], Muhammad Arshad[f], Adel Moatamed[g,h,i], Abir Mouldi[c,e]

[a] *Department of Biology, College of Science, King Khalid University, Saudi Arabia*
[b] *Department of Botany, Faculty of Science, Kafr El-Sheikh University, Egypt*
[c] *Department of Civil Engineering, College of Engineering, King Khalid University, Saudi Arabia*
[d] *Department of Civil Engineering, High Institute of Technological Studies, Mrezgua University Campus, Tunisia*
[e] *Higher Institute of Transport and Logistics of Sousse, University of Sousse, Tunisia*
[f] *Department of Chemical Engineering, College of Engineering, King Khalid University, Saudi Arabia*
[g] *Department of Geography, College of Humanities, King Khalid University, Saudi Arabia*
[h] *Prince Sultan Bin Abdul-Aziz Center for Environment and Tourism Research and Studies, King Khalid University, Saudi Arabia*
[i] *Department of Geography, Faculty of Arts, Assiut University, Assiut, Egypt*

Received 12 October 2019; accepted 19 December 2019
Available online 6 January 2020

KEYWORDS
Blue carbon;
Carbon sequestration;
Carbon stocks;
Climate change;
Coastal ecosystems

Summary The aim of this study was to conduct the first comprehensive evaluation of carbon stock in the sediments of *Avicennia marina* (black mangrove) and *Rhizophora mucronata* (red mangrove) along the coastline of an arid region (Farasan Islands, Saudi Arabia). Such information is necessary for the development of any management plan for the mangrove ecosystems along the Saudi Red Sea islands and provide a rationale for the restoration of mangrove forests in Saudi Arabia. *A. marina* and *R. mucronata* locations showed significant ($P < 0.001$) differences in sediment bulk density (SBD) and sediment organic carbon (SOC) concentration with higher mean values for both in the sediments of *A. marina*. Considering the whole depth of

* Corresponding author at: Department of Botany, Faculty of Science, Kafr El-Sheikh University, Kafr El-Sheikh 33516, Egypt. Tel.: 00966 55 2717026; fax: 00966 17 241 8205.
E-mail addresses: ebrahem.eid@sci.kfs.edu.eg, eeid@kku.edu.sa, ebrahem.eid@gmail.com (E.M. Eid).
Peer review under the responsibility of the Institute of Oceanology of the Polish Academy of Sciences.

Production and hosting by Elsevier

https://doi.org/10.1016/j.oceano.2019.12.001

sediment sampled (0—50 cm), the highest value of SOC stock (12.3 kg C m^{-2}) was recorded at *A. marina* locations and the lowest (10.8 kg C m^{-2}) at *R. mucronata* locations. Thus, the SOC stock of *A. marina* was greater than that of *R. mucronata* by 114.3%. Consequently, considering the rate of carbon sequestration and the area of mangrove forests (216.4 ha), the total carbon sequestration potential of mangroves in the Farasan Islands ranged between 10.3 Mg C yr^{-1} and 11.8 Mg C yr^{-1} for *R. mucronata* and *A. marina* locations, respectively. Thus, it is necessary to protect and restore these ecosystems for the sequestration of carbon and for their other valuable ecosystem services.

1. Introduction

Climate change is a major global issue (Eid et al., 2016), and CO_2, one of the greenhouse gases, has a major role in climate change and global warming (Shaltout et al., 2019). Land use changes (such as deforestation) and combustion of fossil fuels are thought to lead to high concentrations of CO_2 in the atmosphere (IPCC, 2007). The highest levels of carbon in the terrestrial carbon cycle are found in soil reservoirs (Sahu and Kathiresan, 2019). These levels are twice more than those in the atmosphere and three times more than those in vegetation (Sahu and Kathiresan, 2019). Thus, many scientists have indicated that CO_2 sequestration in soil organic carbon (SOC) may contribute substantially to reducing the effects of climate change (see Taillardat et al., 2018). Furthermore, increasing soil carbon stocks and protecting carbon rich soils are essential for reaching the climate targets of the Paris Climate Agreement (Rumpel et al., 2018).

Blue carbon has received international interest for its potential role in the mitigation of CO_2 emissions (Taillardat et al., 2018). Mangrove forests constitute one of the ecosystems with the greatest density of carbon in the world with most of the carbon stored in the soil, and organic-rich sediments of several metres depth have been observed in some mangrove ecosystems (Twilley et al., 1992). Therefore, mangroves are now being considered an important means of combatting climate change through approaches such as REDD+ and blue carbon (Alongi, 2012). Sanderman et al. (2018) described the need to record the distribution of carbon stock in mangrove forests so that they can be utilised in attempts to ease climate change. Therefore, accurate, location-specific quantification of carbon stocks is essential to understand the spatial range of coastal blue carbon and to estimate future carbon stocks as a result of habitat preservation, loss, degradation, or restoration (Radabaugh et al., 2018).

Mangrove forests are efficient ecosystems existing at the land—sea margin. Globally, these forests comprise approximately fifty-four species from twenty families of vascular plants (Tomlinson, 2016). Alongi (2012) described them as the sole woody halophytes existing in saltwater along tropical and subtropical coastal regions. The significance of mangrove forests in terms of social, economic, and ecological benefits are well documented worldwide as being crucial for both the wellbeing of humans and the environment (Shaltout et al., 2019). Mangroves aid in stabilising shorelines and decreasing the effects of natural disasters, including those of tsunamis and hurricanes. Mangrove forests are one of the coastal vegetation ecosystems that raise the seabed via soil accretion of autochthonous and allochthonous material, supporting a natural coastline protection system against sea level rise (Saderne et al., 2018). They serve as nursing grounds for marine biota, conserve biodiversity, and provide fuel, medicine, food, and material for construction to coastal communities. They also sequester and store large quantities of carbon, which help in the mitigation of climate change and enrich the ocean by providing organic inputs (Jennerjahn and Ittekot, 2002). The mean economic value assigned to mangroves has been approximated as second only to the value of estuaries and seagrass meadows and greater than the economic value of coral reefs, continental shelves, and the open sea (Costanza et al., 1997).

Mangroves cover approximately 137,600 km^2 of coastline in 118 countries with 38.7% found in Asia, 20.3% in Latin America and the Caribbean, 20% in Africa, 11.9% in Oceania, 8.4% in North America, and 0.7% in the European Overseas Territories (Bunting et al., 2018). The net primary production of carbon is formed partially (10%) from mangrove forests and these forests also result in a quarter of carbon burial in coastal zones worldwide — this, despite existing only along 0.7% of the coastal zones worldwide (Alongi, 2007). Donato et al. (2011) indicated that between 50% and 90% of the total carbon of the mangrove ecosystem is made up of SOC. Twilley et al. (2018) supported this by describing how mangroves comprise a greater amount of sedimentary carbon per m^2 than terrestrial regions, indicating that within the first metre, 36.1 kg m^{-2} of blue carbon can be found (Sanderman et al., 2018). This amount is 3.3-, 3.2-, 2.8-, 2.7-, 2.4-, 2.3-, 2.1-, 1.8-, 1.7-, 1.5-, and 1.4-fold greater than the soil carbon stocks estimated for closed shrublands, savannas, croplands, deciduous broadleaf forests, evergreen broadleaf forests, grasslands, open shrublands, mixed forests, evergreen needleleaf forests, permanent wetlands, and deciduous needleleaf forests, respectively (Sanderman et al., 2018).

Even though mangrove ecosystems are advantageous in so many ways, both changes in land use and growth of urban regions are threatening their survival. For instance, one study determined that the mass deforestation of 278,049

ha of a mangrove area (equalling 1.67% of the total area worldwide) occurred in 2000 and this led to between 30.4 and 122.0 Tg C (111.0–447.0 Tg CO_2) of committed emissions (Sanderman et al., 2018). Thus, the change in land use between 2000 and 2015 led to emissions of somewhere in this range from the soils of these mangrove forests. Considering the current rate of loss, Duke et al. (2007) estimated that all mangroves would disappear within a decade. Thus, understanding the distribution of SOC stock in mangrove forests is very important for prioritising protection and restoration efforts for climate change mitigation (Sanderman et al., 2018).

The location of the Red Sea mangroves, at the most northern point of their spread in the Indo-Pacific, confers them with great importance in terms of their ecology and biogeography (PERSGA, 2004). Saifullah (1994) demonstrated the significance of this mangrove owing to its growth in an area that should be considered uninhabitable in that it has a paucity of rain, the land is dry, rivers are absent, and salt levels are high. Hard-bottomed and euhaline–metahaline mangroves are the two forms of these forests present in the Red Sea (Price et al., 1987). The common species, *Avicennia marina*, has been the subject of various studies performed on mangrove forests in the Saudi Arabian Red Sea to determine their carbon sequestration potential (CSP). These studies were conducted at several locations with the majority being in the southern regions, two in the central areas, and one in a northern area. The efficacy of *A. marina* in carbon sequestration was examined by Eid et al. (2016) along the Saudi Arabian coast of the Red Sea. The central coast of the Red Sea in the Saudi Arabian region was similarly investigated for its carbon sequestration rate (CSR) and SOC stocks by Almahasheer et al. (2017). The southern Red Sea coast of Saudi Arabia was studied by Arshad et al. (2018), and the CSR in regions determined to be polluted and non-polluted was evaluated. *A. marina* was also studied in the southern area of the Red Sea in Saudi Arabia next to Jizan city by Eid et al. (2019) who sought to determine how differences in land use could affect the SOC stock in the sediments of this southern coastal region that was converted from areas flourishing with *A. marina* to shrimp farms. Another study examined the variation in the carbon sequestration capacity of *A. marina* with variation in the accessibility to nutrients and along a salinity gradient along the Saudi Arabian Red Sea (Shaltout et al., 2019).

To the best of our knowledge, this is the first study to compare *A. marina* and *Rhizophora mucronata* in Saudi Arabia with respect to sediment bulk density (SBD), SOC concentration, and SOC stock. Our null hypothesis is that both *A. marina* and *R. mucronata* locations have the same SBD, SOC concentration, and SOC stock. Through this study, we will be able to enhance our understanding of the part played by arid mangroves in sequestering carbon. Our specific research questions were what are the carbon stocks of the mangroves of the Farasan Islands? and how do they differ between *A. marina* and *R. mucronata* locations? The results from this study are expected to increase knowledge on the carbon stock in mangroves and to inform current discussions on blue carbon. This will be useful to government departments regarding the management of mangrove forests and will also improve the attitude and increase the concern of societies towards the conservation of mangroves.

2. Material and methods

2.1. Study area

The Farasan Islands were declared a nature reserve in 1989 owing to the presence of the last population of the Arabian Gazelle (Alfarhan et al., 2002). The region is protected and is currently seen as Saudi Arabia's most significant marine nature reserve. Alfarhan et al. (2002) also described other crucial needs of this region, including as a nesting area for migrating birds and as an area that is conducive to supporting various endemic snakes. Al Mutairi et al. (2012) described the high biodiversity of the region and the presence of various species that are either endemic or endangered and this was attributed to the exclusive location of these islands in the region between the west of Asia and the east of Africa in an arid setting. The fauna and flora of the region are also quite distinct as they are part of various phytogeographical areas including Africa, the Mediterranean, and Asia. The habitats within these islands are also diverse and comprise salt marshes (both wet and dry), sand plains, sand dunes, rocky regions, and mangroves (El-Demerdash, 1996).

The Farasan Islands can be found in the southern area of the Red Sea at a location ca. 50 km away from the axial trough of the Red Sea and approximately 40 km from Jizan City (Fig. 1). The Farasan Islands are a group of 128 islands that together shape the Farasan bank, totalling an area of 3,000 km^2 (Bantan, 1999). Khalil (2012) estimated the complete land area covered by the islands as 600 km^2. Three islands are currently inhabited; namely, Qummah, 14.9 km^2; Sajid, 109 km^2; and Farasan Al-Kabir, 369 km^2. There are other islands that are large in size but remain uninhabited, except by the coast guard – the Disan, Zifaf, and Dumsuk Islands. The other islands are used for picnicking and by fishermen as rest areas. The population of the island is estimated at 4,500 and the majority of the inhabitants are either fishermen or work in agriculture (Alwelaie et al., 1993). An uplifted coral reef is the main material that forms the islands mostly consisting of fossils, with coastal regions comprising eroded coral sands or cliffs and also coral surfaces along the wadis and runnels (Dabbagh et al., 1984). The mean surface level is not greater than 20 m a.s.l. but attains a height of 70 m in certain regions (Alwelaie et al., 1993). The two species investigated in this study, *R. mucronata* and *A. marina*, can be found in the lagoons and the island shorelines (Al-Mutairi et al., 2012). Al-Mutairi et al. (2012) describes *A. marina* as the main species of mangrove established in this region either as a pure community or mixed with *R. mucronata*. Two other studies describe a massive monospecific *R. mucronata* population in the north-eastern region of the Farasan Jetty (Alwelaie et al., 1993; El-Demerdash, 1996).

The climate in the islands is between arid and subtropical. Temperatures of 29.8°C are reached on average with rainfall being less than 130 mm yr^{-1}. Most of the year is humid with high humidity levels of between 70% to 80% in winter and decreasing in summer to between 65% and 78% (El-Demerdash, 1996). The saltiness of the water in the region of the Farasan Islands in the southern area of the Red Sea is also high ranging from ca. 37% in winter to ca. 38% in summer (Bantan, 1999). Abu-Zeid et al. (2011) described how owing to the raised levels of evaporation in the islands'

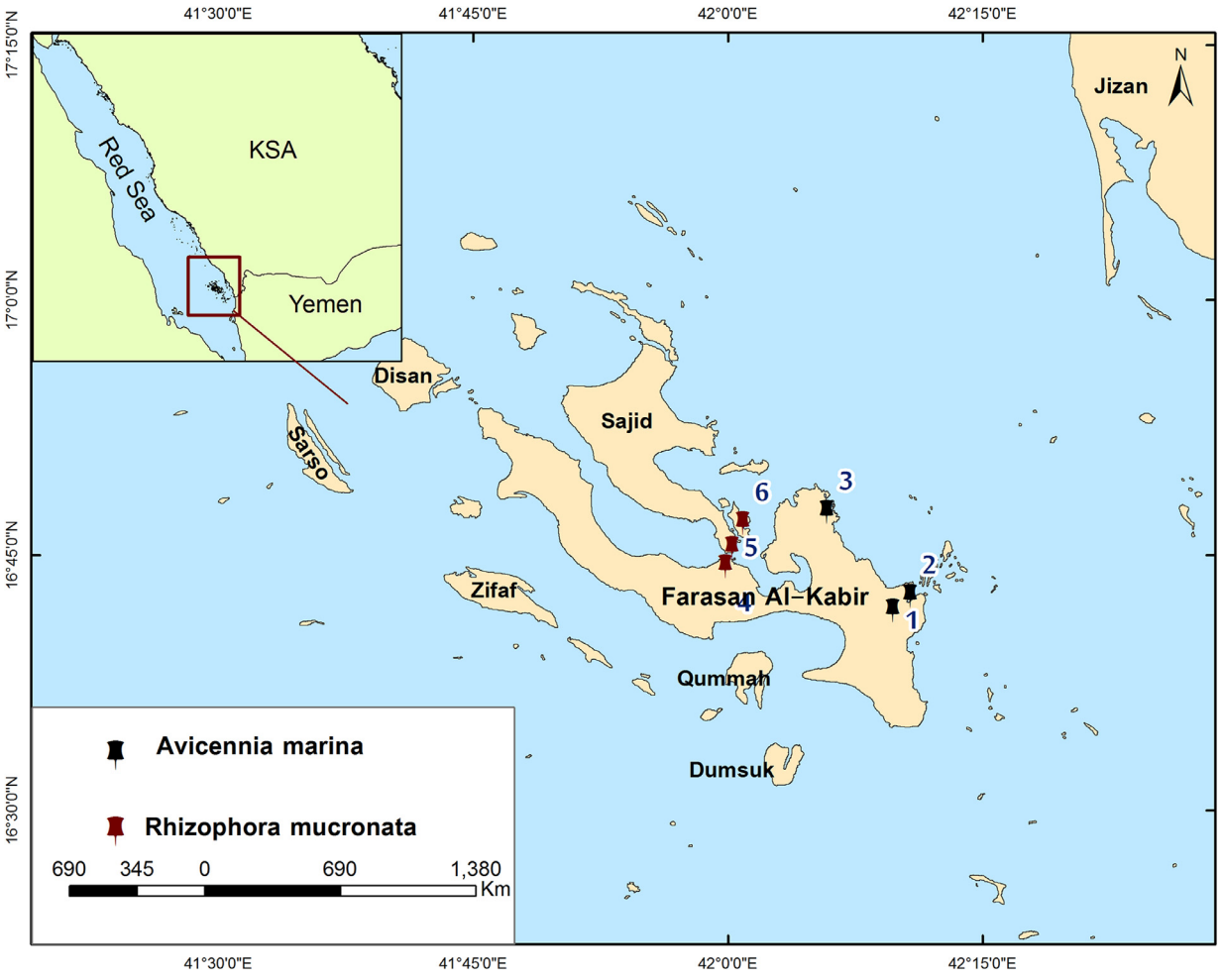

Figure 1 Map of the study area indicating the six sampling locations.

lagoon, the salinity tends to reach levels as high as 40%. The tide is every 11 h (diurnal) and low, with a mean spring range of 0.5 m at the region of the Farasan Islands (Bantan, 1999). As the Farasan Islands are located in the southern Red Sea, their climate is a monsoon climate. The region is influenced by the monsoon winds coming from the north in the summer and those coming from the south-east in the winter (Marcos, 1970). This results in the southern Red Sea surface water currents being affected around the Farasan Islands. In this region, the surface currents flow in a southerly direction in the summer months and in a northerly direction in the winter months.

2.2. Sediment sampling

Six locations were selected for sampling which was conducted in July of 2019. Locations representative of the *A. marina* monospecific stands were 17°48′28.7″N, 41°51′57.0″E; 17°47′31.5″N, 41°53′18.5″E; and 17°10′43.9″N, 42°22′2.1″E and for the *R. mucronata* stands: 17°47′37.5″N, 41°53′49.9″E; 17°46′40.8″N, 41°54′37.3″E; and 17°13′17.0″N, 42°20′20.5″E. All these locations were along the coastline of the Farasan Islands (Fig. 1). Kauffman and Donato's (2012) the *Rule of Twelfths* was used for sampling during low tides (<0.3 m water depth) in locations that were accessible on foot. At each sampling location, seven sites were selected and seven soil cores were collected from each one. Samples from both *A. marina* and *R. mucronata* locations were collected using a hand sediment corer (made of stainless steel, 100 cm long with an inner diameter of 70 mm). To collect the core, the researchers pushed the corer down into the soil to a depth of 50 cm. This depth was selected owing to the presence of raised coral/rock and subfossil at depths below 50 cm. Next, the sediment core was slowly extracted out of the corer and then, divided into ten 5 cm sections: 0–5, 5–10, 10–15, 15–20, 20–25, 25–30, 30–35, 35–40, 40–45, and 45–50 cm. Each section was then stored in a plastic container which was sealed with parafilm and volatilisation loss was prevented along with a decrease in the activity of microbes by storing the container on ice until further analysis (Eid and Shaltout, 2016). Thus, from each of the ten layers of soil, one sample was collected, and this was done for each of the 42 sites that were sampled (21 sites for each species). Overall, 420 samples of sediment were gathered for the analysis of SBD, SOC stock, and SOC concentration.

2.3. Sample analysis

The sediment samples were first oven dried at a temperature of 105°C over 3 days. The samples were then weighed to establish SBD [g cm^{-3}] as per Wilke's (2005)

methodology:

$$\rho_{sj} = \frac{m_j}{v_j},$$

where ρ_{sj} is the SBD [g cm^{-3}] of the j^{th} layer, m_j is the mass of the sediment sample [g] of the j^{th} layer dried at 105°C, and v_j is the volume of the sediment sample [cm^3] of the j^{th} layer. Once dried, the samples were ground and sieved to ensure particle size was below 2 mm. SOC concentrations were established for each sample by measuring the sediment organic matter (SOM). The loss-on-ignition method was used which was performed for two hours at 550°C as described by Jones (2001). SOC concentration was established as [g C kg^{-1}] = 0.50 [Pribyl, 2010] × SOM [g C kg^{-1}]. A CHN analyser was not available to the researchers at the time of the study, and therefore, as per the recommendations of Nóbrega et al. (2015), the loss-of-ignition methodology was employed instead. This was required to establish a precise approximation of SOC in the sediments from the mangroves. Next, following the methodology of Meersmans et al. (2008), SOC stock [kg C m^{-2}] was quantified using the following equation:

$$SOC_s = \frac{\sum_{j=1}^{k} \rho_{sj} \times SOC_j \times T_j}{\sum_{j=1}^{k} T_j} \times D_r,$$

where SOC_s is SOC stock [kg C m^{-2}], ρ_{sj} is the SBD [g cm^{-3}] of the j^{th} layer, SOC_j is the SOC concentration [g C kg^{-1}] of the j^{th} layer, D_r is the reference depth [= 0.5 m], T_j is thickness [m] of the j^{th} layer, and k is the number of layers [= 10].

CSR [g C m^{-2} yr^{-1}] was estimated based on the sedimentation rate, SBD, and SOC concentration (Xiaonan et al., 2008):

$$CSR_i = \rho_{si} \times SOC_i \times R,$$

where CSR_i is the CSR [g C m^{-2} yr^{-1}] of the i^{th} location, ρ_{si} is the mean SBD [g cm^{-3}] of the i^{th} location, SOC_i is the mean SOC concentration [%] of the i^{th} location, and R is the sedimentation rate in the mangrove forests (the mean for Saudi Arabia = 2.2 mm yr^{-1}; Almahasheer et al., 2017).

CSP [Mg C yr^{-1}] was calculated as follows (Xiaonan et al., 2008):

$$CSP = CSR \times A,$$

where CSP is the CSP [Mg C yr^{-1}] of the mangrove stands and A is the area [m^2] of the mangrove stands (216.4 ha; Khan et al., 2010).

2.4. Statistical analysis

Before analysis, the data was evaluated for normality of distribution and homogeneity of variance using the Shapiro-Wilk's W test and Levene's test, respectively. Log transformation was performed on the data when necessary prior to conducting analysis of variance (ANOVA). Two-way ANOVA (ANOVA-2) was used to identify statistically significant differences in SBD and SOC concentrations in *A. marina* and *R. mucronata* samples for each of the ten sediment depths. Significant difference between means among the ten sediment depths were identified using the Tukey's HSD test at $P < 0.05$. Non-linear regression and Pearson correlation coefficient were used to evaluate the association between the SOC concentration and SBD (Shaltout et al., 2019). Student's *t*-test was used to identify significant differences among the *A. marina* and *R. mucronata* locations for the total means of SOC stock, SOC concentration, SBD, CSP, and CSR. All statistical analyses were performed using SPSS 15.0 (SPSS, 2006).

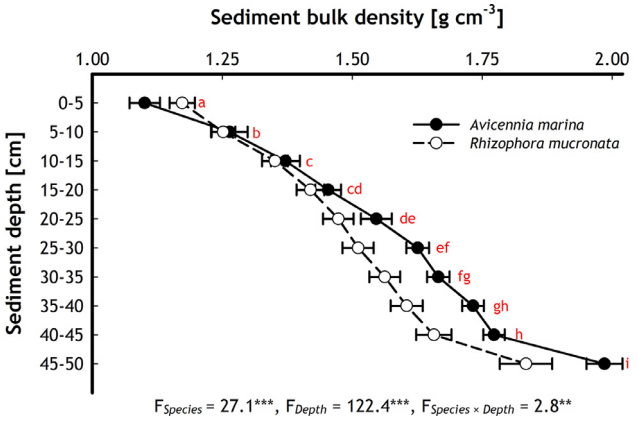

Figure 2 Distribution of sediment bulk density [g cm^{-3}] in relation to sediment depth [cm] in *Avicennia marina* and *Rhizophora mucronata* locations along the coastline of the Farasan Islands, Saudi Arabia. Horizontal bars indicate the standard error of the means [n = 21]. *F*-values represent results of the two-way ANOVAs. Means followed by different letters are significantly different at $P < 0.05$ according to the Tukey's HSD test. Location: *A. marina*/*R. mucronata*; Depth: 0–5, 5–10, 10–15, 15–20, 20–25, 25–30, 30–35, 35–40, 40–45, 45–50 cm. **: $P < 0.01$, ***: $P < 0.001$.

3. Results

Differences in SBD were significant between the *A. marina* and *R. mucronata* locations with a *t*-value of 4.1 ($P < 0.001$) and the greatest mean values belonging to *A. marina*; thus, these findings demonstrate that the null hypothesis is not true (Table 1). Variation in SBD at the *A. marina* locations was clearly high as it increased from 1.10 g cm^{-3} at the depth of 0–5 cm to 1.99 g cm^{-3} at the depth of 45–50 cm (Fig. 2). In comparison, for *R. mucronata*, SBD increased from 1.17 g cm^{-3} at the depth of 0–5 cm to 1.83 g cm^{-3} at the depth of 45–50 cm.

Significant differences were also observed for the SOC concentrations with *t*-values of 7.7 ($P < 0.001$) between the *A. marina* and *R. mucronata* locations. The greater average differences were in the sediments from the *A. marina* locations; thus, the null hypothesis was once again disproved (Table 1). A decrease was noted in the SOC concentrations at the *A. marina* locations from 23.4 g C kg^{-1} at the depth of 0–5 cm to 13.2 g C kg^{-1} at the depth of 45–50 cm (Fig. 3). At the *R. mucronata* locations, the SOC concentrations clearly declined from 20.4 g C kg^{-1} to 11.8 g C kg^{-1} at the depth of 0–5 cm to 45–50 cm, respectively. SOC concentration (g C kg^{-1}) and SBD (g cm^{-3}) had a significant and an inverse relationship, which was described by the following non-linear regression equations: SBD = 0.879 + 10.021 $e^{-0.172 \times \text{SOC concentration}}$ ($r = -0.633$, $P < 0.001$) and SBD = 1.059 + 9.638 $e^{-0.219 \times \text{SOC concentration}}$

Table 1 Mean ± standard error of sediment bulk density – SBD [g cm^{-3}], sediment organic carbon (SOC) concentration [g C kg^{-1}], SOC stock [kg C m^{-2}], carbon sequestration rate – CSR [g C m^{-2} yr^{-1}], and carbon sequestration potential – CSP [Mg C yr^{-1}] of *Avicennia marina* and *Rhizophora mucronata* locations along the coastline of the Farasan Islands, Saudi Arabia.

Species	SBD	SOC concentration	SOC stock	CSR	CSP
A. marina	1.55 ± 0.02 [n = 210]	16.3 ± 0.3 [n = 210]	12.3 ± 0.1 [n = 21]	5.4 ± 0.1 [n = 210]	11.8 ± 0.1 [n = 210]
R. mucronata	1.48 ± 0.02 [n = 210]	14.9 ± 0.2 [n = 210]	10.8 ± 0.2 [n = 21]	4.8 ± 0.1 [n = 210]	10.3 ± 0.1 [n = 210]
t-value	4.1***	7.7***	6.0***	10.9***	10.9***

t-values represent the Student's t-test. ***: $P < 0.001$.

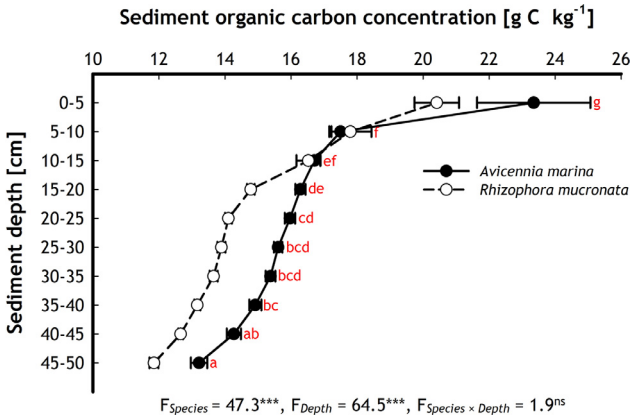

Figure 3 Distribution of sediment organic carbon concentration [g C kg^{-1}] in relation to sediment depth [cm] in the *Avicennia marina* and *Rhizophora mucronata* locations along the coastline of the Farasan Islands, Saudi Arabia. Horizontal bars indicate the standard error of the means [n = 21]. F-values represent results of the two-way ANOVAs. Means followed by different letters are significantly different at $P < 0.05$ according to the Tukey's HSD test. Location: *A. marina*/*R. mucronata*; Depth: 0–5, 5–10, 10–15, 15–20, 20–25, 25–30, 30–35, 35–40, 40–45, 45–50 cm. ***: $P < 0.001$, *ns*: not significant [i.e. $P > 0.05$].

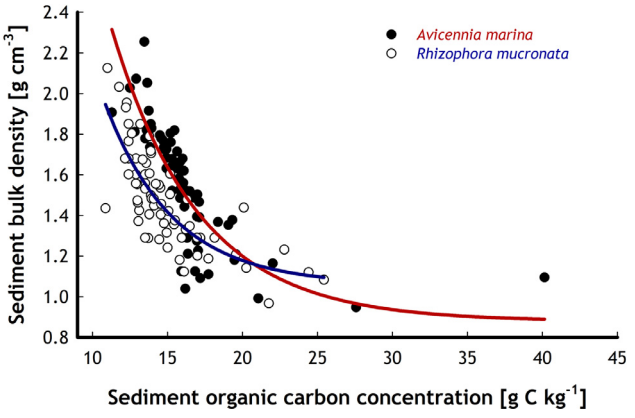

Figure 4 Non-linear correlation between sediment organic carbon concentration [g C kg^{-1}] and sediment bulk density [g cm^{-3}] of 420 sediment samples from *Avicennia marina* and *Rhizophora mucronata* locations along the coastline of the Farasan Islands, Saudi Arabia.

($r = -0.718$, $P < 0.001$) for *A. marina* and *R. mucronata* locations, respectively (Fig. 4).

Allowing for the entire sediment interval depth from 0 to 50 cm, the greatest SOC stock value was observed at *A. marina* locations (12.3 kg C m^{-2}), whereas the least value for the SOC stock was observed at *R. mucronata* locations (10.8 kg C m^{-2}). Thus, SOC stock was 114.3% greater for *A. marina* locations than for *R. mucronata* locations (Table 1). Therefore, the null hypothesis was once again disproved. A significantly greater mean CSR was observed at *A. marina* locations (5.4 g C m^{-2} yr^{-1}) than at *R. mucronata* locations (4.8 g C m^{-2} yr^{-1}) with a t-value of 10.9 ($P < 0.001$). Considering the mangrove forest area of 216.4 ha and the CSR values, the mangroves of the Farasan Islands had a total CSP ranging from 10.3 Mg C yr^{-1} at *R. mucronata* locations to 11.8 Mg C yr^{-1} at *A. marina* locations.

4. Discussion

The SBD is a dynamic feature that differs with structural conditions within the sediment (Pravin et al., 2013). It is frequently employed as a measure of two soil features, namely, ventilation and moisture (Huang, 2015). The mechanical resistance of the soil with regard to the growth of plants is also established using SBD; it may also affect the distribution of SOC concentration while playing a significant part in the approximation of this parameter (Johnston et al., 2004). The coastline of the Farasan Islands has mangrove forests along it; the SBD of this mangrove forest is within the value range described for mangroves inhabiting the Red Sea coast (Table 2). Additionally, as depth increased, so did SBD for both *A. marina* and *R. mucronata* locations. This finding has been described by other authors, including for the coast along the Egyptian Red Sea (Eid and Shaltout, 2016), along an approximate 1134 km of the coast of the Saudi Arabian Red Sea (Shaltout et al., 2019), and along the southern region of the coastline of the Saudi Arabian Red Sea (Arshad et al., 2018; Eid et al., 2016). Such variation in SBD has been attributed to the build-up of the remains of plants and tailings in the various layers of the sediment (surface and subsurface) (Sherry et al., 1998). These lead to changes in the organic matter content, porosity, and compaction (Pravin et al., 2013).

Underground roots, dropped litter, autochthonous matter, and other forms of material produced locally by mangroves are the initial contributors to SOC concentrations in mangrove forests (Alongi, 1998); as also benthic algae (Yong et al., 2011); seagrass and seaweed captured in the area (Mandura et al., 1988); and matter brought

Table 2 Mean of sediment bulk density – SBD [g cm^{-3}], sediment organic carbon (SOC) concentration [g C kg^{-1}], SOC stock [kg C m^{-2}], and carbon sequestration rate – CSR [g C m^{-2} yr^{-1}], of *Avicennia marina* and *Rhizophora mucronata* locations along the coastline of the Farasan Islands, Saudi Arabia compared with those reported for different mangrove forests around the globe.

Location	Species	SBD	SOC concentration	SOC stock	CSR	Depth [cm]	Reference
Farasan Islands, Saudi Arabia	*Avicennia*	1.55	16.3	12.3	5.4	50	Present study
	Rhizophora	1.48	14.9	10.8	4.8	50	
Red Sea coast, Saudi Arabia	*Avicennia*	1.5-1.9	14.4-18.1	6.7-10.5	5.0-6.0	50	Shaltout et al. (2019)
Southern Saudi Red Sea coast	*Avicennia*	1.66	17.7	29.2		100	Eid et al. (2019)
Southern Saudi Red Sea coast	*Avicennia*	1.53-1.66	12.6-15.7	9.9-11.5	4.4-5.1	50	Arshad et al. (2018)
Central Saudi Red Sea coast	*Avicennia*		2.0-15.0	2.5-7.6	1.5-5.5	100	Almahasheer et al. (2017)
Southern Saudi Red Sea coast	*Avicennia*	1.5	28.7	17.0	11.9	40	Eid et al. (2016)
Arabian Gulf, United Arab Emirates	*Avicennia*			10.2-15.6		100	Schile et al. (2017)
Red Sea coast, Egypt	*Avicennia*	1.4	15.5	8.5	6.1	40	Eid and Shaltout (2016)
Africa' Sahel, Senegal	*Avicennia & Rhizophora*			7.4-10.7		40	Woomer et al. (2004)
Ambanja and Ambaro bays, Madagascar	*Avicennia & Rhizophora*	0.52-1.39	6.0-61.0	32.4-51.7		150	Jones et al. (2014)
Zambezi River Delta, Mozambique	*Avicennia & Rhizophora*	0.72-0.95	14.5-23.6	27.5-31.4		200	Stringer et al. (2015)
Tropical Pacific, Micronesia	*Rhizophora*		130.0-150.0	51.7-94.7		100	Donato et al. (2012)
Yap Island, Micronesia	*Rhizophora*	0.27-0.51	73.0-137.0	12.1		100	Kauffman et al. (2011)
Pohnpei Island, Micronesia	*Avicennia*	0.10-0.43	114.6-364.9	177.1-211.6	53.0-93.0	365	Fujimoto et al. (1999)
Babeldaob Island, Palau	*Rhizophora*				69.8-369.7	60	Mackenzie et al. (2016)
Babeldoab Island, Palau	*Rhizophora*	0.18-0.36	120.0-215.0	56.7		100	Kauffman et al. (2011)
Moanaanuanu Estuary, New Zealand	*Avicennia*			6.9-7.0	31.8-57.6	40	Pérez et al. (2017)
Australian coast	*N.A.*			48.1-101.2		200	Sanders et al. (2016)
Pilbara coast, Australia	*Avicennia*		14.0-70.0	11.8		100	Alongi et al. (2000), Alongi et al. (2003)
	Rhizophora		23.0-65.0	16.9		100	
Lagoons and estuaries, Sri Lanka	*Avicennia & Rhizophora*	0.97-1.37	53.0-97.0	31.6-58.1		45	Perera and Amarasinghe (2019)
Batticaloa Lagoon, Sri Lanka	*Avicennia & Rhizophora*	0.40-1.60	3.0-51.0	100.9-784.6		80	Jonsson and Hedman (2019)
Mekong region, Vietnam	*Rhizophora*				121.0-602.7	60	Mackenzie et al. (2016)
Mekong Delta, Vietnam	*Avicennia & Rhizophora*	0.52-0.86	17.9-52.0	66.7		250	Dung et al. (2016)
Mekong Delta, Vietnam	*Avicennia & Rhizophora*	0.61-1.20	13.0-33.0	58.4-65.5		250	Tue et al. (2014)
Pulau Ubin Island, Singapore	*Avicennia & Rhizophora*	0.73	45.0	30.7		100	Phang et al. (2015)
Honda Bay, Philippines	*Avicennia*	0.48-0.62	64.3-87.3	85.2		300	Castillo et al. (2017)
Sawi Bay, Thailand	*Avicennia & Rhizophora*		22.5-54.3			100	Alongi et al. (2001)
Zhangjiang Estuary, China	*Avicennia*	0.94	12.7	9.6		100	Gao et al. (2019)
	Rhizophora	1.24	12.1	8.5		100	

(*continued on next page*)

Table 2 (*continued*)

Location	Species	SBD	SOC concentration	SOC stock	CSR	Depth [cm]	Reference
Hainan Dongzhaigang Wetlands, China	*Avicennia*			9.6		100	Xin et al. (2018)
	Rhizophora			5.6		100	
Leizhou Peninsula, China	*Avicennia & Rhizophora*	0.93-1.12	7.1-16.4	7.1-14.0	37.0-205.0	90	Yang et al. (2014)
Zhangjiang Estuary, China	*Avicennia*		10.0-12.7			60	Xue et al. (2009)
Segara Anakan Lagoon, Kongsi Island and Thousand Islands, Indonesia	*Avicennia & Rhizophora*	0.62-1.35	8.0-77.0	3.7-48.5	2.4	100	Kusumaningtyas et al. (2019)
Bay of Bengal, India	*Avicennia*	0.56	9.2	2.8		N.A.	Sahu and Kathiresan (2019)
	Rhizophora	0.57	8.4	2.6		N.A.	
Sundarbans, India	*Avicennia*		5.1-6.5	2.6		30	Ray et al. (2011)
Tampa Bay, USA	*Avicennia & Rhizophora*	0.44-0.90	63.0-110.0	10.1		50	Radabaugh et al. (2018)
La Paz Bay, Mexico	*Avicennia & Rhizophora*	0.9		10.0-23.9		45	Ochoa-Gómez et al. (2019)
Pantanos de Centle Wetland, Mexico	*Avicennia & Rhizophora*	0.49	131.0	13.7-200.3		300	Kauffman et al. (2016)
Yucatan Peninsula, Mexico	*Rhizophora*	0.11-0.95	32.0-351.0	28.6-116.6		100	Adame et al. (2013)
Ceará State, Brazil	*N.A.*			8.2		40	Nóbrega et al. (2019)
Crumahú River, Brazil	*Avicennia & Rhizophora*		163.0-266.0			80	Ferreira et al. (2010)
Tamandaré, Brazil	*N.A.*	0.61-1.33	10.9-214.2			45	Sanders et al. (2010)
Sepetiba Bay, Brazil	*Avicennia*		38.0-61.0			15	Lacerda et al. (1995)
	Rhizophora		27.0-28.0			15	
Caribbean coast, Venezuela	*Avicennia*	0.26-0.39	100.0-120.0	3.1-3.8		20	Barreto et al. (2016)
	Rhizophora	0.22-0.23	170.0-200.0	3.7-4.4		20	
Amboa Swamp, New Caledonia	*Avicennia*	0.24-0.45	51.0-115.3	25.6		100	Jacotot et al. (2018)
	Rhizophora	0.33-0.44	54.7-110.8	31.5		100	
Coastal wetlands, Dominican Republic	*Avicennia & Rhizophora*	0.30	175.0	75.3		195	Kauffman et al. (2014)

from nearby coastal areas by tidal flux, i.e. allochthonous material (Allisaon et al., 2003). All this material eventually ends up in the mangroves (Bouillon et al., 2003). On a worldwide scale, the organic carbon content of mangrove soil is highly variable with values ranging from 5 g kg^{-1} to above 400 g kg^{-1} and this is dependent on the composition and age of the forest, productivity, biomass, soil texture, geographical and morphological settings, tidal range, regional climate, and anthropogenic effects (Donato et al., 2011; Gao et al., 2019; Otero et al., 2017; Sanders et al., 2016). The average SOC concentration of 14.9 to 16.3 g C kg^{-1} observed in this study was below the global value of 22.0 g C kg^{-1} (Kristensen et al., 2008) and also below values estimated in the mangrove forests of many other nations, as shown in Table 2, including Thailand, Micronesia, Sri Lanka, Indonesia, Philippines, Australia, Palau, Brazil, Vietnam, New Caledonia, Singapore, Mexico, USA, Venezuela, Dominican Republic, and Madagascar. The values observed in this study were, however, greater than those estimated in China, Egypt, and India.

Zimmerman and Canuel (2000) described how input and decomposition systems at the various sediment depths are responsible for the concentration of SOC. SOC concentration decreased slowly starting from the surface and moving towards the bottom of the cores of the sediment in both *A. marina* and *R. mucronata* locations analysed in this study. *A. marina* sediments of the Saudi Arabian Red Sea mangroves showed a similar structuring as those of *A. marina* in Egypt (Eid and Shaltout, 2016). A study by Schile et al. (2017) also described a similar structuring in sediments of *A. germinans* and *A. marina* along the coast of the United Arab Emirates. This was further supported by previous research on the mangrove forests in Vietnam (Tue et al., 2011), Australia (Saintilan et al., 2013), the Asia-Pacific region (Donato et al., 2011), Mexico (Adame et al., 2013), and the Gulf of Mexico (Bianchi et al., 2013). It is clear that as depth increases, the SOC concentration decreases and this is thought to be due to variation in the ratio of matter obtained from the mangroves and allochthonous material, such as seston, as well as from sources of organic carbon contained in sediments and organic material mineralisation in the sediments of mangroves (Bouillon et al., 2003; Tue et al., 2012). Changes in the concentrations of SOC with increasing depth could also be caused by the interplay between various complex systems including decomposition, leaching, hydrologic regimes (sediment regimes), biological cycling, soil erosion, atmospheric decomposition, illuviation, and weathering of minerals (Girmay and Singh, 2012; Sanderman et al., 2018).

An indirect exponential association was observed between the SOC concentration and SBD at all *A. marina* and *R. mucronata* locations investigated in this study. SBD is a crucial factor for the approximation of the SOC stock; nevertheless, only a limited number of research studies have concurrently detailed SOC concentrations together with those of SBD when analysing the sediments of mangroves. The indirect association between SBD and the SOC concentration determined in this study, therefore adds a beneficial methodology for the approximation of SOC stock in mangrove forests (Donato et al., 2011). Furthermore, the negative association between the SBD and the SOC concentration also indicates that various factors may be affected by SBD including soil permeability, porosity, ventilation, and structure of the soil, all of which also affect the build-up of the soil (Gao et al., 2019). This study determined that SBD in the sediments diminishes with greater SOC concentrations. This association was also noted in previous studies including that for the *A. marina* sediments of the Saudi Arabian Red Sea (Arshad et al., 2018; Eid et al., 2016, 2019; Shaltout et al., 2019), *A. marina* sediments along the Red Sea coast of Egypt (Eid and Shaltout, 2016), and for four Chinese mangrove forests (Gao et al., 2019). This was also consistent with results of other studies including one near the United Arab Emirates coastline that was conducted on the sediments of *A. marina* and *A. germinans* (Schile et al., 2017), a study in Vietnam that examined tropical species of *Rhizophora* and *Avicennia* (Dung et al., 2016; Tue et al., 2014), an examination of species of *Avicennia* and *Rhizophora* present on the Venezuelan Caribbean coast (Barreto et al., 2016), and a study on *Rhizophora* species in the tropics (Donato et al., 2011). Thus, the negative association between SBD and SOC concentrations observed in this study are consistent with findings in different sediments in different regions of the globe.

The primary elements that contribute to establishing the SOC stock are SBD, SOC concentration, and the full depth at which the approximations are integrated (Stringer et al., 2015). Matsui (1998) described how beneficial conditions are produced for organic carbon preservation as a result of the anaerobic nature and the low rate of decomposition of mangrove sediments. The behaviour and quantity of SOC stock in the soil varies extensively in the various mangroves, and this is initiated by the particular carbon dynamics of the location and differences that result from the age of the forest, composition of the species, productivity and biomass of the vegetation, fertility of the soil, location of the inter-tide, sedimentation of suspended materials, edaphic conditions of soil (such as pH, salt content, and redox potential), and structure of the community (Alongi et al., 2003; Gleason and Ewel, 2002; Khan et al., 2007; Ray et al., 2011; Sanderman et al., 2018; Twilley et al., 2018).

Sanderman et al. (2018) noted that large amounts of soil carbon can build up in many mangrove forests but not in others. Significant differences can be found in the stocks of soil carbon in the various mangrove forests (Jardine and Siikamäki, 2014) and within the same forest of mangroves (Kauffman et al., 2011). Previous studies have also shown the differences in carbon stock across the globe in various mangrove forests (Donato et al., 2011; Kauffman et al., 2011; Khan et al., 2007). Generally, lower SOC stocks are found in mangroves located in arid and sub-humid areas than in humid areas (Schile et al., 2017). Moreover, a significant difference in the SOC stock for each unit area through the latitudinal bands was determined for mangroves from 0° to 10° S, with these two points indicating the greatest SOC stock levels of 351 Mg C ha^{-1}, whereas those between 20° and 30° N had the least, at 222 Mg C ha^{-1} (Atwood et al., 2017). Table 2 lists the data for blue carbon across the globe. It is clear that the carbon stocks from sediments of *A. marina* and *R. mucronata* that flourish in the Farasan Islands are low to fair relative to the global values. In this study, the mean SOC stock (11.6 kg C m^{-2}) determined for the mangrove sediments of the Farasan Islands was 3.1 times lower than the worldwide mean values described for mangroves,

such as 36.1 kg C m^{-2} by Sanderman et al. (2018). The low level of SOC stock in the Farasan Islands may be because of small supplies of allochthonous matter or extreme environments that could have resulted in restricted levels of mangrove growth with trees that were dwarf-like with low biomass levels and increased rates of sediment respiration (Almahasheer et al., 2016a, b, 2017). Moreover, the sequestration of carbon may not have been encouraged by certain features of the habitats or by the geomorphological environment not being beneficial for their growth (Almahasheer et al., 2017). The results of Ren et al. (2010) further support this as they describe how stressful environments may lead to low SOC stocks that result from small supply levels of dead roots throughout a certain time period together with a low rate of falling debris. Furthermore, the value for SOC stock in this study may have been underestimated as a depth of over 3 m was recorded for the mangrove organic sediment in certain regions (Donato et al., 2011); however, this study only involved coring to depths of 0.5 m.

The build-up of organic carbon in the soil is the consequence of autochthonous matter being supplied via primary processes or the deposit of allochthonous matter and this being balanced against the loss of matter through erosion, mineralisation or decomposition, and leaching (Alongi, 2014). Sediment tends to be efficiently trapped and held in mangrove forests and this is attributed to the structure of the stems and their widespread roots (Furukawa et al., 1997; Krauss et al., 2003). The low rate of decomposition of root biomass together with the sediment's anoxic environment, leads to the build-up of a lot of organic carbon (Middleton and McKee, 2001). Climatic elements may also affect the sequestration of carbon in mangroves, such as through rainfall, temperature, and evapotranspiration (Alongi, 2008). Moreover, it could occur via coastal oceanographic systems such as currents, tidal heights, and geomorphology (Alongi, 2008). Other influences include the access to nutrients as described by Lovelock et al. (2014) and the functional traits of plants, including their turnover, the production inputs both above and below ground level, and the distribution of carbon (De Deyn et al., 2008; Nordhaus et al., 2006).

In this study, significant differences in CSR were demonstrated between *A. marina* and *R. mucronata* locations with greater average values in the *A. marina* sediments. These outcomes were consistent with the findings in the Vellar–Coleroon estuary, India, where higher results were observed for *A. marina* with a CSR that was 75% greater than that of *R. mucronata* (Kathiresan et al., 2013). The average CSR measured for the mangrove forests of Farasan Islands was from 4.8 to 5.4 g C m^{-2} yr^{-1}. This is similar to results of the study on the southern Saudi Arabian Red Sea mangrove sediments where a value of 4.7 g C m^{-2} yr^{-1} was described (Arshad et al., 2018). The results of this study are also similar to those reported by Shaltout et al. (2019) who registered a mean CSR value of 5.6 g C m^{-2} yr^{-1} in the mangroves of the Red Sea. All these values, however, are greater than those recorded by Almahasheer et al. (2017) who described a mean CSR value of 3.5 g C m^{-2} yr^{-1} for the mangrove sediments of the central region of the Red Sea. Alongi (2012) described the mean CSR values at the global level as 174.0 g C m^{-2} yr^{-1}, which is 34.1 times greater than that in the present study. The low levels determined in this study are probably caused by the following: absence of freshwater, oligotrophic aspects, low levels of allochthonous matter supplied to the Red Sea, and man-made stressors (Almahasheer et al., 2017; Kathiresan et al., 2013); extremely arid conditions affecting mangrove growth (Almahasheer et al., 2017); lower primary productivity in Red Sea mangrove forests (Arshad et al., 2018); high temperature and water eutrophication (Shaltout et al., 2019); and heavy metal pollution that may negatively influence primary production (Bouillon et al., 2008; Arshad et al., 2018). High temperature is known to have a strong influence on litter decomposition (Hanson et al., 1984). According to Schlesinger (1997), the decomposition rate doubles with every 10°C increase in temperature which means a low CSR. In addition, it has been reported that the disposal of nutrients (e.g. N and P) can accelerate the decomposition of mangrove SOM and thereby reduce SOC stocks (Feller et al., 2003; Suárez-Abelenda et al., 2014). Furthermore, coarse carbonates that are biogenic in nature are the primary building material of the mangroves in the soil of the Farasan Islands. This may also be indicated as a reason for the lower CSR levels of the mangroves that flourish in environments that are uninviting for the accretion of soil, production of biomass, and preservation than in mangroves from subtropical or temperate regions (Almahasheer et al., 2017).

5. Recommendations

The past five decades have seen the loss of one-third of the Earth's mangroves, which makes them one of the highly threatened ecosystems (Alongi, 2002). This is because these ecosystems are the source of fuel, food, timber, and medicine (Alongi, 2002). The change in the manner of mangrove land utilisation results in the loss of stored carbon into the atmosphere. It also affects other benefits provided by this ecosystem such as a habitat for marine life, greater levels of biodiversity, and protection at the coastal level (Castillo et al., 2017). This study evaluated the CSP of *R. mucronata* and *A. marina* locations along the coastline of the Farasan Islands and estimated values of 10.3 and 11.8 Mg C yr^{-1}, respectively. By employing conversion factor of 3.67 by Sahu and Kathiresan (2019), it was determined that *R. mucronata* and *A. marina* can sequester CO_{2e} yr^{-1} at levels of 37,801 and 43,306, respectively, which is equivalent to 6.3×10^{-8} and 7.2×10^{-8}, respectively, of the complete carbon emissions of Saudi Arabia for 2014 (601,047 kt CO_{2e}) (Trading Economics, 2019). It is, therefore, imperative that these ecosystems are not only protected but also re-established to ensure they play their part in the sequestration of carbon and for all the other benefits that they provide.

Acknowledgements

The authors extend their appreciation to the Deanship of Scientific Research at King Khalid University for funding this work through Research Group Project under grant number R.G.P. 2/56/40.

References

Abu-Zied, R.H., Bantan, R.A., Basaham, A.S., El Mamoney, M.H., Al-Washmi, H.A., 2011. Composition, distribution, and taphonomy of nearshore benthic foraminifera of the Farasan Islands, Southern Red Sea, Saudi Arabia. J. Foraminifer Res. 41 (4), 349—362, https://doi.org/10.2113/gsjfr.41.4.349.

Adame, M.F., Kauffman, J.B., Boone, J., Medina, I., Gamboa, J.N., Torres, O., Caamal, J.P., Reza, M., Herrera-Silveira, J.A., 2013. Carbon stocks of tropical coastal wetlands within the karstic landscape of the Mexican Caribbean. PLOS One 8 (2), e56569, https://doi.org/10.1371/journal.pone.0056569.

Al Mutairi, K., El-Bana, M., Mansor, M., Al-Rowaily, S., Mansor, A., 2012. Floristic diversity, composition, and environmental correlates on the arid, coralline islands of the Farasan Archipelago, Red Sea, Saudi Arabia. Arid Land Res. Manage. 26 (2), 137—150, https://doi.org/10.1080/15324982.2012.656179.

Alfarhan, A.H., Al-Turki, T.A., Thomas, J., Basahy, R.A., 2002. Annotated list to the flora of Farasan Archipelago, Southern Red Sea, Saudi Arabia. Taeckholmia 22 (1), 1—33.

Allison, M.A., Khan, S.R., Goodbred Jr., S.L., Kuehl, S.A., 2003. Stratigraphic evolution of the late Holocene Ganges-Brahmaputra lower delta plain. Sediment Geol. 155 (3-4), 317—342, https://doi.org/10.1016/S0037-0738(02)00185-9.

Almahasheer, H., Duarte, C., Irigoien, X., 2016a. Nutrient limitation in central Red Sea mangroves. Front. Mar. Sci. 3, art. no. 271, https://doi.org/10.3389/fmars.2016.00271.

Almahasheer, H., Duarte, C., Irigoien, X., 2016b. Phenology and growth dynamics of *Avicennia marina* in the central Red Sea. Sci. Rep. 6 (1), art. no. 37785, https://doi.org/10.1038/srep37785.

Almahasheer, H., Serrano, O., Duarte, C., Arias-Ortiz, A., Masque, P., Irigoien, X., 2017. Low carbon sink capacity of Red Sea mangroves. Sci. Rep. 7 (1), art. no. 9700, https://doi.org/10.1038/s41598-017-10424-9.

Alongi, D.M., 1998. Coastal Ecosystem Processes. CRC Press, Florida, 448 pp.

Alongi, D.M., 2002. Present state and future of the world's mangrove forests. Environ. Conserv. 29 (3), 331—349, https://doi.org/10.1017/S0376892902000231.

Alongi, D.M., 2007. The contribution of mangrove ecosystems to global carbon cycling and greenhouse gas emissions. In: Tateda, Y., Upstill-Goddard, R., Goreau, T., Alongi, D., Nose, A., Kristensen, E., Wattayakorn, G. (Eds.), Greenhouse Gas and Carbon Balances in Mangrove Coastal Ecosystems. Maruzen, Tokyo, 1—10.

Alongi, D.M., 2008. Mangrove forests: Resilience, protection from tsunamis, and responses to global climate change. Estuar. Coast. Shelf Sci. 76 (1), 1—13, https://doi.org/10.1016/j.ecss.2007.08.024.

Alongi, D.M., 2012. Carbon sequestration in mangrove forests. Carbon Manage. 3 (3), 313—322, https://doi.org/10.4155/cmt.12.20.

Alongi, D.M., 2014. Carbon cycling and storage in mangrove forests. Annu. Rev. Mar. Sci. 6 (1), 195—219, https://doi.org/10.1146/annurev-marine-010213-135020.

Alongi, D.M., Clough, B.F., Dixon, P., Tirendi, F., 2003. Nutrient partitioning and storage in arid-zone forests of the mangroves *Rhizophora stylosa* and *Avicennia marina*. Trees 17 (1), 51—60, https://doi.org/10.1007/s00468-002-0206-2.

Alongi, D.M., Tirendi, F., Clough, B., 2000. Below-ground decomposition of organic matter in forests of the mangroves *Rhizophora stylosa* and *Avicennia marina* along the arid coast of Western Australia. Aquat. Bot. 68 (2), 97—122, https://doi.org/10.1016/S0304-3770(00)00110-8.

Alongi, D.M., Wattayakorn, G., Pfitzner, J., Tirendi, F., Zagorskis, I., Brunskill, G., Davidson, A., Clough, B., 2001. Organic carbon accumulation and metabolic pathways in sediments of mangrove forests in southern Thailand. Mar. Geol. 179 (1—2), 85—103, https://doi.org/10.1016/S0025-3227(01)00195-5.

Alwelaie, A.N., Chaudary, S.A., Alwetaid, Y., 1993. Vegetation of some Red Sea islands of the Kingdom of Saudi Arabia. J. Arid Environ. 24 (3), 287—296, https://doi.org/10.1006/jare.1993.1025.

Arshad, M., Alrumman, S., Eid, E.M., 2018. Evaluation of carbon sequestration in the sediment of polluted and non-polluted locations of mangroves. Fund. Appl. Limnol. 192 (1), 53—64, https://doi.org/10.1127/fal/2018/1127.

Atwood, T.B., Connolly, R.M., Almahasheer, H., Carnell, P.E., Duarte, C.M., Lewis, C.J.E., Irigoien, X., Kelleway, J.J., Lavery, P.S., Macreadie, P.I., Serrano, O., Sanders, C.J., Santos, I., Steven, A.D.L., Lovelock, C.E., 2017. Global patterns in mangrove soil carbon stocks and losses. Nat. Clim. Chang. 7, 523—528, https://doi.org/10.1038/nclimate3326.

Bantan, R.A., 1999. Geology and Sedimentary Environments of Farasan Bank (Saudi Arabia) Southern Red Sea: A Combined Remote Sensing and Field Study. University of London, London, 296 pp.

Barreto, M.B., Lo Mónaco, S., Díaz, R., Barreto-Pittol, E., López, L., Peralba, M.C.R., 2016. Soil organic carbon of mangrove forests (*Rhizophora* and *Avicennia*) of the Venezuelan Caribbean coast. Org. Geochem. 100 (1), 51—61, https://doi.org/10.1016/j.orggeochem.2016.08.002.

Bianchi, T.S., Allison, M.A., Zhao, J., Li, X., Comeaux, R.S., Feagin, R.A., Kulawardhana, R.W., 2013. Historical reconstruction of mangrove expansion in the Gulf of Mexico: Linking climate change with carbon sequestration in coastal wetlands. Estuar. Coast. Shelf Sci. 119 (1), 7—16, https://doi.org/10.1016/j.ecss.2012.12.007.

Bouillon, S., Borges, A., Casteneda-Moya, E., Diele, K., Dittmar, T., 2008. Mangrove production and carbon sinks: A revision of global budget estimates. Global Biogeochem. Cy. 22 (2), GB2013, https://doi.org/10.1029/2007GB003052.

Bouillon, S., Dahdouh-Guebas, F., Rao, A.V.V.S., Koedam, N., Dehairs, F., 2003. Sources of organic carbon in mangrove sediments: variability and possible ecological implications. Hydrobiologia 495 (1—3), art. no. 3339, https://doi.org/10.1023/A:1025411506526.

Bunting, P., Rosenqvist, A., Lucas, R.M., Rebelo, L.-M., Hilarides, L., Thomas, N., Hardy, A., Itoh, T., Shimada, M., Finlayson, C.M., 2018. The global mangrove watch-A new 2010 global baseline of mangrove extent. Remote Sens. 10 (1), art. no. 1669, https://doi.org/10.3390/rs10101669.

Castillo, J.A.A., Apan, A.A., Maraseni, T.N., Salmo III, S.G., 2017. Soil C quantities of mangrove forests, their competing land uses, and their spatial distribution in the coast of Honda Bay, Philippines. Geoderma 293 (1), 82—90, https://doi.org/10.1016/j.geoderma.2017.01.025.

Costanza, R., d'Arge, R., de Groot, R., Farber, S., Grasso, M., Hannon, B., Limburg, K., Naeem, S., O'Neill, R.V., Paruelo, J., Raskin, R.G., Sutton, P., van den Belt, M., 1997. The value of the world's ecosystem services and natural capital. Nature 387, 253—260, https://doi.org/10.1038/387253a0.

Dabbagh, A., Hölzl, H., Schnier, H., 1984. Farasan Islands. In: Tado, A., Zötl, J.G. (Eds.), Quaternary Periods in Saudi Arabia, 2. Springer-Verlag, Wienn & New York, 212—220.

De Deyn, G., Cornelissen, J.H.C., Bardgett, R.D., 2008. Plant functional traits and soil carbon sequestration in contrasting biomes. Ecol. Lett. 11 (5), 516—531, https://doi.org/10.1111/j.1461208;0248.2008.01164.x.

Donato, D., Kauffman, J., Murdiyarso, D., Kurnianto, S., Stidham, M., Kanninen, M., 2011. Mangroves among the most carbon-rich forests in the tropics. Nat. Geosci. 4 (5), 293—297, https://doi.org/10.1038/ngeo1123.

Donato, D.C., Kauffman, J.B., Mackenzie, R.A., Ainsworth, A., Pfleeger, A.Z., 2012. Whole-island carbon stocks in the tropi-

cal Pacific: Implications for mangrove conservation and upland restoration. J. Environ. Manage. 97 (1), 89—96, https://doi.org/10.1016/j.jenvman.2011.12.004.

Duke, N.C., Meynecke, J.O., Dittmann, S., Ellison, A.M., Anger, K., Berger, U., Cannicci, S., Diele, K., Ewel, K.C., Field, C.D., Koedam, N., Lee, S.Y., Marchand, C., Nordhaus, I., Dahdouh-Guebas, F., 2007. A world without mangroves? Science 317, 41—42, https://doi.org/10.1126/science.317.5834.41b.

Dung, L.V., Tue, N.T., Nhuan, M.T., Omori, K., 2016. Carbon storage in a restored mangrove forest in Can Gio Mangrove Forest Park, Mekong Delta, Vietnam. Forest Ecol. Manage. 380 (1), 31—40, https://doi.org/10.1016/j.foreco.2016.08.032.

Eid, E.M., Arshad, M., Shaltout, K.H., El-Sheikh, M.A., Alfarhan, A.H., Picó, Y., Barcelo, D., 2019. Effect of the conversion of mangroves into shrimp farms on carbon stock in the sediment along the southern Red Sea coast, Saudi Arabia. Environ. Res. 176, 108536, https://doi.org/10.1016/j.envres.2019.108536.

Eid, E.M., El-Bebany, A.F., Alrumman, S.A., 2016. Distribution of soil organic carbon in the mangrove forests along the southern Saudi Arabian Red Sea coast. Rend. Fis. Acc. Lincei. 27 (4), 629—637, https://doi.org/10.1007/s12210-016-0542-6.

Eid, E.M., Shaltout, K.H., 2016. Distribution of soil organic carbon in the mangrove *Avicennia marina* (Forssk.) Vierh. along the Egyptian Red Sea coast. Reg. Stud. Mar. Sci. 3 (1), 76—82, https://doi.org/10.1016/j.rsma.2015.05.006.

El-Demerdash, M.A., 1996. The vegetation of the Farasān Islands, Red Sea, Saudi Arabia. J. Veg. Sci. 7 (1), 81—88, https://doi.org/10.2307/3236419.

Feller, I.C., McKee, K.L., Whigham, D.F., O'Neill, J.P., 2003. Nitrogen vs. phosphorus limitation across an ecotonal gradient in a mangrove forest. Biogeochemistry 62 (2), 145—175, https://doi.org/10.1023/A:1021166010892.

Ferreira, T.O., Otero, X.L., de Souza Junior, V.S., Vidal-Torrado, P., Macías, F., Firme, L.P., 2010. Spatial patterns of soil attributes and components in a mangrove system in Southeast Brazil (São Paulo). J. Soils Sediments 10 (6), 995—1006, https://doi.org/10.1007/s11368-010-0224-4.

Fujimoto, K., Imaya, A., Tabuchi, R., Kuramoto, S., Utsugi, H., Murofushi, T., 1999. Belowground carbon storage of Micronesian mangrove forests. Ecol. Res. 14 (4), 409—413, https://doi.org/10.1046/j.1440-1703.1999.00313.x.

Furukawa, K., Wolanski, E., Mueller, H., 1997. Currents and sediment transport in mangrove forests. Estuar. Coast. Shelf Sci. 52 (3), 505—514, https://doi.org/10.1006/ecss.1996.0120.

Gao, Y., Zhou, J., Wang, L., Guo, J., Feng, J., Wu, H., Lin, G., 2019. Distribution patterns and controlling factors for the soil organic carbon in four mangrove forests of China. Global Ecol. Conserv. 17, e00575, https://doi.org/10.1016/j.gecco.2019.e00575.

Girmay, G., Singh, B.R., 2012. Changes in soil organic carbon stocks and soil quality: land-use system effects in northern Ethiopia. Acta Agric. Scand., Sect. B — Soil Plant Sci. 62 (6), 519—530, https://doi.org/10.1080/09064710.2012.663786.

Gleason, S.M., Ewel, K.C., 2002. Organic matter dynamics on the forest floor of a Micronesian mangrove forest: An investigation of species composition shifts. Biotropica 34 (2), 190—198, https://doi.org/10.1111/j.1744-7429.2002.tb00530.x.

Hanson, B.J., Cummins, K.W., Barnes, J.R., Carter, M.V., 1984. Leaf litter processing in aquatic systems: A two variable model. Hydrobiologia 111, 21—29, https://doi.org/10.1007/BF00007376.

Huang, L.Y., 2015. Distribution Characteristics and Influential Factors of Soil Organic Carbon in Mangrove Wetlands in Guangdong Province M.Sc. thesis. Guangxi Teachers Education University, Guangxi.

IPCC (Intergovernmental Panel on Climate Change), 2007. The Fourth Assessment Report Climate Change 2007. IPCC, Geneva.

Jacotot, A., Marchand, C., Rosenheim, B.E., Domack, E.W., Allenbach, M., 2018. Mangrove sediment carbon stocks along an elevation gradient: Influence of the late Holocene marine regression (New Caledonia). Mar. Geol. 404 (1), 60—70, https://doi.org/10.1016/j.margeo.2018.07.005.

Jardine, S.L., Siikamäki, J.V., 2014. A global predictive model of carbon in mangrove soils. Environ. Res. Lett. 9 (10), 104013, https://doi.org/10.1088/1748-9326/9/10/104013.

Jennerjahn, T.C., Ittekot, V., 2002. Relevance of mangroves for the production and deposition of organic matter along tropical continental margins. Naturwissenschaften 89 (1), 23—30, https://doi.org/10.1007/s00114-001-0283-x.

Johnston, C.A., Groffman, P., Breshears, D.D., Cardon, Z.G., Currie, W., Emanuela, W., Gaudinski, J., Jackson, R.B., Lajtha, K., Nadelhoffer, K., Nelson, D., Post, W.M., Retallack, G., Wielopolski, L., 2004. Carbon cycling in soil. Front. Ecol. Environ. 2 (10), 522—528, https://doi.org/10.1890/1540-9295(2004)002[0522:CCIS]2.0.CO;2.

Jones, J.B., 2001. Laboratory Guide for Conducting Soil Tests and Plant Analysis. CRC Press, Florida.

Jones, T., Ratsimba, H., Ravaoarinorotsihoarana, L., Cripps, G., Bey, A., 2014. Ecological variability and carbon stock estimates of mangrove ecosystems in northwestern Madagascar. Forests 5 (1), 177—205, https://doi.org/10.3390/f5010177.

Jonsson, M.N., Hedman, A.M., 2019. Carbon stock assessment of mangrove ecosystems in Batticaloa Lagoon, Sri Lanka, with different degree of human disturbances. Singapore J. Trop. Geo. 40 (2), 199—218, https://doi.org/10.1111/sjtg.12267.

Kathiresan, K., Anburaj, R., Gomathi, V., Saravanakumar, K., 2013. Carbon sequestration potential of *Rhizophora mucronata* and *Avicennia marina* as influenced by age, season, growth and sediment characteristics in southeast coast of India. J. Coast Conserv. 17 (3), 397—408, https://doi.org/10.1007/s11852-013-0236-5.

Kauffman, J.B., Donato, D.C., 2012. Protocols for the Measurement, Monitoring and Reporting of Structure, Biomass and Carbon Stocks in Mangrove Forests. Working paper 86. CIFOR, Bogor, 44 pp., https://doi.org/10.17528/cifor/003749.

Kauffman, J.B., Heider, C., Cole, T.G., Dwire, K.A., Donato, D.C., 2011. Ecosystem carbon stocks of Micronesian mangrove forests. Wetlands 31 (2), 343—352, https://doi.org/10.1007/s13157-011-0148-9.

Kauffman, J.B., Heider, C., Norfolk, J., Payton, F., 2014. Carbon stocks of intact mangroves and carbon emissions arising from their conversion in the Dominican Republic. Ecol. Appl. 24 (3), 518—527, https://doi.org/10.1890/13-0640.1.

Kauffman, J.B., Trejo, H.H., Garcia, M.d.C.J., Heider, C., Contreras, W.M., 2016. Carbon stocks of mangroves and losses arising from their conversion to cattle pastures in the Pantanos de Centle, Mexico. Wetlands Ecol. Manage. 24 (2), 203—216, https://doi.org/10.1007/s11273-015-9453-z.

Khalil, H.M., 2012. Pliocene-Pleistocene stratigraphy and macrofauna of the Farasan Islands, South East Red Sea, Saudi Arabia. Arab. J. Geosci. 5 (6), 1223—1245, https://doi.org/10.1007/s12517-011-0300-0.

Khan, M.A., Kumar, A., Muqtadir, A., 2010. Distribution of mangroves along the Red Sea coast of the Arabian Peninsula: Part 2. The southern coast of western Saudi Arabia. Earth Sci. India 3 (3), 154—162.

Khan, M.N.I., Suwa, R., Hagihara, A., 2007. Carbon and nitrogen pools in a mangrove stand of *Kandelia obovata* (S., L.) Yong: vertical distribution in the soil-vegetation system. Wetlands Ecol. Manage. 15 (2), 141—153, https://doi.org/10.1007/s11273-006-9020-8.

Krauss, K.W., Allen, J.A., Cahoon, D.R., 2003. Differential rates of vertical accretion and elevation change among aerial root types in Micronesian mangrove forests. Estuar. Coast. Shelf Sci. 56 (2), 251—259, https://doi.org/10.1016/S0272-7714(02)00184-1.

Kristensen, E., Bouillon, S., Dittmar, T., Marchand, C., 2008. Organic carbon dynamics in mangrove ecosystems: A review. Aquat. Bot. 89 (2), 201—219, https://doi.org/10.1016/j.aquabot.2007.12.005.

Kusumaningtyas, M.A., Hutahaean, A.A., Fischer, H.W., Pérez-Mayo, M., Ransby, D., Jennerjahn, T.C., 2019. Variability in the organic carbon stocks, sources, and accumulation rates of Indonesian mangrove ecosystems. Estuar. Coast. Shelf Sci. 218, 310—323, https://doi.org/10.1016/j.ecss.2018.12.007.

Lacerda, L., Ittekkot, V., Patchineelam, S., 1995. Biogeochemistry of mangrove soil organic matter: A comparison between *Rhizophora* and *Avicennia* soils in south-eastern Brazil. Estuar. Coast. Shelf S. 40 (6), 713—720, https://doi.org/10.1006/ecss.1995.0048.

Lovelock, C.E., Feller, I.C., Reef, R., Ruess, R.W., 2014. Variable effects of nutrient enrichment on soil respiration in mangrove forests. Plant Soil 379 (1-2), 135—148, https://doi.org/10.1007/s11104-014-2036-6.

Mackenzie, R.A., Foulk, P.B., Klump, J.V., Weckerly, K., Purbospito, J., Murdiyarso, D., Donato, D.C., Nam, V.N., 2016. Sedimentation and belowground carbon accumulation rates in mangrove forests that differ in diversity and land use: A tale of two mangroves. Wetlands Ecol. Manage. 24 (2), 245—261, https://doi.org/10.1007/s11273-016-9481-3.

Mandura, A.S., Khafaji, A.K., Saifullah, S.M., 1988. Ecology of a mangrove stand of a central Red Sea coast area: Ras Hatiba (Saudi Arabia). Proc. Saudi Biol. Soc. 11 (1), 85—112.

Matsui, N., 1998. Estimated stocks of organic carbon in mangrove roots and sediments in Hinchinbrook Channel, Australia. Mangroves Salt Marshes 2 (4), 199—204, https://doi.org/10.1023/A:1009959909208.

Meersmans, J., De Ridder, F., Canters, F., De Baets, S., Van Molle, M., 2008. A multiple regression approach to assess the spatial distribution of soil organic carbon (SOC) at the regional scale (Flanders Belgium). Geoderma 143 (1—2), 1—13, https://doi.org/10.1016/j.geoderma.2007.08.025.

Middleton, B.A., McKee, K.L., 2001. Degradation of mangrove tissues and implications for peat formation in Belizean Island forests. J. Ecol. 89 (5), 818—828, https://doi.org/10.1046/j.0022-0477.2001.00602.x.

Morcos, S.A., 1970. Physical and chemical oceanography of the Red Sea. Oceanogr. Mar. Biol. Ann. Rev. 8, 73—202.

Nóbrega, G.N., Ferreira, T.O., Artur, A.G., Mendonça, E.S., Leão, R.A., Teixeira, A.S., Otero, X.L., 2015. Evaluation of methods for quantifying organic carbon in mangrove soils from semi-arid region. J. Soil. Sediment. 15 (2), 282—291, https://doi.org/10.1007/s11368-014-1019-9.

Nóbrega, G.N., Ferreira, T.O., Neto, M.S., Mendonça, E.S., Romero, R.E., Otero, X.L., 2019. The importance of blue carbon soil stocks in tropical semiarid mangroves: A case study in Northeastern Brazil. Environ. Earth Sci. 78 (12), art. no. 369, https://doi.org/10.1007/s12665-019-8368-z.

Nordhaus, I., Wolff, M., Diele, K., 2006. Litter processing and population food intake of the mangrove crab *Ucides cordatus* in a high intertidal forest in northern Brazil. Estuar. Coast. Shelf Sci. 67 (1—2), 239—250, https://doi.org/10.1016/j.ecss.2005.11.022.

Ochoa-Gómez, J.G., Lluch-Cota, S.E., Rivera-Monroy, V.H., Lluch-Cota, D.B., Troyo-Diéguez, E., Oechel, W., Serviere-Zaragoza, E., 2019. Mangrove wetland productivity and carbon stocks in an arid zone of the Gulf of California (La Paz Bay, Mexico). Forest Ecol. Manage. 442, 135—147, https://doi.org/10.1016/j.foreco.2019.03.059.

Otero, X.L., Méndez, A., Nóbrega, G.N., Ferreira, T.O., Santiso-Taboada, M.J., Meléndez, W., Macías, F., 2017. High fragility of the soil organic C pools in mangrove forests. Mar. Pollut. Bull. 119 (1), 460—464, https://doi.org/10.1016/j.marpolbul.2017.03.074.

Perera, K.A.R.S., Amarasinghe, M.D., 2019. Carbon sequestration capacity of mangrove soils in micro tidal estuaries and lagoons: A case study from Sri Lanka. Geoderma 347, 80—89, https://doi.org/10.1016/j.geoderma.2019.03.041.

Pérez, A., Machado, W., Gutierrez, D., Stokes, D., Sanders, L., Smoak, J.M., Santos, I., Sanders, C.J., 2017. Changes in organic carbon accumulation driven by mangrove expansion and deforestation in a New Zealand estuary. Estuar. Coast. Shelf Sci. 192, 108—116, https://doi.org/10.1016/j.ecss.2017.05.009.

PERSGA (the Regional Organization for the Conservation of the Environment of the Red Sea and Gulf of Aden), 2004. Status of Mangroves in the Red Sea and Gulf of Aden. PERSGA Technical Series no. 11. PERSGA, Jeddah.

Phang, V.X.H., Chou, L.M., Friess, D.A., 2015. Ecosystem carbon stocks across a tropical intertidal habitat mosaic of mangrove forest, seagrass meadow, mudflat and sandbar. Earth Surf. Proc. Land. 40 (10), 1387—1400, https://doi.org/10.1002/esp.3745.

Pravin, R., Dodha, V., Vidya, D., Manab, C., Saroj, M., 2013. Soil bulk density as related to soil texture, organic matter content and available total nutrients of Coimbatore soil. Int. J. Sci. Res. Publ. 3 (2), 1—8.

Pribyl, D.W., 2010. A critical review of the conventional SOC to SOM conversion factor. Geoderma 156 (3—4), 75—83, https://doi.org/10.1016/j.geoderma.2010.02.003.

Price, A.R., Medley, P.A., McDowall, R.J., Dawson-Shepherd, A.R., Hogarth, P.J., Ormond, R.F., 1987. Aspects of mangal ecology along the Red Sea coast of Saudi Arabia. J. Nat. Hist. 21 (2), 449—464, https://doi.org/10.1080/00222938700771121.

Radabaugh, K.R., Moyer, R.P., Chappel, A.R., Powell, C.E., Bociu, I., Clark, B.C., Smoak, J.M., 2018. Coastal blue carbon assessment of mangroves, salt marshes, and salt barrens in Tempa Bay, Florida, USA. Estuar. Coast. 41 (5), 1496—1510, https://doi.org/10.1007/s12237-017-0362-7.

Ray, R., Ganguly, D., Chowdhury, C., Dey, M., Das, S., Dutta, M., Mandal, S., Majumder, N., De, T., Mukhopadhyay, S., Jana, T., 2011. Carbon sequestration and annual increase of carbon stock in a mangrove forest. Atmos. Environ. 45 (28), 5016—5024, https://doi.org/10.1016/j.atmosenv.2011.04.074.

Ren, H., Chen, H., Li, Z., Han, W., 2010. Biomass accumulation and carbon storage of four different aged *Sonneratia apetala* plantations in Southern China. Plant Soil 327 (1—2), 279—291, https://doi.org/10.1007/s11104-009-0053-7.

Rumpel, C., Amiraslani, F., Koutika, L.-S., Smith, P., Whitehead, D., Wollenberg, E., 2018. Put more carbon in soils to meet Paris climate pledges. Nature 564 (7734), 32—34, https://doi.org/10.1038/d41586-018-07587-4.

Saderne, V., Cusack, M., Almahasheer, H., Serrano, O., Masqué, P., Arias-Ortiz, A., Krishnakumar, P.K., Rabaoui, L., Qurban, M.A., Duarte, C.M., 2018. Accumulation of carbonates contributes to coastal vegetated ecosystems keeping pace with sea level rise in an arid region (Arabian Peninsula). J. Geophys. Res. Biogeo. 123, 1498—1510, https://doi.org/10.1029/2017jg004288.

Sahu, S.K., Kathiresan, K., 2019. The age and species composition of mangroves forest directly influence the net primary productivity and carbon sequestration potential. Biocatalysis Agr. Biotechnol. 20, 101235, https://doi.org/10.1016/j.bcab.2019.101235.

Saifullah, S.M., 1994. Mangrove ecosystem of Saudi Arabian Red Sea coast — An overview. J. K.A.U.: Mar. Sci. 7, 263—270.

Saintilan, N., Rogers, K., Mazumder, D., Woodroffe, C., 2013. Allochthonous and autochthonous contributions to carbon accumulation and carbon store in southeastern Australian coastal wetlands. Estuar. Coast. Shelf Sci. 128, 84—92, https://doi.org/10.1016/j.ecss.2013.05.010.

Sanderman, J., Hengl, T., Fiske, G., Solvik, K., Adame, M., Benson, L., Bukoski, J., Carnell, P., Cifuentes-Jara, M., Donato, D., Duncan, C., Eid, E., zu Ermgassen, P., Ewers Lewis, C., Macreadie, P., Glass, L., Gress, S., Jardine, S., Jones, T.,

Nsombo, E., Rahman, M., Sanders, C., Spalding, M., Landis, E., 2018. A global map of mangrove forest soil carbon at 30 m spatial resolution. Environ. Res. Lett. 13 (5), 12. Art. no. 055002 https://doi.org/10.1088/1748-9326/aabe1c.

Sanders, C.J., Maher, D.T., Tait, D.R., Williams, D., Holloway, C., Sippo, J.Z., Santos, I.R., 2016. Are global mangrove carbon stocks driven by rainfall? J. Geophys. Res. Biogeo. 121 (10), 2600—2609, https://doi.org/10.1002/2016JG003510.

Sanders, C.J., Smoak, J.M., Naidu, A.S., Sanders, L.M., Patchineelam, S.R., 2010. Organic carbon burial in a mangrove forest, margin and intertidal mud flat. Estuar. Coast. Shelf Sci. 90 (3), 168—172, https://doi.org/10.1016/j.ecss.2010.08.013.

Schile, L.M., Kauffman, J.B., Crooks, S., Fourqurean, J.W., Glavan, J., Megonigal, J.P., 2017. Limits on carbon sequestration in arid blue carbon ecosystems. Ecol. Appl. 27 (3), 859—874, https://doi.org/10.1002/eap.1489.

Schlesinger, W.H., 1997. Biogeochemistry, an Analysis of Global Change. Acad. Press, San Diego, California, 688 pp.

Shaltout, K.H., Ahmed, M.T., Alrumman, S.A., Ahmed, D.A., Eid, E.M., 2019. Evaluation of the carbon sequestration capacity of arid mangroves along nutrient availability and salinity gradients along the Red Sea coastline of Saudi Arabia. Oceanologia 62 (1), 14 pp. in press https://doi.org/10.1016/j.oceano.2019.08.002 .

Sherry, S., Ramon, A., Eric, M., Richard, E., Barry, W., Peter, D., Susan, T., 1998. Precambrian shield wetlands: Hydrologic control of the sources and export of dissolved organic matter. Clim. Change 40 (2), 167—188, https://doi.org/10.1023/A:1005496331593.

SPSS, 2006. SPSS Base 15.0 User's Guide. SPSS Inc., Chicago.

Stringer, C.E., Trettin, C.C., Zarnoch, S.J., Tang, W., 2015. Carbon stocks of mangroves within the Zambezi River Delta, Mozambique. Forest Ecol. Manage. 354, 139—148, https://doi.org/10.1016/j.foreco.2015.06.027.

Suárez-Abelenda, M., Ferreira, T.O., Camps-Arbestain, M., Rivera-Monroy, V.H., Macías, F., Nóbrega, G.N., Otero, X.L., 2014. The effect of nutrient-rich effluents from shrimp farming on mangrove soil carbon storage and geochemistry under semi-arid climate conditions in northern Brazil. Geoderma 213, 551—559, https://doi.org/10.1016/j.geoderma.2013.08.007.

Taillardat, P., Friess, D.A., Lupascu, M., 2018. Mangrove blue carbon strategies for climate change mitigation are most effective at the national scale. Biol. Lett. 14 (10), 20180251, https://doi.org/10.1098/rsbl.2018.0251.

Tomlinson, P.B., 2016. The Botany of Mangroves. 2nd edn., Cambridge Univ. Press, Cambridge, 436 pp.

Trading Economics, 2019. Saudi Arabia — CO2 emissions (kt). https://tradingeconomics.com/saudi-arabia/co2-emissions-kt-wb-data.html (accessed 25. Sept. 2019).

Tue, N.T., Dung, L.V., Nhuan, M.T., Omori, K., 2014. Carbon storage of a tropical mangrove forest in Mui Ca Mau National Park, Vietnam. Catena 121, 119—126, https://doi.org/10.1016/j.catena.2014.05.008.

Tue, N.T., Hamaoka, H., Sogabe, A., Quy, T.D., Nhuan, M.T., Omori, K., 2011. The application of δ^{13} C and C/N ratios as indicators of organic carbon sources and paleoenvironmental change of the mangrove ecosystem from Ba Lat Estuary, Red River, Vietnam. Environ. Earth Sci. 64 (5), 1475—1486, https://doi.org/10.1007/s12665-011-0970-7.

Tue, N.T., Ngoc, N., Quy, T.D., Hamaoka, H., Nhuan, M.T., Omori, K., 2012. A cross-system analysis of sedimentary organic carbon in the mangrove ecosystems of Xuan Thuy National Park Vietnam. J. Sea Res. 67 (1), 69—76, https://doi.org/10.1016/j.seares.2011.10.006.

Twilley, R.R., Chen, R.H., Hargis, T., 1992. Carbon sinks in mangroves and their implications to carbon budget of tropical coastal ecosystems. Water Air Soil Pollut. 64 (1—2), 265—288, https://doi.org/10.1007/BF00477106.

Twilley, R.R., Rovai, A.S., Riul, P., 2018. Coastal morphology explains global blue carbon distributions. Front. Eco. Environ. 16 (9), 503—508, https://doi.org/10.1002/fee.1937.

Wilke, B.M., 2005. Determination of chemical and physical soil properties. In: Margesin, R., Schinner, F. (Eds.), Manual for Soil Analysis-Monitoring and Assessing Soil Bioremediation. Springer, Heidelberg, 47—95.

Woomer, P.L., Tieszen, L.L., Tappan, G., Touré, A., Sall, M., 2004. Land use change and terrestrial carbon stocks in Senegal. J. Arid Environ. 59 (3), 625—642, https://doi.org/10.1016/j.jaridenv.2004.03.025.

Xiaonan, D., Xiaoke, W., Lu, F., Zhiyun, O., 2008. Primary evaluation of carbon sequestration potential of wetlands in China. Acta. Ecol. Sinica 28 (2), 463—469, https://doi.org/10.1016/S1872-2032(08)60025-6.

Xin, K., Yan, K., Gao, C., Li, Z., 2018. Carbon storage and its influencing factors in Hainan Dongzhangang mangrove wetlands. Mar. Freshwater Res. 69 (5), 771—779, https://doi.org/10.1071/MF17101.

Xue, B., Yan, C., Lu, H., Bai, Y., 2009. Mangrove-derived organic carbon in sediment from Zhangjiang Estuary (China) mangrove wetland. J. Coast. Res. 25 (4), 949—956, https://doi.org/10.2112/08-1047.1.

Yang, J., Gao, J., Liu, B., Zhang, W., 2014. Sediment deposits and organic carbon sequestration along mangrove coasts of the Leizhou Peninsula, southern China. Estuar. Coast. Shelf Sci. 136, 3—10, https://doi.org/10.1016/j.ecss.2013.11.020.

Yong, Y., Baipeng, P., Guangcheng, C., Yan, C., 2011. Processes of organic carbon in mangrove ecosystems. Acta Ecol. Sinica 31 (3), 169—173, https://doi.org/10.1016/j.chnaes.2011.03.008.

Zimmerman, A.R., Canuel, E.A., 2000. A geochemical record of eutrophication and anoxia in Chesapeake Bay sediments: Anthropogenic influence on organic matter composition. Mar. Chem. 69 (1—2), 117—137, https://doi.org/10.1016/S0304-4203(99)00100-0.

Oceanologia (2020) 62, 214—225

Available online at www.sciencedirect.com

ScienceDirect

journal homepage: www.journals.elsevier.com/oceanologia

ORIGINAL RESEARCH ARTICLE

Effects of oxytetracycline on growth and chlorophyll *a* fluorescence in green algae (*Chlorella vulgaris*), diatom (*Phaeodactylum tricornutum*) and cyanobacteria (*Microcystis aeruginosa* and *Nodularia spumigena*)

Grzegorz Siedlewicz[a,*], Adam Żak[b], Lilianna Sharma[a], Alicja Kosakowska[a], Ksenia Pazdro[a]

[a] *Department of Marine Chemistry and Biochemistry, Institute of Oceanology, Polish Academy of Sciences, Sopot, Poland*
[b] *Department of Plant Physiology and Biotechnology, University of Gdańsk, Gdańsk, Poland*

Received 19 July 2019; accepted 27 December 2019
Available online 8 January 2020

KEYWORDS
Antibiotics;
Cyanobacteria;
Microalgae;
Chlorophyll *a* fluorescence;
Toxicity studies

Summary The study aimed at measuring the influence of a wide range of oxytetracycline concentrations, with particular attention to the low levels of the antibiotic on cyanobacteria *Microcystis aeruginosa* and *Nodularia spumigena*, diatom *Phaeodactylum tricornutum* and the model green algae *Chlorella vulgaris* by conducting prolonged toxicity tests (lasting 10 days). Standard measurements (cell number, optical density, chlorophyll *a* concentration) were combined with photosynthetic parameters measurements. The obtained results show that concentrations of oxytetracycline present in the environment can affect tested microorganisms. It was found to decrease photosystem II efficiency and disrupt the photosynthesis process. A careful interpretation of photosynthetic parameters allowed a better understanding of the mode of action of oxytetracycline in relation to non-target photoautotrophic organisms like cyanobac-

* Corresponding author at: Department of Marine Chemistry and Biochemistry, Institute of Oceanology, Polish Academy of Sciences, Powstańców Warszawy 55, 81—712 Sopot, Poland. Tel.: +48587311735; fax: +48585512130.
E-mail address: gsiedlewicz@iopan.gda.pl (G. Siedlewicz).
Peer review under the responsibility of the Institute of Oceanology of the Polish Academy of Sciences.

Production and hosting by Elsevier

https://doi.org/10.1016/j.oceano.2019.12.002

teria and microalgae. In conclusion, it would appear that the use of standard chronic toxicity tests (72 h) does not allow to accurately and reliably assess the chronic impact of bioactive compounds including drugs and their metabolites on water organisms. On this basis, we recommend the application of extended duration tests.

1. Introduction

The consumption of pharmaceuticals in terms of quantity and expenditure is increasing globally (Van Boeckel et al., 2014; Xu et al., 2014). Antibiotics have been broadly used in human and veterinary medicine to prevent and treat infections, as well as for other purposes including growth promotion in livestock production, prevention of bacteria-induced crop damage and as feed additives in aquacultures (Boxall et al., 2004). The most important pathways of antibiotic dissemination into the aquatic environment are wastewater effluents, manure application, aquacultures discharge and surface runoff (Kümmerer, 2009; McArdell et al., 2003). The majority of studies focused on the prevalence of antibiotics in freshwater bodies (lakes, rivers, groundwater). However several studies reported their presence in coastal or estuarine marine systems (e.g. Björlenius et al., 2018; Borecka et al., 2013, 2015, Gulkowska et al., 2007; Nödler et al., 2014; Pazdro et al., 2016; Siedlewicz et al., 2014, 2016, 2018; Wille et al., 2010, Yang 2011). The constant release of antibiotics, their bioactive properties, and continuous presence even at relatively low environmental concentrations ranging from ng dm^{-3} to $\mu g\ dm^{-3}$ in surface waters and from ng g^{-1} to $\mu g\ g^{-1}$ in sediments have caused major concerns about potential risks to aquatic ecosystems (Hernando et al., 2006; Ji et al., 2012; Kümmerer, 2010). Although the major environmental issue is associated with the development of resistance mechanisms in bacteria, the toxicity of antibiotics to non-target organisms also raises serious concerns (González-Pleiter et al., 2013). Phytoplankton species forming the basis of all marine food webs are extremely important as primary producers and shall be included in the risk group. For this reason, data from ecotoxicity tests with different phytoplankton species and the most commonly detected antibiotics is of great importance to illustrate the potential adverse effects. Nevertheless, most of the numerous available reports on the ecotoxicity of pharmaceuticals deal with freshwater organisms and acute ecotoxicity studies still predominate in comparison to the chronic ones (Arnold et al., 2014; Santos et al., 2010). It may also contribute to the increase of inaccuracy of the estimations of risk assessments often relayed on recalculations based on different backgrounds and/or trophic levels (EC, 2003).

Oxytetracycline is a bacteriostatic drug belonging to a group of tetracyclines being a class of inexpensive, broad-spectrum antimicrobial substances used in human and veterinary medicine. Antibiotics from this group are commonly used worldwide including all Baltic Sea countries (Schmidt et al., 2000; Wang et al. 2010). Oxytetracycline does not undergo metabolism and is renally and biliary excreted in unchanged form (Agwuh and MacGowan, 2006). In the euphotic zone of marine waters, oxytetracycline seems to easily photodegrade (Leal et al., 2016) which corresponds with the results from laboratory tests (Jiao et al., 2008; Pereira et al., 2011). Despite this, oxytetracycline is very often detected in the marine environment (Capone et al. 1996; Chen et al., 2015; Lalumera et al., 2004). Moreover, existing data suggest a long persistence of oxytetracycline in the aquatic sediments (Wang et al., 2010). In our previous studies concerning the Baltic Sea sediments, oxytetracycline concentration up to 1.515 $\mu g\ g^{-1}$ d.w. was reported, which was the highest value of all analyzed antibiotics in this region (Siedlewicz et al., 2018). Moreover, except results described by Ando et al. (2007), Guo et al. (2016) and Holten Lützhøft et al. (1999) most of existing ecotoxicological tests applying algae and cyanobacteria typically do not exceed the exposure period of 96 hours (Fu et al., 2017; Kolar et al., 2014; Kołodziejska et al., 2013). Therefore the full impact of oxytetracycline on aquatic phototrophic organisms and their ability to effectively carry out photosynthesis remains highly ambiguous. Furthermore, it can be assumed that oxytetracycline is continuously introduced to the environment so it is worth to know, how or if at all, it can affect phototrophic microorganisms in longer than reported in the literature period (up to 7 days) used in chronic tests (Dewez et al., 2018; Halling-Sørensen, 2000).

The photosynthetic apparatus efficiency has been reported to be the most sensitive factor for evaluating the degree of antibiotic-related stress damage in higher plants (Rachmilevitch et al., 2006). Recently, changes in the chlorophyll *a* fluorescence transient (OJIP transient) have been used to evaluate the extent of damage to the photosynthetic apparatus under several abiotic stresses. The OJIP transient is defined by O, J, I, and P steps, corresponding to the redox states of photosystem II (PSII) and photosystem I (PSI) and the efficiencies of electron transfer through the intersystem chain to the end electron acceptors at the PSI acceptor side (Strasser et al., 2000, 2004). Besides, the OJIP transient approach has useful and practical advantages: it is non-destructive, relatively easy to perform and allows rapid testing of any type of chlorophyll-containing sample regardless of its form (Strasser et al., 2000, 2004; Zushi et al., 2012). As it has been previously reported in the literature, the measurement of chlorophyll *a* fluorescence is a sensitive and reliable method of detection and quantification of organic pollution stress-induced changes in the PSII and PSI of plants (Chen et al., 2017; Gao and Tam, 2011; Pan et al. 2008; Żak et al. 2012). Despite this, so far only a few studies have been conducted on the impact of oxytetracycline or tetracycline on the photosynthesis system of marine autotrophic microorganisms (Guo et al. 2016; Van der Grinten et al., 2010; Xu et al. 2019).

The study aimed at measuring the influence of a wide range of oxytetracycline concentrations, with particular attention to levels of the antibiotic occurring in the Baltic Sea sediments, on selected algae and cyanobacteria by performing long-term exposure toxicity tests (10—11 days) lasting longer than standard toxicity tests. The extending of the toxicity test period may help to assess their utility in the estimation of the impact of contaminants continuously introduced to the environment. Microalgae and cyanobacteria have been selected due to their ecological relevance, sensitivity and because they are easily cultivated in the laboratory. *Chlorella vulgaris* Beijerink is a cosmopolitan species inhabiting fresh, brackish and marine waters and is commonly used as a reference organism in ecotoxicity tests (Borecka et al., 2016). *Phaeodactylum tricornutum* Bohlin is a model diatom representing a heterogeneous group of photosynthetic eukaryotes prevalent in freshwater and marine habitats. *Nodularia spumigena* Mertens ex Bornet & Flahault is a bloom-forming, filamentous cyanobacterium occurring in many brackish and estuarine waters worldwide. *Microcystis aeruginosa* Kützing is another marine/freshwater widespread cyanobacteria, which can form harmful blooms and is characterized by small cells usually organized into colonies. These four species were selected based on their occurrence in the Baltic Sea as well as their ubiquitous presence in aquatic ecosystems. In presented investigations standard measurements (optical density, chlorophyll *a* concentration) were combined with OJIP fluorescence transitions measurements, therefore results should also help in understanding the impact of oxytetracycline on photosynthesis apparatus in different species of autotrophic microorganisms.

2. Material and methods

2.1. Algal and cyanobacterial monocultures

As target species, we used: (1) green algae A1-76 *C. vulgaris* (Culture Collection IO PAN, Sopot) isolated from the Baltic Sea; (2) diatom *P. tricornutum* SAG 1090-1a (Culture Collection of Algae, University of Göttingen, Germany); (3) cyanobacteria PCC-7820 *M. aeruginosa* purchased from Pasteur Culture Collection of Cyanobacteria (Pasteur Institute, France) and CCNP1401 *N. spumigena* obtained from Division of Marine Biotechnology, University of Gdańsk. All species were grown on a liquid medium in the flasks (batch cultures) at 22°C ± 1, at continuous light (80 μmol photons m^{-2} s^{-1}). Cyanobacterial species were cultivated on: *M. aeruginosa* — 616 medium and *N. spumigena* — BG11 medium in salinity 7‰ (Stanier et al., 1971). For the culture of green algae *C. vulgaris* BBM medium was used (Bischoff and Bold, 1963) and for diatom *P. tricornutum* f/2 medium (salinity 7 ‰) (Guillard, 1975) prepared based on artificial seawater (Lyman and Fleming, 1940) was applied. Cultures used as inocula were in the logarithmic phase of growth.

2.2. Growth assay

Oxytetracycline standards were purchased from Sigma-Aldrich (Germany). Standard stock solutions were prepared in Milli-Q water before the start of the experiments.

Four experiments were performed, each on different species of microorganisms. Sterile cell-free medium with oxytetracycline was added to flasks containing target species *C. vulgaris, P. tricornutum, M. aeruginosa*, and *N. spumigena*. The total volume of medium in the flasks was 49 cm^3 and the inoculum of *C. vulgaris* corresponded to 4 × 105 cells cm^{-3}; initial optical densities (OD, λ=680) of *P. tricornutum, M. aeruginosa*, and *N. spumigena* equalled to 0.08, 0.06 and 0.06 respectively. The oxytetracycline was added to the flasks with green algae, diatom and cyanobacteria in the volume of 1 cm^3 reaching the five final concentrations: 0.01 μg cm^{-3}, 0.1 μg cm^{-3}, 1 μg cm^{-3}, 4 μg cm^{-3}, 8 μg cm^{-3}. Control samples were prepared by adding 1 cm^3 of Mili-Q water to 49 cm^3 of fresh medium with tested species. All variants of the assay were performed in three independent experiments. To be able to determine a real effect of the chronic exposition on the growth and physiology of the microorganism even in low doses of antibiotics, experiments were carried out for 10/11 days. Subsamples were collected for measurements on days 3, 5, 7, 9, 11 (the end of the experiment) and in case of *P. tricornutum* on days 2, 4, 8, 10 (the end of the experiment). The *C. vulgaris* and *P. tricornutum* cells were counted with a Bürker chamber under a light microscope. Samples were diluted if needed. OD measurements were performed using HITACHI U-2800 UV-VIS spectrophotometer for all species: *C. vulgaris, M. aeruginosa, N. spumigena* and *P. tricornutum*. Simultaneously, oxytetracycline stability (nominal versus measured concentration) was monitored. Samples with medium and oxytetracycline at concentrations: 1 μg cm^{-3}, 4 μg cm^{-3}, 8 μg cm^{-3} were incubated applying the same experimental conditions as described earlier, and as a control — medium kept in the dark for the same period was used. Samples were analysed by absorbance measurements using HITACHI U-2800 UV-VIS spectrophotometer (λ=355). The growth rate was calculated based on OD value on the equation given by Karło et al. (2015) and Krzemińska et al. (2014).

2.3. Chlorophyll *a* and pheophytin concentration

Chlorophyll *a* and pheophytin concentration was determined using the spectrophotometric method according to Strickland and Parsons (1968, 1972) and Edler (1979). Aliquots of culture medium with live cells were filtered through the glass-fibre filters (GF/C Whatman). Next, filters were homogenised and extracted in 90% acetone for 2 h at 4°C in the dark. After extraction samples were centrifuged (3800g, 20 min) and the supernatant was collected. In order to estimate the concentration of pheophytin, the measurements were performed after 2 min following the addition of 60 μl of 1M HCl to 5 cm^3 of supernatant. The absorbance measurements for chlorophyll *a* and pheophytin were recorded by HITACHI U-2800 UV-VIS spectrophotometer at wavelengths: 750, 665, 645, 630 nm and 750, 665 nm respectively. Concentrations of both chlorophyll *a* and pheophytin were calculated according to Lorenzen (1967).

2.4. Fluorescence measurements

All fluorescence measurements were made using ultra-high sensitive (up to 0.5 μg chl dm^{-3}) AquaPen Ap-100C handheld

Table 1 Explanation of chlorophyll *a* fluorescence transient (OJIP transient) parameters. Formulas derived from Strasser et al., 2000.

Formula abbreviation	Formula explanation
F_0	$F_0 = F_{50\ \mu s}$, fluorescence intensity at 50 μs
F_J	F_J = fluorescence intensity at J-step (at 2 ms)
F_M	F_M = maximal fluorescence intensity
F_V	$F_V = F_M - F_0$ (maximal variable fluorescence)
V_J	$V_J = (F_J - F_0)/(F_M - F_0)$
F_M/F_0	Ratio
F_V/F_0	Ratio
F_V/F_M	Maximum quantum efficiency of PS II
M_0 or $(dV/dt)_0$	$M_0 = TR_0/RC - ET_0/RC = 4\ (F300 - F_0)/(F_M - F_0)$
Phi_P_0	Phi_$P_0 = 1 - (F_0/F_M)$ (or F_V/F_M)
Psi_$_0$	Psi_$_0 = 1 - V_J$
Phi_D_0	Phi_$D_0 = 1$ − Phi_$P_0 - (F_0/F_M)$
ABS/RC	ABS/RC = M_0. (1/V_J). (1/Phi_P_0)
TR_0/RC	$TR_0/RC = M_0$. (1/V_J)
ET_0/RC	$ET_0/RC = M_0$. (1/V_J). Psi_$_0$
DI_0/RC	DI_0/RC = (ABS/RC) − (TR_0/RC)

fluorometer (Photon Systems Instruments, Czech Republic). Both LED blue and red emitters (blue excitation light 455 nm; red excitation light 620 nm) were used throughout the experiments. The blue emitter is suitable for measuring fluorescence in algal suspensions, while the red emitter is applicable for measuring fluorescence in cyanobacterial cultures. All measurements were carried out in single-use polystyrene cuvettes (maximum volume 4 cm^3, optical length 1 cm) on dark-adapted samples. QY (Quantum Yield) and OJIP (Chlorophyll Fluorescence Induction Kinetics) parameters were quantified according to the formulas described by Strasser et al. (2000) (Table 1). QY is a measure of the photosystem II efficiency. In a dark-adapted sample, it is equivalent to F_V/F_M.

2.5. Data analysis

All results are presented as means ± standard deviation (SD) of three replicates (n = 3). Statistical analysis and comparison of group data were performed with one-way ANOVA and Dunnett's multiple comparison post-hoc test with GraphPad Prism software. Relationships were considered significant when $p < 0.05$.

3. Results

The stability test of oxytetracycline level in medium showed that light conditions used in the experiment did not increase the degradation of the antibiotic to a significant extent. Difference between control kept in the dark and samples did not exceed 10%, furthermore a decrease from an initial concentration of oxytetracycline to the end of the experiment did not exceed 32% (Fig. S1) Therefore it can be assumed that during the experiment organisms were constantly exposed to oxytetracycline.

The main part of the work was related to the change in growth, chlorophyll synthesis and photosynthetic processes efficiency to comprehensively assess a physiological state of four investigated microorganisms exposed to oxytetracycline.

The influence of oxytetracycline at given concentration (0.01 μg cm^{-3}, 0.1 μg cm^{-3}, 1 μg cm^{-3}, 4 μg cm^{-3}, 8 μg cm^{-3}) on the growth of *Chlorella vulgaris*, *Phaeodactylum tricornutum*, *Nodularia spumigena*, and *Microcystis aeruginosa*, expressed as a change of the OD values (λ=680 nm) during incubation time, is presented in Fig. 1.

When considering the results of these studies, it could be assumed that concentrations of 8 μg cm^{-3} and 4 μg cm^{-3} would affect analysed microorganisms. On the other hand, concentrations corresponding to 1 μg cm^{-3}, 0.1 μg cm^{-3} and 0.01 μg cm^{-3}, similar to those detected in marine sediments, would be expected to have no or little impact. Indeed, as shown in Fig. 1 the growth of all tested microorganisms at oxytetracycline concentrations of 8 μg cm^{-3}, 4 μg cm^{-3} was significantly reduced after the 5th day of the experiment. On the last day of the measurements, growth of *C. vulgaris*, *P. tricornutum*, *N. spumigena*, *M. aeruginosa* dropped by 78%, 89%, 95%, 93% (at concentration of 8 μg cm^{-3}) and by 52%, 85%, 67%, 92% (at concentration of 4 μg cm^{-3}). No, statistically significant differences of the growth rate compared to the control sample were found for most of the 0.01–0.1 μg cm^{-3} concentrations of oxytetracycline, except the decline of growth of *C. vulgaris* by 13–17% at a concentration of 0.01 μg cm^{-3} on the 5th and 7th day of the experiment. The oxytetracycline concentration equalled to 1 μg cm^{-3} strongly affected the growth of *C. vulgaris* (83%, 78% decline after fifth and seventh day respectively) and *P. tricornutum* (51% decline after 10 days) (Fig. 1). The growth rate for control was on the levels of 0.29–0.20 day^{-1} for *C. vulgaris*, 0.23-0.02 day^{-1} for *P. tricornutum*, 0.38–0.29 day^{-1} for *M. aeruginosa* and 0.35–0.24 day^{-1} for *N. spumigena*. After five days to the end of experiment, for all organisms, in concentration 4 and 8 μg cm^{-3} grow rate was lower than in the control sample and was on the level of 0.19–0.12 day^{-1} for *C. vulgaris*, 0.03–0.00 day^{-1} for *P. tricornutum*, 0.21–0.00 day^{-1} for *M. aeruginosa* and 0.02–0.00 day^{-1} for *N. spumigena*.

A similar tendency was observed for chlorophyll *a* concentration analysed at the end of the experiment (Table 2). The decrease in chlorophyll *a* content was noticed for all studied organisms exposed to concentrations of 8 μg cm^{-3} and 4 μg cm^{-3}: *C. vulgaris* (97% and 79 % decline respectively), *P. tricornutum* (95% and 94%), *N. spumigena* (100% and 98%) and *M. aeruginosa* (85% and 49 %). The significant influence of 1μg cm^{-3} and 0.1μg cm^{-3} oxytetracycline concentrations was observed on *C. vulgaris* (36% and 30% decline respectively) and *N. spumigena* (36%, 23%) and 1μg cm^{-3} on *P. tricornutum* (67%). Changes of phaeopigment and chlorophyll *a* content per cell also show a decrease of the pigments content with increasing oxytetracycline concentration (Table 2). However, in the case of *C. vulgaris* concentration of 0.1 μg cm^{-3} appeared to have a higher impact on chlorophyll *a* per cell value than that of 1 μg cm^{-3}

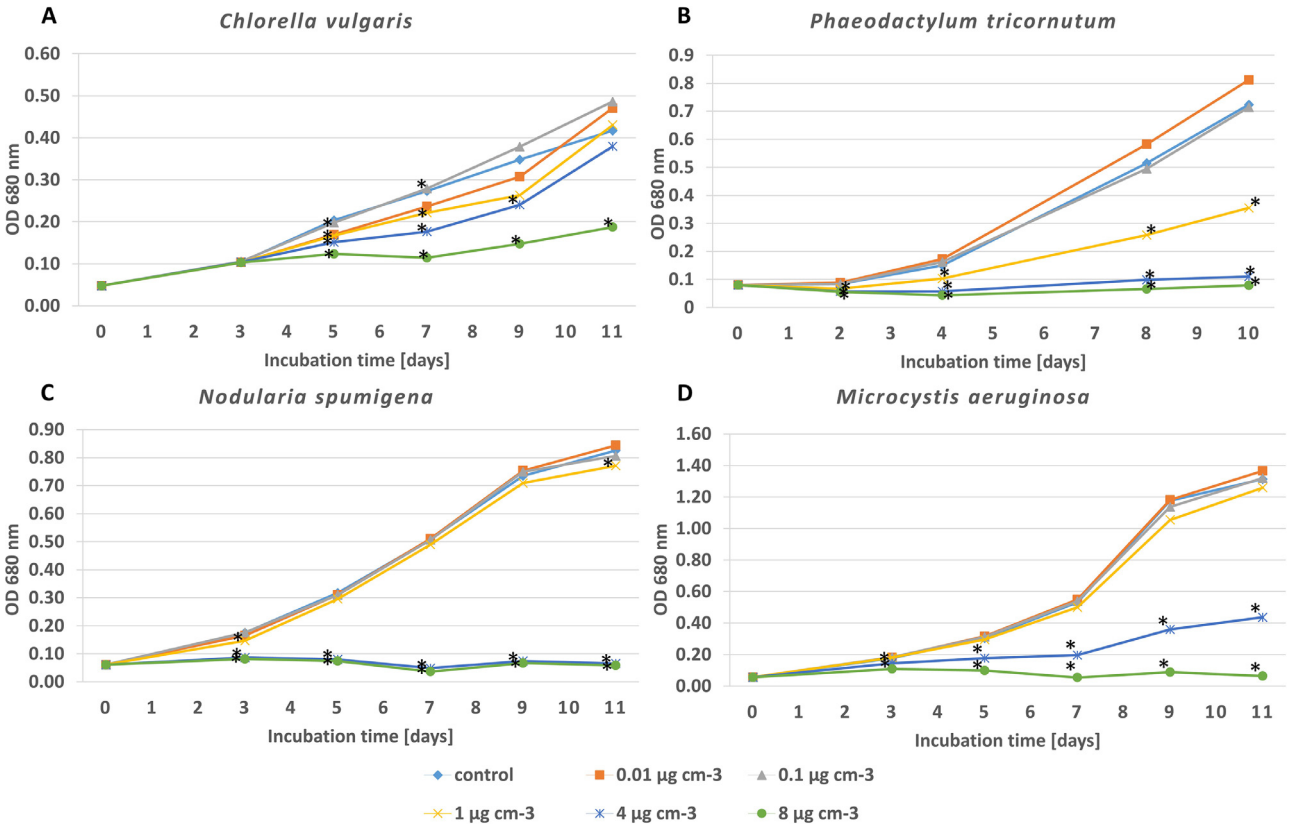

Figure 1 The influence of oxytetracycline on the growth of *Chlorella vulgaris* (A), *Phaeodactylum tricornutum* (B), *Nodularia spumigena* (C) and *Microcystis aeruginosa* (D) expressed as a change of the OD values (λ=680 nm) during incubation time. * differences statistically significant in comparision to the control.

(57% versus 80% of control respectively). This phenomenon was presumably caused by a higher presence of dead cells in 1 µg cm^{-3} oxytetracycline concentration variant. That directly correlates with phaeopigment concentration and is a likely reason for overestimation.

The effect of oxytetracycline on photosynthetic apparatus and photochemistry of the photosystem II was investigated by a fluorescence transient (OJIP) analysis. The measured photosynthetic-fluorescence parameters are presented in Figs. 2, 3, 4 and in supplementary materials (Fig. S2, S3, S4). Changes in parameters in comparison to control were observed already after 72–96 h. However, a longer period of observation (7 and 10–11 days), shows some interesting phenomena about the physiology of the tested microorganisms. It should be mentioned that, after the 7th day of the experiment and/or for concentrations 4 and 8 µg cm^{-3}, in some cases, relatively high errors were observed in measurements. It can be caused by some damage to PSII, and these results are hard to interpret.

One of the most important parameters is F_V/F_M representing the maximum quantum yield of the photosystem II and can be treated as the efficiency of PSII (Fig. 2, Fig. S2). For all investigated organisms, the presence of oxytetracycline in concentrations above 1 µg cm^{-3} caused a significant decrease of F_V/F_M values. In the case of 0.1 µg cm^{-3}, the decrease was observed for *P. tricornutum* during the whole period of the experiment, and for both cyanobacteria in the early stages of the experiment. Exposure to higher concentrations of oxytetracycline (8 µg cm^{-3} and 4 µg cm^{-3}) resulted in a reduction of F_V/F_M values from 26% to 100% in relation to control, thereby indicating a reduction of PSII ability to carry on photochemical reactions.

The ratio of the harvesting complex absorption per reaction centre (ABS/RC) presented a significant increase (Fig. 3 and S3). The trends in the increase of ABS/RC was observed for all investigated organisms in concentration from 1 µg cm^{-3} and, in case of cyanobacteria, even from 0.01 µg cm^{-3}. However, a statistically significant increase was observed mainly for higher concentrations (4 and 8 µg cm^{-3}) for all tested organisms as well as in the initial phase of an experiment for *P. tricornutum* and *N. spumigena* in concentrations 0.1 and 1 µg cm^{-3}. An interesting observed phenomenon was an intensive increase of ABS/RC value for 4 or/and 8 µg cm^{-3} on a 4–5th day for all species. In the case of *N. spumigena*, the value approached an even 1000% rise. Subsequently, ABS/RC values decreased and stabilized at the end of the experiment. Higher concentrations of oxytetracycline (4 and 8 µg cm^{-3}) have been observed to have a high influence on the effective energy dissipation of an active reaction centre (DI_0/RC) (Fig. S5). The increase of ABS/RC and DI_0/RC values was detected up to the 5th day of the test, followed by a steady decrease till the eleventh day, when the subsequent values of those parameters were even five-time lower compared to the 5th day of exposure.

Table 2 The influence of oxytetracycline on chlorophyll a and pheopigment concentration in *Chlorella vulgaris*, *Phaeodactylum tricornutum*, *Nodularia spumigena*, and *Microcystis aeruginosa* cultures (pigment concentrations measured at the end of the experiment). Data are given as a mean ± SD (n = 3) and % of control (C). Bold values indicate statistically significant differences in comparision to the control.

Oxytetracycline concentration [μg cm^{-3}]	pigments concentration [μg dm^{-3}]			pigment concentration per cell [pg cell^{-1}]	
	active chlorophyll *a*		pheopigment	chlorophyll *a*	
	Average± SD	%C	Average± SD	Average	%C
Chlorella vulgaris					
Control [0]	3743 ± 511	100	656 ± 152	2.43	100
0.01	2723 ± 159	73 ± 4	364 ± 169	1.75	72
0.1	**2618 ± 555**	**70 ± 15**	**553 ± 74**	**1.39**	**57**
1	**2387 ± 204**	**64 ± 5**	**342 ± 76**	**1.94**	**80**
4	**769 ± 68**	**21 ± 2**	**126 ± 33**	**1.19**	**49**
8	**130 ± 20**	**3 ± 1**	**69 ± 24**	**0.65**	**27**
Phaeodactylum tricornutum					
Control [0]	1228 ± 125	100	81 ± 51	5.27	100
0.01	1185 ± 113	96 ± 9	84 ± 14	4.43	84
0.1	1092 ± 56	88 ± 4	31 ± 1	2.83	54
1	**409 ± 54**	**33 ± 5**	**17 ± 17**	**2.92**	**55**
4	**82 ± 20**	**6 ± 1**	**7 ± 8**	**1.88**	**36**
8	**61 ± 3**	**5 ± 0.2**	**3 ± 5**	**1.82**	**34**
Nodularia spumigena					
Control [0]	2195 ± 98	100	107 ± 10		
0.01	1992 ± 159	91 ± 7	122 ± 15		
0.1	**1698 ± 0**	**77 ± 0**	**104 ± 8**		
1	**1396 ± 33**	**64 ± 2**	**100 ± 14**		
4	**49 ± 2**	**2 ± 1**	**10 ± 1**		
8	**0 ± 0**	**0 ± 0**	**6 ± 0**		
Microcystis aeruginosa					
Control [0]	310 ± 52	100	1 ± 1		
0.01	315 ± 14	101 ± 5	5 ± 3		
0.1	320 ± 2	103 ± 1	10 ± 3		
1	260 ± 5	84 ± 1	5 ± 4		
4	**158 ± 166**	**51 ± 54**	**6 ± 6**		
8	**46 ± 7**	**15 ± 2**	**8 ± 1**		

Additionally, the capacity of PSII electron transport per active reaction centre (ET_0/ RC) was analysed (Fig. 4). This value shows an effective energy move from the reaction centre to the electron transport chain and corresponds to the amount of transported energy that can be used in the photosynthesis process. In general, in the case of samples where the effect on the electron transport chain was observed, the ET_0/RC values decreased in comparison to control. However, in the case of *N. spumigena* exposed to 4 μg cm^{-3} and *P.tricornutum* exposed to 1, 4, 8 μg cm^{-3} the significant increase of the ET_0/ RC were observed.

4. Discussion

Microalgae and cyanobacteria have been widely recommended as test organisms because of their ecological relevance, sensitivity and owing to the fact that they are easily cultivated in the laboratory (Seoane et al., 2014). For these reasons, *Chlorella vulgaris*, *Phaeodactylum tricornutum*, *Nodularia spumigena*, *Microcystis aeruginosa* have been selected for evaluating the effects of oxytetracycline in the current ecotoxicological study. Moreover, those species are ubiquitous in brackish and estuarine ecosystems including the Baltic Sea waters. Our results demonstrated the negative impact of high concentrations of oxytetracycline on all tested organisms in terms of growth, chlorophyll *a* concentration and photosynthetic-fluorescence parameters (F_V/F_M, ABS/RC, ET_0/RC). Furthermore, the present findings indicate that lower concentrations can also adversely affect studied organisms. According to the literature, the EC_{50} values obtained for oxytetracycline in the case of *C. vulgaris* are in the range from <3.58 to 7.05 μg cm^{-3} (Eguchi et al. 2004; Kołodziejska et al. 2013). The EC_{50} value for *P. tricornutum* equals to 1.73 μg cm^{-3} (following International Standard ISO 10253:1995) (De Orte et al. 2013). In case of investigated cyanobacteria, EC_{50} values have been reported only for *M. aeruginosa* in 6—7 day tests and were placed in the range from 0.207 μg cm^{-3} to 0.23 μg cm^{-3} (Ando et al., 2007; Holten Lützhøft et al., 1999). When considering the results of these studies, it could be assumed that concentrations of 8 μg cm^{-3} and 4 μg cm^{-3} would affect analysed microorganisms. On the other hand, concentrations corresponding to 1 μg cm^{-3}, 0.1 μg cm^{-3} and

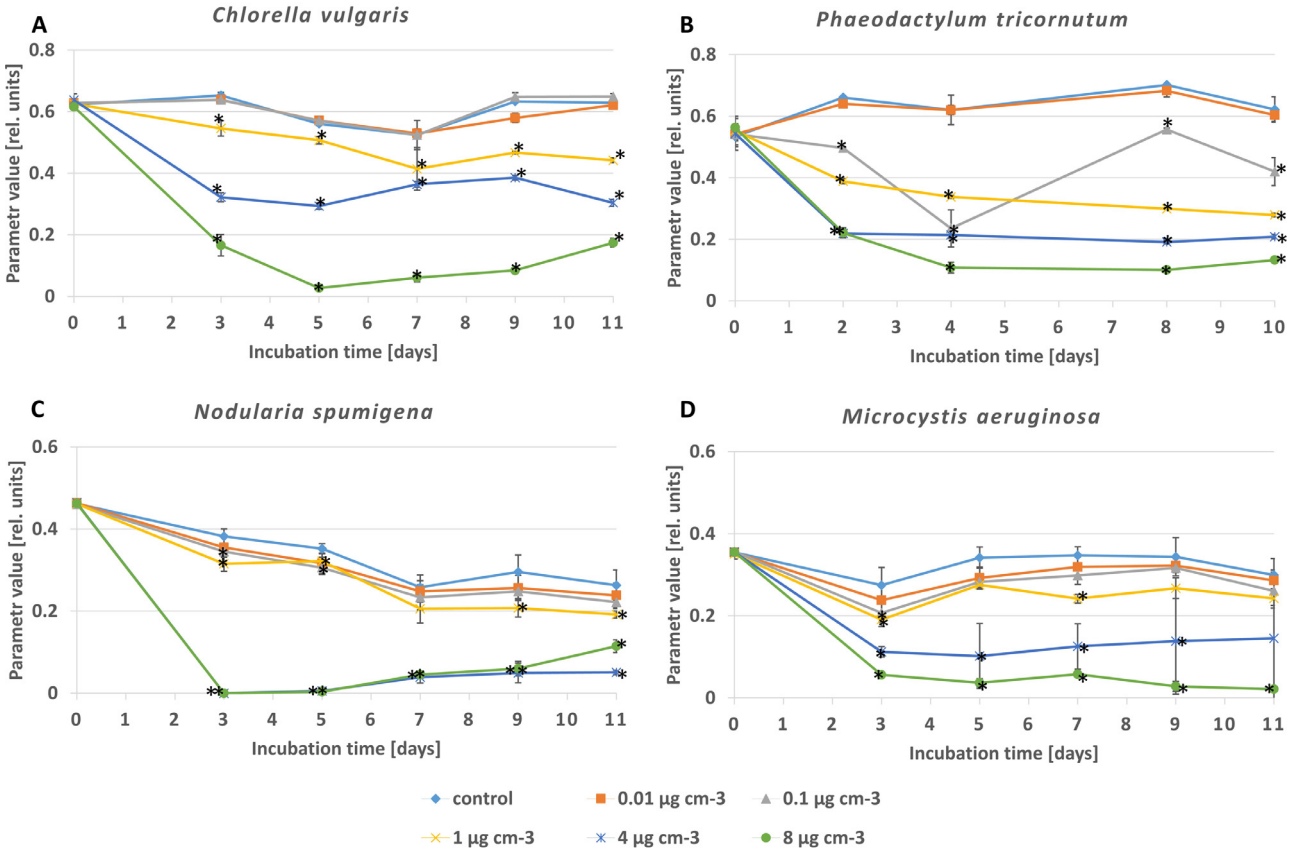

Figure 2 Photochemical efficiency of PSII (F_V/F_M) changes for the *Chlorella vulgaris* (A), *Phaeodactylum tricornutum* (B) and *Nodularia spumigena* (C) and *Microcystis aeruginosa* (D); .* differences statistically significant in comparision to the control.

0.01 µg cm^{-3}, similar to those detected in marine sediments, would be expected to have no or little impact. Eguchi et al. (2004) demonstrated that oxytetracycline exerted influence on the growth of algae in the early stages of the incubation period and consequently suggested that the probability it would cause damage to algae when released continuously into the environment is high. Impact of oxytetracycline on the growth of cyanobacteria and algae was also confirmed by Ando et al. (2007) and Holten Lützhøft et al. (1999) in 6–7 days tests. The values showed by these authors (EC_{50}= 0.2 µg cm^{-3}) were lower than used in this study. Our investigations also revealed that oxytetracycline inhibits pigment synthesis. Similar results were described by Seoane et al. (2014); the cells exposed to oxytetracycline were characterized by lower chlorophyll *a* content. The authors suggest that a significant decrease of pigments in cultures exposed to antibiotics can result from the inhibition of the increase of active cell volume compared to the control cultures. Guo et al. (2016), Tsiaka et al. (2013) and Zhang et al. (2012) also demonstrated that some compounds such as carbamazepine, tylosin, lincomycin, and trimethoprim can inhibit the synthesis of chlorophyll *a*. Moreover, the decline of pigments levels in cells could be caused by the enhancement of oxidative stress-related effects (Tsiaka et al., 2013). As it was mentioned before, in the case of *C. vulgaris* oxytetracycline concentration of 0.1 µg cm^{-3} had a higher impact on chlorophyll *a* per cell value than 1 µg cm^{-3}. Unfortunately, we do not have yet enough data to fully investigate this phenomenon. Differences in chlorophyll *a* concentration can be caused by the cell cycle. Cultures incubated with different oxytetracycline concentration variants were not harmonised, so cells could have been in a different growth phase. Cells before division are bigger and have more chlorophyll *a* per cell than cells after division. However, the growth curve (Fig. 1A) shows that 1 µg cm^{-3} seems to be one of the limit concentrations and can significantly impact the growth of the culture. Based on that, we assume it directly contributes to decreasing in overall cell divisions, while maintaining still quite high chlorophyll *a* production.

In the present studies, classical measurements were supported by photosynthetic-fluorescence parameters analysis. Results show that those parameters seem to be reliable biomarkers of oxytetracycline toxicity on tested organisms. Similar conclusions were reported by van der Grinten et al. (2010) in case of F_V/F_M parameter and by Dewez et al. (2018), where those parameters, among others, were used as markers of the global physiological state of the *Lemna gibba* L. affected by silver nanoparticles. We believe that findings reported in our studies can help in understanding how oxytetracycline impacts the PSII of listed species. It has been shown that in most cases concentrations of 1, 4 and 8 µg cm^{-3} caused a high increase of harvesting complex absorption of an active reaction centre (ABS/RC) and effective energy dissipation of an active RC emitted as a heat (DI_0/RC). It did not necessarily correlate with efficient usage of energy bound to the reaction centre and transported

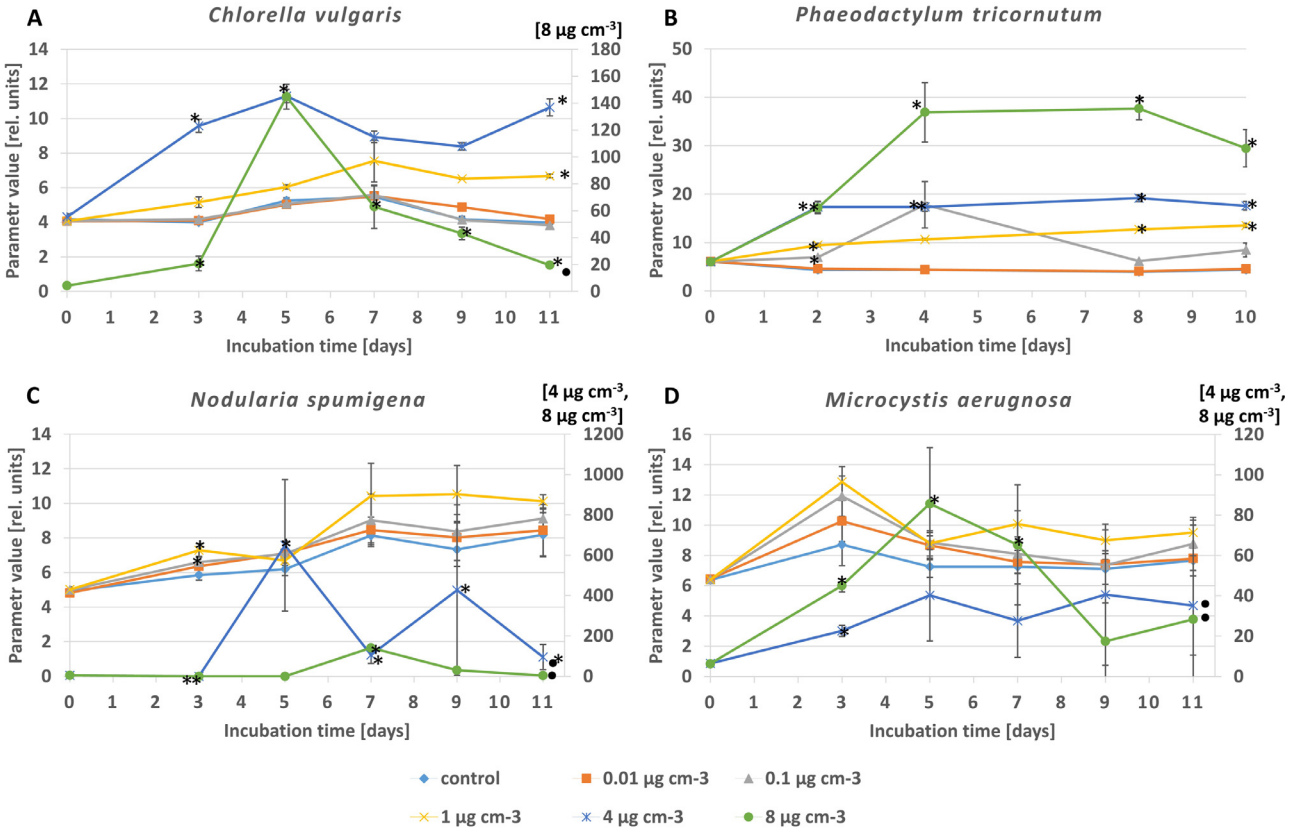

Figure 3 ABS/RC changes for the *Chlorella vulgaris* (A), *Phaeodactylum tricornutum* (B) and *Nodularia spumigena* (C) and *Microcystis aeruginosa* (D). * differences statistically significant in comparision to the control; • data series related to the auxiliary (right side) axis.

to be used in the photosynthesis (ET_0/RC), but always significantly corresponded with the decrease of photosystem II efficiency (F_V/F_M). The exposure of tested organisms to oxytetracycline in concentrations of 1, 4, 8 µg cm^{-3} affects by some means PSII that leads to an increase of effective antenna size (directly correlated to chlorophyll *a* concentration) necessary to keep energy assimilation on the acceptable level to maintain effective photosynthesis. Unfortunately, the attempt was not successful as antennas' effectiveness in energy assimilation decreased and remaining energy was radiated as heat (DI_0/RC). We speculate that it can be attributed to some defence mechanisms involved in the protection of the reaction centre from destruction. Therefore that may be an explanation why in some cases (8 µg cm^{-3}) ET_0/RC value decreased and the electron started to move to the electron transport chain after a few days of the adaptation period. Simultaneously, the decrease of photosystem II efficiency (F_V/F_M) and in some cases decline of a number of cells in the samples were noticeable. A similar pattern was observed by Oh et al. (2005) for seaweed (*Porphyra yezoensis* Ueda) exposed to oxytetracycline. Also, Chen et al. (2017) showed that oxytetracycline (in concentrations exceeding 10 µg g^{-1}) diminished the photosynthetic capacity of rape (*Brassica campestris* L.). Moreover, van der Grinten et al. (2010) reported EC_{50} values for the oxytetracycline inhibition of the photosynthetic yield (Fv/F_M) for *M. aeruginosa* (5.4 µg cm^{-3}) and *P. subcapitata* (0.6 µg cm^{-3}), which in case of cyanobacteria are higher than it would be concluded from our data. Pan et al. (2008) also observed toxic inhibitory effects of amoxicillin on the donor side, electron transfer and the acceptor side of PSII. The decrease of active centre resulted in reduced electron transfer (ET_0/RC) and increased dissipation of heat at the level of the antenna (DI_0/RC). Our results are also consistent with previous studies described by Xu et al. (2019) for tetracycline and its degradation products, where authors observed the impact on the growth, cell structure and algal cell oxidative stress of *C. vulgaris* during the 96h incubation period. Those studies showed that concentration of tetracycline > 5 µg cm^{-3} caused oxidative stress, structural changes in the cells such as plasmolysis and starch granule deposition appeared, the thylakoid lamellae in the chloroplasts became blurred and deformed, and the vacuoles became larger.

The reported results also show differences between tested species in response to stress caused by oxytetracycline. Cyanobacteria are closer in taxonomy to bacteria when compared to green algae so the predicted impact of oxytetracycline on those microorganisms is expected to be higher. The results demonstrated this assumption is true for some parameters like growth or photosynthetic parameters (F_V/F_M, ABS/RC, ET_0/RC), but no for chlorophyll *a* concentration. The impact on *C. vulgaris* and *N. spumigena* was moderately higher than on *M. aeruginosa*. Higher resistance of *M. aeruginosa* to oxytetracycline was also described by van der Grinten et al. (2010). Of course, this issue needs

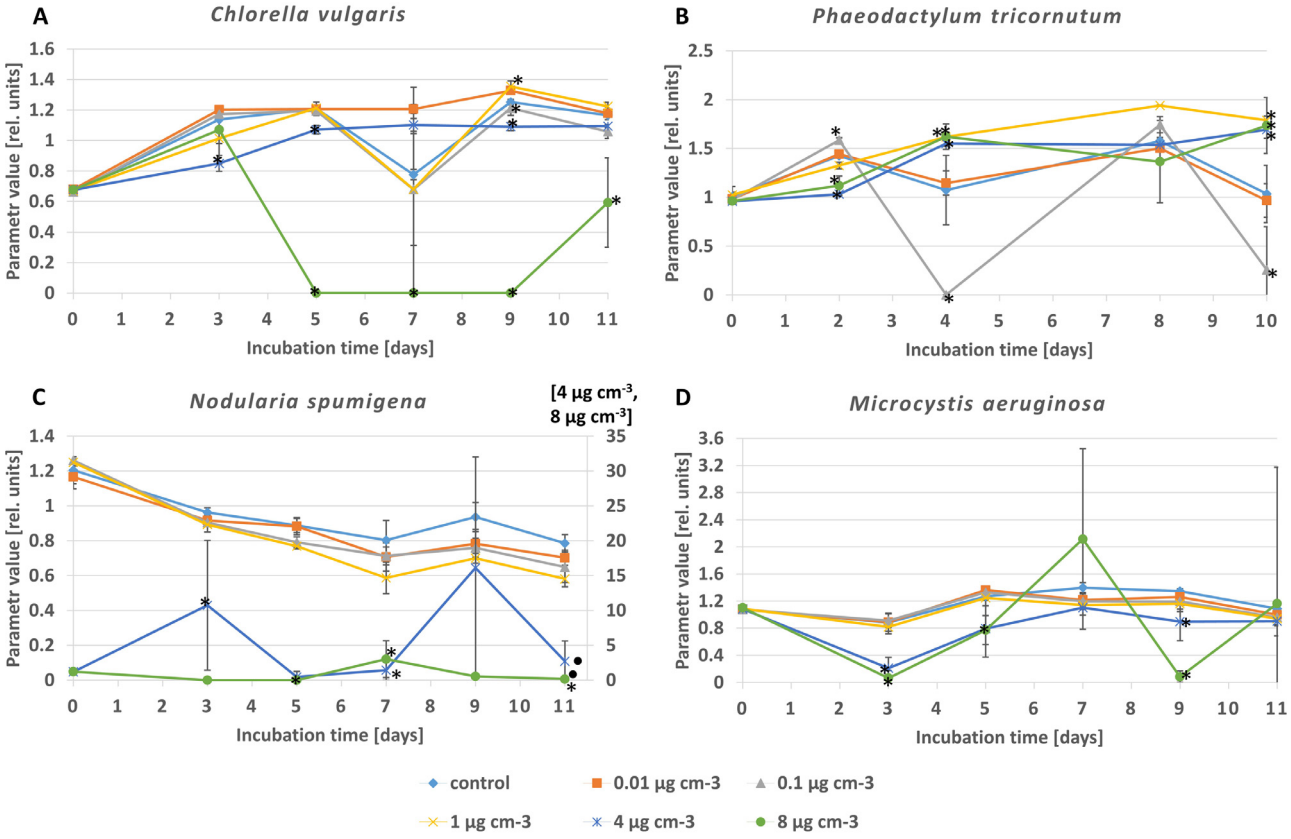

Figure 4 ET_0/ RC changes for the *Chlorella vulgaris* (A), *Phaeodactylum tricornutum* (B) and *Nodularia spumigena* (C) and *Microcystis aeruginosa* (D). * differences statistically significant in comparision to the control; • data series related to the auxiliary (right side) axis.

further investigations but authors speculate that it can be due to differences in cell and or exocellular polymeric matrix structures. Moreover, it may indicate that factors other than taxonomical similarities can be critical for the non-target organism.

The chronic character of the presented studies can be useful in risk assessment estimations. To make data more useful the obtained results were compared with no observed effect concentration (NOEC) values presented in the literature. Eguchi et al. (2004) reported NOEC for *C. vulgaris* equals 3.58 µg cm^{-3} which is higher than statistically significant concentration affecting organisms reported in our studies (0.1 µg cm^{-3}). Likewise, Ando et al. (2007) reported NOEC for *Nostoc* sp. at the level of 0.78 µg cm^{-3}. In this study, minimal concentration affecting *N. spumigena* of the same order (Nostocales),was equal to 0.1 µg cm^{-3}. However, in the same publication, Ando et al. (2007) reported NOEC for *M. aeruginosa* as 0.031 µg cm^{-3} which is lower than minimal concentration affecting this cyanobacterium presented in the current study.

Our results show that the changes in measured parameters started to disclose after the second-third day of the experiment. This allows the conclusion that standard 48–72 h chronic tests should be enough to observe the effect of the antibiotic on investigated organisms but the nature of changes can be hard to identify and interpret. On the other hand tests longer than 10 days do not seem to be too long and labour-intensive compared to the obtained results. In our opinion test from 7 to 10 days should be enough to observe the chronic effect and help to understand the potential mechanism of the negative impact of oxytetracycline on the non-target microorganism.

5. Conclusion

In summary, our results show that oxytetracycline at concentration levels reported in the marine environment can potentially affect photoautotrophic microorganism. The photosynthetic parameters applied along with growth and pigment analysis can be a very sensitive tool for examining the influence of various antibiotics on autotrophic microorganisms. Furthermore, the present findings provide additional information about the mode of action of oxytetracycline concerning non-target organisms like cyanobacteria, diatoms, and microalgae. This allows the conclusion that the use of standard toxicity tests (72 h) does not allow to accurately and reliably assess the chronic impact of bioactive compounds including drugs and their metabolites on water organisms. To improve our knowledge of the emerging risks to aquatic species and to better understand the interactions between those compounds in the environment, more studies should be carried out, focusing particularly on chronic toxicity and toxicity of the mixtures of antibiotics.

Acknowledgements

The reported results were obtained within the financial support of the Institute of Oceanology of the Polish Academy of Sciences (statutory task no. II.2 and II.3) and the following research projects: WaterPUCK BIOSTRATEG3/343927/3/NCBR/2017, financed by the National Centre for Research and Development (NCBiR) within the BIOSTRATEG III program, PharmSeepage 2016/21/B/ST10/01213, funded by the Polish National Science Centre.

Supplementary materials

Supplementary material associated with this article can be found, in the online version, at doi:https://doi.org/10.1016/j.oceano.2019.12.002.

References

Agwuh, K.N., MacGowan, A., 2006. Pharmacokinetics and pharmacodynamics of the tetracyclines including glycylcyclines. J. Antimicrob. Chemother. 58 (2), 256—265, https://doi.org/10.1093/jac/dkl224.

Ando, T., Nagase, H., Eguchi, K., Hirooka, T., Nakamura, T., Miyamoto, K., Hirata, K., 2007. A novel method using cyanobacteria for ecotoxicity test of veterinary antimicrobial agents. Environ. Toxicol. Chem. 26 (4), 601—606.

Arnold, K.E., Brown, A.R., Ankley, T.G., Sumpter, J.P., 2014. Medicating the environment: assessing risks of pharmaceuticals to wildlife and ecosystem. Philos. Trans. R. Soc. B. Biol. Sci. 369 (1656), 1—11, http://dx.doi.org/10.1098/rstb.2013.0569.

Bischoff, H.W., Bold, H.C., 1963. Phycological Studies IV. Some Soil Algae from Enchanted Rock and Related Algal Species. Univ. Texas Publ. 6318, 1—95.

Björlenius, B., Ripszám, M., Haglund, P., Lindberg, R.H., Tysklind, M., Fick, J., 2018. Pharmaceutical residues are widespread in Baltic Sea coastal and offshore waters — Screening for pharmaceuticals and modelling of environmental concentrations of carbamazepine. Sci. Total. Environ. 633, 1496—1509, https://doi.org/10.1016/j.scitotenv.2018.03.276.

Borecka, M., Białk-Bielińska, A., Siedlewicz, G., Kornowska, K., Kumirska, J., Stepnowski, P., Pazdro, K., 2013. A new approach for the estimation of expanded uncertainty of results of an analytical method developed for determining antibiotics in seawater using solid-phase extraction disks and liquid chromatography coupled with tandem mass spectrometry technique. J. Chrom. A. 1304, 138—146, https://doi.org/10.1016/j.chroma.2013.07.018.

Borecka, M., Siedlewicz, G., Haliński, Ł.P., Sikora, K., Pazdro, K., Stepnowski, P., Białk-Bielińska, A., 2015. Contamination of the southern Baltic Sea waters by the residues of selected pharmaceuticals: method development and field studies. Mar. Pollut. Bull. 94, 62—71, https://doi.org/10.1016/j.marpolbul.2015.03.008.

Borecka, M., Białk-Bielińska, A., Haliński, Ł, Pazdro, K., Stepnowski, P., Stolte, S., 2016. The influence of salinity on the toxicity of selected sulfonamides andtrimethoprim towards the green algae *Chlorella vulgaris*. J Haz. Mat. 308, 179—186, http://dx.doi.org/10.1016/j.jhazmat.2016.01.041.

Boxall, A.B.A., Fogg, L.A., Blackwell, P.A., Kay, P., Pemberton, E.J., Croxford, A., 2004. Veterinary medicines in the environment. Rev. Environ. Contam. Toxicol. 180, 1—91.

Capone, D.G., Weston, D.P., Millera, V., Shoemakera, C., 1996. Antibacterial residues in marine sediments and invertebrates following chemotherapy in aquaculture. Aquaculture 145, 55—75, https://doi.org/10.1016/S0044-8486(96)01330-0.

Chen, H., Liu, S., Xu, X.R., Zhou, G.J., Liu, S.S., Yue, W.Z., Sun, K.F., Ying, G.G., 2015. Antibiotics in the coastal environment of the Hailing Bay region, South China Sea: spatial distribution, source analysis and ecological risks. Mar. Pollut. Bull. 95 (1), 365—373, https://doi.org/10.1016/j.marpolbul.2015.04.025.

Chen, Y., Wang, Z., Shen, Z., Ou, Z., Xu, D., Yuan, Z., Zhou, S., 2017. Effects of Oxytetracycline on Growth and Chlorophyll Fluorescence in Rape (Brassica campestris L.). Pol. J. Environ. Stud. 26 (3), 995—1001, https://doi.org/10.15244/pjoes/67575.

de Orte, M.R., Carballeira, C., Viana, I.G., Carballeira, A., 2013. Assessing the toxicity of chemical compounds associated with marine land-based fish farms: The use of mini-scale microalgal toxicity tests Chem. Ecol. 29 (6), 554—563, https://doi.org/10.1080/02757540.2013.790381.

Dewez, D., Goltsev, V., Kalaji, H.M., Oukarroum, A., 2018. Inhibitory effects of silver nanoparticles on photosystem II performance in Lemna gibba probed by chlorophyll fluorescence. Curr. Plant. Biol. 16, 15—21, https://doi.org/10.1016/j.cpb.2018.11.006.

EC, 2003 European Commission Technical Guidance Document in Support of Commission Directive 93//67/EEC on Risk Assessment for New Notified Substances and Commission Regulation (EC) No. 1488/94 on Risk Assessment for Existing Substance, Part II Retrieved 10 July, 2019, from https://echa.europa.eu/documents/10162/16960216/tgdpart2_2ed_en.pdf

Edler, L., 1979. Recommendations for marine biological studies in the Baltic Sea: Phytoplankton and chlorophyll. Baltic Mar. Biol. Publ. 5, 1—38.

Eguchi, K., Nagase, H., Ozawa, M., Endoh, Y.S., Got, K., Hirata, K., Miyamoto, K., Yoshimura, H., 2004. Evaluation of antimicrobial agents for veterinary use in the ecotoxicity test using microalgae. Chemosphere 57, 1733—1738, https://doi.org/10.1016/j.chemosphere.2004.07.017.

Fu, L., Huang, T., Wang, S., Wang, X., Su, L., Li, C., Zhao, Y., 2017. Toxicity of 13 different antibiotics towards freshwater green algae *Pseudokirchneriella subcapitata* and their modes of action. Chemosphere 168, 217—222, https://doi.org/10.1016/j.chemosphere.2016.10.043.

Gao, Q.T., Tam, N.F.Y., 2011. Growth, photosynthesis and antioxidant responses of two microalgal species, *Chlorella vulgaris* and *Selenastrum capricornutum*, to nonylphenol stress. Chemosphere 82 (3), 346—354, https://doi.org/10.1016/j.chemosphere.2010.10.010.

González-Pleiter, M., Gonzalo, S., Rodea-Palomares, I., Legane, F., Rosal, R., Boltes, K., Marco, E., Fernandez-Piñas, F., 2013. Toxicity of five antibiotics and their mixtures towards photosynthetic aquatic organisms: implications for environmental risk assessment. Water Res. 47, 2050—2064, https://doi.org/10.1016/j.watres.2013.01.020.

Guillard, R.R.L., 1975. Culture of phytoplankton for feeding marine invertebrates. In: Smith, W.L., Chanley, M.H. (Eds.), Culture of Marine Invertebrate Animals. Plenum Press, New York, 26—60.

Gulkowska, A., He, Y., So, M.K., Yeung, L., Giesy, J.P., Lam, P.K., Martin, M., Richardson, B.J., 2007. The occurrence of selected antibiotics in Hong Kong coastal waters. Mar. Poll. Bull. 54, 1287—1293, https://doi.org/10.1016/j.marpolbul.2007.04.008.

Guo, J., Selby, K., Boxall, A., 2016. Comparing the sensitivity of chlorophytes, cyanobacteria and diatoms to major-use antibiotics. Environ. Toxicol. Chem. 35, 2587—2596, https://doi.org/10.1002/etc.3430.

Halling-Sørensen, B., 2000. Algal toxicity of antibacterial agents used in intensive farming. Chemosphere 40 (7), 731—739, https://doi.org/10.1016/S0045-6535(99)00445-2.

Hernando, M.D., Mezcua, M., Fernandez-Alba, A.R., Barcelo, D., 2006. Environmental risk assessment of pharmaceutical residues in wastewater effluents, surface waters and sediments. Talanta 69, 334—342, https://doi.org/10.1016/j.talanta.2005.09.037.

Holten Lüzhøft, H.C., Halling-Sørensen, B., Jørgensen, S.E., 1999. Algal toxicity of antibacterial agents applied in Danish fish farming. Arch. Environ. Contam. Toxicol. 36, 1—6, https://doi.org/10.1007/s002449900435.

Ji, K., Kim, S., Han, S., Seo, J., Lee, S., Park, Y., Choi, K., Kho, Y-L., Kim, P.-G., Park, J., Choi, K., 2012. Risk assessment of chlortetracycline, oxytetracycline, sulfamethazine, sulfathiazole, and erythromycin in aquatic environment: Are the current environmental concentrations safe? Ecotoxicology 21, 2031—2050, https://doi.org/10.1007/s10646-012-0956-6.

Jiao, S., Zheng, S., Yin, D., Wang, L., Chen, L., 2008. Aqueous oxytetracycline degradation and the toxicity change of degradation compounds in photoirradiation process. J. Environ. Sci. 20 (7), 806—813, https://doi.org/10.1016/S1001-0742(08)62130-0.

Karło, A., Wilk, A., Ziembińska-Buczyńska, A., Surmacz-Górska, J., 2015. Cultivation parameters adjustment for Effective algal biomass production. Rocz. Ochr. Śr. 17, 275—288.

Kolar, B., Arnuš, L., Jeretin, B., Gutmaher, A., Drobne, D., Durjava, M.K., 2014. The toxic effect of oxytetracycline and trimethoprim in the aquatic environment. Chemosphere 115, 75—80, https://doi.org/10.1016/j.chemosphere.2014.02.049.

Kołodziejska, M., Maszkowska, J., Białk-Bielińska, A., Steudte, S., Kumirska, J., Stepnowski, P., Stolte, S., 2013. Aquatic toxicity of four veterinary drugs commonly applied in fish farming and animal husbandry. Chemosphere 92, 1253—1259, https://doi.org/10.1016/j.chemosphere.2013.04.057.

Krzemińska, I., Pawlik-Skowrońska, B., Trzcińska, M., Tys, J., 2014. Influence of photoperiods on the growth rate and biomass productivity of green microalgae. Bioprocess Biosyst. Eng. 37, 735—741, https://doi.org/10.1007/s00449-013-1044-x.

Kümmerer, K., 2009. Antibiotics in the environment. In: Kümmerer, K. (Ed.), Pharmaceuticals in the Environment. Springer, Berlin, 75—88.

Kümmerer, K., 2010. Pharmaceuticals in the Environment. Annual Review of Environment and Resources 35 (1), 57—75, http://dx.doi.org/10.1146/annurev-environ-052809-161223.

Lalumera, G.M., Calamari, D., Galli, P., Castiglioni, S., Crosa, G., Fanelli, R., 2004. Preliminary investigation on the environmental occurrence and effects of antibiotics used in aquaculture in Italy. Chemosphere 54 (5), 661—668, https://doi.org/10.1016/j.chemosphere.2003.08.001.

Leal, J.F., Esteves, V.I., Santos, E.B.H., 2016. Use of sunlight to degrade oxytetracycline in marine aquaculture's waters. Environ. Pollut. 213, 932—939, http://dx.doi.org/10.1016/j.envpol.2016.03.040.

Lorenzen, C.J., 1967. Determination of chlorophyll and pheopigments: spectrophotometric equations. Limnol. Oceanogr. 12, 343—346, https://doi.org/10.4319/lo.1967.12.2.0343.

Lyman, J., Fleming, R.H., 1940. Composition of sea water. J. Mar. Res. 3, 134—146.

McArdell, C.S., Molnar, E., Suter, M.J.F., Giger, M., 2003. Occurrence and Fate of Macrolide Antibiotics in Wastewater Treatment Plants and in the Glatt Valley Watershed, Switzerland. Environ. Sci. Technol. 37 (24), 5479—5486, https://doi.org/10.1021/es034368i.

Nödler, K., Voutsa, D., Licha, T., 2014. Polar organic micropollutants in the coastal environment of different marine systems. Mar Pollut. Bull. 85, 50—59, https://doi.org/10.1016/j.marpolbul.2014.06.024.

Oh, M-H., Kang, Y., Lee, C., Chung, I., 2005. Effects of Six Antibiotics on the Activity of the Photosynthetic Apparatus and Ammonium Uptake of Thallus of Porphyra yezoensis. Algae 20 (2), 121—125, https://doi.org/10.4490/algae.2005.20.2.121.

Pan, X., Deng, C., Zhang, D., Wang, J., Mu, G., Chen, Y., 2008. Toxic effects of amoxicillin on the photosystem II of *Synechocystis* sp. characterized by a variety of in vivo chlorophyll fluorescence tests. Aquat Toxicol. 89 (4), 207—213, https://doi.org/10.1016/j.aquatox.2008.06.018.

Pazdro, K., Borecka, M., Siedlewicz, G., Białk-Bielińska, A., Stepnowski, P., 2016. Analysis of the Residues of Pharmaceuticals in Marine Environment: State-of-the-art, Analytical Problems and Challenges. Curr. Anal. Chem. 12 (3), 202—226, http://dx.doi.org/10.2174/1573411012666151009193536.

Pereira, J.H.O.S., Vilar, V.J.P., Borges, M.T., González, O., Esplugas, S., Boaventura, R.A.R., 2011. Photocatalytic degradation of oxytetracycline using TiO2 under natural and simulated solar radiation. Sol. Energy. 85 (11), 2732—2740, https://doi.org/10.1016/j.solener.2011.08.012.

Rachmilevitch, M., DaCosta, Huang, B., 2006. Physiological and biochemical indicators for stress tolerance. In: Huang, B. (Ed.), Plant—Environment Interactions. Taylor & Francis, Boca Raton, FL, 321—355.

Santos, L.H.M.L.M., Araújo, A.N., Fachini, A., Pena, A., Delerue-Matos, C., Montenegro, M.C.B.S.M., 2010. Ecotoxicological aspects related to the presence of pharmaceuticals in the aquatic environment. J. Haz. Mat. 175, 45—95, https://doi.org/10.1016/j.jhazmat.2009.10.100.

Schmidt, A.S., Bruun, M.S., Dalsgaard, I., Pedersen, K., Larsen, J.L., 2000. Occurrence of antimicrobial resistance in fish-pathogenic and environmental bacteria associated with four Danish rainbow trout farms. Appl. Environ. Microbiol. 66 (11), 4908—4915, https://doi.org/10.1128/AEM.66.11.4908-4915.2000.

Seoane, M., Rioboo, C., Herrero, C., Cid, Á., 2014. Toxicity induced by three antibiotics commonly used in aquaculture on the marine microalga *Tetraselmis suecica* (Kylin) Butch. Mar. Environ. Res. 101, 1—7, https://doi.org/10.1016/j.marenvres.2014.07.011.

Siedlewicz, G., Pazdro, K., Borecka, M., Kornowska, K., Białk—Bielińska, A., Stepnowski, P., 2014. Determination of Tetracyclines Residues in the Gulf of Gdansk (Southern Baltic Sea) Sediments Using a Tandem Solid-Phase Extraction with Liquid Chromatography Coupled with Tandem Mass Spektrometry. In: Zieliński, T., Pazdro, K., Dragan-Górska, A., Weydmann, A. (Eds.), Insights on Environmental Changes. GeoPlanet: Earth and Planetary Sciences. Springer, Switzerland, 33—45.

Siedlewicz, G., Borecka, M., Białk-Bielińska, A., Sikora, K., Stepnowski, P., Pazdro, K., 2016. Determination of antibiotic residues in southern Baltic Sea sediments using a tandem solid-phase extraction and liquid chromatography coupled with tandem mass spectrometry. Oceanologia 58 (3), 221—234, https://doi.org/10.1016/j.oceano.2016.04.005.

Siedlewicz, G., Borecka, M., Białk-Bielińska, A., Winogradow, K., Stepnowski, P., Pazdro, K., 2018. Presence, concentrations and risk assessment of selected antibiotic residues in sediments and near-bottom waters collected from the Polish coastal zone in the southern Baltic Sea — Summary of 3 years of studies. Mar. Pollut. Bull. 129 (2), 787—801, https://doi.org/10.1016/j.marpolbul.2017.10.075.

Stanier, R.Y., Kunisawa, R., Mandel, M., Cohen-Bazire, G., 1971. Purification and properties of unicellular blue-green algae (Order Chroococcales). Bacteriol. Rev. 35, 171—205.

Strasser, R.J., Srivastava, A., Tsimilli-Michael, M., 2000. The fluorescence transient as a tool to characterize and screen photosynthetic samples. In: Yunus, M., Pathre, U., Mohanty, P. (Eds.), Probing Photosynthesis: Mechanism, Regulation and Adaptation. Taylor and Francis, UK, 445—483.

Strasser, R.J., Tsimilli-Michael, M., Srivastava, A., 2004. Analysis of the chlorophyll *a* fluorescence transient. In: Papadogeorgiou, G.C., Govindjee (Eds.), Chlorophyll *a* Fluorescence: A Signature of Photosynthesis. Springer, Netherlands, 321—362.

Strickland, J.D.H., Parsons, T.R., 1968. A practical handbook of seawater analysis. Fish Res. Board Can. Bull. 169. Fish Res. Board of Canada, Ottawa, 293 pp.

Strickland, J.D.H., Parsons, T.R., 1972. A practical handbook of seawater analysis. Fish Res. Board Can. Bull. 167, 2nd edn., Fish Res. Board of Canada, Ottawa, 310 pp.

Tsiaka, P., Tsarpali, V., Ntaikou, I., Kostopoulou, M.N., Lyberatos, G., Dailianis, S., 2013. Carbamazepine-mediated prooxidant effects on the unicelular marine algal species *Dunaliella tertiolecta* and the hemocytes of mussel *Mytilus galloprovincialis*. Ecotoxicology 22, 1208—1220, https://doi.org/10.1007/s10646-013-1108-3.

Van Boeckel, T.P., van Gandra, S., Ashok, A., Caudron, Q., Grenfell, B.T., Levin, S.A., Laxminarayan, R., 2014. Global antibiotic consumption 2000 to 2010: an analysis of national pharmaceutical sales data. The Lancet Infectious Diseases 14, 742—750, https://doi.org/10.1016/S1473-3099(14)70780-7.

Van der Grinten, E., Pikkemaat, M.G., Van den Brandhof, E.J., Stroomberg, G.J., Kraak, M.H.S., 2010. Comparing the sensitivity of algal, cyanobacterial and bacterial bioassays to different groups of antibiotics. Chemosphere 80, 1—6, https://doi.org/10.1016/j.chemosphere.2010.04.011.

Wang, J., Hu, J., Zhang, S., 2010. Studies on the sorption of tetracycline onto clays and marine sediment from seawater. J. Colloid Interface Sci. 349, 578—582, https://doi.org/10.1016/j.jcis.2010.04.081.

Wille, K., Noppe, H., Verheyden, K., Vanden Bussche, J., De Wulf, E., Van Caeter, P., Janssen, C.R., De Brabander, H.F., Vanhaecke, L., 2010. Validation and application of an LC-MS/MS method for the simultaneous quantification of 13 pharmaceuticals in seawater. Anal. Bioanal. Chem. 397, 1797—1808, https://doi.org/10.1007/s00216-010-3702-z.

Xu, D., Xiao, Y., Pan, H., Me, i Y., 2019. Toxic effects of tetracycline and its degradation products on freshwater green algae. Ecotoxicol. Environ. Safe. 174, 43—47, https://doi.org/10.1016/j.ecoenv.2019.02.063.

Xu, J., Zhang, Y., Zhou, C, Guo, C., Wang, D., Du, P., Luo, Y., Wan, J., Meng, W., 2014. Distribution, sources and composition of antibiotics in sediment, overlying water and pore water from Taihu Lake, China. Sci. Total Environ. 497—498, 267—273, https://doi.org/10.1016/j.scitotenv.2014.07.114.

Yang, Y., Fu, J., Peng, H., Hou, L., Liu, M., Zhou, J.L., 2011. Occurrence and phase distribution of selected pharmaceuticals in the Yangtze Estuary and its coastal zone. J. Hazard. Mater. 190, 588—596, https://doi.org/10.1016/j.jhazmat.2011.03.092.

Zhang, W., Zhang, M., Lin, K., Sun, W., Xiong, B., Guo, M., Cui, X., Fu, R., 2012. Ecotoxicological effect of carbamazepine on *Scenedesmus obliquus* and *Chlorella pyrenoidosa*. Environ. Toxicol. Pharmacol. 33 (2), 344—352, https://doi.org/10.1016/j.etap.2011.12.024.

Zushi, K., Kajiwara, S., Matsuzoe, N., 2012. Chlorophyll a fluorescence OJIP transient as a tool to characterize and evaluate response to heat and chilling stress in tomato leaf and fruit. Scientia Horticulturae 148, 39—46, https://doi.org/10.1016/j.scienta.2012.09.022.

Żak, A., Musiewicz, K., Kosakowska, A., 2012. Allelopathic activity of the Baltic cyanobacteria against microalgae, Estuar. Coast. Shelf Sci. 112, 4—10, https://doi.org/10.1016/j.ecss.2011.10.007.

Oceanologia (2020) 62, 226—242

Available online at www.sciencedirect.com

ScienceDirect

journal homepage: www.journals.elsevier.com/oceanologia

ORIGINAL RESEARCH ARTICLE

Effects of Global Climate Oscillations on Intermonthly to Interannual Variability of Sea levels along the English Channel Coasts (NW France)

Imen Turki*, Nicolas Massei, Benoit Laignel, Hassan Shafiei

UMR CNRS 6143 — Continental and Coastal Morphodynamics 'M2C', University of Rouen, Mont-Saint-Aignan Cedex, France

Received 25 May 2019; accepted 20 January 2020
Available online 5 February 2020

KEYWORDS
Sea level;
Extreme surges;
Multiscale variability;
Storms;
Climate oscillations;
Multiresolution analysis

Summary This work examines the multiscale variability in sea level along the English Channel coasts (NW France) using a wavelet multiresolution decomposition of water level values and climate oscillations in order to gain insights in the connection between the global atmospheric circulation and the local-scale variability of the monthly extreme surges. Changes in surges have exhibited different oscillatory components from the intermonthly (~3—6-months) to the interannual scales (~1.5-years, ~2—4-years, ~5—8-years) with mean explained variances of ~40% and ~25% of the total variability respectively. The correlation between the multiresolution components of surges and 28 exceptional stormy events with different intensities has revealed that energetic events are manifested at all timescales while moderate events are limited to short scales.

By considering the two hypotheses of (1) the physical mechanisms of the atmospheric circulation change according to the timescales and (2) their connection with the local variability improves the prediction of the extremes, the multiscale components of the monthly extreme surges have been investigated using four different climate oscillations (Sea Surface Temperature (SST), Sea-Level Pressure (SLP), Zonal Wind (ZW), and North Atlantic Oscillation (NAO)); results show statistically significant correlations with ~3—6-months, ~1.5-years, ~2—4-years, and ~5—8-years, respectively. Such physical links, from global to local scales, have been

* Corresponding author at: Imen Turki, UMR CNRS 6143 — Continental and Coastal Morphodynamics 'M2C', University of Rouen, 76821 Mont-Saint-Aignan Cedex, France.
E-mail addresses: imen.turki@univ-rouen.fr (I. Turki), nicolas.massei@univ-rouen.fr (N. Massei), benoit.laignel@univ-rouen.fr (B. Laignel), hassan.shafiei@univ-rouen.fr (H. Shafiei).
Peer review under the responsibility of Institute of Oceanology of the Polish Academy of Sciences.

Production and hosting by Elsevier

https://doi.org/10.1016/j.oceano.2020.01.001

considered to model the multiscale monthly extreme surges using a time-dependent Generalized Extreme Value (GEV) distribution. The incorporation of the climate information in the GEV parameters has considerably improved the fitting of the different timescales of surges with an explained variance higher than 30%. This improvement exhibits their nonlinear relationship with the large-scale atmospheric circulation.

1. Introduction

With the present context of global climate change, most of researchers claim that the sea-level variability and the increase of storminess are considered significant hazards for several low-lying coastal communities (e.g. Hanson et al., 2011; Nicholls et al., 2011). Hence, many efforts have been devoted to better understand the natural processes driving the multiscale variability of the extreme sea levels to produce a more accurate estimation of their fluctuations and ensuring reliable coastal risk assessments. This challenge serves as the basis for implementing an appropriate adaptation strategy reducing the disastrous risks of the coastal flooding. The sea-level changes, encompassing cyclical seasonal components superimposed on long-term trends and stochastic variability, are one of the most important physical processes affecting the coastal systems. These changes are due to the frequent temporal shifts linked to the nonlinear, stochastic, or transient effects of external factors such as the global climate patterns (Pasquini et al., 2008).

Changes in sea levels are largely driven by the large-scale atmospheric and oceanic circulation patterns operating on intermonthly and interannual timescales. Moreover, studying the links of the sea-level variability with the climate teleconnections, related to prominent atmospheric modes as proxies, is necessary to fully understand the interplay between the climate oscillations and the oceanographic processes (e.g. Dangendorf et al., 2012; Levin, 1992; Yan, 2004; Zampieri et al., 2017). Some works have been implemented to understand and extract the signature of internal climate variability from the observed sea-level patterns (e.g. Dangendorf et al., 2012; Levin, 1992; Yan, 2004; Zampieri et al., 2017) with the aim of contributing in the multiscale sea-level predictions that emerge as urgent priorities in the state-of-the-art climate research.

Large timescale studies around the English Channel (South coast of UK) have been presented in Haigh et al. (2009) work, where changes in the mean sea levels have been investigated by the use of hourly sea-level records extended by data archaeology. They have found that mean sea-level trends vary between 0.8 and 2.3 mm/year around the Channel. A new approach of spectral analysis has been used by Turki et al. (2015a) to investigate the annual and the intermonthly changes of the sea level along the English Channel coasts (NW France). Such multiscale changes have been linked to a combination of meteorological and North Atlantic Oscillation (NAO) climate drivers, involving several processes over a wide range of spatial and temporal scales.

Being an alarming problem for the coastal vulnerability, extreme events have gained the attention of the scientists who have reported the dynamics (e.g., Haigh et al., 2010; Idier et al., 2012; Masina and Lamberti, 2013; Tomasin and Pirazzoli, 2008; Turki et al., 2019) and the projections (e.g., Vousdoukas et al., 2017) of extreme sea levels considering the stationary and the nonstationary contributions from tides, waves, sea-level-rise components (e.g., Brown et al., 2010; Idier et al., 2017), and large-scale climate oscillations (e.g., Colberg et al., 2019; Turki et al., 2019).

A number of studies have examined the relationship between the global atmospheric patterns and the local sea levels to estimate sea-level extreme values by the use of nonstationary statistical approaches. Regional studies of extreme sea levels have been conducted in various works using different methodologies; the most common of them is related to the Generalized Extreme Value (GEV) models. A review of extreme analyses has been performed by Mendez and Woodworth (2010); they applied a nonstationary extreme value model to the monthly maxima with a special focus on NAO to study the variability of the extreme sea levels along the European coasts. Masina and Lamberti (2013) have used a nonstationary GEV model to demonstrate a coherent behavior between the regional and the global scales from a detailed analysis of the annual mean sea-level evolution in the Adriatic sea with the NAO and AO (Arctic Oscillation) indices; they have suggested that the increase in the extreme water levels since the 1990s is related to the changes in the wind regime and the intensification of Bora and Sirocco winds after the second half of the 20 th century.

In the English Channel, the extreme sea levels have been addressed by several works (e.g. Haigh et al., 2010; Idier et al., 2012; Tomasin and Pirazzoli, 2008; Turki et al., 2019) with the aim of investigating their dynamics at different timescales and their connections to the atmospheric circulation patterns.

Haigh et al. (2010) investigated the interannual and the interdecadal extreme surges in the English Channel and their strong relationship with the NAO index. Their results showed weak negative correlations throughout the Channel and strong positive correlations at the boundary along the Southern North Sea. Using a numerical approach, Idier et al. (2012) studied the spatial evolution of some historical storms in the Atlantic Sea and their dependence on tides.

Recently, Turki et al. (2019) have examined the multiscale variability of the sea-level changes in the Seine Bay (NW France) in relation with the global climate oscillations from the SLP composites; they have demonstrated dipolar patterns of high-low pressures suggesting positive and

negative anomalies at the interdecadal and the interannual scales, respectively.

Despite these important advances, no particular studies exist on sea-level dynamics and extreme events linked to the large-scale climate oscillations along the English Channel coastlines. The aforementioned works of Turki et al. (2015a, 2019) have focused on the multiscale sea-level variability along the French coasts related to the NAO and the Sea-Level Pressure (SLP) patterns; however, they have not addressed the regional behavior of the extreme sea levels in relation with the global climate oscillations.

The present contribution aims to investigate the regional dynamics of the sea level and the extreme events in some selected English Channel coasts (NW France) and seeks to understand their multiscale connection to the large-scale atmospheric circulation. A spectral approach based on the continuous and multi-resolution wavelet techniques has been used herein in order to (i) visualize and investigate the spectral content of the sea levels on intermonthly to the interannual scales, (ii) identify the links between the sea-level fluctuations and the increase of the historical storm events, (iii) quantify the multiscale changes in the monthly maxima of extreme surges and their connection with the atmospheric circulation by applying a nonstationary approach using the climate oscillations.

The rest of the paper is organized into four sections: Section 2 gives a description of the data sources and the methodological approach used to investigate the multiscale variability of the sea level with the atmospheric circulation. Local-scale changes in sea levels along the English Channel and their connection with the climate oscillations have been addressed and discussed in sections 3 and 4, respectively. Finally, all findings are summarized and concluded in Section 5.

2. Data and methods

2.1. Sea-level and climate datasets

The present research is focused on the Normandy coasts along the Southern side of the English Channel (North of France); it has been conducted in the framework of the French research program ANR RICOCHET and the international project COTEST funded by CNES-TOSCA and related to the future mission Surface Water and Ocean Topography (SWOT).

Sea-level data, obtained from three tide gauge sites, are used in the present study: (1) Dunkirk station which is a few kilometers away from Belgian borders, (2) Le Havre stations situated on the right bank of the estuary of the Seine River, and (3) Cherbourg station located on the Cotentin Peninsula and at the opening of the Atlantic Sea. These stations provide time-series of hourly observations measured between 1964 and 2010. The tide gauges are operated and maintained by the National French Center of Oceanographic Data (SHOM). The observations which correspond to the hydrographic zero level are referenced to zero tide gauge (Fig. 1). The storm events produced in the English Channel largely occurred along Cherbourg, Le Havre, and Dunkirk coasts. The surges in these regions are equal or higher than the values of 2year return period (Re) which represents 1.2 m, 1.3 m, and 1.6 m, respectively (SHOM).

The large-scale atmospheric circulations are represented in the present analysis by four different climate indices which are considered as fundamental drivers in the Atlantic regions: the Sea Surface Temperature (SST), the North Atlantic Oscillation (NAO), the Zonal Wind (ZW) component extracted at 850hPa, and the Sea-Level Pressure (SLP). Monthly time-series of climate index have been provided by the NCEP-NCAR Reanalysis fields[1] with the same period during which the sea-level observations were conducted (i.e. 1964–2010).

2.2. Methods

The total sea-level height, resulting from the astronomical and the meteorological processes, exhibits a temporal non-stationarity which is explained by a combination of the effects of the long-term trends in the mean sea level, the modulation by the deterministic tidal component and the stochastic signal of surges, and the interactions between tides and surges. The occurrence of extreme sea levels is controlled by periods of astronomically-generated high tides, in particular, at inter-annual scale when two phenomena of precession cause systematic variation of high tides. The modulation of the tides contributes to the enhanced risk of coastal flooding. Therefore, the separation between tidal and non-tidal signal is an important task in any analysis of sea-level time-series.

By the hypothesis of independence between the astronomical tides and the stochastic residual of surges, the non-linear relationship between the tidal modulation and surges is not considered in the present analysis. Using the classical harmonic analysis, the tidal component has been modeled as the sum of a finite set of sinusoids at specific frequencies to determine the determinist phase/ amplitude of each sinusoid and predict the astronomical component of tides. In order to obtain a quantitative assessment of the non-tidal contribution in storminess changes, technical methods based on MATLAB t-tide package have been used to estimate year-by-year tidal constituents. A year-by-year tidal simulation (Shaw and Tsimplis, 2010) has been applied to the sea-level time-series to determine the amplitude and the phase of tidal modulations using harmonic analysis fitted to 18.61-, 9.305-, 8.85-, and 4.425-year sinusoidal signals (Pugh, 1987). The radiational components have been also considered for the extraction of the stochastic component of surges (Williams et al., 2018). The hourly sea-level measurements present some short gaps (of some days) distributed during the first 30 years (1964–1995) of the total time-series. These gaps, with respect to the total series, represent 2% in Cherbourg and Le Havre and 5% in Dunkirk; they have been processed by the hybrid model for filling gaps developed by Turki et al. (2015b). The model applies a purely statistical approach to the stochastic component of the sea level (residual component) based on Autoregressive Moving Average (ARMA) techniques with introducing SLP in ARMA as a main physical process driving the residual

[1] http://www.esrl.noaa.gov/psd/data/gridded/data.ncep.reanalysis.derived.html

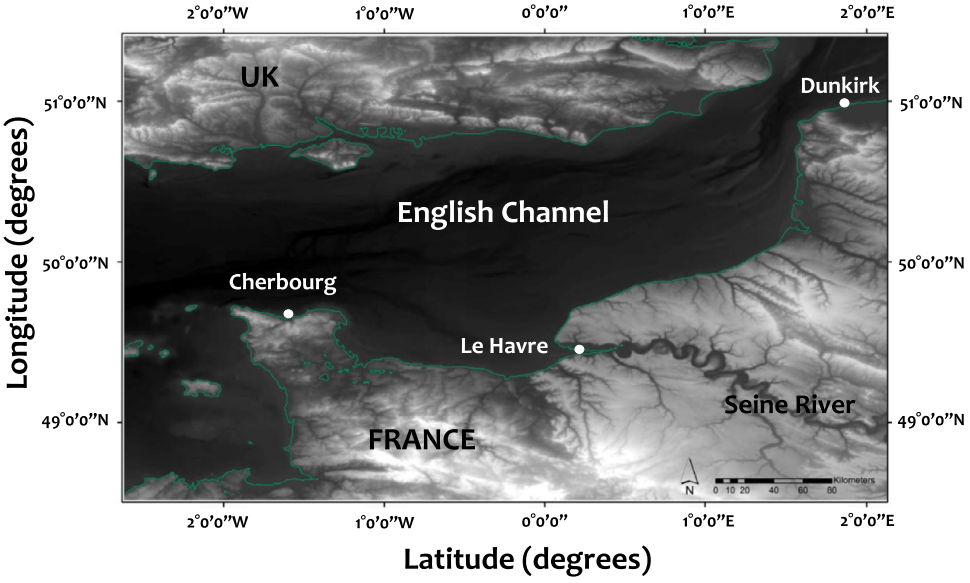

Figure 1 Geographical location of the study area and the different tide gauges along the Southern English Channel coasts (NW France): Dunkirk, Le Havre, and Cherbourg.

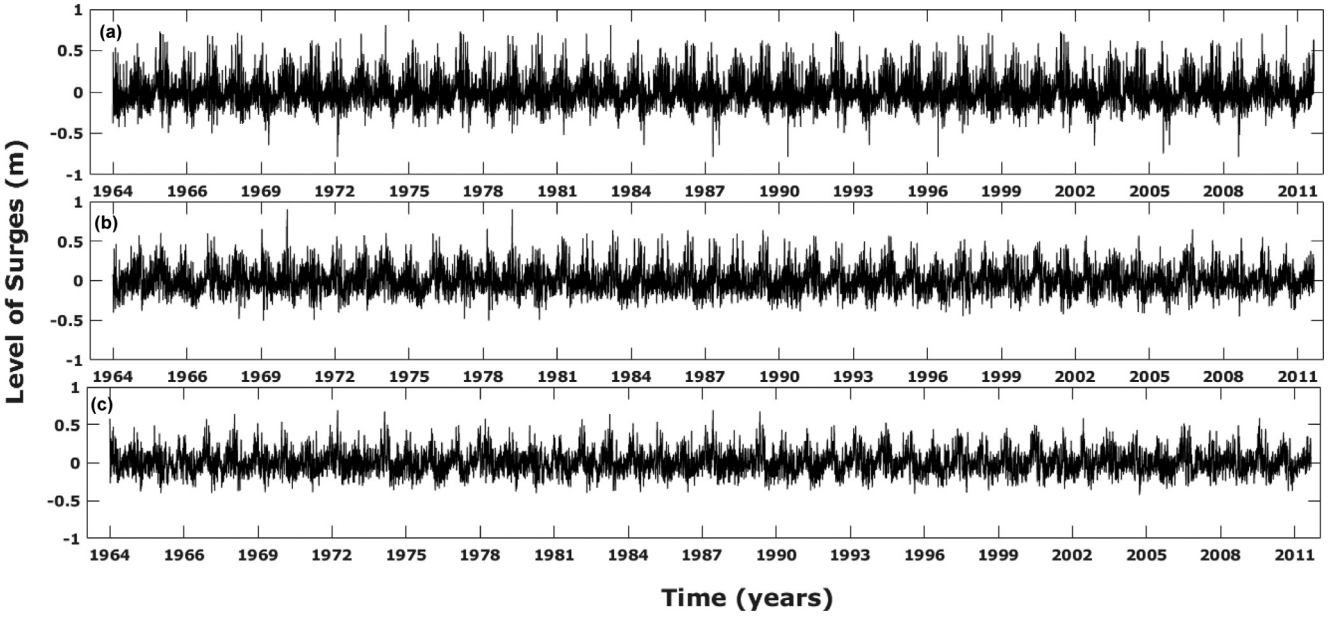

Figure 2 The hourly surges during the period 1964–2010 in (a) Dunkirk, (b) Le Havre, and (c) Cherbourg.

sea level. They have used this model to process the sea-level records provided by the tide gauges along the Atlantic French coasts. The model has been used also by Turki et al. (2019) for data processing. The total sea level and surges at Dunkirk, Le Havre, and Cherbourg are illustrated in Fig. 2.

The general approach developed herein intends to: (1) identify the main timescales of the variability of the total sea levels and surges, (2) characterize the multiscale relationships between the local-scale hydro-climatological signal of the surges and the historical storm events on large scales, (3) examine the ability of the potential monthly climate predictors (NAO, ZW, SLP, SST) to describe the time-scale decomposition of the monthly extreme surges by identifying the physical link between both variables at each time scale. Such physical link has been used for a multiscale parameterization of the non-stationary GEV models. Firstly, the hourly hydro-climatological signals (i.e. total sea level and surges) have been analyzed using continuous wavelet transform (CWT) to explore the spectral content of oceanographic signals. The typical scales of the sea-level variability (Turki et al., 2015a, 2019) have been detected from different records.

The CWT is a well-known method that has been used over the past decade for data analysis in hydrology, geophysics, and environmental sciences (Labat, 2005; Sang, 2013; Torrence and Compo, 1998). The continuous wavelet transform produces either a time-scale or time-period with the means of the Fourier transform contour diagram on

which time is indicated on the *x*-axis, period, or scale on the *y*-axis, and amplitude (or variance, or power, etc.) on the *z*-axis.

Secondly, the hourly surges have been decomposed by wavelet multiresolution analysis into different internal components corresponding to different time-scales. Briefly, the multiresolution analysis consists of the iterative filtering of the time-series using a series of low-pass and high-pass filters which eventually produce one high-frequency "rough" component called "wavelet detail" and one lower frequency "coarse" component called "smooth" or "approximation".

The smooth, produced at each scale, is then subsequently decomposed into a second wavelet detail and a second smooth, the latter is decomposed again in the same way until one last smooth remains and will no longer be decomposed. Summing up all wavelet details and the last smooth (i.e. the lowest-frequency component) gives back the original signal. In summary, the total signal has been separated into a relatively small number of wavelet components from high to low frequencies that altogether explains the variability of the signal; this will be illustrated later using the hourly measurements and the monthly maxima of surges.

Finally and with the aim of addressing the nonstationary behavior of extreme surges, the monthly maxima of the surges have been calculated and decomposed with the multiresolution analysis. Then, a nonstationary extreme value analysis based on the GEV distribution with time-dependent parameters (Coles, 2001) has been implemented to model the series of the monthly maxima surges. There are several GEV families which depend on the shape parameter, e.g. Weibull ($\varepsilon < 0$), Gumbel ($\varepsilon = 0$), and Fréchet ($\varepsilon > 0$). The three parameters of the GEV (i.e. location μ, scale ψ, shape ε) are estimated by the maximum likelihood function.

The nonstationary effect was considered by incorporating the selected climate indices (NAO, SST, ZW, and SLP) into the parametrization of the GEV models. Akaike Information Criterion (AIC) has been used to select the most appropriate probability function models. The methods of maximum likelihood were used for the estimation of the distributions parameters. The approach used considers the location (μ), the scale (ψ), and the shape (ε) parameters with relevant covariates, which are described by a selected climate index:

$$\mu(t) = \beta_{0,\mu} + \beta_{1,\mu} Y_1 + \ldots + \beta_{n,\mu} Y_n, \quad (1)$$

$$\psi(t) = \beta_{0,\psi} + \beta_{1,\psi} Y_1 + \ldots + \beta_{n,\psi} Y_n, \quad (2)$$

$$\varepsilon(t) = \beta_{0,\varepsilon} + \beta_{1,\varepsilon} Y_1 + \ldots + \beta_{n,\varepsilon} Y_n, \quad (3)$$

where β_0, β_1,..., β_n are the coefficients, and Y_i is the covariate represented by the climate index. For each spectral component, only one climate index can be used among the parameters μ, ψ, and ε of the nonstationary GEV model. With the aim of optimizing the best use of the climate index into the different GEV parameters, a series of sensitivity analyses were implemented for each time scale. The AIC measures the goodness of fit of the model (Akaike, 1974) to the relation $AIC = -2l + 2K$; where l is the log-likelihood value estimated for the fitted model, and K is the number of the model parameters. Higher ranked models should result from lower AIC scores.

3. Results

3.1. The multiscale sea-level variability

The variability of the total sea level (SL) and the surges (S) has been investigated using the continuous wavelet transform (CWT). In the spectrum of Fig. 3, the color scale represents an increasing power (variance) from blue to red. The CWT diagrams highlight the existence of several modes of variability; each color represents one of the energy bands with certain ranges of frequencies. The annual mode is clearly illustrated for SL while it is largely dissipated for S spectrum with a diminution higher than 90% in Dunkirk and Cherbourg. The dissipation of the annual spectrum becomes less important (with a spectrum diminution of 72%) for S in Le Havre as it gets closer to the Seine Bay. where the hydrological signature, induced by the Seine River, still remains to be observed within the stochastic component of the sea level.

At the interannual scales, the CWT diagrams highlight two modes of ~2–4-yr and ~5–8-yr at all the stations, particularly Cherbourg and Le Havre. Such low frequencies are well-structured with 45% and 65% of the explained variance higher than those calculated from the CWT of SL. The CWT diagrams of S display a new mode of ~1.5-yr while the annual mode, observed in the SL diagrams, has been disappeared.

The multiresolution analysis has been applied to local surges with the aim of achieving the full timescale decomposition of the signal. The process results in separation of different components or wavelet details for each signal (Figs. 4–6). We focused only on frequencies ranging between ~3-months and ~5–8-years, whose fluctuations correspond to the oscillation periods less than half the length of the record and exhibit a high-energy contribution on the variance of the total signal.

Results have been explored to investigate the dynamics of surges at different timescales. The variability is clearly dominated by the high-frequencies of ~3-months and ~6-months, explaining a variance between 35% and 45% of the total energy respectively (Table 1). Then, the low frequency components of ~1.5-yr, ~2–4-yr, and ~5–8-yr explain a mean variance of 25% of the total energy (Table 1).

Figs. 4–6 show a series of oscillatory components of surges from intermonthly to interannual scales, not clearly identified by a simple visual inspection of the signal. Similarities of surge components have been highly observed for the interannual modes of ~5–8-yr and ~2–4-yr while they seem to be significantly less important for high frequencies of ~3-months and ~6-months. This result suggests that different physical phenomena should be considered to explain the local variability of surges (~3-months and ~6-months); they are induced by combining the effects of meteorological and oceanographic forces including changes in atmospheric pressures and wind velocities in shallow water areas. Beyond the ~1.5-yr timescale, the large-scale patterns of surges, described by the low frequency components, tend to be quite similar between the different sites in terms of intensity and amplitude. Such variability exhibits a global contribution of some physical processes related to the climate oscillations. The extent of these oscillations is not

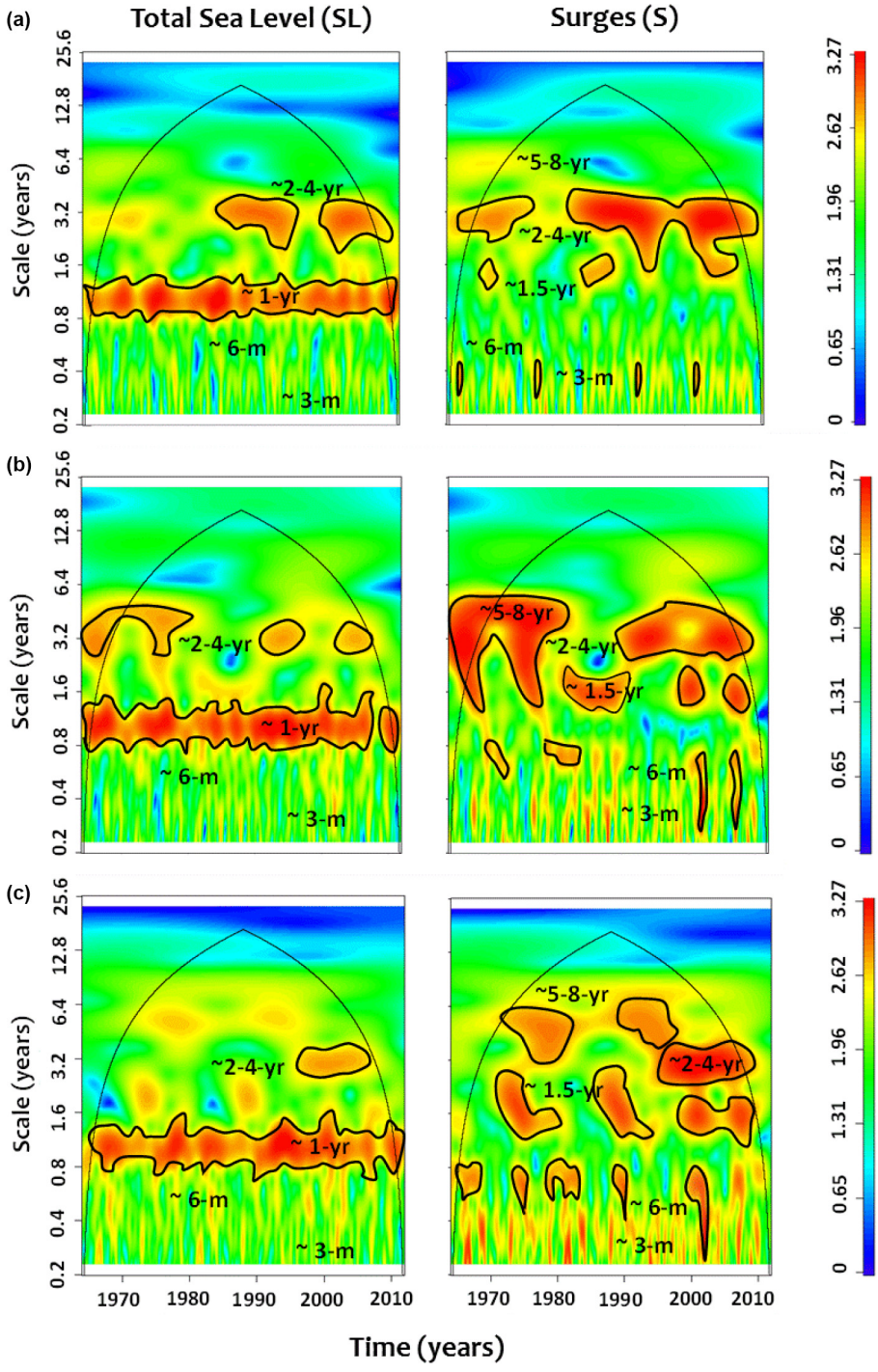

Figure 3 Continuous wavelet transform (CWT) of the total and the non–tidal (surges) sea level at (a) Dunkirk, (b) Le Havre and (c) Cherbourg during the period 1964–2010.

Table 1 The explained variance expressed as percentage of total variance of surges for all sites: Dunkirk, Le Havre and Cherbourg.

	~ 3 months	~ 6 months	~ 1.5- y	~ 2–4 -y	~ 5–8-y
Dunkirk	20 %	15.6 %	12.8 %	8.6 %	5.3 %
Le Havre	27.7 %	18.2 %	14 %	8.8 %	5.7 %
Cherbourg	28.8 %	20.5 %	15.4 %	8.9 %	4.2 %

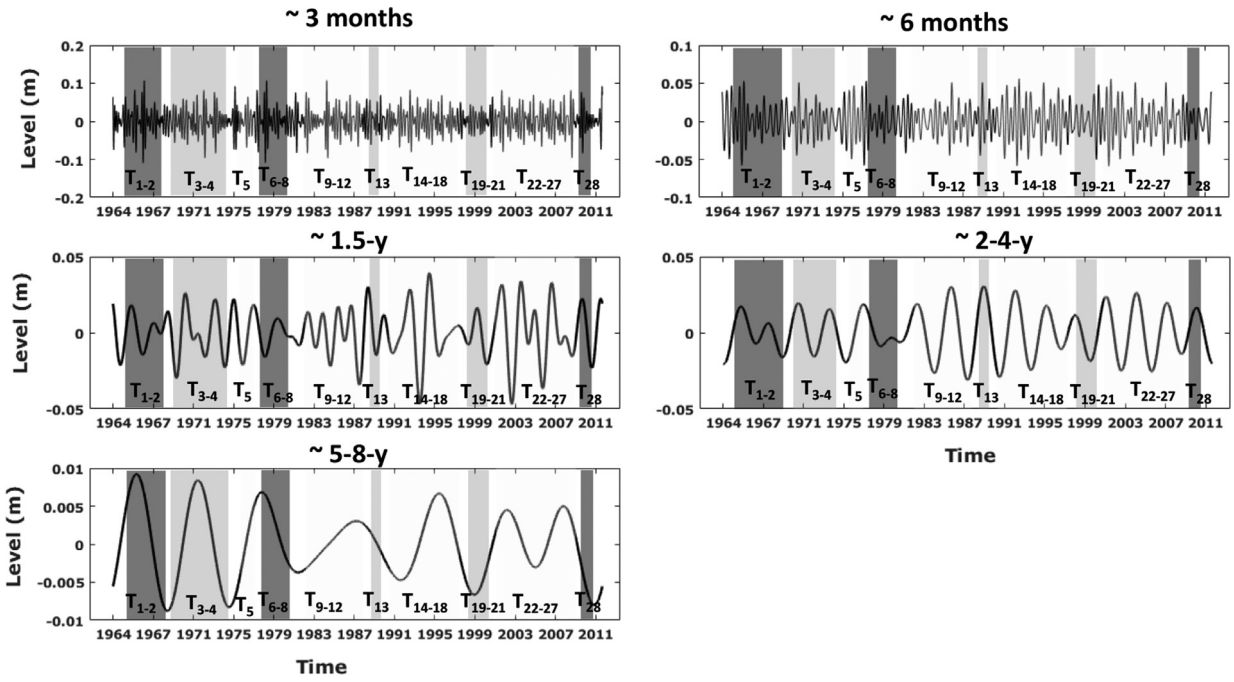

Figure 4 Wavelet details (components) resulting from multiresolution analysis of surges from 1964 to 2012 at the intermonthly (∼3 months, ∼ 6 months) and interannual (∼1.5-yr, ∼2—4-yr, ∼5—8-yr) time scales in Dunkirk. The black, grey and white boxes are used for storms manifested similarly in Le Havre and Cherbourg (same return period observed), similarly in Cherbourg and Dunkirk and similarly for all sites, respectively.

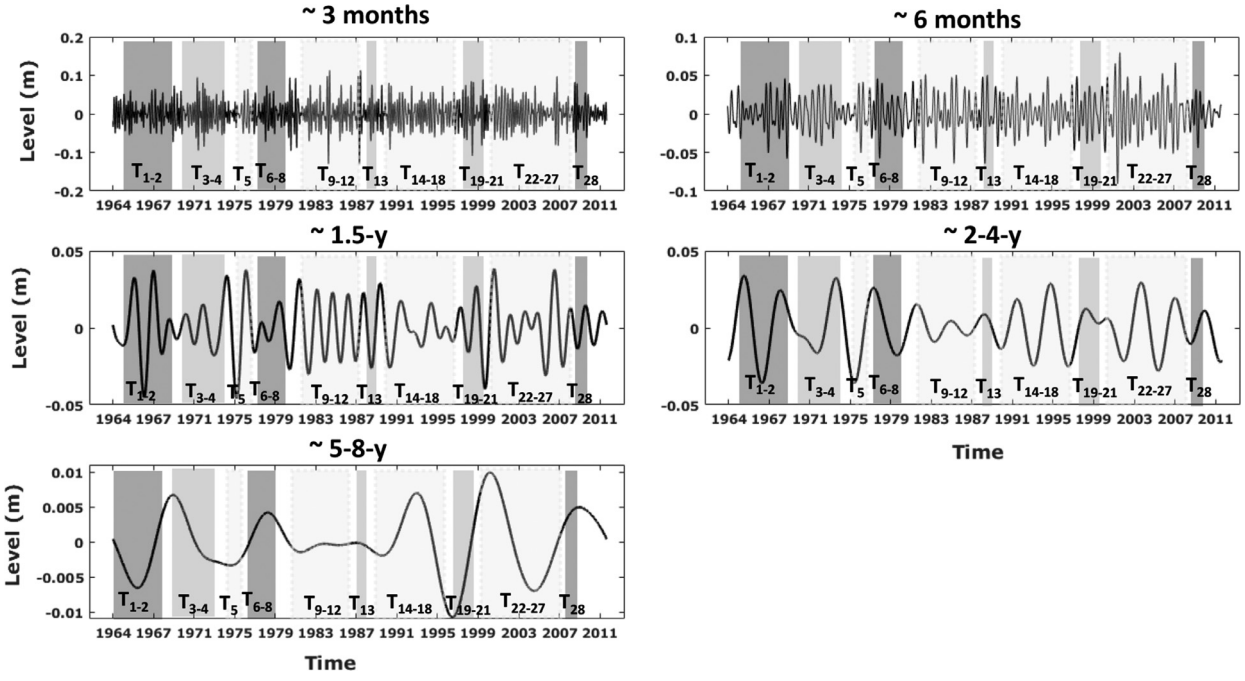

Figure 5 Wavelet details (components) resulting from multiresolution analysis of surges from 1964 to 2012 at the intermonthly (∼3 months, ∼6 months) and interannual (∼1.5-yr, ∼2—4-yr, ∼5—8-yr) time scales in Le Havre. The black, grey and white boxes are used for storms manifested similarly in Le Havre and Cherbourg (same return period observed), similarly in Cherbourg and Dunkirk and similarly for all sites, respectively.

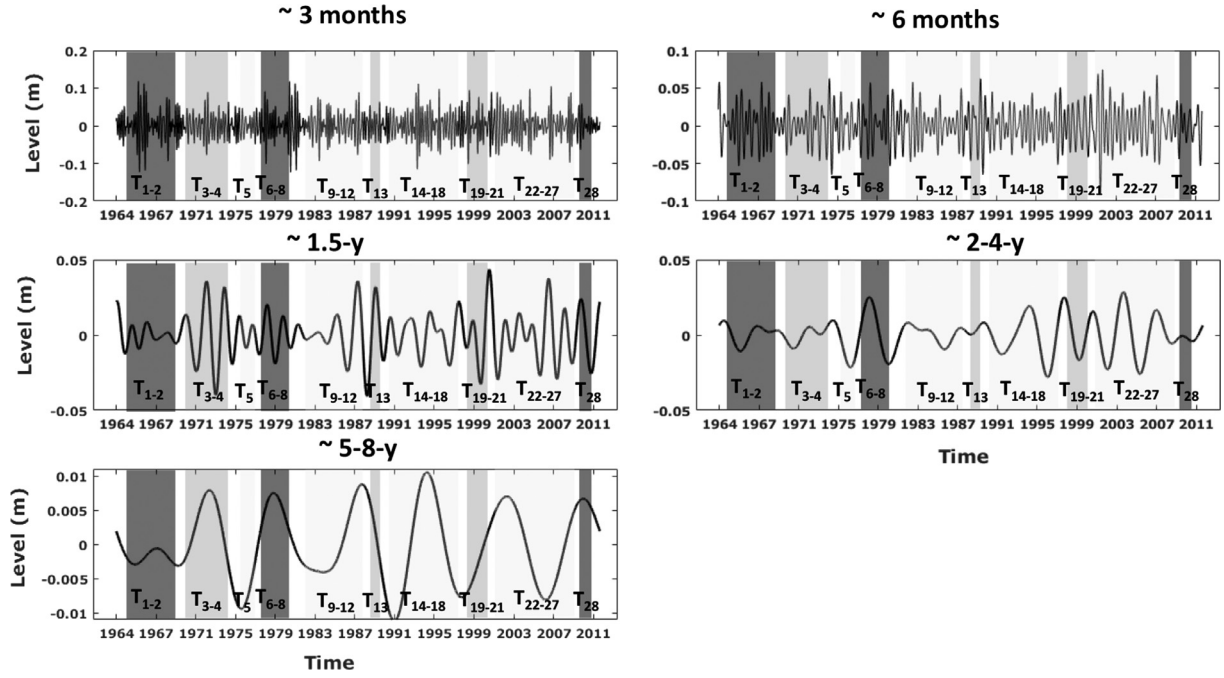

Figure 6 Wavelet details (components) resulting from multiresolution analysis of surges from 1964 to 2012 at the intermonthly (~3 months, ~6 months) and interannual (~1.5-yr, ~2–4-yr, ~5–8-yr) time scales in Cherbourg. The black, grey and white boxes are used for storms manifested similarly in Le Havre and Cherbourg (same return period observed), similarly in Cherbourg and Dunkirk and similarly for all sites, respectively.

strictly similar and changes according to the timescale variability since the dynamics of surges is not necessarily related to the same type of atmospheric circulation process. This relationship will be addressed later in the second part of this section.

A total of 28 historical stormy events (from T_1 to T_{28}), produced in the English Channel during the period 1964–2010 and with surges higher than 2-yr return period level (Re), have been extracted from SHOM data base (Table 2). The historical events have been attached to the different spectral components of surges (Figs. 4–6) by vertical bars with different colors (black, grey and white).

In these figures, we distinguish three types of events: (1) the first one, depicted by the black bars, represents the storms occurring in Le Havre and Cherbourg with the same Re; (2) the second one, depicted by the white bars, shows the storms similarly manifested in Cherbourg, Le Havre and Dunkirk; (3) the third one, depicted by the grey bars, illustrates the storms occurring in Le Havre and Cherbourg with the same Re .The percentages of each of the bars are 21.4, 57.2, and 21.4%, respectively.

The storms in Figs. 4–6 show that the signature of each event is fully identified at the intermonthly scales while it is manifested differently at the interannual scales.

The events of November 1965 (T_1) and January 1968 (T_2), produced at neap tides, are highlighted by the peak of the surges at the interannual scales; they are limited to ~1.5-yr and ~2–4-yr in Le Havre and Cherbourg where Re is of 2–5 years. The storms T_3 (July 1969) and T_4 (February 1974) exhibit a high energy for most of the components in Le Havre (Re of 5–10 years), as shown in Fig. 5; furthermore, their effects are limited to ~1.5-yr component in Dunkirk and Cherbourg. As documented by Bessemoulin (2002), these storms (in particular T_3) were resulted from the big atmospheric depression Ex-Bertha with high wind velocities (more than 150 km/h) and barometric gradients (maximum of 14 hPa). T_5 is manifested in different locations with Re of 2-years; its impact is restricted to the ~1.5-yr component of surges. Similar behavior has been identified for the events T_{9-12}, T_{15-16}, and T_{18} produced at neap tides. The events T_6 (January 1978), T_{13} (February 1989), and T_{14} (January 1990, 'DARIA') coincide with spring tides and high return period (Re > 5 years); they have been recorded at the interannual scales in Le Havre and Cherbourg. According to the previous works of Bessoumoulin (2002) and Pirazzoli et al. (2005), these events were induced by cold fronts known as Kata split front responsible for decreasing of the pressure and a shift of the wind from SSW to WSW.

The events T_7, T_8, and T_{17} were produced during winter periods at the equinoxes of spring tides with Re of 5–10 years; they are manifested at the full interannual timescales (from ~1.5-yr to ~5–8-yr) in Le Havre and Cherbourg. Such events were generated by two huge anticyclones with large pressure gradients from the North to the West: the first one was resulting from the NW winds; the second one was coming from the Atlantic to reach the North Sea and the Scandinavian countries, responsible for more than 70% of the submersion phenomena in the NW France (Costa et al., 2004).

The two storms of T_{19} (December 1999) and T_{20} (December 2001) highlighted a clear signature limited to ~1.5-yr in Dunkirk and Cherbourg while they are manifested at different interannual scales than Le Havre, close to the Seine Bay, where the influence of the hydrological variability is

Table 2 List of storminess with a surge return period (Re) higher than 2 years and produced between 1964 and 2010 in Dunkirk, Le Havre, and Cherbourg. The black, grey, and white boxes are used for storms manifested similarly in Le Havre and Cherbourg (same return period observed), similarly in Cherbourg and Dunkirk and similarly for all sites, respectively.

Code	Date	Surge return period	Tide cycle
T_1	November, 1965	H_5–H_{10} (Dunkirk) H_2–H_5 (Le Havre, Cherbourg)	Neap tide
T_2	January, 1968	H_5–H_{10} (Dunkirk) H_2–H_5 (Le Havre, Cherbourg)	Neap tide
T_3	July, 1969	H_2 (Dunkirk, Cherbourg) H_5–H_{10} (Le Havre)	Neap tide
T_4	February, 1974	H_2 (Dunkirk, Cherbourg) H_2–H_5 (Le Havre)	Spring tide
T_5	December, 1976	H_2 (Dunkirk, Le Havre, Cherbourg)	Neap tide
T_6	January, 1978	H_5–H_{10} (Dunkirk) H_5 (Le Havre, Cherbourg)	Spring tide (equinoxes)
T_7	December, 1979	H_5–H_{10} (Le Havre, Cherbourg) H_5 (Dunkirk)	Spring tide (equinoxes)
T_8	December, 1981	H_5–H_{10} (Le Havre, Cherbourg) H_5 (Dunkirk)	Spring tide
T_9	December, 1982	H_2 (Dunkirk, Le Havre, Cherbourg)	Neap tide
T_{10}	January, 1984	H_2 (Dunkirk, Le Havre, Cherbourg)	Neap tide
T_{11}	March, 1986	H_2 (Dunkirk, Le Havre, Cherbourg)	Neap tide
T_{12}	October, 1987	H_2 (Dunkirk, Le Havre, Cherbourg)	Neap tide
T_{13}	February, 1989	H_5–H_{10} (Cherbourg, Dunkirk) H_2–H_5 (Le Havre)	Spring tide
T_{14}	January, 1990 (DARIA)	H_5–H_{10} (Dunkirk, Le Havre, Cherbourg)	Neap tide
T_{15}	May, 1992	H_2 (Dunkirk, Le Havre, Cherbourg)	Neap tide
T_{16}	September, 1993	H_2 (Dunkirk, Le Havre, Cherbourg)	
T_{17}	December, 1995	H_5–H_{10} (Dunkirk, Le Havre, Cherbourg)	Spring tide (equinoxes)
T_{18}	October, 1998	H_2 (Dunkirk, Le Havre, Cherbourg)	Neap tide
T_{19}	December, 1999	H_2 (Dunkirk, Cherbourg) H_5–H_{10} (Le Havre)	Spring tide
T_{20}	December, 2001	H_2 (Dunkirk, Cherbourg) H_5–H_{10} (Le Havre)	Spring tide
T_{21}	February, 2004	H_5–H_{10} (Dunkirk, Cherbourg) H_5 (Le Havre)	Neap tide
T_{22}	April, 2005	H_2–H_5 (Dunkirk, Le Havre, Cherbourg)	Spring tide
T_{23}	March, 2006	H_2–H_5 (Dunkirk, Le Havre, Cherbourg)	Spring tide (equinoxes)
T_{24}	November, 2007	H_2 (Dunkirk, Le Havre, Cherbourg)	Neap tide
T_{25}	March, 2008	H_5–H_{10} (Dunkirk, Le Havre, Cherbourg)	Spring tide (equinoxes)
T_{26}	January, 2009	H_2–H_5 (Dunkirk, Le Havre, Cherbourg)	Neap tide
T_{27}	February, 2010	H_5–H_{10} (Dunkirk, Le Havre, Cherbourg)	Spring tide
T_{28}	December, 2010	H_2–H_5 (Dunkirk) H_5–H_{10} (Le Havre, Cherbourg)	Neap tide

important during the flooding events between 20th century and the beginning of 21st century (Massei et al., 2017).

T_{21} (February 2004) was produced at neap tides with strong winds of 140 km/h (SHOM, 2014); this event is mainly carried out by the interannual components. T_{22} and T_{23} (Re between 2 and 5 years), were recorded for the sites at the scales of ∼1.5-yr and ∼2–4-yr while T_{24} (Re of 2 years) is limited to ∼1.5-yr. The last events T_{25}, T_{27}, and T_{28} (Re > 5 years) occurred during the winter periods the equinoxes of spring tides, are manifested at all timescales in Le Havre and Cherbourg and seem to be limited to ∼4–8-yr component in Dunkirk.

Accordingly, the multiscale variability of the surges, as a response to extreme events, highlights that 14% of storms are manifested at all the interannual timescales while 32% of them are limited to ∼2–4-yr. This correspondence suggests the relationship between the return period of the storms and the multiscale variability of the surges; storms with Re < 5 years are manifested at timescales smaller than 5 years while storms with high Re of 5–10 years should be observed from the intermonthly to the interannual scales of ∼5–8-yr.

This diagnosis of the historical events and their manifestation along the North French coasts (From Dunkirk to Cherbourg) allows the following classification: (i) the events produced at neap tides and similarly affecting the studied sites of the Normandy coasts at the interannual scales of ∼1.5-yr (T_5, $T_{9\text{-}12}$, $T_{15–16}$, and T_{18}) and ∼2–4-yr (T_{22} and T_{23}); (ii) the events induced by Kata split font under spring tides and evolving similarly in Le Havre and Cherbourg and with higher impact in Dunkirk (T_6 and $T_{13–14}$); (iii) the events induced by a combination of two anticyclones effects, from the Atlantic to the North Sea, and affecting similarly Le Havre and Cherbourg and with a less remarkable impact in Dunkirk (T_{17} and $T_{7\text{-}8}$); (vi) the events produced at spring tides and highly affecting Le Havre at different timescales compared to Dunkirk and Cherbourg where their manifestation is limited to ∼1.5-yr ($T_{3–4}$ and $T_{19–21}$).

The distribution of the storms is not homogenous in time; moreover, their manifestation, according to different categories of return period, takes a nonlinear behavior since the number of the events in a window of one year is not the same throughout the time. Indeed, all significant events (Re > 2 years) have been identified during only 20 years of measurements from 46 years, the total period of the present study (1964–2010). These dynamics explain the altering phases of high (Re > 2 years) and moderate (Re < 2 years) storms in accordance with their return period. Moderate phases are longer with 3–4 successive years during the first 35 years (1964–2000) and decrease to 2 years after 2000. The phases of high storms exhibit different categories of events: 75% of them are produced between November and February and 25% of them are produced between March and October.

Hence, the distribution of storminess is controlled by a series of seasonal patterns related to changes in ocean wave climate and energy conditions. These seasonal oscillations are clearly identified at the intermonthly surges (∼3–6-months) for all sites. At this scale, similar oscillations have been demonstrated by Tsimplis and Woodworth (1994) from the analysis of the mean sea levels. According to the obtained results, the stormy events, produced under specific meteorological and oceanographic conditions on tides, have exhibited a strong seasonal dependence on the tides which underline a complex network induced by a nonlinear contribution of many physical processes. The hydrological effect should be also considered in the present context of the Seine Bay where the river discharge contributes in the total variability of the stochastic component, in particular during the extreme events of the flooding produced between 1999 and 2001.

Haigh el al. (2010) used English Channel sea-level dataset from 18 tide gauges to evaluate the changes in the extremes throughout the 20 th century. They have identified different intra- and inter-decadal variability in surges with the strongest intensity on the late 1950s. Their studies have shown strong relationship between the storm surges and the NAO index with weak negative correlations throughout the Channel and strong positive correlations at the boundary along the Southern North Sea. The interactions of tides with surges have also been investigated by the same authors showing their increase eastward along the English Channel. The tide-surge interaction has been also studied by Idier et al. (2012) using a numerical approach to compute some historical storms in the Atlantic and the North Sea. According to their analyses, the tide-surge interaction in the English Channel is significantly important; it increases in the eastern half of the English Channel and decreases in westerly direction. In the present research, the stochastic signal of surges has been individually studied and its interaction with tides has not taken into account. The neap-spring tidal cycle has been considered to investigate the dynamics of the stormy events along the French coasts and their signatures in different intermonthly and interannual components of the extreme surges.

3.2. How does the variability in extreme surges depend on the global atmospheric circulation?

This part focuses on the connection between the multiscale variability of the local surges along the French coasts and the global climate oscillations.

The monthly extrema have been simulated from the hourly records of surges in the considered sites. The monthly distribution of the extreme values has been calculated for each scale from the intermonthly to the interannual modes and illustrated by the means of boxplot presentations (example for Dunkirk in Fig. 7). These distributions exhibit that the maximum surges change according to the timescale; the multiscale evolution shows an oscillatory behavior for the short-scales (intermonthly and the first interannual of ∼1.5-yr) shifting between high and low changes in April and September. This shift is more visible at the intermonthly scales of ∼3-months and ∼6-months. For larger scales, the extreme surges display a uniform evolution during the time.

With the aim of addressing the nonstationary behavior of the extreme surges, we have applied the wavelet multiresolution decomposition of monthly extrema for each site. The process has resulted in the separation of different components, i.e. 5 wavelet details traduced by two intermonthly scales (∼3-months and ∼6-months) and three interannual scales (∼1.5-yr, ∼2–4-yr, and ∼5–8-yr). The explained

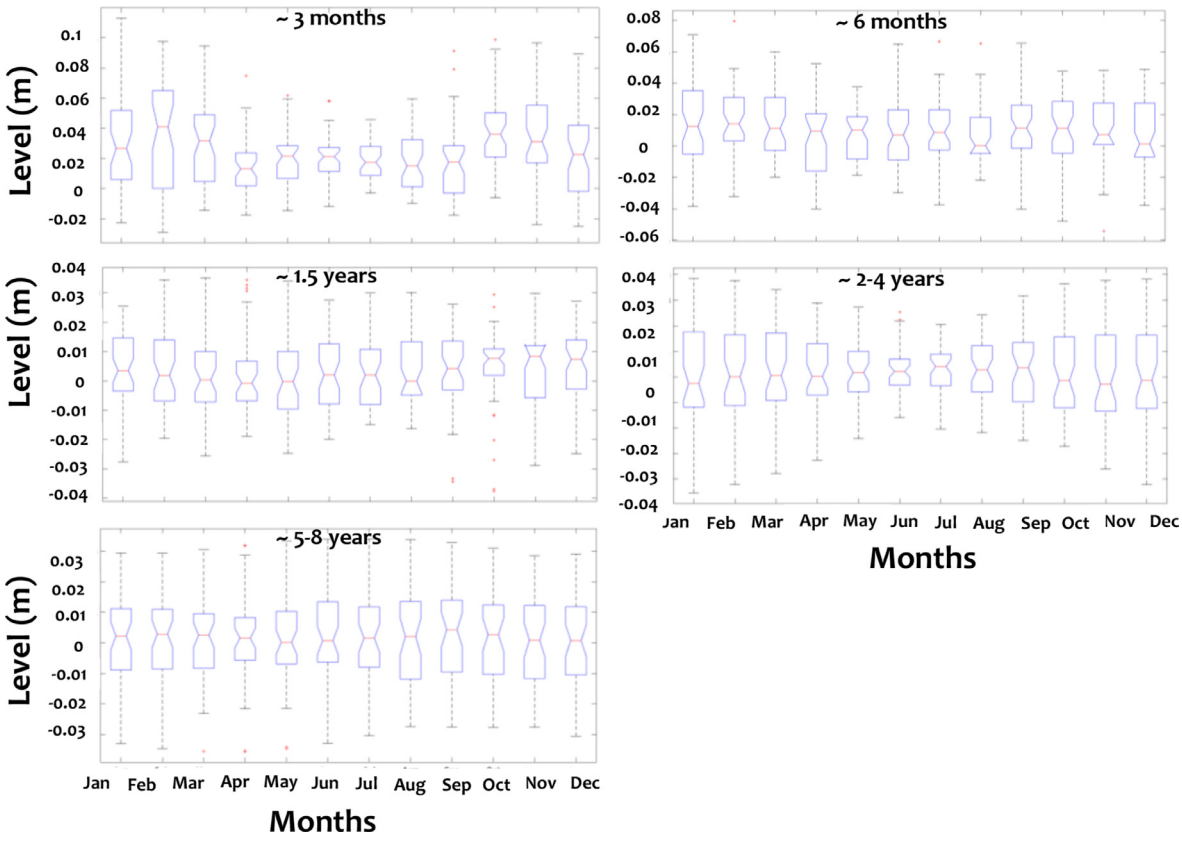

Figure 7 The boxplot of the monthly maxima of surges on the intermontly (∼3 months and ∼6 months) to the interannual (∼1.5-yr; ∼2–4-yr and ∼5–8-yr) scales; case of Dunkirk.

variances of these scales are higher than those resulting from the multiresolution analysis of the hourly surges: the variance of the intermonthly scales has a mean percentage of 45% of the total signal while the interannual scales vary between 28% and 36%.

Then, the nonstationary behavior of the monthly extreme surges has been addressed by investigating their physical connections with the different climate indices (i.e. SST, SLP, ZW, and NAO). The total signal (not decomposed) of the climate indices has been linked to the extreme components calculated previously. For each spectral component, a series of Monte Carlo simulations have been carried out to identify the most statistically significant correlation with the climate index. The best correlation of each surge component (i.e. ∼3-months and ∼6-months, ∼1.5-yr, ∼2–4-yr and 5–8-yr) with the suitable climate index (i.e. SST, SLP, ZW, and NAO) is illustrated in Fig. 8. The correlation coefficients vary between 0.5 and 0.6 at the intermonthly scales (i.e. ∼3-months and ∼6-months) showing good agreements of SST index with the extreme surges. The ∼1.5-yr component is linked to SLP index with correlation coefficients varying between 0.65 and 0.7. Significant coefficients higher than 0.7 have been observed for the interannual scales of ∼2–4-yr and ∼5–8-yr exhibiting strong links with ZW and NAO indices respectively.

In the second part of this section, a stationary and a nonstationary extreme value analyses based on the GEV distribution with time-dependent parameters (Coles, 2001) have been implemented to model the spectral component of the monthly maxima of the surges.

Here, we are interested to separately model the different components of the extreme surges by using the GEV distribution. The GEV distribution uses the maximum likelihood method with a parametrization of the different parameters of location, scale, and shape.

Five stationary GEV models (GEV01, GEV02, GEV3, GEV04, and GEV05) have been used to fit the different spectral components of the monthly extreme surges. The AIC criterion has been calculated for each spectral component (Table 3) to compare their distributions. Results show higher AIC scores for the intermonthly scales of ∼3-months and ∼6-months (GEV01 and GEV02); they decrease at larger-scales of ∼5.8-yr (GEV05). The differences between the observed extreme values and the empirical ones, calculated from the stationary GEV models (from GEV01 to GEV05), should be explained by significant discrepancies which vary according to the timescale of the extreme surges. These discrepancies decrease in the sites where the interannual scales (i.e. GEV04 and GEV05) experience a uniform trend of extremes.

With the aim of improving the modelling of extreme surges, five nonstationary GEV models (GEV1, GEV2, GEV3, GEV4 and GEV5) have been applied to all spectral components. The parameters of the nonstationary GEV distribution have been estimated using the maximum likelihood method (Coles, 2001). Maximizing the log-likelihood function has

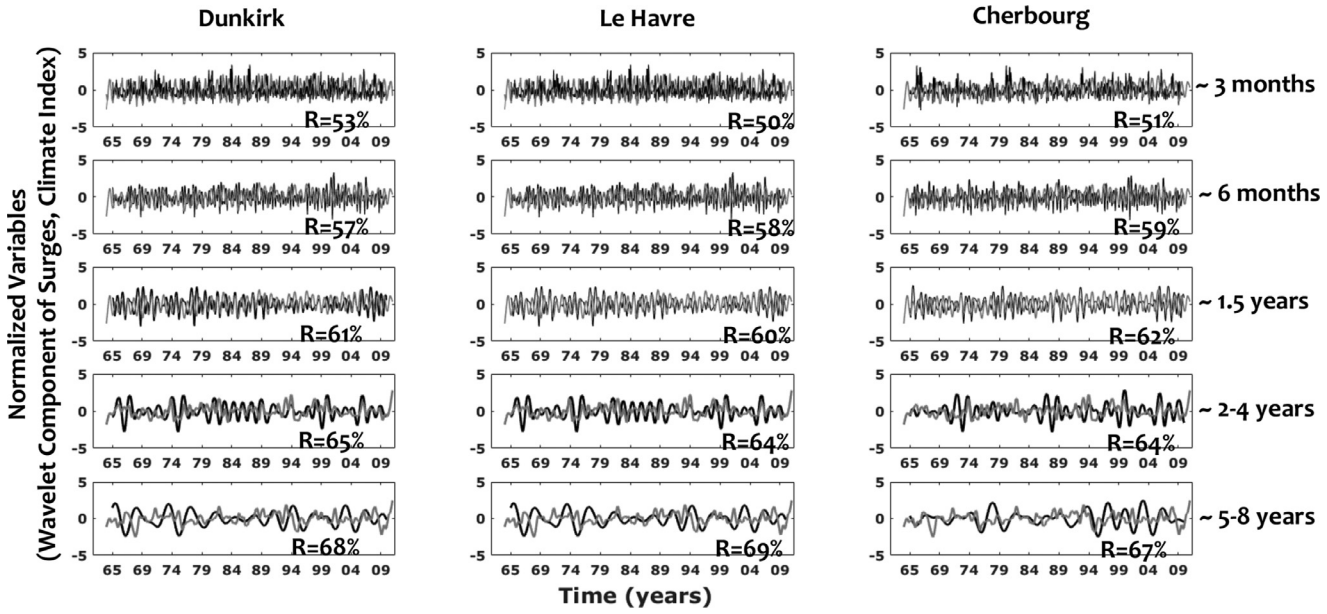

Figure 8 Multiresolution decomposition of the monthly maxima of surges (black line). The signal of climate oscillations associated with the different indices SST, SLP, ZW, NAO (grey line) has been correlated to the spectral components of surges. Only the connection maximizing the correlation coefficient between a selected climate index and the component of surges (from intermonthly to interannual timescales) is presented (the normalized values have been calculated to superpose both signals). The correlation coefficients are also displayed at each time scale.

Table 3 Akaike Information Criterion (AIC) test results for distribution models of extreme surges using the stationary GEV model.

	~ 3 months	~ 6 months	~ 1.5- y	~ 2–4 –y	~ 5–8-y
Dunkirk	-450	-352	-324	-352	-345
Le Havre	-410	-322	-320	-350	-352
Cherbourg	-395	-301	-314	-345	-350

Table 4 Akaike Information Criterion (AIC) test results for the distribution models of the extreme surges using the nonstationary GEV model.

	~ 3 months/*SST*	~ 6 months/*SST*	~ 1.5- y/*SLP*	~ 2–4 –y/*ZW*	~ 5–8-y/*NAO*
Dunkirk	-310	-282	-266	-248	-232
Le Havre	-308	-279	-260	-252	-243
Cherbourg	-315	-285	-264	-245	-245

been performed by means of the 'trust region reflective algorithm' (Coleman and Li, 1996).

For each model, the best climate index describing the internal oscillations of the monthly maxima has been used as a covariable in GEV distribution to address the nonstationary behavior of the extreme values. For each spectral component, the structure of the most appropriate nonstationary GEV distribution has been selected by choosing the most adequate climate index that minimizes the Akaike information criterion (Akaike, 1974). Here, the total signal of the climate index has been used as shown in Fig. 8. The goodness of the fit of each model has been checked through the visual inspection of the quantile-quantile (Q-Q) plots; these plots compare the empirical quantiles against the quantiles of the fitted model. The substantial departure from the diagonal indicates an inadequacy of the GEV model.

Results provided by GEV1–5 reveal a better performance (the lowest values of AIC) of extreme estimation compared to the previous models of GEV01–05 and give the most appropriate distributions by the use of the climate oscillations. Indeed, the SLP, ZW, and NAO indices have been used for the interannual scales of ~1.5-yr, ~2–4-yr, and ~5–8-yr respectively while the SST index has been selected as the most adequate for the intermonthly scales of ~3-months and ~6-months (Table 4). The Q-Q plots for the all timescales of the monthly maxima in Dunkirk are illustrated in Fig. 9; they confirm the suitability of the selected models.

Accordingly, the nonstationary GEV models have exhibited high improvements at all timescales, in particular at the intermonthly scales (GEV01/GEV1; GEV02/GEV2) where the AIC scores have significantly decreased.

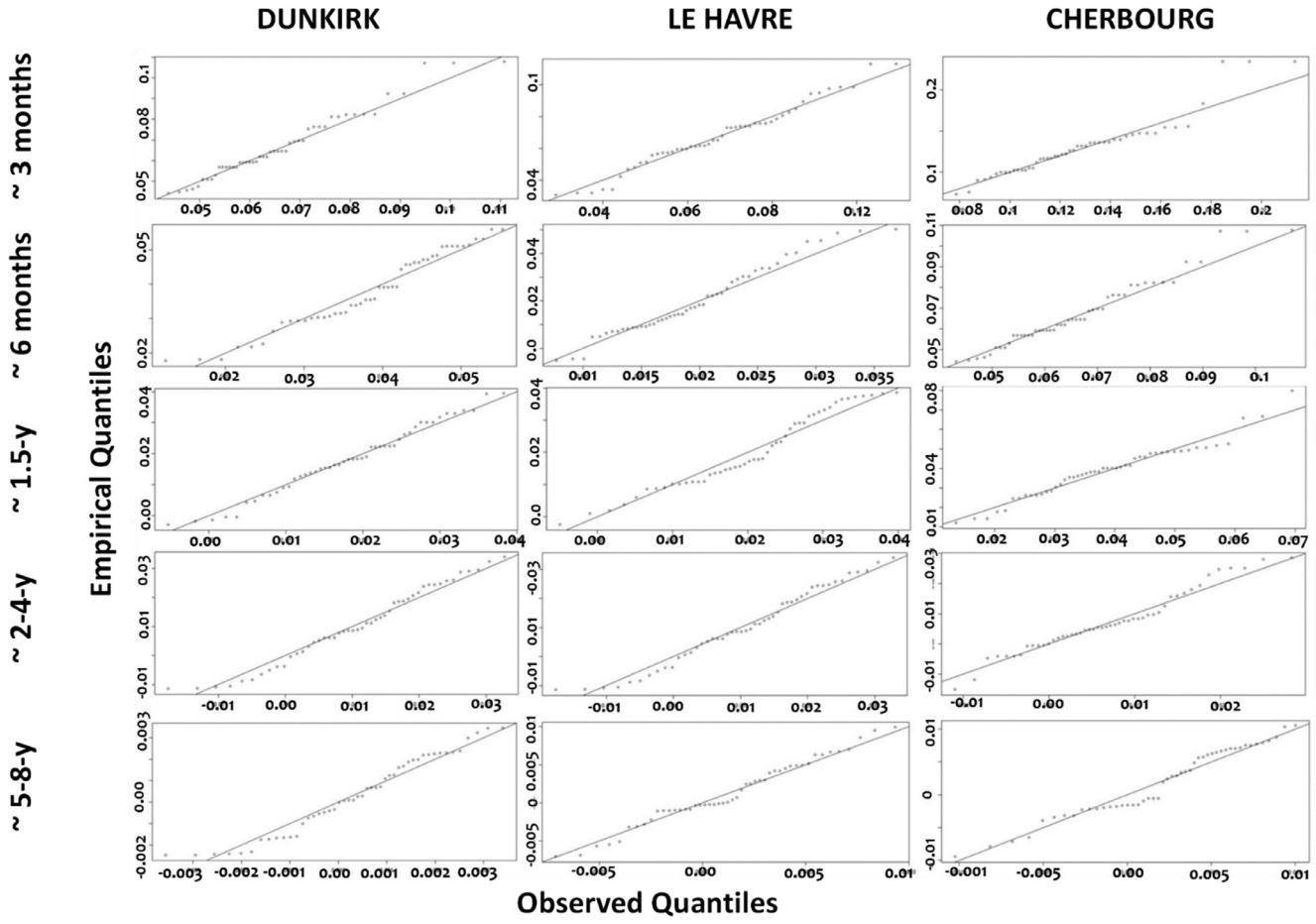

Figure 9 The quantile plot between observed and modelled extreme surges obtained using the nonstationary GEV model at different time scales.

4. Discussion

Results provided in the present research highlight the origin of the nonlinear relationship between large- and local-scales. Indeed, the intermonthly and the interannual extreme surges may be related to different combinations of several, not necessarily similar, oscillating atmospheric patterns. The use of a multiresolution approach to investigate the dynamics of the extreme surges into the downscaling studies proves to be useful for assessing the nonlinear interactions between large-scale climate variability and local-scale hydrodynamic changes of the sea-level hydrodynamics.

Investigating the physical relationships of the climate oscillations with the multiscale surges have shown that the multimodel climate ensemble should be used to better understand this complexity, in particular for extreme events.

The seasonal and the interannual physical relationships between the local hydrodynamics and the climate variability have been investigated in numerous previous works. They focused on the atmospheric circulation with different related mechanisms (e.g., Feliks et al., 2011; Lopez-Parages et al. 2012; Zampieri et al., 2017).

The use of the SST index to estimate the intermonthly extreme surges shows that their seasonal variability should be related to the variation of temperature in the sea surface controlled by an important atmosphere-ocean interaction in the Atlantic Sea. For short-scales, Bell and Goring (1998) investigated the relationship between the seasonal variations of the sea level and the SST along the north-east coasts of the New Zeland. They have demonstrated that the dominant influence of SST on the annual cycle of sea level is related to the thermo-steric sea-level adjustments with 50—80% of the variance in the annual frequency. Their works have suggested that the sea level generally peaks at the end of April (austral autumn) lagging the SST cycle by around 2 months, and its seasonal modulation is explained by changes in the oceanic current patterns and the seasonal coupling of climate oscillation effects. Previous studies have indicated the impact of the midlatitude SST gradients on the atmospheric circulation influencing the amplitude and the location of the storm tracks (e.g., Nakamura and Yamane 2009; O'Reilly and Czaja 2015; Small et al., 2014). For large-scales, the key role of SST in the atmosphere-ocean interaction has been also addressed by several works. According to some observational studies, the meridional shifts in the location of the Gulf Stream extension fronts are significantly linked to the large-scale variations in the atmospheric circulation at the intraseasonal timescales (e.g., Frankignoul et al., 2011). Recently, Wills et al. (2016) have examined the atmosphere-ocean interaction over the Gulf Stream and its relation with two potential different patterns of atmospheric circulation

anomalies: one pattern leads to SST field and another resultant pattern lags the SST field and is considered as an atmospheric response to midlatitude ocean forcing (Wills et al., 2016).

The spatial distribution of the SST anomalies is strongly related to the study area, the influence of the seabed topography and the runoff conditions. Considering the cases of the Bristol Channel (Mayes and Wheeler, 2013) and the Seine Bay in the English Channel, negative anomalies of SST are generally located near to coastal zones connected to hydrological systems and influenced by rivers and the annual regime of precipitations. The Northern Atlantic SST fields have been hypothesized to be linked to the interannual and the decadal persistence of atmospheric circulation anomalies (Namias, 1969; 1972). These anomalies have been defined to be connected to the Atlantic Multidecadal Oscillation (AMO) as a natural mode of variability (e.g., Schlesinger and Ramankutty, 1994).

Lopez-Parages et al. (2012) have studied the statistical predictability of the rainfall variability and stated that it can be improved by selecting the most suitable predictors depending on the period on which the prediction is carried out. They have also suggested that the nonstationary link of the rainfall with SST takes place when the dipolar patterns of the rainfall are reinforced with the negative phases of the AMO (Atlantic Multidecadal Oscillation) along the 20th century. In this study, the seasonal modulations of surges have displayed strong links with changes in SST phases. The SST patterns, due to the intrinsic modes of the atmospheric circulation variability, play a key role in regulating the global climate change and thus providing a source of potential predictability for the climate fluctuations on seasonal timescales. For larger scales, the SST index can be related to the Atlantic Multidecadal Oscillation.

The correlation between the ~1.5-yr interannual variability of extreme surges and the SLP index has been demonstrated for the study sites in this work. In this context, Turki et al. (2019) investigated the connection between the local dynamics of the surges and the global atmospheric circulation from SLP composites. They have suggested dipolar patterns of high-low pressures with a series of anomalies at the interannual and the interdecadal scales which should be related to the physical mechanisms linked to the North-Atlantic and ocean/atmospheric circulation oscillating at the same timescales. As documented by Frankignoul et al. (2011), the SLP fields and the baroclinic instability of wind stress are related to the Gulf Stream path as given by NCEP reanalysis; the dominant signal is a northward (southward) displacement of the Gulf Stream when the NAO reaches positive (negative) extrema. Zampieri et al. (2017) used the daily mean SLP fields to analyze the influence of the Atlantic sea temperature variability on the day-by-day sequence of large-scale atmospheric circulation patterns over the Euro-Atlantic region. They have found significant changes in the frequencies of certain weather regimes associated with the phase shifts of the AMO. For hydrological applications, several works have investigated the multiscale relationships between the local hydrological changes and the climate variability. Lavers et al. (2010) associated the 7.2-yr timescales to SLP patterns which are not exactly reminiscent of the NAO and define centers of action which are shifted to the North.

The relationship between the ZW index and the ~2-4-yr interannual variability of extreme surges has been significantly validated for the different sites of the English Channel coasts (as shown by GEV4). The ZW is generally associated with the atmospheric jets induced by the geostrophic equilibrium with the zonal mean height gradients. The wind-stress anomalies induce a zonal wind-stress increasing over the subtropical and the subpolar gyre boundaries. The fast barotropic response to the wind stress is explained by easterly winds in the Tropics and westerly winds in the midlatitude (Wang, 2001). According to some previous works (e.g., L'Heureux and Thompson 2006; Seager et al. 2003), the inter-hemispheric symmetry of both temperature and zonal wind bears great resemblance to regression patterns associated with the observed El Niño. Lu et al. (2008) investigated El Niño minus La Niña composites for the air temperature, zonal wind, and the tropopause pressure level. They derived these parameters from the difference of patterns between 14 warm years and 12 cold years. They have demonstrated that the tropospheric zonal wind is intensified near the equatorward flank of the jet, resulting in a equatorward strengthening of the jet. Andrade et al. (2012) investigated the extreme temperature in Europe and its occurrence in relation to the large-scale atmospheric circulation. They used the zonal wind component at 850 hPa to identify the positive and negative phases of the extreme periods. They suggested that both phases of extreme temperature changes are commonly connected to strong large-scale changes in zonal and meridional transports of heat and moisture, resulting in changes in the temperature patterns over western and central Europe (Corte-Real et al., 1995; Trigo et al., 2002). The studies from Mizuta (2012) and Zappa et al (2013) have demonstrated the physical links between the ZW and the extreme events from 11 Global Climate Model runs, suggesting the complex relationship between the climate oscillation and the jet stream activity. They have found a slight increase in the frequency and strength of the storms over the central Europe and decreases in the the number of the storms over the Norwegian and Mediterranean seas.

In the English Channel and along the UK and the Northern coasts, changes in trends of the extreme waters and storm surges have been explained by the variations of the energy pressure and ZW variability additional to the thermosteric fluctuations. These studies are in closer agreements with the present research where strong physical links between the ZW and the interannual component ~2-4-yr of the extreme surges have been demonstrated along the English Channel coasts (North France)

In the present study, the larger scales of the ~5-8-yr extreme surges have been linked to the NAO index. In agreement with other previous works (e.g. Marcos et al., 2012; Philips et al., 2013), the NAO is considered as an influencing climate driver for the large-scale atmospheric circulation. The physical mechanisms explaining the effects of the continuous changes in NAO patterns on the sea-level variability have been addressed in several studies (e.g., Trisimplis and Josey, 2001). Investigating the low frequencies of the sea levels has shown the existence of the long-term oscillations that originate from large-scale climate variability and thus control the interannual extreme surges along the English Channel. The key role of the NAO on the interannual

sea-level variability has been explained by some previous works: Philips et al. (2013) investigated the influence of the NAO on the mean and the maximum extreme sea levels in the Bristol Channel/Severn Estuary. They have demonstrated that when high NAO winters increase in the positive phase, wind speeds also escalate while increasing the negative NAO warmers results in low wind speeds. Then, the correlation between the low/high extreme surges and the NAO in the Atlantic has demonstrated a proportionality between NAO values and the augmentation in the winter storms. Feliks et al. (2011) defined significant oscillatory modes periods of ∼2.8-yr, ∼4.2-yr, and ∼5.8-yr in both observed NAO index and NAO atmospheric marine boundary layer simulations forced with SST; they have suggested that the atmospheric oscillatory modes should be induced by the Gulf Stream oceanic front.

We can conclude that different atmospheric oscillations could be related to the variations in the extreme surges according to the timescale considered; for each scale, its best physical connection with a specific climate oscillation is proven. This result suggests that the atmospheric circulation acts as a regulator controlling the multiscale variability of extreme surges with a nonlinear connection between the large-scale atmospheric circulation and the local scale hydrodynamics. Such nonlinear characteristics depend on the dynamics of the different sequences of the atmospheric and water vapour transport patterns during the month prior to the sea-level observations (e.g., Lavers et al., 2015).

The multiscale dependence of the local-scale hydrodynamic changes on the internal modes of the global-scale climate oscillations is still under debate. The use of the diverse indices of SST, NAO, ZW, and SLP could improve the estimation of the extreme values in the oceanography tasks and deepen the scientific understanding of the physical dynamics of surges in coastal environments.

In this work, the signal of surges has been linearly extracted from the total sea level time-series by the use of the classical harmonic analysis and thanks to the assumption that the water level is the sum of the mean sea level, tides, and surges. This assumption is not completely valid in the English Channel where the significant tide-surge interactions (Tomassin & Pirazzoli, 2008) and the effects of the sea-level rise on tides and surges are important (e.g. Idier et al., 2017).

Neglecting this nonlinear interaction between the surges, tides, and the sea-level rise in the present work suggests some uncertainties in the estimation of the spectral components from the instantaneous and monthly extreme surges. These uncertainties, extracted from the multiresolution analysis of, could not affect the main results of the present work since the nonstationary downscaling from the global atmospheric circulation to the local surges should be similar to upscaling the short scales of less than days to the scales of months, i.e. the upscaling in which the significant interaction between the surges and tides is more important

5. Conclusion

The results of the study explain key role of the climate patterns in the nonstationy dynamics of the extreme surges; the 'switch on' and 'off' of each climate index is strongly related to the multiscale variability. The use of the climate drivers could help improving the intermonthly and the interannual forecasting. Furthemore, they can be considered for GCM simulations that are designed to look for the physical mechanisms explaining the teleconnections between the atmospheric circulation and the sea-level variability.

Depending on the atmospheric circulation, described by the climate indices and weather forecasts, the stochastic models necessary for estimating the extreme surges can be developed and improved according with their multiscale variability and their physical connections with the global climate oscillations. Furthermore, similar assessments should be undertaken to improve understanding of the storminess uncertainty.

Acknowledgments

The authors are grateful to the international project COTEST funded by CNES-TOSCA and related to the future mission of Surface Water and Ocean Topography (SWOT). Authors also would like to thank National Navy Hydrographic Service and National Center for Environmental Prediction for providing sea level and atmospheric data. Finally, the authors would like to express their gratitude to the editor and the unknown reviewers for the excellent suggestions, which improved the original manuscript.

References

Akaike, H., 1974. Information theory as an extension of the maximum likelihood principle. In: Petrov, B.N., Csaki, F. (Eds.), Second International Symposium on Information Theory. Akademiai Kiado, Budapest, 267–281.

Andrade, C., Leite, S.M., Santos, J.A., 2012. Temperature extremes in Europe: overview of their driving atmospheric patterns. Nat. Hazards Earth Syst. Sci. 12, 1671–1691, https://doi.org/10.5194/nhess-12-1671-2012.

Bell, R., Goring, G., D., G., 1998. Seasonal Variability of Sea Level and Sea-surface Temperature on the North-east Coast of New Zealand. Estuar. Coast. Shelf. Sci. 46 (2), 307–319, https://doi.org/10.1006/ecss.1997.0286.

Bessoumoulin, P., 2002. Les tempêtes en France. Annales des Mines 9–14.

Brown, J., Souza, A., Wolf, J., 2010. Surge modelling in the eastern Irish Sea: Present and future storm impact. Ocean Dynam. 60 (2), 227–236, https://doi.org/10.1007/s10236-009-0248-8.

Colberg, F., McInnes, K.L., Grady, J., Hoeke, R., 2019. Atmospheric circulation changes and their impact on extreme sea levels around Australia. Nat. Hazards Earth Syst. Sci. 19, 1067–1086, https://doi.org/10.5194/nhess-19-1067-2019.

Coleman, T.F., Li, Y., 1996. An interior trust region approach for nonlinear minimization subject to bounds. SIAM J. Optim. 6 (2), 418–445, https://doi.org/10.1137/0806023.

Coles, S. , 2001. An Introduction to Statistical Modeling of Extreme Values. Springer, London, 209 pp.

Corte-Real, J., Zhang, Z., Wang, X., 1995. Large-scale circulation regimes and surface climatic anomalies over the Mediterranean. Int. J. Climatol. 15, 1135–1150, https://doi.org/10.1002/joc.3370151006.

Costa, S., Cantat, O., Pirazzoli, P.A., Lemaitre, M., Delahaye, D., 2004. Vents forts et submersions de tempête en Manche Orientale: analyse météo-marine sur la période historique ré-

cente. Actes du Colloque de l'Association Internationale de Climatologie. Climat, mémoire du temps. Les relations climat-espace-société, 277—280.

Dangendorf, S., Wahl, T., Hein, H., Jensen, J., Mai, S., Mudersbach, C., 2012. Level Variability and Influence of the North Atlantic Oscillation on Long-Term Trends in the German Bight. Water 4 (1), 170—195, https://doi.org/10.3390/w4010170.

Feliks, Y., Ghil, M., Robertson, A.W., 2011. The atmospheric circulation over the North Atlantic as induced by the SST field. J. Clim. 24 (2), 522—542, https://doi.org/10.1175/2010JCLI3859.1.

Frankignoul, C., Sennechael, N., Kwon, Y-O., Alexander, M.A., 2011. Influence of the Meridional Shifts of the Kuroshio and the Oyashio Extensions on the Atmospheric Circulation. J. Climate 24, 762—777, https://doi.org/10.1175/2010JCLI3731.1.

Haigh, I., Nicolls, R., Wells, N., 2009. Mean sea level trends around the English Channel over the 20th century and their wider context. Cont. Shelf. Res. 29, 2083—2098, https://doi.org/10.1016/j.csr.2009.07.013.

Haigh, I., Nicolls, R., Wells, N., 2010. Assessing changes in extreme sea levels: Application to the English Channel 1900—2006. Cont. Shelf. Res 30, 1042—1055, https://doi.org/10.1016/j.csr.2010.02.002.

Hanson, S., Nicholls, R., Ranger, N., Hallegatte, S., Dorfee-Morlot, J., Herweijer, C., Chateau, J., 2011. A global ranking of port cities with high exposure to climate extremes. Clim. Change. 104 (1), 89—111, https://doi.org/10.1007/s10584-010-9977-4.

Idier, D., Dumas, F., Muller, H., 2012. Tide-surge interaction in the English Channel. Nat. Hazards Earth Syst. Sci. 12, 3709—3718, https://doi.org/10.5194/nhess-12-3709-2012.

Idier, D., Paris, F., Le Cozannet, G., Boulahya, F., Dumas, F., 2017. Sea-level rise impacts on the tides of the European Shelf. Cont. Shelf. Res. 137, 56—71, https://doi.org/10.1016/j.csr.2017.01.007.

Labat, D., 2005. Recent advances in wavelet analyses: Part 1. A review of concepts. J. Hydrol. 314 (1—4), 275—288, https://doi.org/10.1016/j.jhydrol.2005.04.003.

Lavers, D.A., Hannah, D.M., Bradley, C., 2015. Connecting large-scale atmospheric circulation, river flow and groundwater levels in a chalk catchment in southern England. J. Hydrol. 523, 179—189, https://doi.org/10.1016/j.jhydrol.2015.01.060.

Lavers, D.A., Prudhomme, C., Hannah, D.M., 2010. Large-scale climate, precipitation and British river flows: Identifying hydroclimatological connections and dynamics. J. Hydrol. 395 (3—4), 242—255, https://doi.org/10.1016/j.jhydrol.2010.10.036.

Levin, S.A., 1992. The problem of pattern and scale in ecology: the Robert H. MacArthur Award Lecture. Ecology 73, 1943—1967.

L'Heureux, M.L., Thompson, D.W.J., 2006. Observed relationships between the El Niño—Southern Oscillation and the extratropical zonal-mean circulation. J. Climate. 19, 276—287, https://doi.org/10.1175/JCLI3617.1.

López-Parages, J., Rodríguez-Fonseca, B., 2012. Multidecadal modulation of El Niño influence on the Euro-Mediterranean rainfall. Geophys. Res. Lett. 39, art. 1009 no. L02704, https://doi.org/10.1029/2011GL050049.

Lu, J., Chen, G., Frierson, D., M., W., 2008. Response of the Zonal Mean Atmospheric Circulation to El Niño versus Global Warming. J. Climate 21, 5835—5851, https://doi.org/10.1175/2008JCLI2200.1.

Marcos, M., Chust, G., Jordá, G., Caballero, A., 2012. Effect of sealevel extremes on the western Basque coast during the 21st century. Clim. Res. 51 (3), 237—248, https://doi.org/10.3354/cr01069.

Masina, M., Lamberti, A., 2013. A nonstationary analysis for the Northern Adriatic extreme sea levels, J. Geophys. Res. 118, 3999—4016, https://doi.org/10.1002/jgrc.20313.

Massei, N., Dieppois, B., Hannah, D.M., Lavers, D.A., Fossa, M., Laignel, B., Debret, M., 2017. Multi-time-scale hydroclimate dynamics of a regional watershed and links to large-scale atmospheric circulation: Application to the Seine river catchment. France. J. Hydrol. 546, 262—275, https://doi.org/10.1016/j.jhydrol.2012.04.052.

Mayes, J., Wheeler, D., 2013. Regional weather and climates of the British Isles - Part 1: Introduction. Weather 68 (1), 3—8, https://doi.org/10.1002/wea.2041.

Menendez, M., Woodworth, P.L., 2010. Changes in extreme high water levels based on a quasi-global tide-gauge data set. J. Geophys. Res. 115, art. no. C10011, https://doi.org/10.1029/2009JC005997.

Mizuta, R., 2012. Intensification of extratropical cyclones associated with the polar jet change in the CMIP5 global warming projections. Geophys. Res. Lett. 39, 1—6. art. no. L19707, https://doi.org/10.1029/2012GL053032.

Nakamura, M., Yamane, S., 2009. Dominant anomaly patterns in the near-surface baroclinicity and accompanying anomalies in the atmosphere and oceans. Part I: North Atlantic basin. J. Climate 22, 880—904, https://doi.org/10.1175/2010JCLI3017.1.

Namias, J., 1969. On the causes of the small number of Atlantic hurricanes in 1968. Mon. Weather Rev. 97 (4), 346—348.

Nicholls, R.J., Marinova, N., Lowe, J.A., Brown, S., Vellinga, P., De Gusmao, D., Hinkel, J., Tol, R.S., 2011. Sea-level rise and its possible impacts given a "beyond 4 C world" in the twenty-first century. Philos. T. Roy. Soc. A 369, 161—181, https://doi.org/10.1098/rsta.2010.0291.

O'Reilly, C.H., Czaja, A., 2015. The response of the Pacific storm track and atmospheric circulation to Kuroshio Extension variability, Q. J. Roy. Meteor. Soc. 141 (686), 52—66, https://doi.org/10.1002/qj.2334.

Pasquini, A.I., Lecomte, K.L., Depetris, P.J., 2008. Climate change and recent water level variability in Patagonian proglacial lakes, Argentina. Global Planet. Change 63, 290—298.

Philips, M.R., Rees, E.F., Thomas, T., 2013. winds, sea level and North Atlantic Oscilation (NAO) influences: An evaluation; Global Planet. Change 100, 145—152, https://doi.org/10.1016/j.gloplacha.2012.10.01.

Pirazzoli, P.A., 2005. A review of possible eustatic, isostatic and tectonic contributions in eight late-Holocene relative sea-level histories from the Mediterranean area. Quaternary Sci. Rev. 24 (18—19), 1989—2001, https://doi.org/10.1016/j.quascirev.2004.06.026.

Pugh, D.J., 1987. Tides, Surges and Mean Sea-Level: A Handbook for Engineers and Scientists. John Wiley, Chichester 472 pp.

Sang, Y.F., 2013. A review on the applications of wavelet transform in hydrology time series analysis. Atmos. Res. 122, 8—15, https://doi.org/10.1016/j.atmosres.2012.11.003.

Schlesinger, M.E., Ramankutty, N., 1994. An oscillation in the global climate system of period 65—70 years. Nature 367, 723—726.

Seager, R., Harnik, N., Kushnir, Y., Robinson, W., Miller, J., 2003. Mechanisms of hemispherically symmetric climate variability. J. Climate 16, 2960—2978.

Shaw, A.G.P., Tsimplis, M.N., 2010. The 18.6 yr nodal modulation in the tides of Southern European Coasts. Cont. Shelf Res. 30 (2), 138—151, https://doi.org/10.1016/j.csr.2009.10.006.

SHOM, 2014. Caractérisation de 7 évènements de tempêtes de l'automne-hiver 2013—2014 N°001/2014.

Small, R.J., Tomas, R.A., Bryan, F.O., 2014. Storm track response to ocean fronts in a global high-resolution climate model. Clim. Dynam. 43, 805—828, https://doi.org/10.1007/s00382-013-1980-9.

Tomasin, A., Pirazzoli, P.A., 2008. Extreme Sea Levels in the English Channel: Calibration of the Joint Probability Method. J. Coastal Res. 24, 1—13, https://doi.org/10.2112/07-0826.1.

Torrence, C., Compo, G.P., 1998. A practical guide to wavelet analysis. B. Am. Meteorol. Soc. 79, 61—78, https://doi.org/10.1175/1520-0477(1998)079⟨0061:APGTWA⟩.0.CO;2.

Trigo, R.M., Osborn, T.J., Corte-Real, J., 2002. The North Atlantic Oscillation influence on Europe: climate impacts and associated physical mechanisms. Clim. Res. 20, 9—17, https://doi.org/10.3354/cr020009.

Trisimplis, M.N., Josey, S.A., 2001. Forcing of the Mediterranean Sea by atmospheric oscillations over the North Atlantic. Geophys. Res. Lett. 28, 803—806.

Tsimplis, M.N., Woodworth, P.L., 1994. The global distribution of the seasonal sea level cycle calculated from coastal tide gauge data. J. Geoph. Res. 99 (C8), 16031—16039.

Turki, I., Laignel, B., Chevalier, L., Massei, N., Costa, S, 2015b. On the Investigation of the Sea Level Variability in Coastal Zones using SWOT Satellite Mission: example of the Eastern English Channel (Western France). IEEE J. Sel. Top. Appl. 8 (4), 1564—1569, https://doi.org/10.1109/JSTARS.2015.2419693.

Turki, I., Laignel, B., Kakeh, N., Chevalier, L., Costa, S., 2015a. Methodology for Filling gaps and Forecast in sea level: application to the eastern English Channel and the North Atlantic Sea (western France). Ocean Dynam. 65 (9—10), 1221—1234, https://doi.org/10.1007/s10236-015-0824-z.

Turki, I., Massei, N., Laignel, B., 2019. Linking Sea Level Dynamic and Exceptional Events to Large-scale Atmospheric Circulation Variability: Case of Seine Bay, France. Oceanologia 61 (3), 321—330, https://doi.org/10.1016/j.oceano.2019.01.003.

Vousdoukas, M.I., Mentaschi, L., Voukouvalas, E., Verlaan, M., Feyen, L., 2017. Extreme sea levels on the rise along Europe's coasts. Earth's Future 5 (3), 304—323, https://doi.org/10.1002/2016EF000505.

Wang, C., 2001. Atlantic Climate Variability and Its Associated Atmospheric Circulation Cells. J. Climate 15, 1516—1536.

Williams, J., Irazoqui Apecechea, M., Saulter, A., Horsburgh, K.J., 2018. Radiational tides: their double-counting in storm surge forecasts and contribution to the Highest Astronomical Tide. Ocean Sci. 14, 1057—1068, https://doi.org/10.5194/os-14-1057-2018.

Wills, S.W., Thompson, D.W.J., Ciasto, L.M., 2016. On the Observed Relationships between Variability in Gulf Stream Sea Surface Temperatures and the Atmospheric Circulation over the North Atlantic. J. Climate 29, 3719—3730, https://doi.org/10.1175/JCLI-D-15-0820.1.

Yan, Z., Tsimplis, M.N., Woolf, D., 2004. Analysis of the relationship between the North Atlantic Oscillation and sea-level changes in northwestern Europe. Int. J. Climatol. 24, 743—758, https://doi.org/10.1002/joc.1035.

Zampieri, M., Toreti, A., Schindler, A., Escoccimarro, E., Gualdi, S., 2017. Atlantic multi-decadal oscillation influence on weather regimes over Europe and the Mediterranean in spring and summer. Global Planet. Change, 151, 92—100, https://doi.org/10.1016/j.gloplacha.2016.08.014.

Zappa, G., Shaffrey, L.C., Hodges, K.I., Sansom, P., Stephenson, D.B., 2013. A multimodel assessment of future projections of North Atlantic and European cyclones in the CMIP5 climate models. J. Climate 26, 5846—5862, https://doi.org/10.1175/JCLI-D-12-00573.1.